KU Leuven
Biomedical Sciences Group
Faculty of Medicine
Department of Biomedical Sciences

KU LEUVEN

**DOCTORAL SCHOOL
BIOMEDICAL SCIENCES**

CLINICAL AND PRECLINICAL APPLICATION OF MAGNETIC RESONANCE SPECTROSCOPY IN AGING AND AMYOTROPHIC LATERAL SCLEROSIS

Akila Weerasekera

<u>Jury</u>:

Promoter: Prof. Uwe Himmelreich
Co-promoter: Prof. Philip Van Damme
                        Dr. Tom Dresselaers

Chair: Prof. Tania Roskams
Secretary: Prof. Ludo Van Den Bosch
Jury members: Prof. Ludo Van Den Bosch
                        Prof. Philippe Demaerel
                        Prof. Margarida Julià-Sapé
                        Prof. Georgios Keliris

Dissertation presented in partial fulfilment of the requirements for the degree of Doctor in Biomedical Sciences

March 2019

Table of Contents

Acknowledgements

"Nothing worth having comes easy"

Undertaking this PhD has been a truly life-changing experience for me and it would not have been possible to do without the support and guidance that I received from many people.

A wide "spectrum" of individuals have contributed to forming of this thesis, for whom I am very grateful. First and foremost, I would like to express my sincere gratitude to my supervisor Prof. Uwe Himmelreich for the continuous guidance and personal support, for his patience, motivation, open-mindedness, enthusiasm, and immense knowledge. Your guidance and encouragement kept me motivated during this project and writing of this thesis. I could not have imagined having a better supervisor and mentor for my PhD study.

I would like to extend my gratitude to my co-supervisors, Dr. Tom Dresselaers and Prof. Philip Van Damme for their expert support and guidance throughout my PhD. I express my special thanks to my "unofficial" co-supervisor Dr. Diana Sima, who from the beginning of my PhD has been a pillar of strength to me. I highly value your insightful comments and sharing your tremendous experience in the subject, I am very grateful and thankful for all your support.

I would also like to express my gratitude to the internal jury members, prof. Ludo Van Den Bosch and prof. Philippe Demaerel, and external jury members, Dr. Margarida Julià-Sapé and prof. Georgios Keliris for being part of my thesis evaluation committee and for helping me to improve the content of this thesis manuscript.

iii

Summary

Amyotrophic lateral sclerosis (ALS) is a rapidly progressing neurodegenerative disorder that affects motor neurons in the brain, brainstem and the spinal cord. ALS is characterized by gradually weakening of muscles due to muscle-size decrease, which results in difficulties in limb movement, verbal fluency, swallowing, and eventually breathing. ALS leads to death in 2-3 years after diagnosis in about 50 % of patients, largely due to respiratory failure. Riluzole is the only currently approved drug for ALS patients in the United States and in Europe, with mild/moderate therapeutic effects seen in some patients. The diagnosis of ALS is currently based on clinical features and the exclusion of other diseases with similar symptoms. Several imaging techniques, including magnetic resonance (MR) modalities have also been used for diagnosis with varying success.

In this doctoral thesis, we mainly evaluated the diagnostic application of proton magnetic resonance spectroscopy (^{1}H-MRS) in the assessment of ALS in clinical and preclinical settings. Since ALS is the most common adult-onset motor neuron disease, we also examined the impact of age-related neurometaboliic changes on motor performance in a cohort of healthy individuals. In addition, we report the results of a methodological study conducted to quantify the neurotransmitters GABA and glutamate-glutamine with edited/unedited MR spectroscopy sequences (MEGA-PRESS) using three different spectral fitting methods.

In the age-related MRS study, we have focused specifically on the neurometabolic integrity of the left motor cortex and the occipital lobe, as both regions are thought to be principal nodes of the sensorimotor network underlying bimanual movement. The primary results of this study are that levels of multiple neurometabolites in both regions of the healthy human brain decreased significantly with age and that age-related declines in bimanual performance are related to low N-acetyl aspartate (NAA, neuronal marker) levels in the left motor cortex. Our findings suggest that the neurometabolites NAA and myo inositol could serve as biomarkers to assess the integrity of motor networks supporting motor control in general and bimanual coordination in particular.

In the clinical ALS study, we utilized conventional and advanced-edited MRS sequences to detect the neurometabolic profiles in patients. Moreover, we examined the relationships between motor cortex neurometabolite concentrations and clinical parameters, including ALS Functional Rating Scale-Revised (ALSFRS-R) score and Forced Vital Capacity (FVC). We showed significant changes in multiple neurometabolites in the motor cortex of ALS patients. Also, we observed that NAA levels in the bulbar-onset patients were significantly lower compared to the limb-onset patients. Changes in myo-inositol and glutamate-glutamine correlated with ALSFR-R score and FVC. Glutathione levels measured in ALS patients, for the first time using the novel edited MRS sequence HERMES showed a decreasing trend compared to healthy controls.

In an MRS methodological study, we compared and validated three currently available spectral fitting methods to assess the in vivo concentration of GABA and Glx (glutamate + glutamine) derived from edited MEGA-PRESS and unedited spectra. We have assessed the inter-subject variability in neurotransmitter levels arising from age effects, finding a good agreement between GABA values

determined by the different spectral fitting methods. Our initial results suggest that conventional MRS sequence with an echo time of 68ms may be used to measure GABA levels accurately in the absence of advanced MRS sequences.

Next, we investigated age-dependent effects of disease onset and progression on regional neurochemistry in the transgenic SOD1^{G93A} ALS mouse model using ^{1}H-MRS. We focused mainly on the brainstem region, since brainstem motor nuclei are severely affected regions in SOD1^{G93A} mice and ALS patients. In addition, a proof-of-concept (PoC) study was conducted to assess the effects of coconut oil supplementation on onset and progression of the disease in SOD^{G93A} mice. In the brainstem region, we discovered a gradual decrease in creatine levels starting from a pre-symptomatic age. At later time points, alterations in the form of decreased NAA, glutamate, glutamine and increased myo-inositol were observed in the motor cortex. The PoC revealed that the coconut oil supplementation of the regular diet delayed disease symptoms, enhanced motor performance, and prolonged survival in the SOD1^{G93A} mouse model. Furthermore, we confirm that ^{1}H-MRS has the potential to be a used as a diagnostic and a therapy monitoring tool in the SOD1^{G93A} ALS mouse model.

In the following preclinical study, we characterized for the first time the hTDP-43^{A315T} ALS mouse model using in vivo PET-MR imaging modalities and histology. Results from the study reveals several important neurochemical and neuropathological alterations in the hTDP-43^{A315T} ALS mouse model. PET data showed significant changes in glucose metabolism in the motor and somatosensory cortices and multiparametric (mp) MRI data revealed significant alterations in neurometabolic composition and transient diffusion property changes in various motor regions of the brain in hTDP-43^{A315T} mice. In addition, we were able to show, previously unreported nuclear clearance of TDP-43 and cytoplasmic TDP-43 proteinaceous inclusions present in the brains of symptomatic, late stage hTDP-43^{A315T} mice. This finding is particularly important since it follows the changes detected by PET imaging, suggesting the potential diagnostic applications. We conclude that multimodal imaging modalities such as PET and MR form a powerful tool for longitudinal non-invasive follow-up of disease progression in preclinical animal models.

Samenvatting

Amyotrofische laterale sclerose (ALS) is een snel vorderende neurodegeneratieve aandoening die de motorneuronen in de hersenen, de hersenstam en het ruggenmerg aantast. ALS wordt gekarakteriseerd door het geleidelijk verzwakken van de spieren door het afnemen van de spiergrootte, wat resulteert in moeilijkheden bij het bewegen van de ledematen, het spreken, het slikken, en uiteindelijk ook bij het ademhalen. 50% van de patiënten sterft binnen de 2-3 jaar na diagnose, voornamelijk door respiratoir falen. Riluzole is momenteel de enige goedgekeurde medicatie voor ALS patiënten in de Verenigde Staten en in Europa, waarbij bij sommige patiënten lichte/gematigde therapeutische effecten waargenomen worden. De diagnose van ALS wordt momenteel gesteld op basis van klinische karakteristieken en de uitsluiting van andere ziekten met gelijkaardige symptomen. Ook verschillende beeldvormingstechnieken, inclusief magnetische resonantie (MR) technieken zijn gebruikt voor diagnose, met wisselend succes.

In deze doctoraatsthesis hebben we voornamelijk de diagnostische toepassing van proton magnetische resonantie spectroscopie (^{1}H-MRS) geëvalueerd bij de studie van ALS in een klinisch en preklinisch kader. Aangezien ALS de meest voorkomende motorneuron aandoening is waarbij de eerste symptomen opduiken op volwassen leeftijd, hebben we ook de invloed van leeftijdsgerelateerde neurometabolische veranderingen op de motorische prestaties onderzocht in een groep van gezonde individuen. Bovendien rapporteren we ook de resultaten van een methodologische studie die uitgevoerd werd om de neurotransmitters GABA en glutamaat-glutamine te kwantificeren met behulp van bewerkte/onbewerkte MR spectroscopie sequenties (MEGA-PRESS), waarbij we gebruik maken van drie verschillende spectrale fitting methodes.

In de leeftijdsgerelateerde MRS-studie hebben we voornamelijk gefocust op de neurometabole integriteit van de linker motorcortex en de occipitale hersenkwab. Van beide regio's wordt gedacht dat ze de principale knooppunten zijn van het sensomotorische netwerk dat de bimanuele beweging onderligt. Het primaire resultaat van deze studie is dat de niveaus van de verschillende neurometabolieten in beide regio's van het gezonde menselijke brein significant dalen met leeftijd. Verder zien we ook dat leeftijdsafhankelijke daling in de bimanuele prestaties verbonden is aan lage N-acetylaspartaat (NAA, een neuronale marker) waarden in de linker motorcortex. Onze resultaten suggereren dat de neurometabolieten NAA en myo-inositol gebruikt zouden kunnen worden als biomerkers voor het bestuderen van de integriteit van motorische netwerken die de motorische controle in het algemeen en de bimanuele coördinatie specifiek ondersteunen.

In de klinische ALS studie gebruikten we conventionele en geavanceerde, bewerkte MRS sequenties om het neurometabole profiel van patiënten te detecteren. Verder bestudeerden we het verband tussen de neurometabole concentraties in de motorcortex en klinische parameters, zoals de 'ALS Functional Rating Scale-Revised (ALSFRS-R)' score en de geforceerde vitale capaciteit (FVC, forced vital capacity). We toonden aan dat er significante veranderingen zijn in verschillende neurometabolieten in de motorcortex van ALS patiënten. Bovendien observeerden we ook dat de NAA niveaus in de patiënten met een bulbaire vorm van ALS significant lager waren dan in patiënten met een ledemaat-type ALS. Veranderingen in myo-inositol en glutamaat-glutamine correleerden met de ALSFR-R score en FVC.

Glutathion niveaus werden voor de eerste maal gemeten in ALS patiënten met de nieuwe, bewerkte MRS sequentie HERMES. Er werd een dalende trend waargenomen in vergelijking met gezonde controles.

In een methodologische MRS studie vergeleken en valideerden we de drie momenteel beschikbare spectrale fitting methoden om de *in vivo* concentraties van GABA en Glx (glutamaat + glutamine) te bestuderen, afgeleid van bewerkte MEGA-PRESS en onbewerkte spectra. We bestuurden de intersubject variabiliteit op niveau van neurotransmitters voortkomend uit leeftijdsgebonden effecten. Hierbij vonden we een goede overeenkomst tussen de GABA waarden die we bepaald hadden met behulp van de verschillende spectrale fitting methoden. Onze initiële resultaten suggereren dat een conventionele MRS sequentie met een echotijd van 68 ms kan gebruikt worden om GABA niveaus accuraat te meten indien er geen meer geavanceerde MRS methoden beschikbaar zijn.

Voorts bestudeerden we de leeftijdsgerelateerde effecten van ziekteaanvang en progressie op regionale neurochemie in het transgene SOD1^{G93A} ALS muismodel met behulp van ^{1}H-MRS. We hebben voornamelijk gefocust op de hersenstamregio, aangezien voornamelijk de motornuclei in de hersenstam worden aangetast in deze muizen en bij ALS patiënten. Verder hebben we een proof-of-concept (PoC) studie uitgevoerd om de effecten van kokosnootoliesupplementen op de aanvang en progressie van de ziekte in SOD1^{G93A} muizen te bestuderen. In de hersenstam ontdekten we een graduele daling in creatine niveaus beginnende van een presymptomatische leeftijd. Op latere tijdspunten werden ook dalingen in NAA, glutamaat, glutamine en een stijging in myo-inositol waargenomen in de motorcortex. De PoC toonde aan dat een toevoeging van kokosnootolie aan het traditionele dieet de ziektesymptomen uitstelde, motorische prestaties verbeterde en de SOD1^{G93A} muizen langer leefden. Bovendien bevestigden we dat ^{1}H-MRS het potentieel heeft om gebruikt te worden als diagnostische en therapeutische monitoringstool in het SOD1^{G93A} ALS muismodel.

In de volgende preklinische studie hebben we voor het eerst het hTDP-43^{A315T} ALS muismodel gekarakteriseerd met behulp van *in vivo* PET-MR beeldvorming en histologie. De resultaten van deze studie tonen aan dat er verschillende belangrijke neurochemische en neuropathologische veranderingen aanwezig zijn in dit muismodel. De PET data tonen aan dat er significante veranderingen zijn in het glucose metabolisme in de motor- en somatosensorische cortex. Multiparametrische (mp) MRI bracht significante veranderingen aan het licht in de neurometabolische samenstellingen en de transiënte diffusie eigenschappen in verschillende motorregio's in het brein van hTDP-43^{A315T} muizen. Verder hebben we voor het eerst aangetoond dat er nucleaire klaring is van TDP-43 en cytoplasmatische TDP-43 proteïne-achtige inclusies in de hersenen van symptomatische, laat-stadium hTDP-43^{A315T} muizen. Aangezien deze bevindingen in lijn zijn met de veranderingen gedetecteerd door PET-beeldvorming, suggereren ze een mogelijke diagnostische toepassing. We besluiten dat multimodale beeldvormingsmodaliteiten zoals PET en MRI een krachtig middel vormen om ziekteprogressie longitudinaal en niet-invasief op te volgen in preklinische diermodellen

List of abbreviations

^{18}F	fluorine-18		MO	middle old
^{1}H	proton		MoCA	montreal cognitive assessment
AD	axial diffusivity		mPFC	medial prefrontal cortex
ADP	adenosine diphosphate		MR	magnetic resonance
ALS	amyotrophic Lateral sclerosis		MRI	magnetic resonance imaging
ALSFRS-R	ALS Functional Rating Scale-Revised		MRS	magnetic resonance spectroscopy
ASL	arterial spin labeling		Mx	motor cortex
ATP	adenosine triphosphate		MY	middle young
B_0	external magnetic field		NA	number of averages
BCT	bimanual coordination task		NAA	n-acetyl-aspartate
CBF	cerebral blood flow		NMR	nuclear magnetic resonance
CCW	counter clockwise		OA	old adults
CW	clockwise		OCC	occipital cortex
Cho	choline		PET	positron emission tomography
Cr	creatine		ppm	parts per million
CSF	cerebrospinal fluid		PPT	purdue pegboard task
DMN	default mode network		PRESS	point resolved spectroscopy
DWI	diffusion weighted imaging		PWI	perfusion weighted imaging
ES	end stage		RCT	randomized clinical trials
FA	fractional anisotropy		RD	radial diffusivity
FDG	flouro-deoxyglucose		RF	radio-frequency
FID	free induction decay		SM1	sensorimotor cortex
FOV	field of view		SNR	signal-to-noise ratio
FTLD	frontotemporal lobar dementia		SOD	superoxide dismutase
FVC	forced vital capacity		STEAM	stimulated echo acquisition mode
GABA	γ-aminobutyric acid		SUV	standard uptake values
Gln	glutamine		T_1	longitudinal relaxation time
Glu	glutamate		T_2	transversal relaxation time
Glx	glutamate+glutamine		TDP	TAR DNA binding protein
GM	gray matter		TE	echo time
GSH	glutathione		TMS	transcranial magnetic stimulation
Hb	hind brain		TR	Repetition time
HC	healthy control		VOI	volume of interest
Hz	hertz		WM	white matter
J	coupling constant		WT	wild type
MD	mean diffusivity		YA	young adults
mIns	myo inositol		γ	gyromagnetic ratio
MM	macromolecules		δ	chemical shift

1. | General Introduction

Understanding of normal aging and neurodegeneration is important in today's world because of the heavy personal and economic impact of neurodegenerative diseases. It is well known that the elderly population is dramatically increasing worldwide and the societal and financial burden due to neurodegenerative diseases is equally increasing. On the other hand life expectancy is also increasing for both males and females likely due to improved sanitation, education, housing and technology based advances in medical care (Denney *et al.*, 2013). It is estimated that around 23 million people worldwide are affected by neurodegenerative diseases (Mayeux *et al.*, 2012). The World Health Organization (WHO) predicts that by the year 2040, as developed countries' populations get older, neurodegenerative diseases such as dementia spectrum disorder (Alzheimer's disease etc.,) as well as disorders that affect primarily motor functions such as Parkinson's disease and amyotrophic lateral sclerosis (ALS), will surpass cancer to become the second leading cause of death after cardiovascular disease (Gammon 2014). In this regard, the use of non-invasive medical imaging modalities have become a key tool in diagnosing neurodegenerative diseases. Recent advances in magnetic resonance imaging (MRI) have tremendous and unique potential to have significant impact on health care, especially since diagnostic tools for neurological disorders have been severely scarce. Furthermore, the interest in developing pharmacological agents for neurodegenerative diseases has been exponentially increasing in the recent years. The overall neurodegenerative drug market alone is currently growing at about 12.0% a year (Atlas, 2009). In 2005, the global drug market for neurodegenerative disorders was valued at $14.5 billion, and by the year 2022 it is predicted to hit $45 billion (Atlas, 2009). It is quite obvious that multi-parametric MR methods will be highly valuable in assessing, guiding and further developing new treatments.

Neuroimaging refers to the use of techniques to non-invasively visualize the structure, chemistry and the function of the nervous system without surgery, incisions or other invasive methods. Mainly because of the non-invasive nature of these techniques neuroimaging has become a powerful tool for medical diagnosis, therapy assessment and basic research.

1.1   Neuroimaging: Background and Theory

The earliest account of non-invasively acquired information on brain activity dates back to 1882, where the Italian neuroscientist Angelo Mosso invented a non-invasive neuroimaging technique by attempting to measure the redistribution of cerebral blood flow (Sandrone *et al.*, 2013). Then in 1918, Walter Dandy, an American surgeon presented a techniques of ventriculography and pneumoencephalography (Hoeffner *et al.*, 2012). The former technique was used to image the brains ventricular system by injecting filtered air into lateral ventricles and the latter was used to image the cerebrospinal fluid (CSF) compartments around the base of the brain. A decade later, the Portuguese neurologist, Egas Moniz invented a cerebral angiography technique, where blood vessels in and around the brain could be visualized with high precision (Artico *et al.*, 2017). The modern era of neuroimaging began with the invention of the computed tomography (CT) which is a noninvasive technique that uses specialized X-

ray based equipment to produce cross-sectional images of the body that could be used for diagnostic and therapy assessment purposes. (Haaga, 1988). Soon after the introduction of CT, the development of radioligands enabled the single photon emission computed tomography (SPECT) and positron emission tomography (PET) of the brain to visualize and measure metabolic and physiological processes (Hutton, 2014). More or less at the same time, magnetic resonance imaging (MRI) was developed by the British physicist Peter Mansfield and the American chemist Paul Lauterbur, who were awarded the Nobel Prize for Physiology or Medicine in 2003. In the early 1980s, MRI was introduced to the clinic. Since then many improvements took place in the field of MR so that MRI became an indispensable diagnostic tool in medicine, in particular for diagnosing diseases of the brain (Edelman, 2014). **Figure 1.1** depicts past and modern neuroimaging modalities.
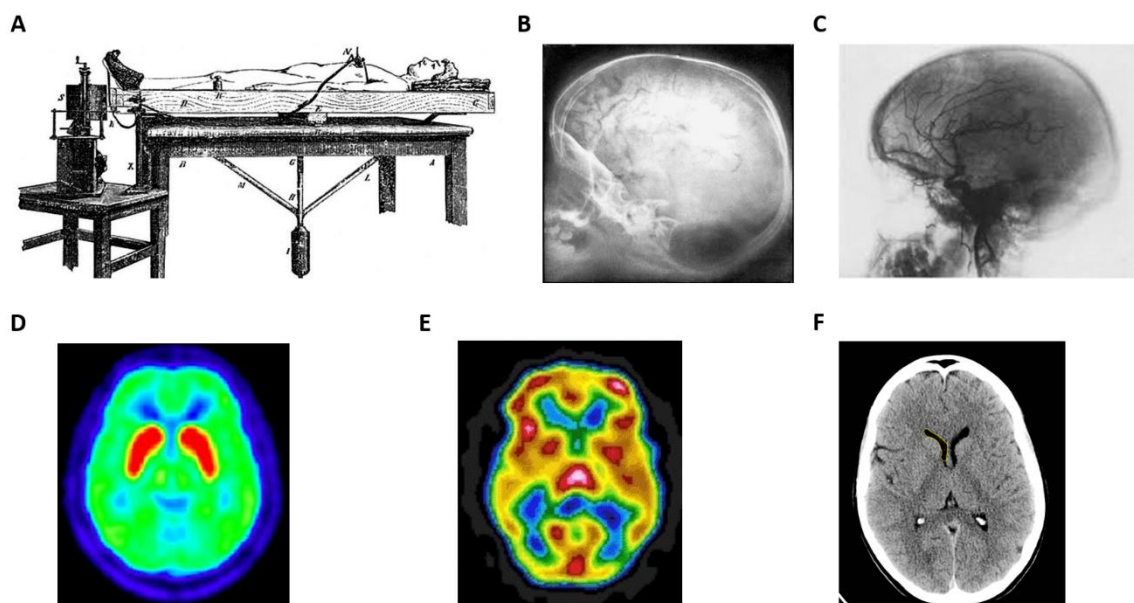
Figure 1.1: (A) Angelo Mosso's "human circulation balance" machine worked like a seesaw to measure blood flow changes to the brain (source: Sandrone *et al.*, 2014, Brain*).* (B) A pneumoencephalogram taken by Walter Dandy in 1919. (C) Angiogram obtained using Egas Moniz's cerebral angiography technique, demonstrating a large temporal mass lesion (source: Antunes, 1974, Neurosurg). (D) ^{11}C-RAC-PET scan of a healthy brain (source: Antonini, 1998, Ann Neurol). (E) SPECT brain image showing neuronal function (source: Uszler, 2017). (F) CT scan of a normal brain (source: Haaga, 1988).

1.1.1   Magnetic Resonance

Magnetic resonance imaging techniques were initially used to study the human brain anatomy. MRI offers excellent soft tissue contrast where high resolution anatomical information can be obtained. The basic principle of MRI is to first place the subject inside a homogenous field of magnetic field (measured in Tesla units) of the MRI scanner. When a subject is exposed to such an external magnetic field (B_0), previously randomly oriented magnetic moment of protons (e.g. as part of the hydrogen nuclei) change their orientation preferably parallel to this external magnetic field. This new orientation of protons

creates a magnetic vector in the direction of the external magnetic field, thus making the subject a magnet himself. This magnetic vector can now be manipulated by high-frequency radio-frequency (RF) pulses which are set to pass through the subject, and hereby disturbing the thermal equilibrium, resulting in the orientation changes of the net magnetic magnetization. After turning off these RF pulses, the protons precess (spinning positive charges) in a plane perpendicular to the magnetic field and then recoil towards the original orientation (returning to theramal equilibrium). This precession of protons creates a magnetic field which then could be measured by specific detectors surrounding the subject (body coils, head coils etc.). Hereby, a current is induced in the RF detectors. By measuring these signals the MR system can then reconstruct the images, reflecting the distribution of the protons and their magnetic properties (e. g. relaxation properties). In addition to the static magnetic field, magnetic field gradients are applied. Due to the field dependency of the precession frequency, these magnetic field gradients are used for the spatial encoding of the origin of the spins. The result of these processes is a high-resolution image of the subject with spatial resolutions ranging from about 0.5 mm^3 to 3 mm^3 (about 100 µm or below for mouse brain). This process is described in detail in section 1.1.1.4. While the early MRI scanners made use of magnetic fields ranging from 0.05 to 0.1 Tesla, current human MRI scanners use 1.5-3 or even to 7 Tesla. Moreover, today's preclinical micro-MR field strengths can range from small-bore animal systems with typically 9.4 to 21 Tesla.

> "Nikola Tesla first discovered the rotating magnetic field, the phenomenon that made magnetic resonance imaging possible, in Budapest, Hungary in 1882. Seventy-four years later scientists commemorated his discovery by naming the Tesla Unit as the official measure of the strength of a magnetic field."

1.1.1.1   Nuclear Magnetic Resonance: NMR and MRI

This discovery of nuclear magnetic resonance (NMR) phenomena led to the development of two technologies that revolutionized modern science and medicine and influenced many other areas: MRI and NMR spectroscopy. The basic principle of MRI and NMR spectroscopy is the same. The only difference is that in MRI, frequency differences are used for spatial encoding and in NMR spectroscopy, they are used for 'chemical' encoding. NMR spectroscopy has become an important tool used in chemistry and physics for analyzing the chemical composition and properties of matter. As mentioned before MRI is a tool used to non-invasively visualize the structure and function of organs and tissues. For clinical applications of NMR spectroscopy, the term MRS is frequently used.

1.1.1.2   Multi-parametric MRI

Since its early medical application about 40 years ago, magnetic resonance imaging has revolutionized neuroimaging providing high-resolution images non-invasively, with high soft tissue contrast and without the use of ionizing radiation. Although conventional MRI is able to generate only anatomical information, advances in the MR techniques have made it possible to provide insight into tissue microstructure, microvasculature, metabolism, function and connectivity (Tsougos 2018). These more advanced MRI techniques, including diffusion weighted and diffusion tensor imaging (DWI/DTI), magnetic resonance spectroscopy (MRS), functional MRI (fMRI) and perfusion imaging are used for investigation of neurodegeneration in routine diagnosing and research environments. DWI/DTI techniques measure the integrity but also the connectivity of tissue using readouts such as apparent

diffusion coefficient (ADC), fractional anisotropy (FA) and mean diffusivity (MD) (Chilla *et al.*, 2015). MRS is a noninvasive technique allowing the detection of the chemical composition/metabolites in target tissues (Tognarelli *et al.*, 2015). Cerebral perfusion and vascularization is also commonly measured in studies of neurodegeneration, including MRI methods like magnetic resonance angiography (MRA) (Schneider) 2005) using either dynamic susceptibility contrast-enhanced (DSC/DCE) MRI or arterial spin labeling (ASL) MRI. In the last two decades, brain function with or without stimulation (resting state, rs-fMRI) has been assessed using either blood oxygenation level dependent (BOLD) MRI or perfusion based MRI methods (Lv *et al.*, 2018).

1.1.1.3 Preclinical MRI

Preclinical animal models provide valuable contribution to improving our understanding of human pathologies, ranging from insights into the systemic and molecular basis of a disorder to the development of novel therapeutic approaches. . MRI is a useful imaging modality for the evaluation of animal models since it provides good spatial resolution without the need for using ionizing radiation. Due to its excellent soft tissue contrast and high resolution, MRI is used to distinguish normal and pathological tissue. Such *In vivo* evaluations exclude the necessity to sacrifice the animal and allows collection of longitudinal data. In addition, due to the possibility of performing repeated intraindividual measurements, the number of experimental groups can also be reduced. A Representative human and mouse brains and respective MR images are depicted in **Figure 1.2**.
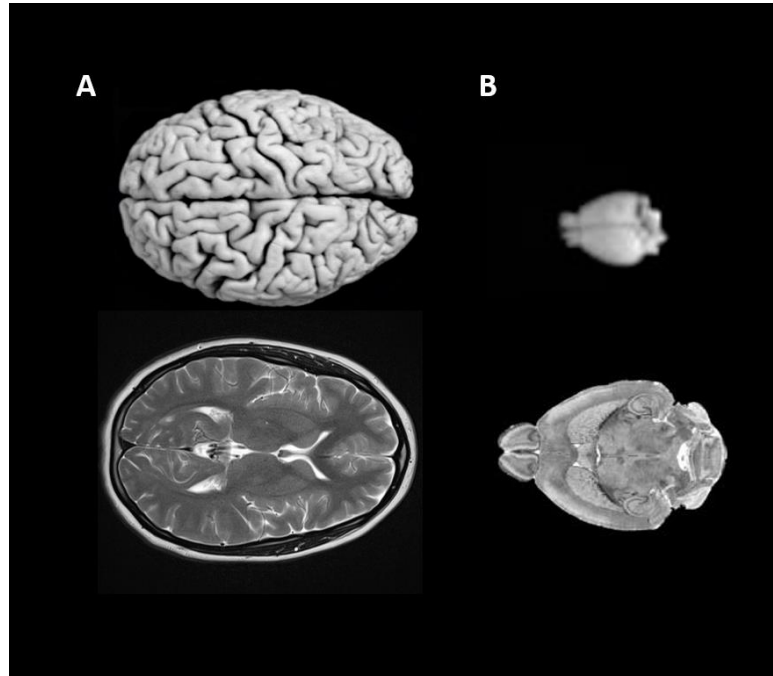
Figure 1.2: (A) Top: The human brain, bottom: Axial MR image of a human brain. **(B)** Top: mouse brain, bottom: Coronal image of a mouse brain. Figures are not to scale. Source: (brain images: Yáñez *et al.*, 2005).

1.1.1.4 MR physics

Atoms constitute of negatively charged electrons and a nuclei containing neutrons and positively charged protons. In NMR, magnetic properties of the nucleus, specifically the rotation (spinning) of the positively charged protons is used for generating a measurable response. This "spinning" of positively charged protons around its own axis creates an electric current that induces a small magnetic field. In the absence of an external magnetic field, these protons "spin" in random directions, not generating a measurable response (**Figure 1.3**). However, when placed in an external magnetic field ($\vec{\mathbf{B_0}}$) the individual magnetic moments of the individual protons align parallel or anti-parallel to this field, and each spin rotates within a cone around ($\vec{\mathbf{B_0}}$), which is called precession.

Spins are randomly oriented   Spins oriented with or against $\vec{\mathbf{B_0}}$
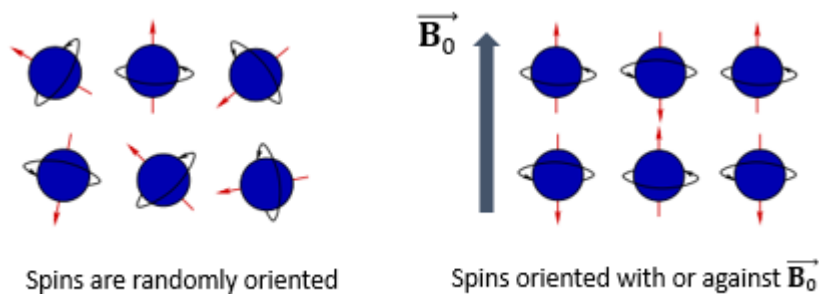
Figure 1.3: Random directions of spins in the absence of an external magnetic field (left) and aligned spins in the presence of an external magnetic field $\vec{\mathbf{B_0}}$ (right).

Larmor frequency and population difference between orientations

How fast the protons precess can be measured as precessional frequency. This precessional frequency, called the Larmor frequency is not constant and depends on the external magnetic field strength $\vec{\mathbf{B_0}}$. The Larmor frequency is calculated by:

$$\omega_0 = \gamma\, \vec{\mathbf{B_0}} \tag{2.1}$$

where γ is the gyromagnetic ratio which is specific to each nucleus, for instance Hydrogen has a gyromagnetic ratio γ = 42.57 MHz/T.

> "Protons exposed to an external magnetic field, $\vec{\mathbf{B_0}}$ = 3T, will have a precessional frequency of 127.74 MHz, which means that the protons will precess 128 million times per second at 3T."

It is more convenient to replace the individual spin by a single magnetization vector representing the spins of all the protons. The resulting net magnetization $\vec{M}$ is the sum of all the spins. In the absence of an external magnetic field, making the assumption of a uniform distribution of the spin orientations (random directions) in a given volume of interest, we end up with $\vec{M} = 0$ (spins cancel each other out). However, under the influence of an external magnetic field $\vec{\mathbf{B_0}}$, spins get aligned in the direction of that field and induce a magnetic vector (force) parallel to $\vec{\mathbf{B_0}}$ at equilibrium (**Figure 1.4**). By the laws of thermodynamics, the number of spins following the parallel orientation induced by $\vec{\mathbf{B_0}}$ (low energy

state, called spin-up) slightly outnumbers the amount of spins anti-parallel to $\overrightarrow{\mathbf{B_0}}$ (high energy state, called spin-down). The difference is small and determined by a Boltzmann distribution:

$$\frac{N_{antiparallel}}{N_{parallel}} = e^{-\frac{\Delta E_{B_0}}{kT}}$$

2.2

where $N_{antiparallel}$ and $N_{parallel}$ are respectively the number of spins in the high and low energy states, ΔE is the energy difference between the two states, k is the Boltzmann constant and T the temperature in Kelvin. Now the new net magnetization vector resulting from $\overrightarrow{\mathbf{B_0}}$, becomes $\vec{M} > 0$
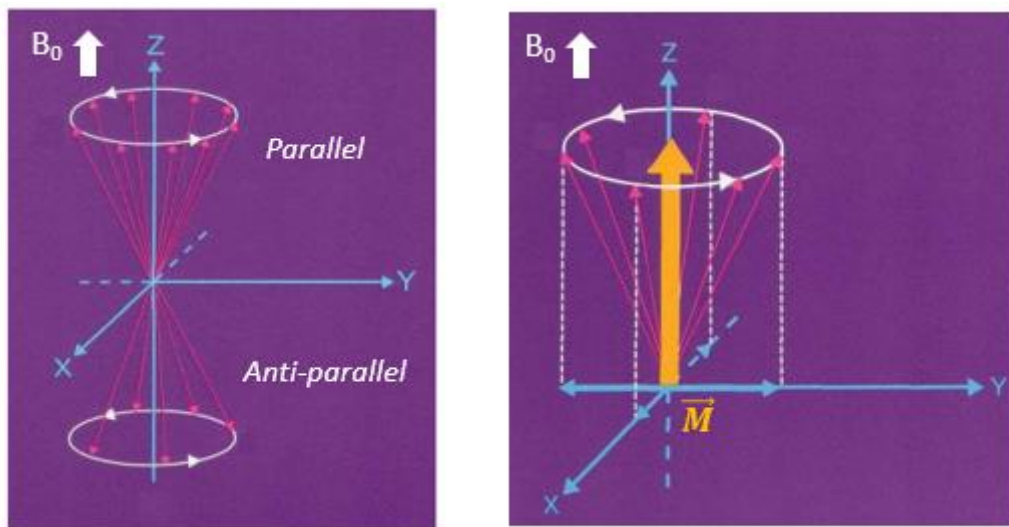
Figure 1.4: Smaller red arrows depict the precessing protons around the external magnetic field B_0 (z-axis). Larger orange arrow depict the magnetic vector created by the precessing protons. Source: Figure adapted from *MRI made easy* (p. 12, 13), by H.H.Schild, 1990, Berlin: Nationales Druckhaus. Copyright 1990 by Schering AG. (Schild 1990).

> "In the case of ^{1}H, at room temperature (296.15K), and for a magnetic field of 3T, there is a difference of 10 protons in favor of low energy protons among a total of 1 million protons. These excess protons give rise to the new magnetization vector $\overrightarrow{\mathbf{M}}$."

The new net magnetization $\vec{M}$ can be decomposed into two components (**Figure 1.4**):

• A longitudinal component $\overrightarrow{M_z}$, i.e. parallel to $\overrightarrow{\mathbf{B_0}}$
• A transverse component $\overrightarrow{M_{xy}}$, orthogonal to $\overrightarrow{\mathbf{B_0}}$

At equilibrium, after an adequate exposure time to $\overrightarrow{\mathbf{B_0}}$, the transverse component becomes, $\overrightarrow{M_{xy}} = 0$ and the longitudinal component $\overrightarrow{M_z} = \vec{M}$. A subject inside an MRI scanner becomes a magnet himself due to this new net magnetization $\overrightarrow{M_z} = \vec{M}$. In MR, it is this new magnetic vector $\vec{M}$ that is used to

acquire a signal. However, $\vec{M}$ cannot be measured directly as it is in the same direction, parallel to $\vec{\mathbf{B}_0}$. For this the transversal component $\overrightarrow{M_{xy}}$, is necessary, so we "excite" the protons.

Excitation

By applying a short burst of RF pulse into the patient inside the scanner, we can perturb the difference in the number of protons between the two energy states. However, not any RF pulse perturbs the alignment of the protons. For this, RF pulse with the Larmor frequency is used.

> "Only when the RF pulse and the protons have the same frequency, can protons pick up some energy from the radio wave, a phenomenon called resonance. This is where the "resonance" in magnetic resonance comes from."

The application of an RF pulse has two effects on the protons (**Figure 1.5**):

- It boosts some protons to a higher energy state. This results in the decrease of $\overrightarrow{M_z}$ (longitudinal magnetization). Depending on the RF pulse (duration, flip angle [α] 90° or 180° etc.) longitudinal magnetization may become, $\overrightarrow{M_z}$ = 0.
- It causes the protons to precess in step (*in-phase*). This establishes a new magnetization vector $\overrightarrow{M_{xy}}$ (transversal magnetization) in the xy plane.
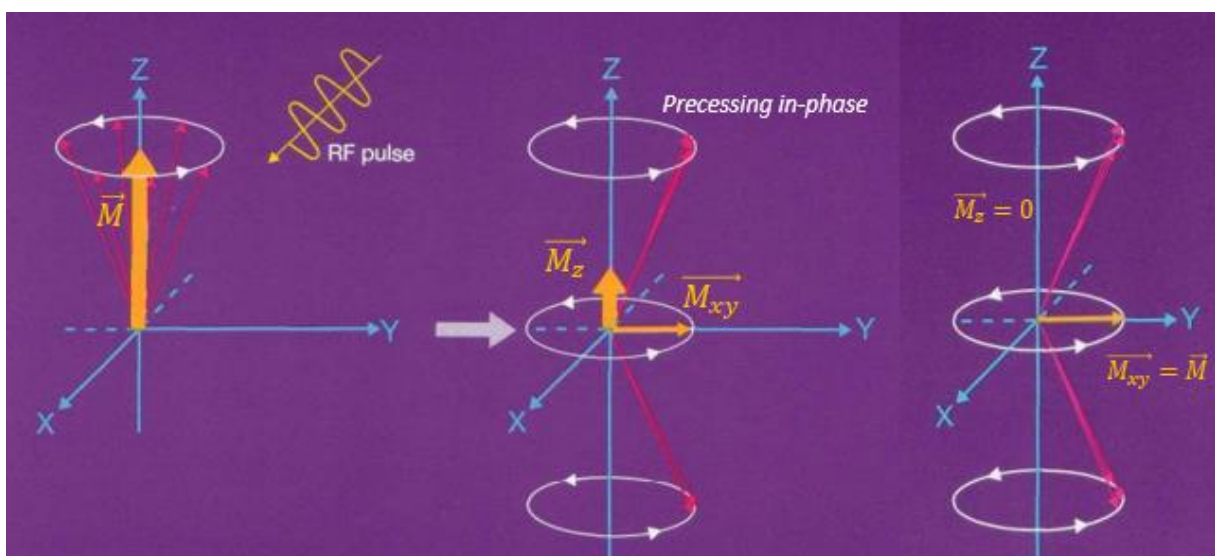
Figure 1.5: (Left) RF-pulse is applied to spin system created by $\vec{\mathbf{B}_0}$. (Middle) An RF-pulse lifts some spins into higher energy state (red arrows pointing down) and causes all spins to precess *in-phase* (red arrows congregate). Note the appearance of the transversal magnetization $(\overrightarrow{M_{xy}})$ and the decreasing longitudinal magnetization ($\overrightarrow{M_z}$). (Right) Depending on the RF-pulse, $\overrightarrow{M_z}$ can even completely disappear. Source: Figure adapted from *MRI made easy* (p. 21, 23), by H.H.Schild, 1990, Berlin: Nationales Druckhaus. Copyright 1990 by Schering AG. (Schild 1990).

The new transversal magnetization $\overrightarrow{M_{xy}}$ rotates with the precessing frequency. Thus for an external observer, $\overrightarrow{M_{xy}}$ constantly changes its direction, hence it can induce an electric current in a receiver coil placed perpendicular to the *xy*-plane. This electric current decays with time (relaxation time) and is

known as the free induction decay (FID). This time domain signal is Fourier transformed and generates is the MR signal used to create an images or spectra of the subject.

Relaxation

After the RF pulse is switched off, the net magnetization vector returns to its thermal equilibrium. This causes the established transverse magnetization $\overrightarrow{M_{xy}} \to 0$ (a process called transversal relaxation), and the longitudinal magnetization $\overrightarrow{M_z}$ grows back to its original size (a process called longitudinal relaxation).

Longitudinal relaxation (T₁): is based on the energy exchange between protons and surrounding molecules. This energy dissipation is characterized by the restoration of the longitudinal component to its equilibrium value. This recovery process is modeled by an exponential function characterized by a time constant T_1, the period for the longitudinal magnetization to recover 63% of its equilibrium value (**Figure 1.6 left**). For a 90°excitation pulse, M_z at time t is given by:

$$M_{z(t)} = M \left(1 - e^{-\frac{t}{T_1}}\right) \tag{2.3}$$

The relaxation process is considered complete after 5 T_1 periods.

Transversal relaxation (T₂): refers to the loss of net magnetization in the transverse plane related to protons dephasing (loss of coherence). Spins not only release energy to surrounding lattice molecules but also to other neighboring non-excited spins. This process is also modeled by an exponential function characterized by another time constant T_2, which corresponds to the period for the transversal component to lose 63% of its value just after the RF pulse (**Figure 1.6 right**):

$$M_{xy(t)} = M \, e^{-\frac{t}{T_2}} \tag{2.4}$$

This dephasing is further increased by local magnetic field inhomogeneities, and a time constant slightly different to T_2, denoted by T_{2^*}, is therefore used. Different brain tissues types are characterized by their respective T_1 and T_2 values, as shown in **Table 1.1**. The intensities of MR images comes from these values.
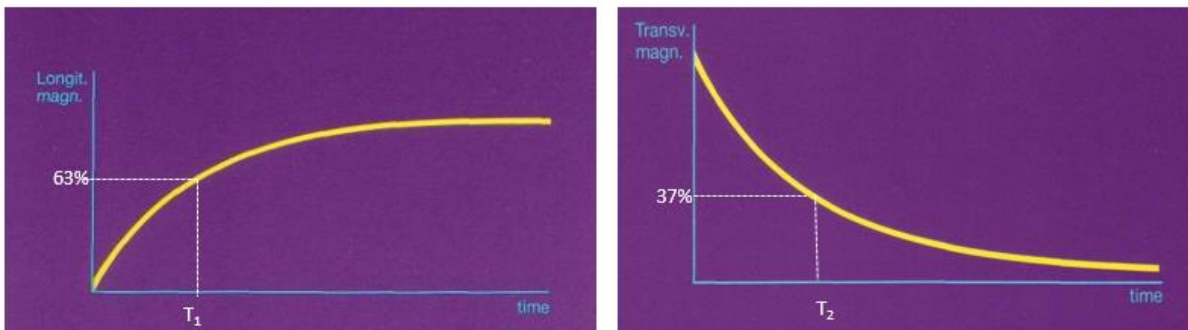
Figure 1.6: (Left) longitudinal magnetization vs time after the RF-pulse (T1-curve). (Right) Transversal magnetization vs. time after the RF-pulse (T2-curve). Source: Figure adapted from *MRI made easy* (p. 27, 30), by H.H.Schild, 1990, Berlin: Nationales Druckhaus. Copyright 1990 by Schering AG. (Schild 1990).

Table 1.1: Relaxation times for different tissues at 1.5T. Sources: [Webb 2003; Meier 2012].

Brain Tissue	T_1 (ms)	T_2 (ms)	%Water
Cerebro-spinal fluid	4000	2000	97
Grey Matter	900	100	80
White Matter	780	90	72
Fat	260	80	0

Pulse sequence and image construction

A pulse sequence is a series of RF-pulses and/or magnetic field gradients applied to an object/subject to produce a specific MR signal. Magnetic field gradients applied during a pulse sequence adjust the $\vec{\mathbf{B}_0}$ field so that the magnetic field varies with spatial position in a linear mode within the scanner. These gradients are represented as G_x, G_y, and G_z to denote physical gradients in 3-spatial dimensions. These three-spatial gradient coils are placed within the bore of the magnet. As a result of these gradients, nuclei at different positions along the gradient direction will experience a different local magnetic field, and due to this slight variation in magnetic field the nuclei will precess with a slightly different frequency. **Figure 1.7** illustrates a basic spin-echo pulse sequence. A gradient G_z in the $\vec{\mathbf{B}_0}$ direction results in a linear intensity variation of the magnetic field that is used to select a slice. In this case, a slice is a plane orthogonal to $\vec{\mathbf{B}_0}$. As mentioned before the spins of a given slice are characterized by the Larmor frequency. After the application of an RF pulse at the frequency related to the target slice, two transient gradients are applied to encode the x and y dimensions in the slice plane. A gradient G_y in the y direction induces a phase shift related to the position along the y axis. This is called the phase encoding. Another gradient G_x in the remaining x direction is applied, leading to a precession frequency variation along the x axis. This is called the frequency encoding. This process performs an acquisition of the spatial data in the frequency domain, called the *k-space*. For each selected slice, an inverse Fourier Transform finally maps the data back into the spatial domain, which is the MR image.

Echo Time and Repetition Time

A pulse sequence is furthermore also characterized by two main operator–selected parameters. The echo time (TE) is the time from the center of the RF-pulse to the center of the echo (MR signal) (**Figure 1.7**), and its systematic variation allows imaging the T_2 contrast between tissues. The repetition time (TR) is the duration between two successive RF- pulses, and its systematic variation allows imaging the T_1 contrast between tissues.

T1-weighted and T2-weighted MRI

The most basic MRI sequences used are spin echo sequences with so called T_1 and T_2-weighting. T_1-weighted images are acquired using short TE and TR times where T_2-weighted images are acquired using long TE and TR times. In these images, the brightness and contrast are primarily determined by the T_1 and T_2 properties of the tissue.

> "In general, T_1- and T_2-weighted images can be easily differentiated by looking at the CSF. CSF is dark on T_1-weighted imaging and bright on T_2-weighted imaging." (Preston 2006)
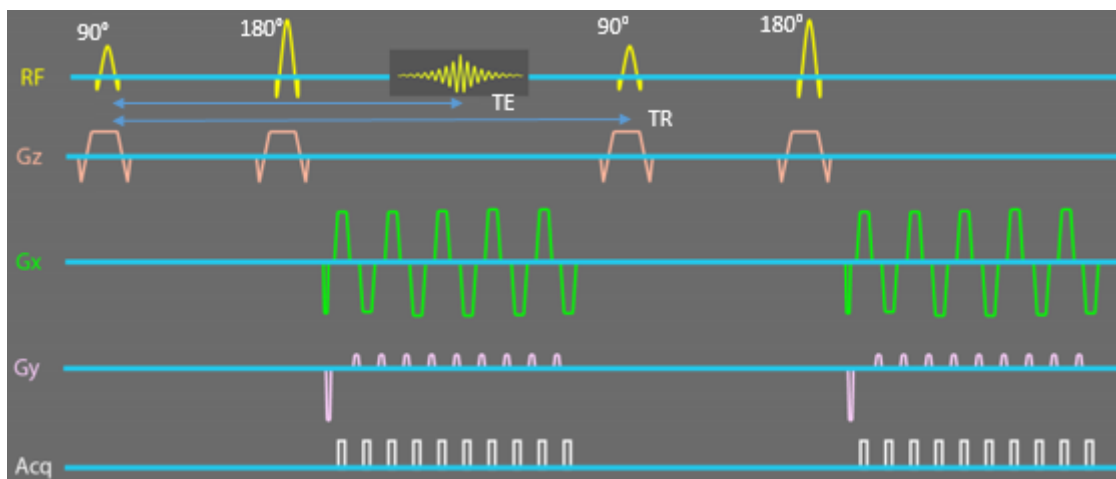
Figure 1.7: A pulse sequence diagram of a spin-echo sequence.

1.1.1.5 Advanced MR techniques

Above-mentioned imaging techniques are capable of providing mostly structural information. They are and usually referred to as "conventional" or 'anatomical' MRI techniques. Successively, physical phenomena that previously often caused image artefacts opened the path to novel imaging contrasts. This is the case of sequences sensitized to diffusion, flow, and local field inhomogeneities induced by physiological and metabolic changes. This has led to the implementation of advanced MR techniques known as diffusion-weighted, perfusion, magnetization transfer, functional MRI and MR spectroscopy. In this thesis, diffusion, perfusion MRI and MR spectroscopy was utilized.

Perfusion weighted MRI

Perfusion weighted MRI (PWI) complements the anatomical information acquired with conventional MRI, as it is mainly applied for investigating vascular and tumoral brain pathologies (Essig *et al.*, 2013). It provides measurements of the parameters of cerebral micro-vascularization, such as cerebral blood volume (CBV) and cerebral blood flow (CBF) (Jahng *et al.*, 2014). It relies on using either an endogenous or exogenous tracer, followed by measurements of the transient signal through the brain during the first pass of the tracer. Arterial spin labeling (ASL) technique uses magnetically labeled blood as an endogenous tracer. The labeling consists of a local magnetization inversion of arterial blood that is

achieved prior to image acquisition using dedicated RF pulses (pulsed ASL). In ASL, the signal is proportional to capillary blood flow, which is comparatively high in rodents. In this thesis, CBF values for the transgenic hTDP-43^{A315T} mouse model were calculated using ASL MRI (**Figure 1.8**).

> "Quantitative CBF measurements have provided information on microvascular alterations in mouse models of Alzheimer's disease" (Weidensteiner *et al*., 2009; Faure *et al*., 2009)
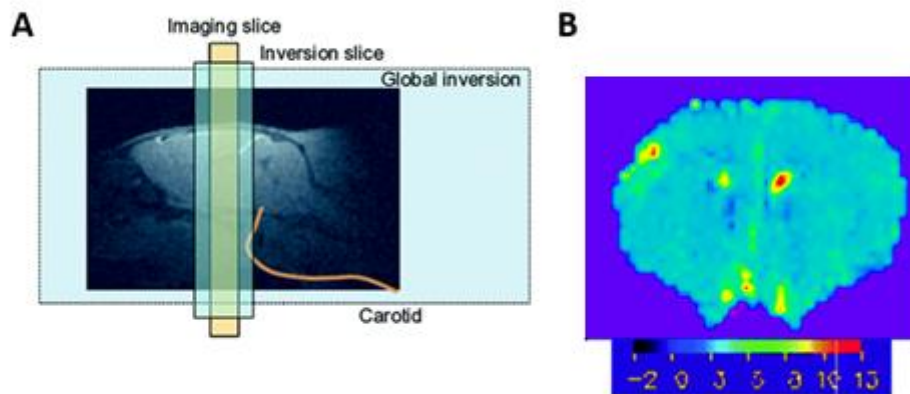
Figure 1.8: (**A**) FAIR pulsed ASL compares the magnetization after either global (control) or slice-selective inversion that is generated symmetrically around the imaging slice [Kober *et al*., 2011]. (**B**) Mouse cerebral blood flow maps (ml/100g/min).

Diffusion MRI

Diffusion MRI is an advanced non-invasive imaging technique which provides information about the movement of water molecules in biological environments, where it can interact with macromolecules, fibers, membranes, or other cellular structures. Directionally dependant diffusion is known as as anisotropic. Usually, inside the brain, three types of diffusion is seen: free isotropic, encountered mostly in CSF or fluid filled lesions, restricted isotropic, encountered mostly in gray matter, and anisotropic, encountered mostly along white matter fiber tracts. In highly organized tissues (e.g., neurons, white matter tracts), diffusion occurs preferentially along one direction. For example, in white matter tracts, myelin sheaths enclose the neurons and prevent the diffusion of water across the myelin sheath but permit to diffuse in the direction of the axons. By acquiring diffusion information in at least 6 different directions, we can calculate diffusion indices such as the fractional anisotropy (FA), mean diffusivity (MD), axial diffusivity (AD) and radial diffusivity (RD) maps. For example, high FA values represent anisotropic diffusion and low FA values indicate restriction in diffusion, usually indicating pathological conditions (**Figure 1.9**).
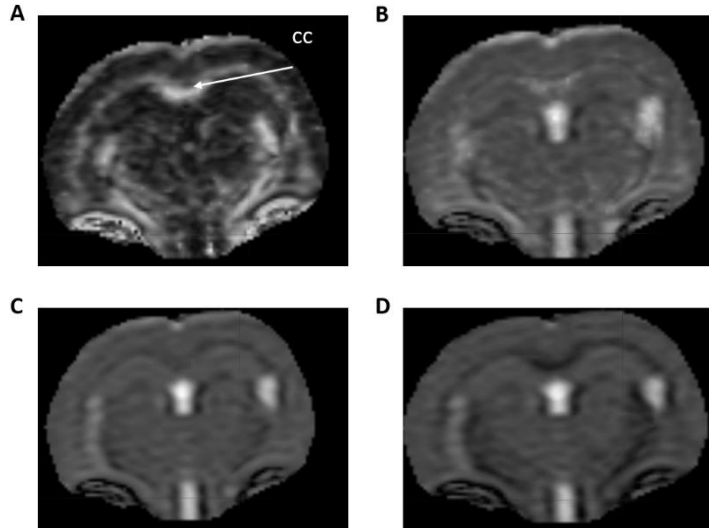
Figure 1.9: Diffusion index maps of axial mouse brain slices. (**A**) Fractional anisotropy. (**B**) Mean diffusivity. (**C**) Axial diffusivity. (**D**) Radial diffusivity. cc: corpus callosum.

Magnetic Resonance Spectroscopy (MRS)

MRS has proven to be a powerful technique to supply information about the chemical structure of molecules. In vitro MRS of biological or synthetic molecules is usually performed on a uniform sample, i.e. the concentration and composition are constant throughout the sample, such that the sample dimension and location need not be considered as an experimental parameter. However, this condition is usually not met for *in vivo* MRS. The concentration, composition, relaxation and other properties of compounds can vary throughout the object under investigation. Such variations can be considerable in cases where normal and pathological tissues (i.e. tumors, infarctions) are studied. Therefore, *in vivo* MRS is often combined with techniques that allow the detection of spatially localized volumes.

Chemical-Shift

The external magnetic field, B0, is normally modulated around the nuclei due to the shielding effects by neighboring electrons. These effects are proportional to the external field and, consequently, the local magnetic field is given by:

$$\mathbf{B}_{local} = \mathbf{B}_0(1 - \sigma) \tag{2.5}$$

where σ is the shielding constant which depends on the chemical environment of the nucleus. The chemical shift δ is defined as:

$$\delta = \frac{\omega - \omega_{ref}}{\omega_{ref}} \tag{2.6}$$

where ω and ω_{ref} are the frequencies of the compound under investigation and of a reference compound, respectively.

Most often, chemical shifts are not expressed in units of Hertz, since it would make chemical shifts dependent on the magnetic field strength. Instead chemical shifts are expressed in terms of ppm by referencing to a standard frequency given at a particular magnetic field strength. By convention the chemical shift (δ) is defined as:

$$\delta = \frac{\omega - \omega_{ref}}{\omega_{ref}} \times 10^6 \tag{2.7}$$

J-coupling

J-couplings, sometimes referred as scalar couplings are interceded through chemical bonds connecting two spins. J-coupling results from indirect interaction between one nucleus to another on the same molecule mediated through bonding electrons. This interaction results in the splitting of spectral peaks into doublets, triplets or higher order multiplets. A spectral peak will be split through J-coupling under certain conditions:

- The nuclei must be non-equivalent (chemically discernible).
- The distance between nonequivalent nuclei must be less than 4 bonds lengths.

This is illustrated using the NMR spectrum of the chloroethane (CH_3-CH_2-Cl) molecule (**Figure 1.10**). Chloroethane contains hydrogen-nuclei in two different chemical environments (nonequivalent): methyl (−CH3) and methylene (−CH2−), with resonances at chemical shifts (δ) 1.2 and 3.6 ppm respectively. As depicted in the spectrum, the two spectral peaks are split into a triplet and quartet respectively due to J-coupling. The distance between the subpeaks in a multiplet is determined by the coupling constant (J), which for chloroethane has a value of about 7 Hz (Castillo *et al.*, 2010).
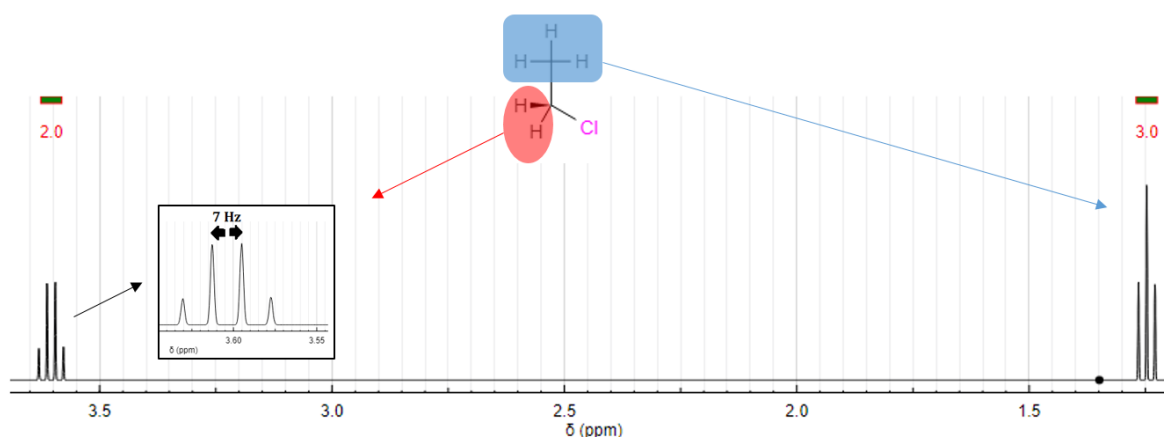
Figure 1.10: ¹H NMR spectrum of chloroethane depicting the splitting of spectral peaks, at chemical shifts *δ* = 1.2 and 3.6 into a triplet and quartet due to *J*-coupling.

1.1.1.6 *In vivo* MRS

In vivo MRS, the technique extensively used in this thesis, complements MR imaging as a non-invasive assessment of tissues. MRS is used to acquire signals from metabolites that are present in tissues at much lower concentrations than water. Peaks in MR spectra correspond to different metabolites and are identified mainly by their resonance frequencies (i.e., position in the spectrum) and expressed as the shift in frequency in parts-per-million (ppm) relative to a standard (typically water at 4.77ppm at body temperature or other known metabolites). The area under each spectral peak is calculated as a measure of the metabolite concentration in a given voxel. However, this association depends on multiple instrumental and biophysical parameters, such as the pulse sequence used, the metabolite relaxation times and J-coupling [Lin *et al.*, 2005]. Principles of MRS and applications parameters are further discussed in following sections.

In vivo MRS considerations

In order to acquire quantitative MRS spectra certain parameters needs to be optimized, these include the echo time (TE), repetition time (TR), voxel size and number of averages (NA).

Echo Time and Repetition Time in MRS

Brain metabolites also have measurable T1 and T2 relaxation times which vary with the local environment (brain region, pathology etc.), and magnetic field strength of the scanner. Average relaxation times measured at 3T for common metabolites are shown in **Table 1.2**. At short TE's (e.g., 20 ms or less) (**Figure 1.11 left**), all metabolic signals will be at their maximum values since due to the short time left for undergoing T2 decay. Moreover, the phase-modulating effects of J-coupling evolution (J-modulations) are also minimized at short TE's. Short TE's are particularly advantageous for visualizing metabolites with short T2 values such as lipids. However, a drawback of using short TE's is that macromolecules having very short T2 values could produce a prominent undulating baseline, which makes quantification of metabolites more challenging.

Table 1.2: Average ^{1}H-Metabolite Relaxation times measured at 3T. Sources: [Träber *et al.*, 2004].

Metabolite	T_1 (ms)	T_2 (ms)
NAA	1400	250
Choline	1100	200
Myo-inositol	1100	200
Glutamate	1200	180
Macromolecules	250	15

Because of T2 relaxation, the intensities of all peaks are reduced with increasing TE. At medium (TE=144ms, **Figure 1.11 middle**) and long (TE≥280ms, **Figure 1.11 right**) TE's, three main peaks (NAA, Cr, and Cho) can be clearly seen due to their relatively high concentration, the absence of J-coupling of

these singlets and their long T2 values. Metabolites of low concentration or short T2 relaxation times will disappear. In this thesis conventional MRS was performed with TE = 20ms for preclinical MRS and TE = 22ms for clinical. Spectral edited MRS was done with TE = 68ms for MEGA-PRESS sequence and TE=80ms for HERMES sequence.
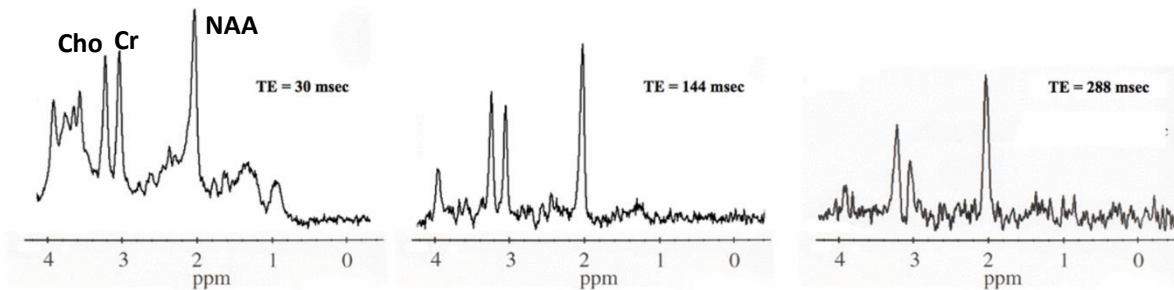
Figure 1.11: ^{1}H-MRS brain spectra acquired at different echo times. *NAA:N-Acetyl-Aspartate, Cr:Creatine, Cho:Choline* Source: Courtesy of Allen D. Elster, MRIquestions.com

As T1-weighting is controlled by the repetition time, using a TR considerably shorter than the T1 of a metabolite does not allow the longitudinal magnetization to fully recover. Hence, the signal intensity of the metabolite is decreased. **Figure 1.12** illustrates this signal intensity reduction of NAA, which has a long T1 (1400ms) acquired at TR = 1500ms.). Ideally, high quality MR spectra could be acquired for all metabolites using relatively long TR values, but at the expense of longer acquisition times since TR is directly proportional to the acquisition time. In general, clinical MRS is usually performed with TR values between 1500 − 2000ms, requiring subsequent compensation/ calibration of the incomplete T1 relaxation.
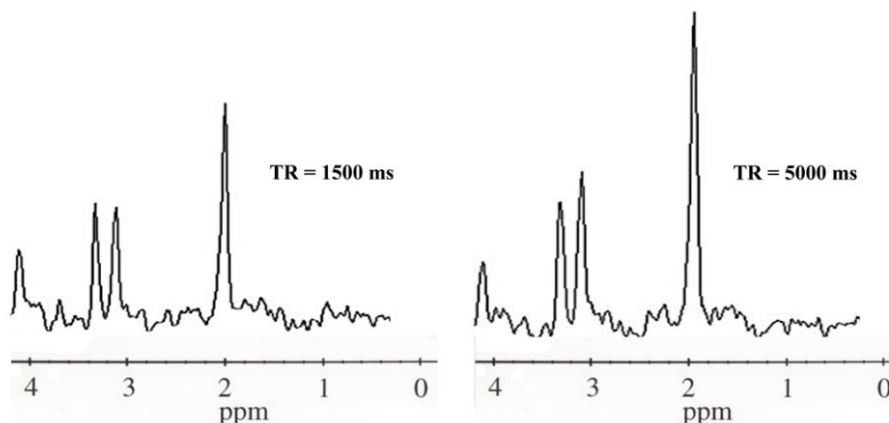
Figure 1.12: ^{1}H-MRS brain spectra acquired at different repetition times. Source: Courtesy of Allen D. Elster, MRIquestions.com.

Voxel selection

Voxel size is directly proportional to the signal-to-noise ratio (SNR) in MRS and has a linear effect. A voxel twice the size will have twice the SNR. In MRS, the signal intensity is approximately proportional to the number of protons giving rise to that peak. As a voxel volume increases, the height of the peaks also increases (**Figure 1.13**).
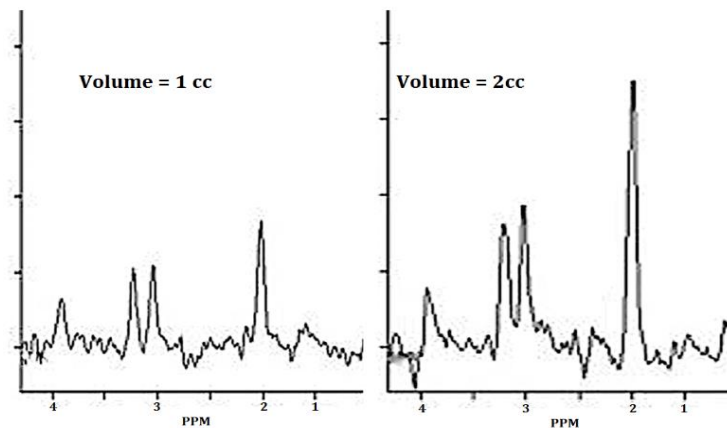
Figure 1.13: ^{1}H-MRS brain spectra acquired from voxel's, 1x1x1 cm^3 (left) and 2x2x2 cm^3 (right). Source: Courtesy of Allen D. Elster, MRIquestions.com

Number of acquisitions

The number of averages (NA) is an important determinant of SNR. SNR and NA are related by

$$SNR \propto \sqrt{NA}$$

This means that a four-fold increase in number of averages results in a 2-fold increase in the SNR. **Figure 1.14** depicts a spectra obtained with TR = 1500 and TE = 144 ms, where reduced baseline and sharper spectral peaks are attained with NA = 256 compared to NA = 8. Note the different SNRs in the depicted MR spectra.
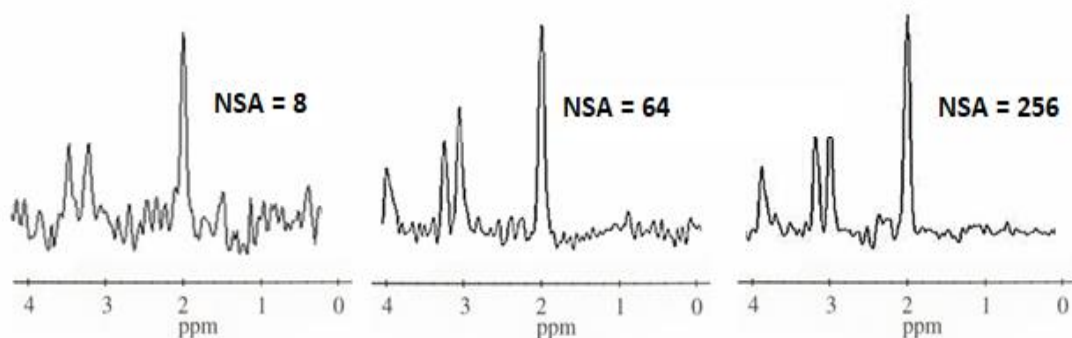
Figure 1.14: ^{1}H-MRS brain spectra acquired using different number of averages. Source: Courtesy of Allen D. Elster, MRIquestions.com

Conventional MRS sequences:

PRESS

The PRESS (Point RESolved Spectroscopy) sequence (Bottomley *et al*., 1987) is one of the most commonly used sequences for *in vivo* MRS. The sequence allows three-dimensional localization in a single acquisition, which is done with three orthogonal slice selecting gradients (**Figure 1.15**).
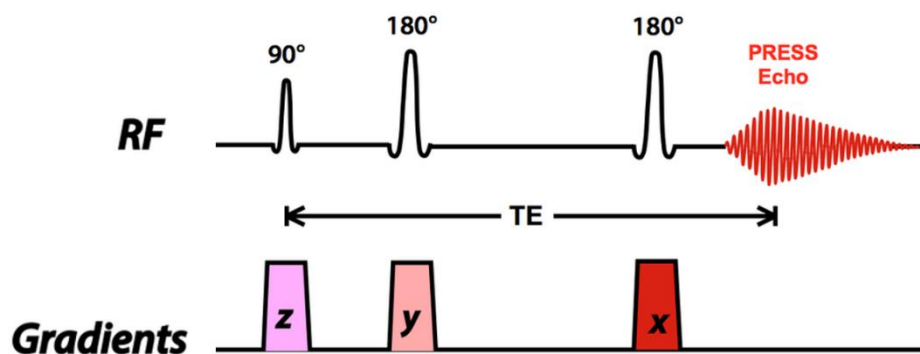
Figure 1.15: Simplified pulse sequence diagram of the PRESS single voxel spectroscopy sequence for MRS. Source: Courtesy of Allen D. Elster, MRIquestions.com

STEAM

STimulated Echo Acquisition Mode (STEAM) is also a widely used MRS sequence that provides a localized single voxel MR spectrum. The STEAM sequence allows limiting the volume of interest to a selected voxel in a single acquisition. One of the advantages of this sequence compared to PRESS is the possibility of use very short TEs (the shortest TE in commercially available clinical scanners is around 3 ms). However, this comes at a cost of only 50% of the SNR achieved with PRESS.

Spectral Editing Techniques

Spectral editing methods are used in MRS to improve the detection of strongly coupled and partially overlapping metabolites of low concentration such as GABA or glutathione (Terpstra *et al*., 2002; Terpstra *et al*., 2003; Edden *et al*., 2012). For this reason advanced spectral editing schemes were developed to isolate these overlapping, low concentration metabolites. Some of these methods are described in the next sections.

J-difference Editing

A conventional short echo [1]H-MR brain spectrum contains many overlapping signals due to the large number of [1]H-containing metabolites and their limited chemical shift range. This complicates the visualization and accurate quantification of especially low concentration metabolites in the presence of other high concentrated signals. For this reason, targeting resonances by *J*-difference editing is commonly used to overcome this issue for *J*-coupled spin systems (Hetherington *et al.*, 1985; Harris *et al.*, 2017). *J*-difference editing technique requires the acquisition of two consecutive spectra in which frequency-selective RF pulses are alternatively switched on and off on one resonance of the coupled spin-system (Wiegers *et al.*, 2017).

MEGA-PRESS sequence

MEGA-PRESS (MEshcher–GArwood Point RESolved Spectroscopy), named after the scientists who first proposed the MEGA suppression scheme (Mescher *et al.*, 1998), has become the standard *J*-difference editing technique used in MRS measurements of GABA and glutathione. In the case of GABA, MEGA-PRESS sequence acquires two interleaved ('ON', 'OFF') datasets, with frequency selected RF pulses applied to the GABA spin system. In one experiment, an RF pulse is applied to the spins of GABA at 1.9 ppm chemical shift in order to selectively refocus the evolution of *J*-coupling to the GABA spins at 3 ppm ('ON spectrum'). In the second experiment, an inversion pulse is applied around 4.7 ppm (or anywhere else) so that the *J*-coupling can evolve through the echo time (referred to as 'OFF spectrum'). Because of the frequency selective manipulation of the spins, the majority of signals in the spectrum are unaffected and subtraction of the edited ON spectrum from the non-edited OFF spectrum removes all the peaks from the subtracted-spectrum and preserves only those peaks that are perturbed by the editing pulses. A schematic representation of this process is showed in **Figure 1.16**. The figure shows that the edited spectrum comprises signals closer to 1.9 ppm, the GABA signal at 3 ppm (*J*-coupled GABA spins at 1.9 ppm), the combined glutamate + glutamine (Glx) peaks at 3.75 ppm (coupled Glx signals at around 2.1 ppm) and J-coupled macromolecular peaks (Mullins *et al* 2012).
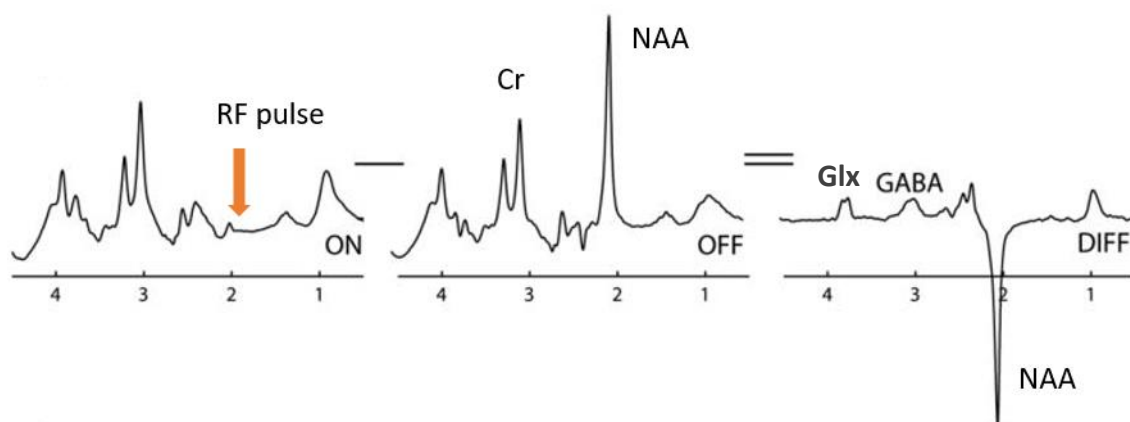
Figure 1.16: Schematic illustration of MEGA-PRESS editing of GABA. Editing RF pulses applied at 1.9 ppm modulate the shape of the GABA signals at 3 ppm. Subtracting scans acquired without these pulses (OFF) from scans acquired with the editing pulses (ON) inverts the NAA peak, removes overlapping creatine (Cr) signals from the edited spectrum, revealing the GABA signal in the difference spectrum (DIFF). Source: [adapted from Mullins *et al.*, 2012].

HERMES sequence

A significant drawback of MEGA-PRESS is that it usually only edits one metabolite at a time from a single brain region. Since editing is typically applied to lower concentration compounds, relatively long acquisition times are required, and studies are almost always severely restricted in terms of both the numbers of brain regions and metabolites that can be studied within the time constraints of an MR examination. Thus, although GABA-edited MRS is increasingly used, it is rarely combined in studies with the detection of other metabolites of interest, such as glutathione. Recently, the Hadamard Encoding and Reconstruction of MEGA-Edited Spectroscopy (HERMES) approach (Chan *et al.*, 2016) has demonstrated that more than one metabolite of overlapping signals can be edited within a single acquisition. In this manuscript, we show that HERMES can be used to simultaneously detect edited signals from GABA and glutathione.
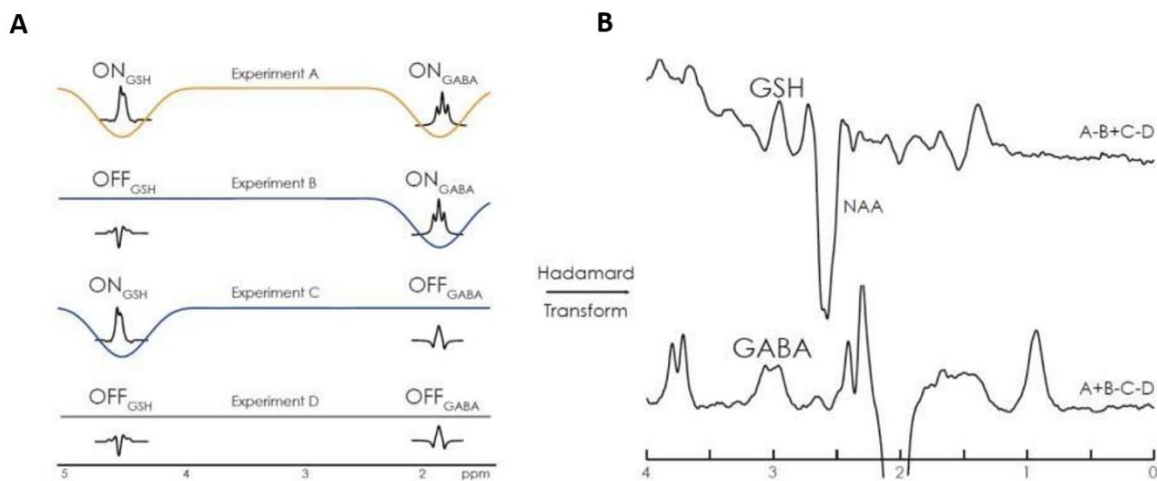
Figure 1.17: HERMES editing of GABA and glutathione. (**A**) Inversion profiles of editing pulses applied in the four sub-experiments A-D. (**B**) The Hadamard spectra show a GSH-edited signal at 2.95 ppm in the A-B+C-D combination and a GABA-edited spectrum in the A+B-C-D combination. Source: [Saleh *et al.*, 2016]. GSH: glutathione

Processing of MR spectra and metabolite quantification

Conventional MRS Post-Processing Methods

The quality and reproducible quantification of an MR spectrum from the measured signal can be enhanced by a variety of post-processing techniques that aim to overcome some of the specific problems inherent to *in vivo* MR spectroscopy. Typically applied methods are:

1. Residual water removal: in most situations water suppression is not complete, and a residual water signal is still left with an amplitude often superior to the amplitudes of the metabolites of interest. The residual water signal can influence the quality of quantification (Cabanes *et al.*, 2001).

2. Apodization: A time-domain filtering technique used to improve the SNR of a spectrum (Poullet *et al.*, 2008).

3. Phase correction: The lineshapes of metabolite peaks and their quantification may be distorted due to phase changes, including first order changes arising from the time delay in FID acquisition (Poullet *et al.*, 2008).

Quantification

Quantification aims at extracting metabolite concentrations from MR spectra. Depending on the acquisition and quantification method used, quantification can result in absolute concentration values (absolute quantification), or be semi-quantitative, when the output are relative metabolite concentrations. Absolute metabolite quantification, despite desirable, requires information that is not always available, such as: the tissue/compartment fractions for each voxel, the relaxation properties of the different metabolites in each compartment, and the knowledge of the evolution of the spins for the used pulse sequence (Gasparovic *et al.*, 2016, Slotboom *et al.*, 1998). Consequently, semi-quantitative methods are more frequently used in *in vivo* clinical applications of MRS. In this thesis, semi-quantitative quantification was performed using QUEST (Quantitation based on QUantum ESTimation, [Ratiney 2004, Ratiney 2005]).

Detectable neurometabolites in *in vivo* ^{1}H-MRS

Figure 1.18 shows a normal MR spectrum of a brain using a PRESS sequence, indicating the resonances of the most important metabolites of the healthy brain. A brief description of the most important brain metabolites observed at 3T is provided below.
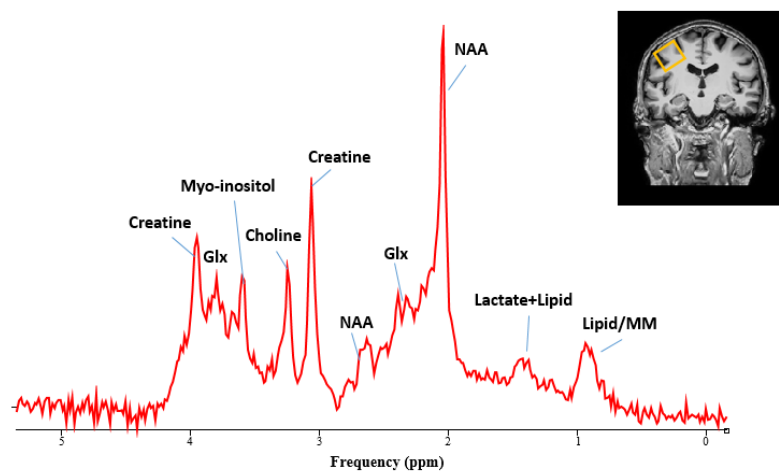
Figure 1.18: Normal brain spectrum acquired using a PRESS sequence. The MR spectrum was collected from the voxel (yellow square) in the reference image. The main visible peaks were assigned to the corresponding metabolites.

N-Acetyl-Aspartate (NAA)

N-Acetyl-Aspartate (NAA) is an amino acid found in the healthy brain at high concentrations (7.9-16.6 mM) (Kreis *et al.*, 1997). The acetyl group of NAA produces a singlet around 2.01 ppm which is one of the most prominent peaks in normal brain spectra. NAA is regarded as a marker for neuronal density. However, low NAA levels are associated not only with neuronal loss but also with neuronal dysfunction that may be reversible in some situations (Govindaraju *et al.*, 2000). Reduced NAA levels have been reported in neurodegenerative diseases such as Huntington's disease (Jenkins *et al.*, 2005), Alzheimer's disease (Dedeoglu *et al.*, 2004) and Amyotrophic Lateral Sclerosis (Andreassen *et al.*, 2001).

Creatine (Cr)

Creatine ^{1}H MR spectrum contains contributions from creatine and to a larger extent from phosphocreatine. The main role of phosphocreatine is to act as an energy buffer (Greenhaff *et al.*, 2001), as it enables the process of converting adenosine diphosphate (ADP) into adenosine triphosphate (ATP), generating creatine in the process. Creatine is again converted into phosphocreatine at the sites of energy transduction, where ATP is consumed and converted into ADP. Therefore, the (total) creatine signal is considered a marker for energy metabolism. In the brain, both metabolites are found in similar concentrations, with a total concentration of 6.4-9.7 mM in the gray matter and 5.2-5.7 mM in the white matter (Govindaraju *et al.*, 2000).

Choline (Cho)

Choline is an important constituent of cell membranes and myelin sheets, and is a precursor of the neurotransmitter acetylcholine (Govindaraju *et al.*, 2000, Mountford *et al.*, 2010). In the normal brain, the main contributors to the ^{1}H MR spectrum of visible choline correspond to 0.5-2.5mM. Choline bound to membranes is not visible by the 1H MRS. The total choline signal typically consists of choline, phosphocholine and glycerophosphocholine. At higher field strength, the ^{1}H MR spectra of the three compounds can be (partially) resolved.

Glutamate and Glutamine (Glu and Gln)

Glutamate and glutamine are two amino-acids found in the brain which are frequently quantified together, due to their complex J-coupling pattern (multiplet), signal overlap and similarity of their spectra. The ensemble of glutamate and glutamine resonances is referred to as "Glx". Glutamate is the principal excitatory neurotransmitter in the vertebrate nervous system [Meldrum 2000] and is found in the brain with a concentration of about 12 mM, making it the most abundant amino acid found in the brain (Govindaraju *et al.*, 2000). Glutamine's major role in the brain is to act as a precursor to the excitatory neurotransmitters glutamate and aspartate, and the inhibitory neurotransmitter gamma-amino butyric acid (GABA) (Albrecht *et al.*, 2010). Glutamate is cytotoxic (Takano *et al.*, 2001) and accumulation of high glutamate concentrations induces an inflammatory response in the surrounding tissue, possibly caused by the neuronal loss resulting from glutamate itself, which is believed to be a possible pathomechanism in neurodegenerative diseases.

γ-aminobutyric acid (GABA)

GABA is the principal inhibitory neurotransmitter in the human brain. GABAergic inhibition shapes and regulates patterns of neuronal activity, serving a key role in cortical information processing and plasticity. Naturally lower levels of GABA in the brain (0.5-1 mM) require spectral editing methods to reliably quantify it with ^{1}H MRS also due to its complex J-coupling pattern and partial signal overlap.

Glutathione (GSH)

Glutathione is the most abundant redox (reduction-oxidation) compound in the brain, serving an important role in minimizing the damage caused by reactive oxygen species. Glutathione can exist in reduced (GSH) or oxidized (GSSH) forms, although it is present in the brain almost exclusively as GSH at concentrations of 1–3 mM (Trabesinger *et al*., 1999; Terpstra] *et al*., 2005). Spectral editing methods are required for quantification by ^{1}H MRS due to overlap with the free amino acids.

Myo-inositol (mIns)

Myo-inositol is considered an astrocyte marker and an osmolyte usually found in the brain with a concentration between 4 and 8 mM (Kreis *et al*., 1997). Elevated *myo*-inositol levels have been previously reported for numerous neurodegenerative diseases, including Alzheimer's disease (Voevodskaya *et al*., 2016), Huntington's disease (Sturrock *et al*., 2015) and ALS (Kalra *et al*., 2006).

Lactate (Lac)

Lactate is a product of anaerobic glycolysis and, consequently is a marker for reduced oxygenation/ anaerobe metabolism (Mountford *et al*., 2010). It is not present in the 'normal' brain at ^{1}H MRS detectable concentrations. Elevated lactate concentrations are typically found in stroke, brain tumors and some abscesses. J-editing (for example, using echo times of 135-144ms) results in a 180° phase shift and better detectability of the lactate dublet (methyl group) at 1.31 ppm.

Macromolecules and Lipids

A substantial proportion of the signal detected by *in vivo* ^{1}H MRS is derived from "macromolecular resonances". The macromolecular signal originates from proteins and 'bound' amino acids and result in signals with short T2 values and subsequently in broad resonances that make a substantial contribution to the baseline of the MR spectrum. Similarly, lipid signals have a short T2 value and broad linewidths, partially masking other metabolites. Both, macromolecular contributions and lipid signals can be suppressed by large echo times.

Other detectable metabolites

A number of other small molecular metabolites may also be detected, including alanine (Ala), aspartate (Asp), glucose, glutathione and taurine (Tau). Many of these metabolites are usually at or below the limit of detection by standard ^{1}H MRS. This together with the complexity of their resonance

peaks means that advanced techniques are required to achieve robust identification and quantification. Some of these metabolites may be robustly quantified when present in elevated concentrations since their MRS resonances do not significantly overlap with other metabolites, such as taurine which is detectable in young infants, or alanine in some cases of lactic acidosis.

MRS processing software

Due to the fact that the MRS signals require specialized algorithms, several software packages have been created for post-processing and quantification of the data. Each available software package provides various tools and features, therefore the user choose these packages according to their specific needs.

jMRUI

The software includes several visualization tools, preprocessing methods and several quantitation routines (Stefan *et al.*, 2009). Apart from visual preprocessing e.g. apodization, jMRUI offers peak removal algorithms e.g. HLSVD. AMARES, QUEST, AQSES and SVD family are the available quantitation methods (Pijnappel *et al.*, 1992; Vanhamme *et al.*, 1997; Graveron-Demilly 2013; Garcia *et al.*, 2010). Most frequently used quantification of metabolites includes the use of linear combinations of reference spectra from the respective metabolites (either simulated or acquired ^{1}H MR spectra). One of the biggest advantages of jMRUI is its plug-in-based approach, which enables every researcher to add new functionalities to jMRUI. The software is available free of charge for educational and public research activities.

LC Model

LCModel is a software package for processing and quantification of magnetic resonance spectra. It process the spectrum as a linear combination of a set of model spectra, called a "basis set" for each metabolite of interest. Processing is automatic (noninteractive) with no subjective input. (http://s-provencher.com/lcmodel.shtml).

GANNET

The GANNET software is the recommended tool for GABA-edited MRS data analysis (Edden *et al.*, 2013). The software is specifically intended as a tool for the batch analysis of whole datasets with minimum user intervention. Gannet is coded within Matlab (The Mathworks, Natick, USA), using Optimization and Statistics toolboxes, and is distributed open-source. The Gannet script and instruction manual can be downloaded from this website: gabamrs.blogspot.com.

Other Packages

There are several other software approaches to the MRS data manipulation, built by research groups customized to their needs, e.g. jSIPRO (Jiru *et al.*, 2013), SPID (Poullet *et al.*, 2007; Sauwen *et al.*, 2015; Sima *et al.*, 2006).

1.1.2 Positron Emission Tomography (PET)

Positron-emission tomography (PET) is a functional imaging modality that is used to visualize metabolic activity in the body (Bailey 2005). The primary measurement in PET is the detection of two photons emitted from a positron (e^+) emitting radionuclide when the emitting positrons interact with electrons. These photons are then converted into electrical signals in a ring of detectors arranged around the sample. By drawing lines between detectors that measure these coincidence within a short time window allows to determine the origin/ location of the positron emitting tracer. A frequently used isotope for PET is the fluorine-18 isotope (^{18}F) due to its relatively long half-life (approx... 120 min). 18F labelled compounds are injected into the body in the form of biologically active molecules known as a radiotracer. Due to its high sensitivity, only tracer concentrations at or below physiological concentrations are required. 3D- images of the radiotracer concentration accumulation within the body are reconstructed after PET data acquisition. In this thesis, the biologically active radiotracer molecule used was 18-fluorodeoxyglucose (^{18}FDG), which is an analogue of glucose. By visualizing the distribution of the FDG radiotracer, we are able to measure the cerebral tissue metabolic activity as it corresponds to regional glucose uptake.
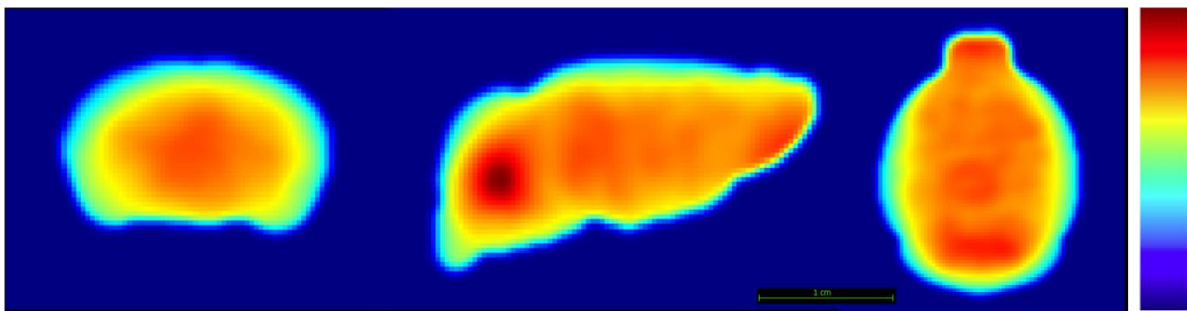
Figure 1.19: Representative PET mouse brain axial, sagittal and coronal images using ^{18}FDG as a radiotracer.

1.1.3 Other imaging methods

Computed tomography (CT), bioluminescence imaging (BLI), fluorescence imaging (FLI) and ultrasound imaging modalities are also used in clinical and preclinical studies, however, these modalities are less specific and not suitable for studying neurodegeneration

1.2   Aging and Amyotrophic Lateral Sclerosis

1.2.1   Aging

"Aging is the progressive accumulation of changes with time that are associated with or responsible for the ever-increasing susceptibility to disease and death which accompanies advancing age"

<div align="right">The Aging Process-Dr. Denham Harman, M.D., Ph.D.</div>

Aging is mainly characterized by the progressive loss of physiological integrity, leading to reduced function and increased vulnerability to death (López-Otín *et al*., 2013). Over the recent years, research in aging has discovered that the rate of aging is controlled by genetic pathways and biochemical processes conserved in evolution. Scientists have identified several hallmarks that characterize common factors of aging in mammals. These include (**Figure 1.20**) genomic instability, telomere attrition, epigenetic alterations, loss of proteostasis, deregulated nutrient sensing, mitochondrial dysfunction, cellular senescence, stem cell exhaustion, and altered intercellular communication (López-Otín *et al*., 2013).

Age is the major risk factor for most prevalent diseases, including neurodegenerative disorders (Niccoli and Partridge 2012). As the world's aging population increases, the number and proportion of individuals affected by neuro-related disorders also increases. Aging is considered a key risk factor for most neurodegenerative diseases such as dementia, including Alzheimer's disease, cognitive impairment, Parkinson's disease and ALS. For example, for Alzheimer's disease the prevalence is expected to double within the next 20 years (Prince *et al*. 2013). Another study found that the number of patients with Parkinson's disease will double between the years 2005 and 2030 (Arthur *et al*., 2016). The same study reports that the number of ALS cases across the world is projected to increase from 222,800 in 2015 to 376,674 in 2040, signifying an increase of 69% (Arthur *et al*., 2016). Arthur *et al* further states that this increase is predominantly due to ageing of the population, particularly in developing nations (Arthur *et al*., 2016).

The brain is one of the most active and energy consuming organs in the body where energy and cellular homeostasis is crucial for its proper function. Therefore, imbalances in energy metabolism could lead to diseases ranging from subtle alterations in neuronal function to cell death and neurodegeneration. Cellular energy is mainly produced within mitochondria, however, the process of energy production also creates formation of toxic reactive oxygen species (ROS) that can be harmful for cellular organelles, including mitochondria itself.

> "Contrary to the prevailing medical belief, having high total cholesterol is not bad for the brain. In fact, high cholesterol actually *reduces* the risk of dementia." (Mielke *et al*., 2005).

Studies of normal aging in the human brain are important for neuroscience but also for clinical diagnosis. Therefore, the investigation of age-related brain chemistry impairments is becoming of increasing interest in order to understand the mechanisms leading to normal aging and neurodegenerative disease. Although many studies have been conducted on diseases related to aging, not many studies in

depth the chemistry of the aging brain in the absence of neurodegenerative disease or the neuropsychological profile of healthy young and older adults. Magnetic resonance spectroscopy (MRS) provides a useful tool to study the effects of aging on brain metabolism. Therefore, this thesis reports also on clinical studies investigating changes of ^{1}H-MRS metabolite concentrations in both normal aging in healthy brain as well as the ALS affected brain.
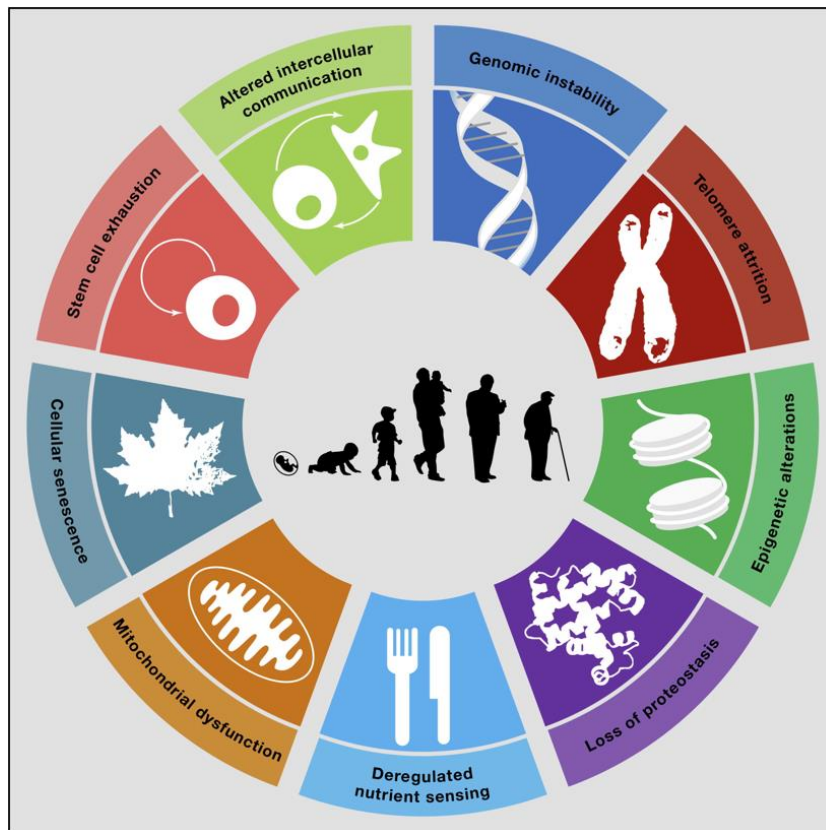
Figure 1.20: The Hallmarks of Aging. The scheme enumerates the nine hallmarks described in this Review: genomic instability, telomere attrition, epigenetic alterations, loss of proteostasis, deregulated nutrient sensing, mitochondrial dysfunction, cellular senescence, stem cell exhaustion, and altered intercellular communication. Source: [López-Otín *et al.*, 2013]

1.2.1.1 Neurobiology of aging

Noninvasive *in vivo* imaging studies have shown effects like the expansion of cerebral ventricles and regional decreases in cerebral volume as a function of age (Craik and Salthouse., 2000; Raz *et al.*, 2005). The brain matter can be classified roughly into grey matter, white matter and cerebrospinal fluid. Gray matter is mainly comprised of neuronal cell bodies in the cortex and subcortical regions and the white matter is comprised of highly structured myelinated axons. A reduction in grey matter volume is reported between the ages of 20-40 and old age, while an increase in white matter volume was reported from age 18-40 with a subsequent reduction (Sowell *et al.*, 2003).

"On average, the brain loses 5-10 percent of its weight between the ages of 20 and 90." (Guttman 2001)

In normal healthy aging, a general increase in the density of protein aggregates (neurofibrillary tangles) has been reported (Anderton *et al*., 2002). Typically, these aggregates are restricted to the olfactory nucleus, parahippocampal gyrus, amygdala and entorhinal cortex. In pathological states, the aggregate density as well as diverse locations of aggregation has been observed (Price *et al*., 1991). In the aging brain as well as in the case of several neurodegenerative diseases, there is a decline in the normal antioxidant defense mechanisms, which increases the vulnerability of the brain to the deleterious effects of oxidative damage (Finkel *et al*., 2000). It was shown that compared to other organs in the body, the mammalian brain is highly susceptible to oxidative damage (Keller *et al*., 2005). Furthermore, protein oxidation and lipid peroxidation are reported to be major contributors of oxidative stress in the brain (Harris *et al*., 2006). Apart from the brain's age-related structural changes, aging processes also lead to a series of pathological and biochemical changes. Studies have identified a number of neurotransmitters, such as glutamate, GABA and dopamine to alter in various brain regions in the process of 'normal' aging. In addition, neurometabolites such as the neuronal markers NAA have shown to decrease during aging (Ross *et al*., 2006; Eyler*et al*., 2016) Studies have shown lower glutamate concertation in the motor cortex of older adults compared to young adults (Kaiser *et al*., 2005). In addition, a significant age-related reduction in glutamate was also observed in parietal grey matter, basal ganglia and frontal white matter (Sailasuta.*et al*., 2008). Since glutamate is also observed to be altered in these location in neurodegenerative diseases associated with aging, brain glutamate levels may serve as a biomarker for age-related brain diseases (Chang *et al*., 2009).

> "Ketones can be a great brain fuel for aging brain and it has been shown to be beneficial in several neuro-diseases such as Alzheimer's and epilepsy." (Stafstrom *et al*., 2012)

1.2.2   Amyotrophic Lateral Sclerosis

1.2.2.1   History of ALS

Amyotrophic Lateral Sclerosis (ALS) or commonly known as Lou Gehrig's disease, is a fatal neurodegenerative disease primarily characterized by progressive and selective degeneration of motor neurons in the brain and spinal cord. In the mid eighteen hundreds, the Scottish surgeon Sir Charles Bell and the French neurologist François Aran first recognized patients with muscle dystrophy and motor function (Turner *et al*., 2010). However, at the time there had been much speculation among neurologists whether muscular dystrophy was due to disease of the muscle or nerve. Studies conducted between 1865 and 1869 by Jean-Martin Charcot, provided the insight into understanding the correlation between clinical signs and autopsy results of patients (Pandey *et al*., 2012). Charcot diagnosed and defined the first cases of ALS as a specific neurological disease associated with a distinct pathology unique from other motor neuron diseases such as primary lateral sclerosis (PLS) and primary muscular atrophy (PMA) (Goetz 2000). Further studies revealed certain ALS pathologies overlap with the rare disease of frontotemporal dementia (Turner *et al*., 2015).

1.2.2.2 Epidemiology

ALS is considered an adult-onset disease where most affected patients are of ages between 40 and 65, with an average age of 52 at the time of diagnosis. The average life-expectancy from onset to death is about 3–4 years. However, younger (age 20-30) and older (age > 70) humans can also develop the disease (**Figure 1.21**). Generally, ALS occurs in higher rate (about 20%) in men than in women. With advancing age, the incidence of ALS tends to be more equal between the genders. The incidence rates for ALS in North America and Europe range between 1.5 and 2.7 per 100,000/year, while prevalence rates range between 2.7 and 7.4 per 100,000 (Worms *et al*., 2001; Logroscino *et al*., 2010; Mehta *et al*., 2014). According to the recent '*ALS* Liga *België'* statistics, there are about 1000 ALS-patients registered in Belgium and more than 200 patients die from the disease each year and roughly the same number of new patients are diagnosed [Annual report ALS research KU Leuven 2017, preview 2018 treatment ALS (Prof. Dr. Philip Van Damme).

Apart from North America and Europe, a study of global epidemiological data by Cronin *et al* concluded that the incidence of ALS might be lower among African, Asian, and Hispanic ethnic groups than among Caucasians (Cronin *et al*., 2007). Risk factors for ALS include increasing age, family history and gender. Additionally, some studies suggests that cigarette smoking is also a risk factor for ALS (Armon *et al*., 2007; Sutedja *et al*., 2007).
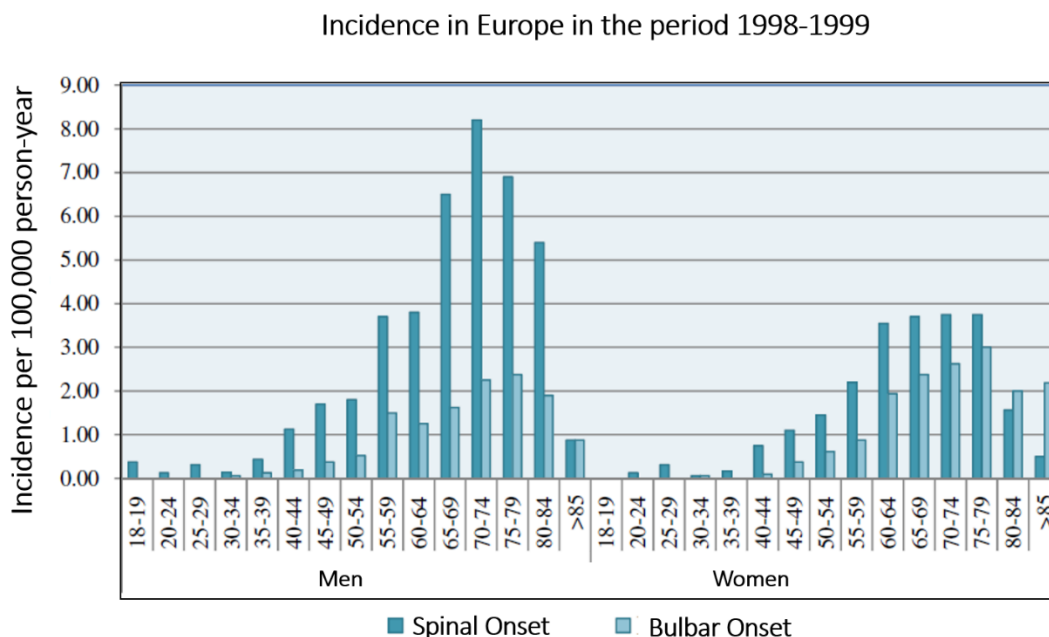
Figure 1.21 Age- and gender-specific incidence rates of ALS in Europe during the 2-year period 1998–1999 classified by site of onset. Source: [Logroscino *et al*., 2015].

1.2.2.3 Clinical features

ALS leads to progressive degeneration of the motor neurons that supply voluntary muscles, including lower motor neurons (LMN) in the brainstem and anterior horn of the spinal cord as well as upper motor neurons (UMN) in the motor cortex. Symptoms of ALS include progressive muscle weakness, muscle atrophy and ultimately leading to death by respiratory failure. In about 65% of ALS patients, symptoms start in the limbs (limb-onset), often in arms, where symptoms include muscle twitches, difficulty in walking and eventually total paralysis. About 35% of patients present symptoms of bulbar dysfunction such as dysarthria, dysphagia, drooling, and atrophied tongue. Eye movement and sensory capabilities are usually spared until advanced stages of the disease. Cognitive impairment is also a commonly reported characteristic of ALS (Phukan *et al.*, 2007; Strong *et al.*, 2009; Elamin *et al.*, 2011). Frontotemporal dementia, which occurs in about 15% of patients with ALS (Elamin *et al.*, 2011) is characterized by personality changes, executive dysfunction or impairments in language.

1.2.2.4 Diagnosis

Diagnosis of ALS is challenging due to the overlap of ALS symptoms with other neurological diseases. Therefore, a neurologist would conduct a differential diagnosis to eliminate disease that mimic ALS. So far, no conclusive diagnostic test exists for ALS. The combination of several clinical (functional rating scales), laboratory (serum, urine protein electrophoresis), nerve conduction tests and imaging studies supports the diagnosis (Hardiman *et al.*, 2011; Wang *et al.*, 2011). Neurofilaments, which are intermediate nanoscale filaments in neurons, have been studied in various neurological conditions, and are considered to be useful as marker of acute and chronic neuronal injury. New evidence is emerging that neurofilament levels can become biomarker for ALS for diagnosing ALS (Poesen & Van Damme 2019).

1.2.2.5 Molecular Biology

Approximately 90% of all ALS cases are sporadic (sALS) with unknown etiology. Familial ALS (fALS) accounts for about 5%-10% of ALS cases and is genetically heterogeneous (Pasinelli *et al.*, 2006; Valdmanis *et al.*, 2009). Mutations in several genes including superoxide dismutase 1 (SOD1), TAR DNA binding protein (TARDBP), chromosome 9 open reading frame 72 (C9ORF72), fused in sarcoma (FUS), valosin-containing protein (VCP), angiogenin (ANG), ubiquilin 2 (UBQLN2) and optineurin (OPTN) have been shown to cause 85% of adult-onset familial ALS and for a smaller fraction be the cause of sporadic ALS cases (Ticozzi *et al.*, 2011). Understanding how variations in these genes cause motor neuron degeneration is key to improving our understanding of the disease's pathophysiology and to the development of more powerful neuroprotective therapies.

> "C9orf72 repeat expansions are a frequent cause of ALS in Belgium, and also in sALS patients." (Rademakers *et al.*, 2013)

1.2.2.1 Pathology

ALS is recognized as a very complex disease. Traditionally, glutamate excitotoxicity, oxidative stress, protein aggregation, mitochondrial damage, and neuroinflammation, altered axonal transport have

been considered as key factors in the pathogenesis of ALS, with the relatively recent addition of disturbances in RNA metabolism (Shaw *et al.*, 1997; Pollari *et al.*, 2014; Blokhuis *et al.*, 2013; Muyderman *Et al.*, 2014; Liu *et al.*, 2017; De Vos *et al.*, 2017; Droppelmann *et al*, 2014).
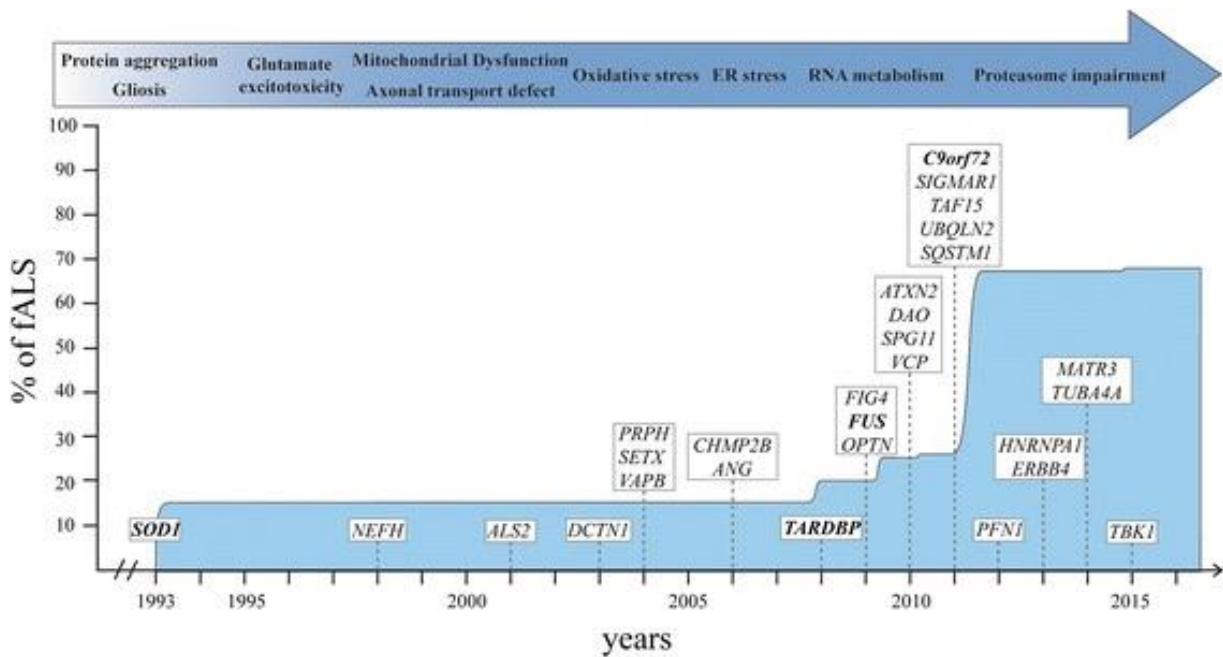
Figure 1.22 Timeline of gene discovery and pathogenic mechanisms in ALS. Schematic illustration of years of discovery of genes associated with ALS. NEFH neurofilament heavy; ALS2 alsin; DCTN1 dynactin; PRPH peripherin; SETX senataxin; VAPB vesicle-associated membrane protein-associated protein B; CHMP2B Charged multivesicular body protein 2B; ANG angiogenin; FIG4 phosphoinositide 5-phosphatase; OPTN optineurin; ATXN2 ataxin 2; DAO D-amino acid oxidase; SPG11 spastic paraplegia 11; VCP valosin containing protein; SIGMAR1 sigma non-opioid intracellular receptor 1; TAF15 TATA-box binding protein associated factor 15; UBQLN2 ubiquilin-2; SQSTM1 sequestosome 1; PFN1 profilin-1; HNRNPA1 heterogeneous nuclear ribonucleoprotein A1; ERBB4 erb-2 receptor tyrosine kinase 4; MATR3 matrin 3; TUBA4A tubulin alpha-4a; TBK1 TANK-binding kinase 1.Source: [Picher-Martel *et al.*, 2016].

> **"Over 95% of all ALS cases involve TDP-43 proteinopathy" (Yang *et al*., 2014)**

1.2.2.1 Therapeutic options

Riluzole (Rilutek) is the only drug approved by the Food and Drug Administration (FDA) in 1995 for ALS treatment. In 2017, a drug known as Edaravone had been approved by the FDA for use in the United States. However, this drug is not approved to be used in Europe. Numerous other drugs established to be efficient in animal models have failed in clinical trials (Petrov *et al.*, 2017).
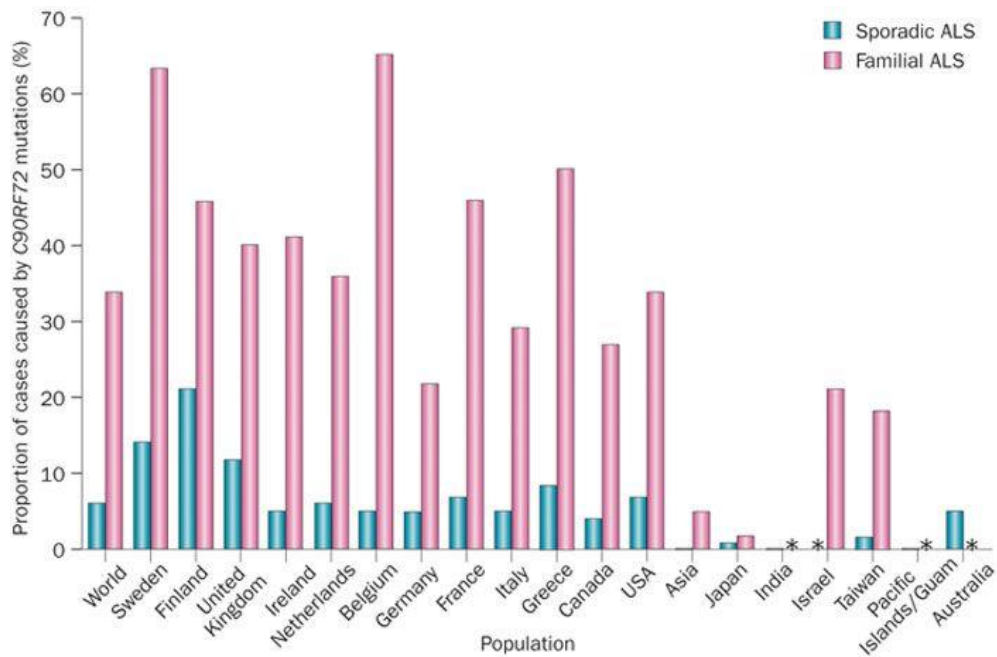
Figure 1.23 Reported frequencies of *C9ORF72* mutations in patients with ALS. Source: [Rademakers *et al.*, 2013].

1.2.2.2 Animal models for ALS

Preclinical animal models provide valuable contributions for improving our understanding of human diseases, ranging from insights into the molecular and cellular background of a disease to the development of novel therapeutic approaches and diagnostics. One of the main advantages of preclinical studies is group homogeneity, which is difficult to achieve in clinical studies. In addition, intensive immunohistochemical and molecular studies are possible in animal models. Procedurally, the application of parallel imaging modalities that are developed for animal models are also applicable to humans, positively affecting the translational potential of animal research (**Figure 1.24**).
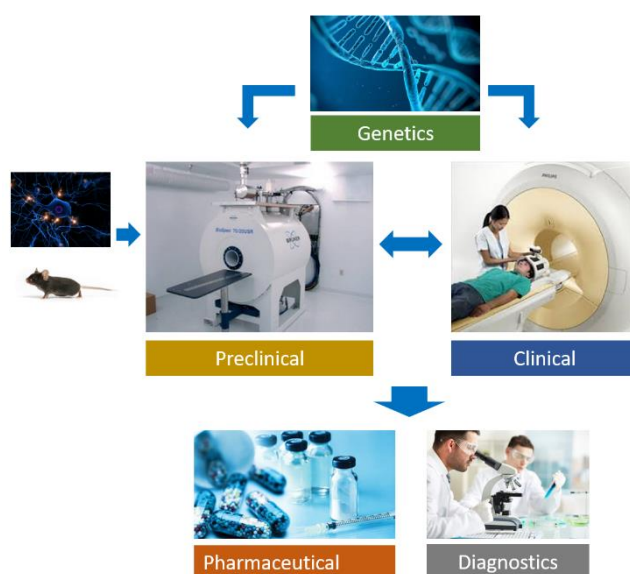
Figure 1.24 Translational research, including the development of advanced imaging approaches.

Development of transgenic animal models is the first phase in understanding the pathophysiology and novel therapies of neurodegenerative diseases like ALS (Ittner *et al.*, 2015). Multiple animal models have been generated to mimic the human disease and to test prospective pharmaceuticals. In this thesis, we use two transgenic ALS mouse models; the SOD1^{G93A} and TDP-43^{A315T} mouse models.

SOD1^{G93A} Mouse model

The generation of ALS animal models started after the identification of SOD1 as a causative gene for this disease (Rosen *et al.*, 1993). SOD1 is a ubiquitously expressed cytosolic metalloenzyme (Cu/Zn) of 153 amino acids encoded by five exons. Although the mutant SOD1 preserves some enzymatic activity (Gurney *et al.*, 1994), binding of copper ions is not as effective as for the wild-type SOD1 enzyme (Pratt *et al.*, 2014). The most widely used mouse strain SOD1^{G93A} (point mutation responsible for a glycine to alanine substitution at position 93) with survival of approximately 140 days overexpresses the normal mRNA levels of mouse SOD1 by 40 folds (Gurney *et al.*, 1994, Jonsson *et al.*, 2006). These mice express most of the clinical (pharyngeal dysphagia, limb muscle weakness and paralysis) and neuropathological findings of ALS (**Figure 1.25 C**).

Because of its regular function in catalyzing the conversion of superoxide anions to hydrogen peroxide, it was first thought that the toxicity of different SOD1 mutants could be a result of decreased free-radicals scavenging activity. However, SOD1 knockout mice do not develop motor symptoms (Reaume *et al.*, 1996) and mice expressing mutant SOD1^{G93A} develop motor neuron disease despite elevation in the SOD1 activity levels (Cleveland, 1999). These results suggest that the mutations in SOD1 provoke a gain of new toxic properties.

> "The G93A mouse line is currently the most widely used experimental model in ALS research and drug testing"

TDP-43^{A315T} Mouse model

The 43-kDa TAR DNA binding protein (TDP-43) is localized in the cell nucleus under normal conditions (**Figure 1.25 A left**). However, ubiquitinated and phosphorylated inclusions of TDP-43 were observed in patients with ALS and in patients with frontotemporal lobar dementia with ubiquitinated inclusions (FTLD-U) (Cairns *et al.*, 2007, Hasegawa *et al.*, 2008). These inclusions were observed in the cytoplasm and nucleus of both, neurons and glial cells (Cairns *et al.*, 2007, Mackenzie *et al.*, 2007). TDP-43 is partly cleared from the nuclei of neurons containing cytoplasmic aggregates (Neumann *et al.*, 2006, Van Deerlin *et al.*, 2008), supporting the notion that pathogenesis of ALS in these cases may be driven, at least in part, by loss of normal TDP-43 function in the nucleus (**Figure 1.25 A right**). TDP-43 inclusions are now recognized as a common characteristic of most ALS patients (Maekawa *et al.*, 2009, Sumi *et al.*, 2009).

The discovery of TDP-43 mutations found in ALS patients had led to the generation of many animal models including the hTDP-43-A315T mouse model. In 2010, Wegorzewska *et al* reported on the first transgenic model of TDP-43 proteinopathy, describing the human mutation TDP-43^{A315T} overexpressed

by mouse prion protein (Prp) promoter, created on a hybrid C57BL/6 and CBA genetic background. These mice are reported to develop gait abnormalities starting from about 3 months of age. The phenotype includes increased paw progression angle of the hind limbs and weight loss at about 4.5 months (**Figure 1.25 B**). However, the TDP-43^{A315T} mouse model, now available on a 100% C57BL6/J congenic genetic background from Jackson laboratory (stock number 010700), reported to develop an early intestinal blockage that prevents the disease phenotype progression and leads to premature death (Esmaeili *et al.*, 2013; Herdewyn *et al.*, 2014). Herdewyn *et al*. also showed that the gastrointestinal dysfunction can be avoided by replacing the standard rodent food pellets with an easily digestible gel diet, allowing time for the development of the pathology in the brain and spinal cord in these mice (Herdewyn *et al.*, 2014). Both male and female TDP-43^{A315T} mice develop significant motor impairment, usually deficits appearing earlier and progressing more rapidly in males.

Despite the broadly expressed transgene in TDP-43^{A315T}, pathological aggregates of ubiquitinated proteins accumulated only in specific neurons, including layer 5 pyramidal neurons in the frontal cortex, as well as spinal motor neurons. Previous studies reported that prp-hTDP-43^{A315T} mice did not reveal cytoplasmic TDP-43 aggregates in the cortical neurons, which is a feature that led to the discovery of TDP-43 as a hallmark of ALS and FTLD-U in patients (Wegorzewska *et al.*, 2009).

> "A high-fat jelly diet restores bioenergetic balance and extends lifespan in the presence of motor dysfunction and lumbar spinal cord motor neuron loss in TDP-43^{A315T}" (Coughlan *et al.*, 2016)
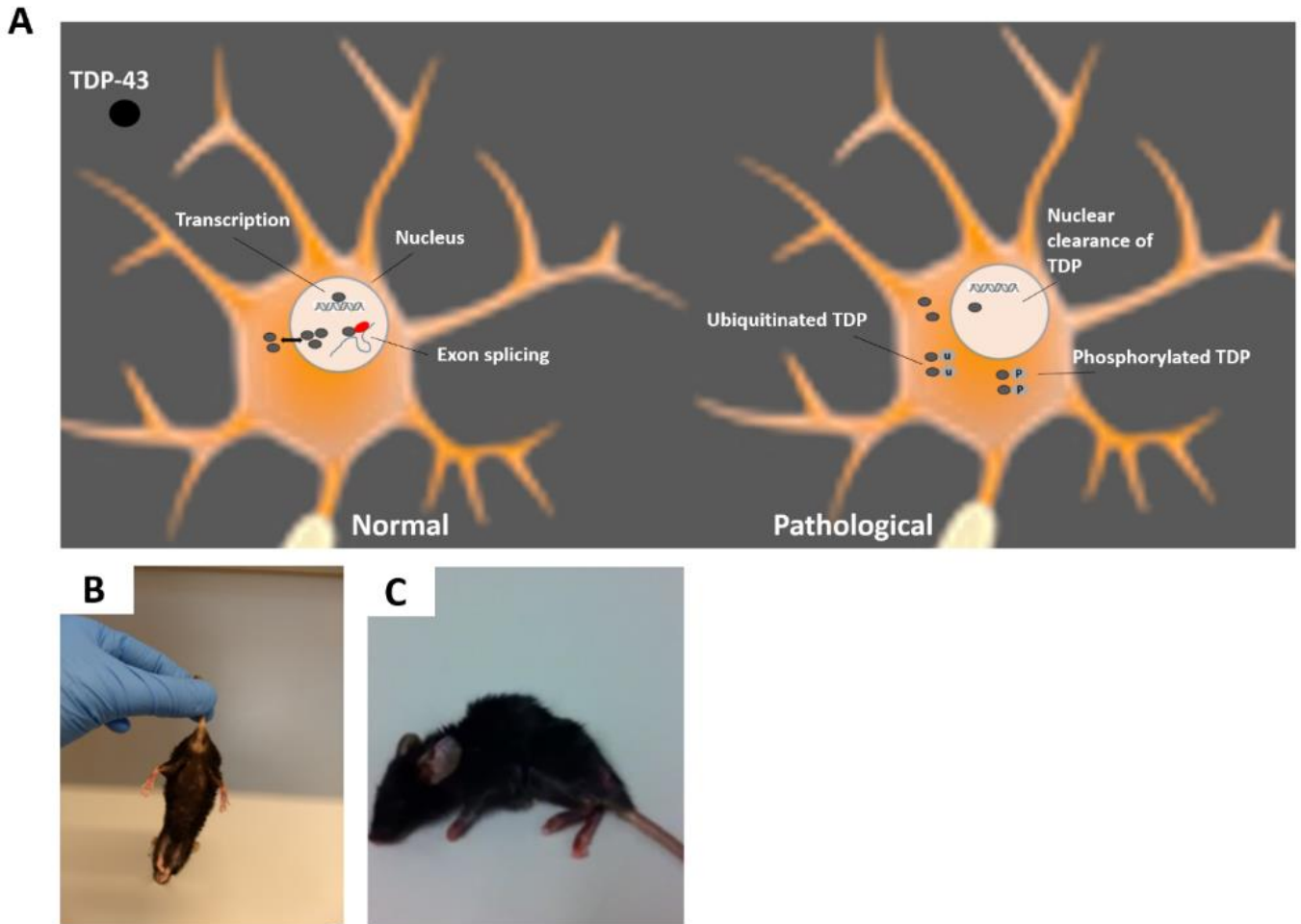
Figure 1.25: (**A**) Normal and pathophysiological TDP-43. Left: under normal physiological conditions, TDP-43 mainly localized in the nucleus, although the protein has the capacity to shuttle between the nucleus and the cytoplasm. TDP-43 has been reported to have roles in regulating transcription and regulating gene splicing, and (**B**) Upon tail elevation, a symptomatic TDP-43[A315T] mouse holds its hindlimbs close to their body and fail to show proper escape extension (spread of hindlimbs). (**C**) An endstage SOD1[G93A] mouse, showing hunched posture, muscle atrophy, paralysis of hindlimbs.

References

Andreassen OA, Jenkins BG, Dedeoglu A, Ferrante KL, Bogdanov MB, Kaddurah-Daouk R, Beal MF. Increases in cortical glutamate concentrations in transgenic amyotrophic lateral sclerosis mice are attenuated by creatine supplementation. *J Neurochem*. 2001; 77:383–390.

Andrew Webb and George C. Kagadis. Introduction to Biomedical Imaging. *Medical Physics*. 2003:30(8): 2267.

Antonini A, Leenders KL, Eidelberg D. [11C]-Raclopride-PET studies of the Huntington's disease rate of progression: Relevance of the trinucleotide repeat length. *Ann Neurol*. 1998; 43:253-5.

Arthur KC, Calvo A, Price TR, Geiger JT, Chiò A, Traynor BJ. Projected increase in amyotrophic lateral sclerosis from 2015 to 2040. *Nature Communications*. 2016; 7:12408.

Artico M, Spoletini M, Fumagalli L, *et al*. Egas Moniz: 90 Years (1927–2017) from Cerebral Angiography. *Frontiers in Neuroanatomy*. 2017; 11:81.

B S Meldrum. Glutamate as a neurotransmitter in the brain: review of physiology and pathology. The *Journal of nutrition*. 2000; 30, 4S Suppl: 1007S–15S, 2000.

Blokhuis AM, Groen EJ, Koppers M, van den Berg LH, Pasterkamp RJ. Protein aggregation in amyotrophic lateral sclerosis. *Acta Neuropathol*. 2013; 125(6):777-94.

Bottomley PA. Spatial localization in NMR spectroscopy *in vivo*. *Ann N Y Acad Sci*. 1987; 508:333-48.

Cabanes E, Confort-Gouny S, Le Fur Y, Simond G, Cozzone PJ. Optimization of residual water signal removal by HLSVD on simulated short echo time proton MR spectra of the human brain. *J Magn Reson*. 2001; 150(2):116-25.

Cairns NJ, Neumann M, Bigio EH, Holm IE, Troost D, Hatanpaa KJ, Foong C, White CL 3rd, Schneider JA, Kretzschmar HA, Carter D, Taylor-Reinwald L, Paulsmeyer K, Strider J, Gitcho M, Goate AM, Morris JC, Mishra M, Kwong LK, Stieber A, Xu Y,Forman MS, Trojanowski JQ, Lee VM, Mackenzie IR. TDP-43 in familial and sporadic frontotemporal lobar degeneration with ubiquitin inclusions. *Am J Pathol*. 2007; 171(1):227-40.

Carolyn E. Mountford, Peter Stanwell, Alexander Lin, Saadallah Ramadan and Brian Ross. Neurospectroscopy: The past, present and future. *Chemical Reviews*. 2010; 110(5): 3060–3086.

Castillo AM, Patiny L, Wist J. Fast and accurate algorithm for the simulation of NMR spectra of large spin systems. *J Magn Reson*. 2011; 209(2):123-30.

Chan KL, Puts NAJ, Schär M, Barker PB, Edden RAE. HERMES: Hadamard Encoding and Reconstruction of MEGA-Edited Spectroscopy. *Magnetic resonance in medicine*. 2016; 76(1):11-19.

Chang L, Jiang CS, Ernst T. Effects of Age and Sex on Brain Glutamate and Other Metabolites. *Magnetic resonance imaging*. 2009; 27(1):142-145.

Chilla GS, Tan CH, Xu C, Poh CL. Diffusion weighted magnetic resonance imaging and its recent trend-a survey. *Quant Imaging Med Surg*. 2015; 5(3):407-22.

Chuck Gasparovic. Adjusting Concentrations for Tissue Composition in Brain: Assumptions & Conundrums. In ISMRM Workshop on MR Spectroscopy, Lake Constance, 2016.

Cleveland DW. From Charcot to SOD1: mechanisms of selective motor neuron death in ALS. *Neuron*. 1999; 24(3):515-20.

Coughlan KS, Halang L, Woods I, Prehn JH. A high-fat jelly diet restores bioenergetic balance and extends lifespan in the presence of motor dysfunction and lumbar spinal cord motor neuron loss in TDP-43A315T mutant C57BL6/J mice. *Dis Model Mech*. 2016; 9(9):1029-37.

Craik, F. I. M., & Salthouse, T. A. (Eds.). (2000). The handbook of aging and cognition (2nd ed.). Mahwah, NJ, US: Lawrence Erlbaum Associates Publishers.

Cronin S, Hardiman O, Traynor BJ. Ethnic variation in the incidence of ALS: a systematic review. *Neurology*. 2007; 27; 68(13):1002-7.

Meier D, Boesiger P, Kozerke. S Magnetic Resonance Imaging in Medicine. University and ETH Zürich, Switzerland, Zürich, 2012.

Sima DM, De Neuter B, Vanhamme P. Lemmerling S. Van Huffel A.W. Simonetti, J.B. Poullet. An open source short echo time MR quantitation software solution: AQSES. *Biomedicine*. 2006. p. 19, p. 28.

De Graaf, Robin A 2007, *In vivo NMR spectroscopy: principles and techniques*, 2nd ed, Wiley; Chichester: John Wiley [distributor], Hoboken, N.J.

Dedeoglu A, Choi JK, Cormier K, Kowall NW, Jenkins BG. Magnetic resonance spectroscopic analysis of Alzheimer's disease mouse brain that express mutant human APP shows altered neurochemical profile. *Brain Res* 2004; 1012:60–65.

De Vos KJ, Hafezparast M. Neurobiology of axonal transport defects in motor neuron diseases: Opportunities for translational research? *Neurobiol Dis*. 2017; 105:283-299.

Droppelmann CA, Campos-Melo D, Ishtiaq M, Volkening K, Strong MJ. RNA metabolism in ALS: when normal processes become pathological. *Amyotroph Lateral Scler Frontotemporal Degener*. 2014; 15(5-6):321-36.

Edden RA, Puts NA, Barker PB. Macromolecule-suppressed GABA-edited magnetic resonance spectroscopy at 3T. *Magn Reson Med*. 2012; 68(3):657-61.

Edelman RR. The history of MR imaging as seen through the pages of radiology. *Radiology*. 2014; 273(2 Suppl):S181-200.

Essig M, Shiroishi MS, Nguyen TB, *et al*. Perfusion MRI: the five most frequently asked technical questions. *AJR Am J Roentgenol*. 2013; 200(1):24-34.

Esmaeili MA, Panahi M, Yadav S, Hennings L, Kiaei M. Premature death of TDP-43 (A315T) transgenic mice due to gastrointestinal complications prior to development of full neurological symptoms of amyotrophic lateral sclerosis. *Int J Exp Pathol*. 2013; 94(1):56-64.

Eylers VV, Maudsley AA, Bronzlik P, Dellani PR, Lanfermann H, Ding XQ. Detection of Normal Aging Effects on Human Brain Metabolite Concentrations and Microstructure with Whole-Brain MR Spectroscopic Imaging and Quantitative MR Imaging. *AJNR Am J Neuroradiol*. 2016; 37(3):447-54.

Faure A, Verret L, Bozon B, El Tannir El Tayara N, Ly M, Kober F, Dhenain M, Rampon C, Delatour B. Impaired neurogenesis, neuronal loss, and brain functional deficits in the APPxPS1-Ki mouse model of Alzheimer's disease. *Neurobiol Aging*. 2011; 32(3):407-18.

Filip Jiru, Antonin Skoch, Dita Wagnerová, Monika Dezortova, and Milan Hájek. jSIPRO analysis tool for magnetic resonance spectroscopic imaging. *Computer Methods and Programs in Biomedicine*. 2013; 112(1):173–188.

Finkel T, Holbrook NJ. Oxidants, oxidative stress and the biology of ageing. *Nature*. 2000; 408(6809):239-47.

Garcia M, D. Sima, F. Nielsen, U. Himmelreich and S. Van Huffel, "Quantification of *in vivo* Magnetic Resonance Spectroscopy signals with baseline and lineshape corrections," *2010 IEEE International Conference on Imaging Systems and Techniques*, Thessaloniki. 2010; 349-352.

Goetz CG. Amyotrophic lateral sclerosis: early contributions of Jean-Martin Charcot. *Muscle Nerve*. 2000; 23(3):336-43.

Govindaraju V, Young K, Maudsley AA. Proton NMR chemical shifts and coupling constants for brain metabolites. *NMR Biomed*. 2000; 13(3):129-53.

Graveron-Demilly. Quantification in magnetic resonance spectroscopy based on semi-parametric approaches. *Magnetic Resonance Materials in Physics, Biology and Medicine*. 2013; 1–8.

Gurney, M. E., H. Pu, A. Y. Chiu, M. C. Dal Canto, C. Y. Polchow, D. D. Alexander, J. Caliendo, A. Hentati, Y. W. Kwon, H. X. Deng and *et al*. Motor neuron degeneration in mice that express a human Cu,Zn superoxide dismutase mutation. *Science.* 1994; 264(5166): 1772-1775.

Guttman M. 2001 February 1. The Aging Brain. Retrieved from https://news.usc.edu/7569/The-Aging-Brain/

Haaga, J. and Alfidi, R. *Computed tomography of the whole body*. St. Louis: Mosby.1988.

Hardiman O, van den Berg LH, Kiernan MC. Clinical diagnosis and management of amyotrophic lateral sclerosis. *Nat Rev Neurol*. 2011; 7(11):639-49.

Harris AD, Saleh MG, Edden RA. *Magn Reson Med*. 2017; 77(4):1377-1389.

Harris SE, Deary IJ, MacIntyre A, Lamb KJ, Radhakrishnan K, Starr JM, Whalley LJ, Shiels PG. The association between telomere length, physical health, cognitive ageing, and mortality in non-demented older people. *Neurosci Lett*. 2006; 406(3):260-4.

Hasegawa M, Arai T, Nonaka T, Kametani F, Yoshida M, Hashizume Y, Beach TG, Buratti E, Baralle F, Morita M, Nakano I, Oda T, Tsuchiya K, Akiyama H. Phosphorylated TDP-43 in frontotemporal lobar degeneration and amyotrophic lateral sclerosis. *Ann Neurol*. 2008; 64(1):60-70.

Herdewyn S, Cirillo C, Van Den Bosch L, Robberecht W, Vanden Berghe P, Van Damme P. Prevention of intestinal obstruction reveals progressive neurodegeneration in mutant TDP-43 (A315T) mice. *Mol Neurodegener*. 2014; 9:24.

Hetherington HP, Avison MJ, Shulman RG. *Proc Natl Acad Sci U S A*. 1985; 82(10):3115-8.

Hoeffner EG, Mukherji SK, Srinivasan A, Quint DJ. Neuroradiology back to the future: brain imaging. *AJNR Am J Neuroradiol*. 2012; 33(1):5-11.

http://casemed.case.edu/clerkships/neurology/Web%20Neurorad/MRI%20Basics.htm

Hutton BF. The origins of SPECT and SPECT/CT. *Eur J Nucl Med Mol Imaging*. 2014; 41 Suppl 1:S3-16.

Ittner A, Bertz J, Suh LS, Stevens CH, Götz J, Ittner LM. Tau-targeting passive immunization modulates aspects of pathology in tau transgenic mice. *J Neurochem*. 2015; 132(1):135-45.

Jan Albrecht, Marta Sidoryk-Wȩgrzynowicz, Magdalena Zielińska and Michael Aschner. Roles of glutamine in neurotransmission. *Neuron Glia Biology.* 2010; 6(04), 263–276.

Jahng GH, Li KL, Ostergaard L, Calamante F. Perfusion magnetic resonanceimaging: a comprehensive update on principles and techniques. *Korean J Radiol*.2014; 15(5):554-77.

Jean-Baptiste Poullet, Diana M. Sima, Arjan W. Simonetti, Bart De Neuter, Leentje Vanhamme, Philippe Lemmerling, and Sabine Van Huffel. An automated quantitation of short echo time MRS spectra in an open source software environment: AQSES. *NMR in Biomedicine.*2007; 20(5):493– 504.

Jenkins BG, Andreassen OA, Dedeoglu A, Leavitt B, Hayden M, Borchelt D, Ross CA, Ferrante RJ, Beal MF. Effects of CAG repeat length, HTT protein length and protein context on cerebral metabolism measured using magnetic resonance spectroscopy in transgenic mouse models of Huntington's disease. *J Neurochem*. 2005; 95:553–562.

Johannes Slotboom, Chris Boesch and Roland Kreis. Versatile frequency domain fitting using time domain models and prior knowledge. *Magnetic Resonance in Medicine*. 1998; 39(6): 899–911.

Kaiser LG, Schuff N, Cashdollar N, Weiner MW. Age-related glutamate and glutamine concentration changes in normal human brain: 1H MR spectroscopy study at 4 T. *Neurobiol Aging*. 2005; 26(5):665-72.

Kalra S, Hanstock CC, Martin WR, Allen PS, Johnston WS. Detection of cerebral degeneration in amyotrophic lateral sclerosis using high-field magnetic resonance spectroscopy. *Arch Neurol*. 2006; 63(8):1144-8.

Keller JN, Schmitt FA, Scheff SW, Ding Q, Chen Q, Butterfield DA, Markesbery WR. Evidence of increased oxidative damage in subjects with mild cognitive impairment. *Neurology*. 2005; 64(7):1152-6.

Kober F., Duhamel G., Callot V. (2011) Cerebral Perfusion MRI in Mice. In: Schröder L., Faber C. (eds) *In vivo* NMR Imaging. Methods in Molecular Biology (Methods and Protocols), vol 771. Humana Press.

Liu J, Wang F. Role of Neuroinflammation in Amyotrophic Lateral Sclerosis: Cellular Mechanisms and Therapeutic Implications. *Front Immunol*. 2017; 8:1005.

Logroscino G, Traynor BJ, Hardiman O, Chiò A, Mitchell D, Swingler RJ, Millul A, Benn E, Beghi E; EURALS. Incidence of amyotrophic lateral sclerosis in Europe. *J Neurol Neurosurg Psychiatry*. 2010; 81(4):385-90.

Logroscino, G., Tortelli, R., Rizzo, G. *et al*. *Curr Geri Rep*. 2015; 4:142.

López-Otín C, Blasco MA, Partridge L, Serrano M, Kroemer G. The hallmarks of aging. *Cell*.; 153(6):1194-217.

Lv H, Wang Z, Tong E, Williams LM, Zaharchuk G, Zeineh M, Goldstein-Piekarski AN, Ball TM, Liao C, Wintermark M. Resting-State Functional MRI: Everything That Nonexperts Have Always Wanted to Know. *AJNR Am J Neuroradiol*. 2018; 39(8):1390-1399.

Mackenzie IR, Bigio EH, Ince PG, Geser F, Neumann M, Cairns NJ, Kwong LK, Forman MS, Ravits J, Stewart H, Eisen A, McClusky L, Kretzschmar HA, Monoranu CM, Highley JR, Kirby J, Siddique T, Shaw PJ, Lee VM, Trojanowski JQ. Pathological TDP-43 distinguishes sporadic amyotrophic lateral sclerosis from amyotrophic lateral sclerosis with SOD1 mutations. *Ann Neurol*. 2007; 61(5):427-34.

Maekawa S, Leigh PN, King A, Jones E, Steele JC, Bodi I, Shaw CE, Hortobagyi T, Al-Sarraj S. TDP-43 is consistently co-localized with ubiquitinated inclusions in sporadic and Guam amyotrophic lateral sclerosis but not in familial amyotrophic lateral sclerosis with and without SOD1 mutations. *Neuropathology*.2009; 29(6):672-83.

Mehta P, Antao V, Kaye W, Sanchez M, Williamson D, Bryan L, Muravov O, Horton K; Division of Toxicology and Human Health Sciences, Agency for Toxic Substances and Disease Registry, Atlanta, Georgia; Centers for Disease Control and Prevention (CDC). Prevalence of amyotrophic lateral sclerosis - United States, 2010-2011. *MMWR Suppl*. 2014; 63(7):1-14.

Mescher M, Merkle H, Kirsch J, Garwood M, Gruetter R. Simultaneous *in vivo* spectral editing and water suppression. *NMR Biomed*. 1998; 11(6):266-72.

Mielke MM, Zandi PP, Sjögren M, Gustafson D, Ostling S, Steen B, Skoog I. High total cholesterol levels in late life associated with a reduced risk of dementia.Neurology. 2005 May 24;64(10):1689-95.

mriquestions.com. "MRS parameters". AD Elster, ELSTER LLC. 24 August 2018. https://www.mriquestions.com/choice-of-trteetc.html

Mullins PG, McGonigle DJ, O'Gorman RL, *et al*. Current practice in the use of MEGA-PRESS spectroscopy for the detection of GABA. *NeuroImage*. 2014; 86:43-52.

Muyderman H, Chen T. Mitochondrial dysfunction in amyotrophic lateral sclerosis - a valid pharmacological target? *Br J Pharmacol*. 2014; 171(8):2191-205.

Neumann M, Sampathu DM, Kwong LK, Truax AC, Micsenyi MC, Chou TT, Bruce J, Schuck T, Grossman M, Clark CM, McCluskey LF, Miller BL, Masliah E, Mackenzie IR, Feldman H, Feiden W, Kretzschmar HA, Trojanowski JQ, Lee VM. Ubiquitinated TDP-43 in frontotemporal lobar degeneration and amyotrophic lateral sclerosis. *Science*. 2006; 314(5796):130-3.

Nicolas Sauwen, Diana M. Sima, Sofie Van Cauter, Jelle Veraart, Alexander Leemans, Frederik Maes, Uwe Himmelreich, and Sabine Van Huffel. Hierarchical non-negative matrix factorization to characterize brain tumor heterogeneity using multi-parametric MRI. *NMR in Biomedicine*, 28(12):1599–1624, 2015.

Pandey S. Jean-martin charcot pathologist, neurologist, psychiatrist and physician. *Ann Indian Acad Neurol*. 2012; 15(4):297-8.

Paul L Greenhaff. The creatine-phosphocreatine system: there's more than one song in its repertoire. *Journal of physiology*. 2001; 537(3):657.

Petrov D, Mansfield C, Moussy A, Hermine O. ALS Clinical Trials Review: 20 Years of Failure. Are We Any Closer to Registering a New Treatment? *Front Aging Neurosci*. 2017; 9:68.

Picher-Martel V, Valdmanis PN, Gould PV, Julien JP, Dupré N. From animal models to human disease: a genetic approach for personalized medicine in ALS. *Acta Neuropathol Commun*. 2016; 11; 4(1):70.

Pijnappel, W.W.F., van den Boogaart, A., de Beer, R., van Ormondt, D. SVD-based quantification of magnetic resonance signals. *Journal of Magnetic Resonance*. 199*2*; 97: 122-134.

Pollari E, Goldsteins G, Bart G, Koistinaho J, Giniatullin R. The role of oxidative stress in degeneration of the neuromuscular junction in amyotrophic lateral sclerosis. *Front Cell Neurosci*. 2014; 8:131.

Poesen K and Van Damme P. Diagnostic and Prognostic Performance of Neurofilaments in ALS. *Front. Neurol*. 2019; 9:1167.

Poullet JB, Sima DM, Van Huffel S. MRS signal quantitation: a review of time- and frequency-domain methods. J *Magn Reson*. 2008; 195(2):134-44.

Preston, David. Magnetic Resonance Imaging (MRI) of the Brain and Spine: Basics. School of medicine, Case Western Reserve University.2006.

Price JS. Change or homeostasis? A systems theory approach to depression. *Br J Med Psychol*. 1991; 64 (Pt 4):331-44.

R. Kreis. Quantitative localized 1H MR spectroscopy for clinical use. *Progress in Nuclear Magnetic Resonance Spectroscopy*. 1997; 31(97): 155–195.

Rademakers R, van Blitterswijk M. Motor neuron disease in 2012: Novel causal genes and disease modifiers. *Nat Rev Neurol*. 2013; 9(2):63-4.

Raz N, Lindenberger U, Rodrigue KM, Kennedy KM, Head D, Williamson A, Dahle C, Gerstorf D, Acker JD. Regional brain changes in aging healthy adults: general trends, individual differences and modifiers. *Cereb Cortex*. 2005; 15(11):1676-89.

Reaume AG, Elliott JL, Hoffman EK, Kowall NW, Ferrante RJ, Siwek DF, Wilcox HM, Flood DG, Beal MF, Brown RH Jr, Scott RW, Snider WD. Motor neurons in Cu/Zn superoxide dismutase-deficient mice develop normally but exhibit enhanced cell death after axonal injury. *Nat Genet*. 1996; 13(1):43-7.

Ross AJ, Sachdev PS, Wen W, Brodaty H. Longitudinal changes during aging using proton magnetic resonance spectroscopy. *J Gerontol A Biol Sci Med Sci*. 2006; 61(3):291-8.

Rosen, D. R., T. Siddique, D. Patterson, D. A. Figlewicz, P. Sapp, A. Hentati, D. Donaldson, J. Goto, J. P. O'Regan, H. X. Deng and *et al*. Mutations in Cu/Zn superoxide dismutase gene are associated with familial amyotrophic lateral sclerosis. *Nature*. 1993; 362(6415): 59-62.

Sailasuta N, Ernst T, Chang L. Regional variations and the effects of age and gender on glutamate concentrations in the human brain. *Magnetic resonance imaging*. 2008; 26(5):667-675.

Saleh MG, Oeltzschner G, Chan KL, *et al*. Simultaneous Edited MRS of GABA and Glutathione. *NeuroImage*. 2016; 142:576-582.

Sandrone S, Bacigaluppi M, Galloni MR, Cappa SF, Moro A, Catani M, Filippi M, Monti MM, Perani D, Martino G. Weighing brain activity with the balance: Angelo Mosso's original manuscripts come to light. *Brain*. 2014; 137(Pt 2):621-33.

Schild HH. (1990). MRI Made Easy. , Berlin: Nationales Druckhaus.

Schneider G, Prince MR, Meaney JFM, Ho VB (eds) (2005) Magnetic resonance angiogra-phy - Techniques, indications and practical applications. Springer, Milan Berlin Heidelberg New York.

Shaw PJ, Ince PG. Glutamate, excitotoxicity and amyotrophic lateral sclerosis. *J Neurol*. 1997; 244 Suppl 2:S3-14.

Sowell ER, Peterson BS, Thompson PM, Welcome SE, Henkenius AL, Toga AW. Mapping cortical change across the human life span. *Nat Neurosci*. 2003; 6(3):309-15.

Stafstrom CE, Rho JM. The ketogenic diet as a treatment paradigm for diverse neurological disorders. *Front Pharmacol*. 2012; 3:59.

Stefan, D., Di Cesare, F., Andrasescu, A., Popa, E., Lazariev, A., Vescovo, E., Strbak, O., Williams, S., Starcuk, Z., Cabanas, M., van Ormondt, D., Graveron-Demilly. D. Quantitation of magnetic resonance spectroscopy signals: the jMRUI software package. *Measurement Science and Technology*. 2009; 20:104035 (9 pp).

Stephen W. Provencher. Automatic quantitation of localized *in vivo* 1h spectra with lcmodel. NMR in *Biomedicine*. 2001; 14(4):260–264.

Sturrock A, Laule C, Wyper K, Milner RA, Decolongon J, Dar Santos R, Coleman AJ, Carter K, Creighton S, Bechtel N, Bohlen S, Reilmann R, Johnson HJ, Hayden MR, Tabrizi SJ, Mackay AL, Leavitt BR. A longitudinal study of magnetic resonance spectroscopy Huntington's disease biomarkers. *Mov Disord*. 2015; 30(3):393-401.

Sumi H, Kato S, Mochimaru Y, Fujimura H, Etoh M, Sakoda S. Nuclear TAR DNA binding protein 43 expression in spinal cord neurons correlates with the clinical course in amyotrophic lateral sclerosis. *J Neuropathol Exp Neurol*. 2009; 68(1):37-47.

Sutedja NA, Veldink JH, Fischer K, Kromhout H, Heederik D, Huisman MH, Wokke JH, van den Berg LH. Exposure to chemicals and metals and risk of amyotrophic lateral sclerosis: a systematic review. *Amyotroph Lateral Scler*. 2009; 10(5-6):302-9.

T Takano, J H Lin, G Arcuino, Q Gao, J Yang and M Nedergaard. Glutamatereleasepromotesgrowthof malignantgliomas. *Nature medicine*. 2001; 7(9):1010–5.

Terpstra M, Henry PG, Gruetter R. Measurement of reduced glutathione (GSH) in human brain using LCModel analysis of difference-edited spectra. *Magn Reson Med*. 2003; 50(1):19-23.

Terpstra M, Ugurbil K, Gruetter R. Direct *in vivo* measurement of human cerebral GABA concentration using MEGA-editing at 7 Tesla. *Magn Reson Med.* 2002; 47:1009–1012.

Terpstra M, Vaughan TJ, Ugurbil K, Lim KO, Schulz SC, Gruetter R. Validation of glutathione quantitation from STEAM spectra against edited 1H NMR spectroscopy at 4T: application to schizophrenia. *Magma.* 2005; 18: 276–282.

Tognarelli JM, Dawood M, Shariff MI, *et al*. Magnetic Resonance Spectroscopy: Principles and Techniques: Lessons for Clinicians. *J Clin Exp Hepatol*. 2015; 5(4):320-8.

Träber F, Block W, Lamerichs R, Gieseke J, Schild HH. 1H metabolite relaxation times at 3.0 tesla: Measurements of T1 and T2 values in normal brain and determination of regional differences in transverse relaxation. *J Magn Reson Imaging*. 2004; 19(5):537-45.

Trabesinger AH, Weber OM, Duc CO, Boesiger P. Detection of glutathione in the human brain *in vivo* by means of double quantum coherence filtering. *Magn Reson Med*. 1999; 42: 283–289.

Tsougos, I. (2018). *Advanced MR Neuroimaging*. Boca Raton: CRC Press.

Turner MR, Swash M, Ebers GC. Lockhart Clarke's contribution to the description of amyotrophic lateral sclerosis. *Brain*. 2010; 133(11):3470-9.

Turner MR, Swash M. The expanding syndrome of amyotrophic lateral sclerosis: a clinical and molecular odyssey. *J Neurol Neurosurg Psychiatry*. 2015; 86(6):667-73.

Uszler J.M. (2017) Neurophysiologic SPECT Brain Function Imaging and Hyperbaric Oxygen Therapy. In: Textbook of Hyperbaric Medicine. Springer, Cham.

Van Deerlin VM, Leverenz JB, Bekris LM, Bird TD, Yuan W, Elman LB, Clay D, Wood EM, Chen-Plotkin AS, Martinez-Lage M, Steinbart E, McCluskey L, Grossman M, Neumann M, Wu IL, Yang WS, Kalb R, Galasko DR, Montine TJ, Trojanowski JQ, Lee VM, Schellenberg GD, Yu CE. TARDBP mutations in amyotrophic lateral sclerosis with TDP-43 neuropathology: a genetic and histopathological analysis. *Lancet Neurol*. 2008; 7(5):409-16.

Vanhamme, L., van den Boogaart, A., Van Huffel, S. Improved method for accurate and efficient quantification of MRS data with use of prior knowledge. *Journal of Magnetic Resonance* 129: 35-43, 1997.

Voevodskaya O, Sundgren PC, Strandberg O, Zetterberg H, Minthon L, Blennow K, Wahlund LO, Westman E, Hansson O; Swedish BioFINDER study group. Myo-inositol changes precede amyloid pathology and relate to APOE genotype in Alzheimer disease. *Neurology*. 2016; 86(19):1754-61.

Wang S, Melhem ER, Poptani H, Woo JH. Neuroimaging in amyotrophic lateral sclerosis. *Neurotherapeutics*. 2011; 8(1):63-71.

Weidensteiner, C., Metzger, F., Bruns, A., Bohrmann, B., Kuennecke, B., von Kienlin, M. Cortical hypoperfusion in the B6.PS2APP mouse model for Alzheimer's disease: comprehensive phenotyping of vascular and tissular parameters by MRI. *Magn. Reson. Med*. 2009; 62: 35–45.

Wegorzewska I, Bell S, Cairns NJ, Miller TM, Baloh RH (2009) TDP-43 mutant transgenic mice develop features of ALS and frontotemporal lobar degeneration. *Proc Natl Acad Sci U S A*. 2009; 106:18809-18814.

Wiegers EC, Philips BWJ, Heerschap A, van der Graaf M. Automatic frequency and phase alignment of *in vivo* J-difference-edited MR spectra by frequency domain correlation. *Magma (New York, N.y)*. 2017; 30(6):537-544.

Worms PM. The epidemiology of motor neuron diseases: a review of recent studies. *J Neurol Sci*. 2001 15; 191(1-2):3-9.

Yáñez IB, Muñoz A, Contreras J, Gonzalez J, Rodriguez-Veiga E, DeFelipe J.Double bouquet cell in the human cerebral cortex and a comparison with other mammals. *J Comp Neurol*. 2005 13; 486(4):344-60.

Yang C, Wang H, Qiao T, Yang B, Aliaga L, Qiu L, Tan W, Salameh J, McKenna-Yasek DM, Smith T, Peng L, Moore MJ, Brown RH Jr, Cai H, Xu Z. Partial loss of TDP-43 function causes phenotypes of amyotrophic lateral sclerosis. *Proc Natl Acad Sci U S A*. 2014; 111(12)

2. | Outline of the Thesis

The discovery of novel, sensitive and specific biomarkers for aging and neurodegenerative diseases is a crucial factor for the development of clinically applicable diagnostic tools and for the development and evaluation of novel therapeutics. For their validation, it is advisable to combine various diagnostic tools. Standardization of the diagnostic protocols before including novel neuroimaging modalities to the routine clinical protocols is essential to achieving better precision in disease diagnosis. The continuous improvements in neuroimaging technologies will ultimately result in the application of more reliable diagnostic tools. These tools will be essential for precession diagnosis and therapy assessment in the disease management process, where more a personalized approach in the care for the patient is the ultimate aim.

The primary focus of this dissertation is the application of MRS in the assessment of the neurodegenerative disease, ALS. Moreover, aging is a major risk factor in the development of all chronic neurodegenerative diseases, including ALS. The mean onset of ALS is between 50 and 65 years of age. Individuals with familial mutations that predispose them to ALS/FTD may live asymptomatically until middle age. Because of this reason, we investigated the neurometabolic changes in the normal aging brain using single voxel MRS in **chapter 3**. Furthermore; we examined the impact of age-related neurometaboliic changes on motor performance. We observed that neurometabolic changes in the aging brain could account for age-related decline of motor performance in healthy older adults. Our study suggests for the first time that decreased levels of NAA and myo-inositol in the motor cortex may reflect neuronal loss and degeneration in brain regions that support bimanual coordination.

In **chapter 4**, we used MRI together with conventional and novel MRS sequences to investigate neurometabolic changes in the motor cortex of ALS patients and their relation to clinical parameters. Neurometabolites were measured using regular PRESS and HERMES MRS sequences. We observed significant alterations in NAA, Glx and myo-inositol levels in the motor cortex of ALS patients. NAA levels in the bulbar-onset group were found to be significantly lower compared to the limb-onset group. Correlations were also found between neurometabolites and ALSFR-R and FVC scores. We have tested to what extent mean neurometabolite concentrations detected in the motor cortex may correlate with clinical and pathological changes in ALS.

Spectral editing methods like the MEGA-PRESS technique provide a promising approach for the discrimination of GABA from glutamate and glutamine signals. But, no comparison has been made so far to compare GABA concentrations derived from edited (MEGA-PRESS) and unedited (MEGA-OFF) MR spectra. Only very few studies have investigated possible changes of GABA levels with advancing age and relatively little is known about the inter-subject variability in neurotransmitter levels arising from age effects. In **chapter 5**, we quantify the GABA and Glx concentrations derived with edited/unedited MEGA-PRESS using three different spectral fitting methods (Gannet, jMRUI-AMARES, jMRUI-QUEST). Age related differences in neurotransmitter levels in a group of healthy young and old adults were investigated using MEGA-PRESS. We have demonstrated that the inter-subject variability for GABA levels was lower than that of Glx for all three fitting methods. We found a good agreement between GABA values estimated with Gannet (edited) and QUEST (MEGA-OFF) spectral fitting methods.

Furthermore, our results indicate that within the motor cortex GABA levels were lower in older as compared to young adults.

In **chapter 6**, we have investigated age-dependent effects of disease onset and progression on regional neurochemistry in the SOD1^{G93A} ALS mouse model using single voxel MRS. The aim of this study was the identification of potential diagnostic markers for the onset and progression of ALS. We focused mainly on the brainstem region and motor cortex motor nuclei since they are the primarily affected regions in SOD1^{G93A} mice and ALS patients. In addition, we have assessed potential neuroprotective effects of coconut oil dietary supplement in these mice in a proof-of-concept study. Potential therapeutic effects were monitored using MRI/ MRS. We observed alterations in creatine, GABA, Glx, NAA, myo-inositol in the brainstem region and altered glutamate, NAA and taurine levels were seen at late stages in the motor cortex. The proof-of-concept study revealed that the coconut oil supplementation together with the regular diet delayed disease symptoms, enhanced motor performance, and prolonged survival in the SOD1^{G93A} mouse model.

In **chapter 7**, we report for the first time on the longitudinal non-invasive PET-MR characterization of the novel ASL hTDP-43^{A315T} mouse model. We employed ^{18}F-FDG PET, MRS, DW-MRI and perfusion MRI techniques to characterize this transgenic mouse model and compared the measured parameters with age-matched control mice. We observed significant changes in the glucose uptake, neurochemistry and functional parameters in the transgenic mouse brain. In addition, we showed the presence of pathological cytoplasmic TDP-43 inclusions in the brains of symptomatic hTDP-43^{A315T} mice, which has not been reported previously. Our results from this study provide novel insight into the neuropathological events in this transgenic mouse model that can be used as a framework for future ALS research.

The overarching goal of this thesis was the identification of magnetic resonance (MR) based biomarkers for early diagnosis and potential treatment follow up of amyotrophic lateral sclerosis (ALS) using preclinical and clinical data. In several studies, MR spectroscopy techniques were further developed and validated, effects of aging on MR spectra of apparently healthy subjects was assessed to determine a baseline for a subsequent study on ALS patients and mouse models of ALS were studied to identify non-invasive diagnostic markers

Figure 2.1: Schematic overview of the experimental outline of the thesis.
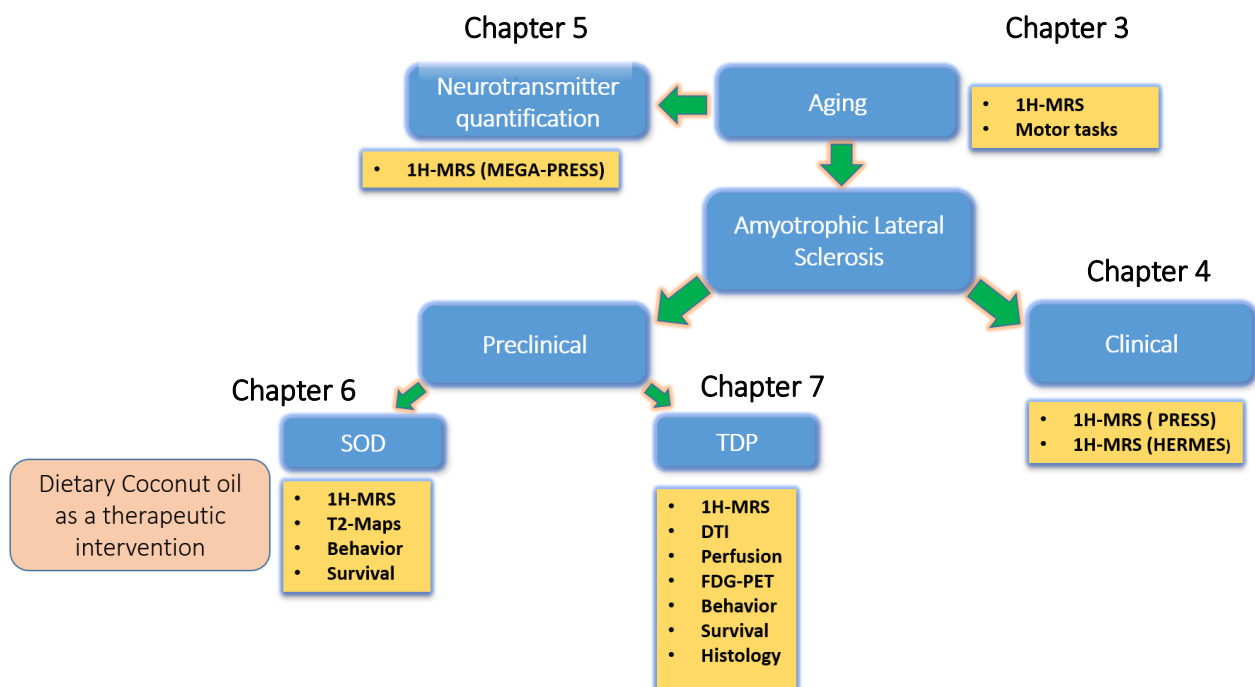
Chapter 3

Sensorimotor Cortex N-acetylaspartate as Correlate of Motor Performance Across the Adult Lifespan: Evidence from a ^{1}H-MRS study

Oron Levin[1]*, **Akila Weerasekera[2]***, Bradley R. King[1], Kirstin F. Heise[1], Diana M. Sima[3], Sima Chalavi[1], Celine Maes[1], Ronald Peeters[4], Stefan Sunaert[4], Koen Cuypers[1, 5], Sabine Van Huffel[3, 6], Dante Mantini[1], Uwe Himmelreich[2], Stephan P. Swinnen[1, 7]

(*) both authors contributed equally to this study

(1) Movement control & Neuroplasticity Research Group Department of Movement Sciences

(2) Biomedical MRI Unit Department of Imaging & Pathology, Group Biomedical Sciences, KU Leuven, Belgium

(3) Department of Electrical Engineering (ESAT), STADIUS Centre for Dynamical Systems, Signal Processing and Data Analytics, KU Leuven, Belgium

(4) Department of Radiology, University Hospitals Leuven, UZ Gasthuisberg, Belgium

(5) REVAL Research Institute, Hasselt University, Agoralaan, Building A, B-3590 Diepenbeek, Belgium

(6) Imec, Leuven, Belgium

(7) KU Leuven, Leuven Brain Institute (LBI), Leuven, Belgium

3. Sensorimotor cortex N-acetylaspartate as correlate of motor performance across the adult lifespan: evidence from a ^{1}H-MRS study

3.1 ABSTRACT

Alterations in neurochemical characteristics of the aging brain can be assessed in-vivo with proton-magnetic resonance spectroscopy (^{1}H-MRS). However, it remains unclear which specific metabolites are the most critical for functional integrity of the motor system. We have explored whether changes in the metabolic profile of the aging brain account for motor performance declines. We focused specifically on neurochemical integrity of the left sensorimotor cortex (SM1) and the occipital lobe (OCC), as both regions are thought to be main nodes of the visuomotor network underlying bimanual control. Aging was accompanied by decreased levels of N-acetylaspartate (NAA), glutamate-glutamine (Glx), creatine (Cr) and myo-inositol (mI) in both regions, and decreased Choline (Cho) in the OCC region. Lower NAA and Glx levels in the SM1 and lower NAA levels in the OCC were related to poorer performance on a bimanual coordination task, suggesting that NAA could serve as a potential biomarker for the integrity of the motor system supporting bimanual control. In addition, NAA, Glx, and mI levels in the SM1 were found to have significant positive correlation with performance on a manual dexterity test. The findings highlight the role for ^{1}H-MRS to study neurochemical correlates of motor performance across the adult lifespan.

3.2 INTRODUCTION

Aging is associated with gradual alterations in structural and neurochemical characteristics of the brain, the latter of which can be assessed in-vivo by the application of proton-magnetic resonance spectroscopy (^{1}H-MRS). In healthy human volunteers, in-vivo quantification of brain neurometabolites with ^{1}H-MRS typically shows age-related declines in regional levels of N-acetylaspartate (NAA), glutamate-glutamine complex (Glx), creatine + phosphocreatine (Cr), and gamma-aminobutyric acid (GABA), among other neurometabolites (Boumezbeur et al, 2010; Ding et al, 2016; Gao et al, 2013; Grachev & Apkarian, 2001; Grachev et al, 2001; Haga et al, 2009, Hermans et al, 2018; Zahr et al, 2013). These alterations may play a pivotal role as mediators of progressive cognitive and motor declines observed during aging. For example, decreased concentrations of various metabolites, including glutamate, choline, myo-inositol and GABA, have been linked to poor cognitive functioning (Zahr et al., 2008; Porges et al., 2017; Tumati et al., 2018). The majority of previous research has focused on the contribution of neurometabolite alterations to cognition, but very little attention has been paid to the neurometabolic correlates of motor functioning in a healthy aging population (Zahr et al., 2013), and in complex tasks in particular (e.g., bimanual coordination).

Importantly, changes in the regional levels of NAA, choline (Cho), myo-inositol (mI), GABA, and Glx have previously been identified as potential biomarkers of disease progression in neurodegenerative disorders such as amyotrophic lateral sclerosis (ALS), Parkinson's disease, or Alzheimer's disease (Ben Salem *et al*, 2008; Block *et al*, 1998; Bonneville *et al*, 2002; Kalra *et al*, 2006; Kantarci *et al*, 2007; Weerasekera *et al*., 2018; Zanigni *et al*, 2015; for reviews see: Duarte *et al*, 2012). Likewise, neurochemical alterations could also be indicative for neurodegenerative processes at the neuronal network levels. The general literature on aging in an apparently healthy population, nonetheless, lacks research efforts examining the relationship between behavioral changes and age-related shifts in the neurochemical profile of the healthy aging brain, with the few exceptions (Porges *et al*, 2017; Zahr *et al*, 2008; Zahr *et al*, 2013). The current study will address this critical knowledge gap.

In addition to the evidence directly associating neurometabolite alterations and performance changes in healthy aging (e.g., Zahr *et al*, 2013), there is also empirical evidence suggesting that age-linked shifts in the biochemical profile affect brain network connectivity (Hu *et al*, 2013; Kapogiannis *et al*, 2013; Lord *et al*, 2017; Thielen *et al*, 2018). For example, Hu *et al* (2013) reported significant associations of ^{1}H-MRS measurements of regional glutamate and GABA with activation/deactivation of the default mode network (DMN) during execution of a working memory task. Considering that integrity of neurochemical systems in the brain may be altered with age, one would expect to find an association between age-related changes in the regional levels of NAA and glutamate (among other neurochemicals and/or neurotransmitters) and degraded coordination performance. Specifically, the NAA concentration is considered to be a common marker of neuronal integrity and was recently associated with age-related changes in brain connectivity (Lord *et al*, 2017) or microstructural deterioration of white matter (WM) tracts in patients with traumatic brain injury (Grossman *et al*. 2015). Age-related decline in levels of glutamate has been previously related to decreases in motor and cognitive functioning in aging (Zahr *et al*, 2008; Zahr *et al*, 2013). Here, we focused specifically on neurochemical integrity of the left sensorimotor cortex (SM1) and the occipital lobe (OCC), as both regions are thought to be principal nodes of the visuomotor network underlying bimanual control. The association between age-related changes in the neurochemical profiles within the two regions of interest and performance changes was tested across multiple visuomotor bimanual tasks.

We primarily used a bimanual coordination task (BCT) analogous to that employed in our previous research (Beets *et al*. 2015; King *et al*, 2017; Sisti *et al*, 2010; Solesio-Jofre *et al*. 2014) and a bimanual Purdue pegboard task (PPT) that aimed to examine age-related declines in performance of (bi)manual dexterity and gross visuomotor skills (Desrosiers *et al*, 1995; Serbruyns *et al*, 2015). The more complex BCT was designed specifically to test multiple coordination constraints (i.e., temporal and spatial) and has been shown to induce activation of widespread brain networks that closely interact with the sensorimotor network (King *et al*, 2017). Therefore, this task was expected to be useful for studying the associations between integrity of neurochemical systems in SM1 and OCC and performance changes in the healthy aging brain. We expected that (1) lower Glx levels in the sensorimotor voxel will be related to decreased performance on BCT as both excitatory and inhibitory interactions between M1 and other brain regions are expected to rely primarily on activation of glutamatergic transmission (Chen, 2004; Liuzzi *et al*., 2010; Perez and Cohen, 2008) and that (2) performance declines in both BCT and PTT will be related to decreases in the level of NAA which is generally considered to be associated with neurodegenerative processes (e.g. Ding *et al*, 2016).

3.3 MATERIALS AND METHODS

3.3.1 Participants

We have included 106 healthy, right-handed (Oldfield, 1971) adults (age range 20.0 − 74.5 years, 49 women) that were from the same pool of participants as in King *et al* (2017). All participants had no past or present history of neurological or psychiatric disorders, no contra-indications for magnetic resonance imaging (as indicated in the guidelines of the University Hospital Leuven), normal or corrected to normal vision, and reported no consumption of psychoactive medications at the time of the experiment. The experimental protocol was approved by the local medical ethics committee (University Hospital Leuven; MEC reference S58441), and a written informed consent was obtained from each of the participants prior to his/her inclusion in the study. Fifteen of the 106 participants were excluded from the final analyses due to missing data and/or poor quality of MRI/MRS acquisition. Two participants voluntarily withdrew from the study before completion of the protocol, and one participant reported changes in medication/health status during the experiment. Finally, two participants were considered statistical outliers (defined as >2 SD from the average score of participants greater than 50 years of age) on the Montreal Cognitive Assessment (MoCA) (Nasreddine *et al*. 2005). Characteristics for the 86 participants that were included in the analyses are detailed in **Table 3.1**.

Table 3.1 Characteristics of the included participants.

	Age groups				
	All (n=86)	YA (20-35 (years) (n=23)	MY (35-50 (years) (n=22)	MO (50-65 (years) (n=21)	OA (65-75 (years) (n=20)
Gender, n(male/female)	47/39	12/11	10/12	11/10	14/6
Mean Age ± SD	48.1 ± 17.3	25.1 ± 4.3	43.2 ± 3.5	57.7 ± 4.9	69.8 ± 2.8
Mean MoCA ± SD				28.0 ± 1.6	27.1 ± 1.7

YA = young adults, MY = middle young, MO = middle old, OA = old adults. Age of the participants was specified as a decimal (in years) and the precise cutoffs for the 4 experimental groups were 20.00–34.99 (YA), 35.00–49.99 (MY), 50.00–64.99 (MO), and ≥65.00 years (OA). Montreal Cognitive Assessment (MoCA) means and SD are provided only for the MO and OA groups.

3.3.2 Procedure and data collection

The experimental protocol consisted of three experimental sessions; see also King *et al* (2017). The first session was used for screening/familiarization purposes, during which participants were informed about the experiment, completed screening-related questionnaires and assessments (i.e., health history, MRI contraindications, MoCA, etc.) and executed familiarization blocks of practice on the bimanual coordination task (BCT) while positioned supine in a mock MRI scanner (see below for BCT details). The subsequent two sessions consisted of MRI scanning and were completed at the University Hospital of KU Leuven. The first scanning session consisted of a standard scanning protocol, including the acquisition of a high-resolution T1-weighted structural image and ^{1}H-MRS (see below for scan acquisition details). The second scanning session was completed approximately one week following the first and consisted of 9 runs of the BCT while functional MR images were obtained (task-related imaging data not presented here).

3.3.3 Motor tasks

3.3.3.1 Purdue pegboard task (PPT)

This task consists of manipulating a maximum number of small pins in two vertical columns with pinholes on a board, within a 30-sec time period (Desrosiers *et al*, 1995; Tiffin and Asher, 1948, see also Serbruyns *et al*. 2015). The task was performed with the right hand, left hand, and with both hands simultaneously (in the bimanual condition). Each of the three subtasks was repeated three times. Before starting, the participants were allowed to practice with four pairs of pins. The dependent variable was the average number of pairs inserted during the three bimanual trials.

3.3.3.2 Bimanual coordination task (BCT)

The BCT and corresponding data have been previously reported (see King *et al* (2017) for a more detailed description of the task. Briefly, participants were positioned supine in the MRS scanner with a non-ferromagnetic device placed on their laps. The device contained two dials (5 cm diameter) to be rotated by the two hands in order to control the movement of a single cursor. The left and right hands controlled movements along the vertical and horizontal axes, respectively. When the left-hand dial was rotated clockwise (CW), the cursor moved up, whereas the cursor moved down when the left-hand dial was rotated counterclockwise (CCW). CW and CCW movements of the right-hand dial resulted in movements to the right and left, respectively. Angular displacements of the dials were registered with non-ferromagnetic high precision optical shaft encoders (HP, 2048 pulses per revolution, sampling frequency of 100 Hz), which were fixed to the movement axes of both dials. Visual information depicting task stimuli and feedback were shown on a LCD projector, visible via a mirror placed in front of the eyes. Four different movement trajectories were included in order to modulate task complexity. The first two trajectories required participants to follow a diagonal line on the screen but differed in terms of the slope of the line and thus the relative velocities (i.e., frequency ratios) at which the two hands had to rotate in order to appropriately perform the task. Participants moved the hands either at a 1:1 velocity ratio, or a 2:5 velocity ratio. The third condition required the two hands to move at a 1:1 frequency ratio, but the trajectory followed a V- or inverted-V shaped pattern (equal number of trials per block) in which participants had to change the direction or angle of their movement. Last, participants again

moved at a 1:1 frequency ratio, but the trajectory abruptly altered directions in a zigzag manner. This Abrupt pattern was either oriented horizontally or vertically (equal number of trials per block). Each BCT session contained eight blocks, with each block consisting of 24 trials (six per movement trajectory) and lasting approximately 6 min. The x and y positions of both the target cursor and the participants' cursor were sampled at 100 Hz and recorded for subsequent offline processing conducted in MATLAB R2016b (The MathWorks, Natick, Massachusetts, USA). Movement accuracy was the primary measure and reflected the percentage of overlap between the target and the participant's trajectory. The dependent variable was the average accuracy score collapsed over all BCT sessions and the four movement trajectories. For more details, see supplemental **Figures S1-S3**.

3.3.4   Brain imaging and ^{1}H-MRS

All scanning sessions were conducted using a Philips 3T Achieva Magnetic Resonance scanner (Philips Healthcare, The Netherlands) with a 32 channel receiver head coil. A high-resolution T1-weighted structural MR image (repetition time (TR) = 9.6 ms, echo time (TE) = 4.6 ms, 0.98 × 0.98 × 1.2 mm³ voxels, field of view: 256 × 256 × 160) was used to acquire a 3D magnetization prepared gradient echo (MPRAGE). [1]H-MR spectra were acquired in two voxel locations, namely the left sensorimotor cortex (SM1) (Fig. 1A) and occipital cortex (OCC) (Fig. 1B) which are parts of the visuomotor system. MRS data were acquired using a PRESS sequence (TR = 2000 ms, TE = 22 ms, number of averages = 128, spectral bandwidth 2000Hz, data size = 1024 points) with excitation water suppression. The voxel size was 1.5 × 1.5 × 1.5 cm³ in both the sensorimotor and occipital cortex voxels. The sensorimotor voxel was centered over the left hand-knob, parallel to the anterior and posterior axis (Yousry *et al.*, 1997). One surface was parallel to the cortical surface in the coronal and axial views (e.g., Greenhouse *et al*, 2016). The occipital voxel was centered on the median line, aligned with the cerebellar tentorium in the sagittal plane, and positioned as posteriorly as possible. The unsuppressed water signal was also acquired for absolute metabolite quantification using the same acquisition parameters, except for number of averages = 16. MR spectra were processed using jMRUI v6.0 (Stefan *et al.*, 2009) and the in-house developed software SPID (Poullet *et al.*, 2007). Signal-to-noise ratios (SNR) were determined by jMRUI QUEST in time-domain (maximum of FID/standard deviation of FID tail). Only spectra with linewidths less than 10 Hz or SNR greater than 5 were included for quantification. Spectra were also visually checked to ensure the absence of artefacts. The excluded data were eliminated from further processing. Metabolite signals and corresponding non-suppressed water signals were quantified in SPID. Averaged spectra from young (20-35 years) and old (65-75 years) participants are shown in **Figure 3.1**. Water-referenced concentrations of NAA, Glx, Cr, Cho, mI and Taurine (Tau) were quantified for each voxel location.

The MPRAGE T1-weighted MR images, acquired for the localization and placement of the MRS voxels were segmented with a statistical parametric mapping approach using SPM8 (http://www.fil.ion.ucl.ac.uk/spm/). Voxel registration was performed using custom-made scripts developed in MATLAB (The MathWorks, Natick, Massachusetts, USA) by Dr. Nia Goulden (Bangor University Wales, UK), which can be accessed at http://biu.bangor.ac.uk/projects.php.en (Sanaei Nezhad *et al*, 2017). Using the T1-weighted MR image and the orientation and location information from the Philips SPAR files, the scripts generate a mask of the voxel location, which is then used to calculate the partial volumes of gray matter (GM), white matter (WM), and cerebrospinal fluid (CSF) percentages within the voxel. The segmented tissue fractions were then used to correct for metabolite concentrations quantified using SPID for differences in CSF content according to Gasparovic *et al.*

(2006). T1 and T2 values used in our study were 1331 ms, 832 ms, and 3817 ms (T1) and 110 ms, 79 ms, and 503 ms (T2) for GM, WM and CSF, respectively. Metabolite relaxation times that were used for calculating the final corrected metabolite concentrations were taken from previous studies (Wansapura *et al.*, 1999; Träber *et al*, 2004).
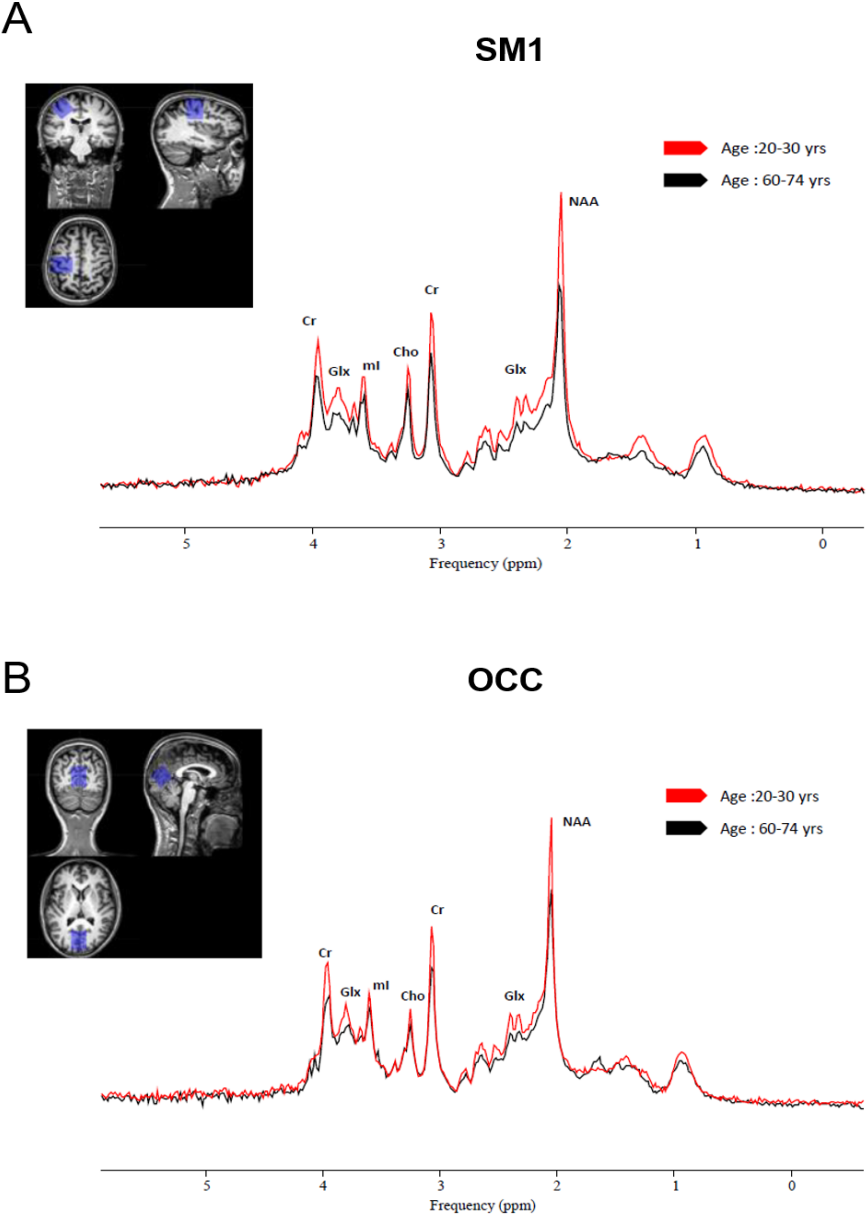
Figure 3.1. Primary sensorimotor (SM1) voxel positioning (A) and occipital cortex (OCC) voxel positioning (B) and their corresponding group averaged spectra from younger (20-35 years old cohort, n=23; blue curve) and older (65-75 years old cohort, n = 20; orange curve) participants.

3.3.5 Statistical analysis

Associations between performance measures and brain neurometabolites were examined using regression analyses. Data for final analyses were obtained from 86 participants (**Table 3.1**). Variables of interest were the average numbers of pairs inserted during performance of the bimanual variant of the PPT, average accuracy (collapsed across blocks, trials and conditions) on the BCT and estimated (water-referenced, tissue-corrected) concentrations of NAA, Glx, Cho, Cr, mI, and Tau in the SM1 and OCC regions. Partial correlations were used to control for confounding effects of age-related changes in tissue composition within a voxel (results are summarized in supplemental **Table S1**). It should be noted that significant changes in voxel tissue composition associated with age were found only for GM in the SM1 voxel ($r = -0.24$, $p = 0.026$). For details, see supplemental **Figure S4**. Next, associations between performance on the two motor tasks and the estimated (tissue-corrected) concentration levels of all six metabolites in the SM1 and OCC regions were studied. We conducted both a bivariate analysis of these associations (i.e., by evaluating the bivariate correlation between each neurometabolite and performance) for the confounding effect of age (through partial correlation analysis; see supplemental **Table S2**). To adjust for multiple correlation tests, we employed a Bonferroni correction: (1) A corrected value of $p < 0.0042$ (= 0.05/12) was set as significance threshold for correlations between age and concentration levels of NAA, Glx, Cho, Cr, mI, and Tau in SM1 and OCC (resulting in 12 correlation tests; i.e., 6 metabolites in 2 voxel locations correlated with age). (2) A corrected value of $p < 0.0021$ (= 0.05/24) was set as significance threshold for correlations between performance on the two coordination tasks and concentration levels of NAA, Glx, Cho, Cr, mI, and Tau in SM1 and OCC (resulting in 24 correlation tests; i.e., BCT and PPT performance scores correlated with 6 metabolites in 2 voxel locations). Finally, Fisher r-to-z transformation was used for comparison between correlations.

In addition to the aforementioned analyses, we employed stepwise multiple regression analyses to determine the unique variance contributed by specific metabolites to the performance of the PPT and BCT. Results of the multiple regression models are summarized in the supplementary Materials. For PPT, see supplemental **Table S3** (output of the standard multiple regression model) and supplemental **Table S4** (output of the stepwise multiple regression model). For BCT, see supplemental **Table S5** (output of the standard multiple regression model) and supplemental **Table S6** (output of the stepwise multiple regression model).

3.4 RESULTS

3.4.1 Age-related bimanual performance declines

3.1. Age-related bimanual performance declines

Our observations revealed significant negative correlations between age and performance on both bimanual tasks, indicating a general decline in coordination abilities with age. **Figure 3.2A** shows the correlation between age and performance scores on the PPT ($r = -0.51$; $p < 0.001$) and **Figure 3.2B** shows the correlation between age and performance scores on the BCT ($r = -0.73$; $p < 0.001$). Finally, the BCT performance scores positively correlated with the performance scores obtained on the PPT ($r = 0.38$; $p < 0.001$). However, the partial correlation between the two performance scores with age inserted as a

covariate was not significant (partial-r = 0.00, p > 0.9), indicating that the two tasks were not related to each other after factoring out the variance explained by age.
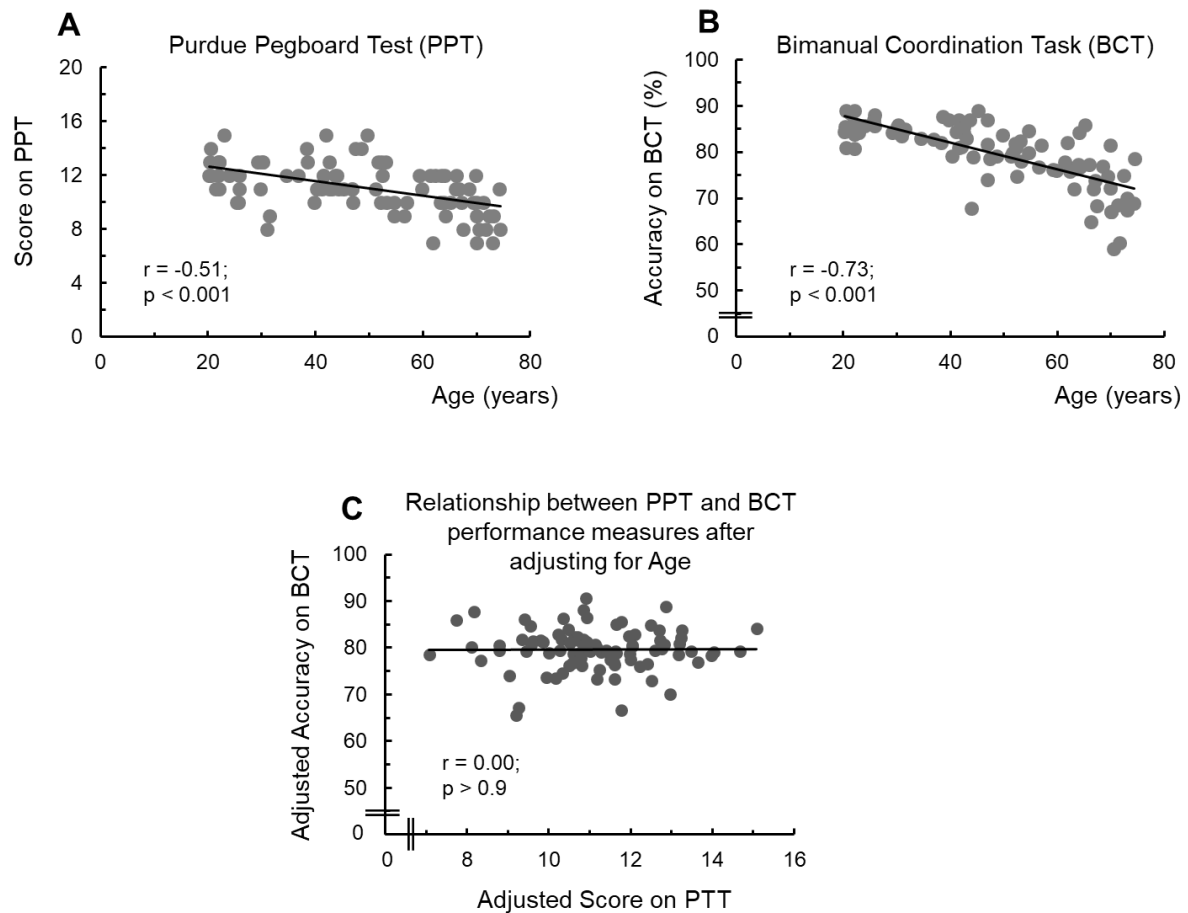
Figure 3.2. Linear-regression plots of performance levels by age for the 86 participants that were included in the statistical analysis. (A) Performance on the Purdue Pegboard Test (PPT), showing the average number of pairs inserted. (B) Performance on the Bimanual Coordination Task (BCT), showing the accuracy scores collapsed over all BCT sessions and the four movement trajectories. (C) Relationship between performance scores on the two motor tasks after adjusting for the variance explained by age did not remain significant (p > 0.9).

3.4.2 Age-related neurometabolic changes

Plots showing the linear regressions between age and the tissue-corrected concentrations of the six neurometabolites in SM1 and OCC regions are shown in **Figure 3.3**. The α-level of significance for Bonferroni correction was set at p ≤ 0.0042; herein correcting for 12 independent correlation tests (6 metabolites × 2 regions). Significant negative correlations between age and neurometabolite concentration levels in the SM1 were found for NAA (r = -0.43, p < 0.001), Glx (r = -0.32, p = 0.003), and Cr (r = -0.33, p = 0.002) (**Figure 3.3A**). Significant negative correlations between age and neurometabolite concentration levels in the OCC were found for NAA (r = -0.43, p < 0.001), Glx (r = -0.37, p < 0.001), Cr (r = -0.36, p = 0.001), and Cho (r = -0.31, p = 0.004) (**Figure 3.3B**). The remaining correlations did not reach statistical significance after correction for multiple comparisons (SM1: Cho, mI, and Tau (all ps > 0.023); OCC: mI, and Tau (both ps ≥ 0.007)). Age-related trajectories were similar across the various

metabolites, as no statistical differences between the age-related changes in concentration (i.e., correlation coefficients) were found; with exception of the differences between SM1 NAA (r = -0.43) and SM1 Tau (r = -0.09); Fisher r-to-z transformation: z = -2.38, p = 0.009 (otherwise all | z | ≤ 1.56, p > 0.05). Finally, results of partial correlations with SM1 or OCC gray matter or white mater fractions as covariates revealed a nearly identical pattern of results (see supplemental **Table S1**; Fisher r-to-z transformation: all | z | < 0.3, p > 0.4), suggesting that changes in concentrations with age cannot be explained by age-related changes in voxels' tissue composition.

3.4.3   Neurometabolic correlates of motor performance

3.4.3.1   Relationship between MRS metrics and motor performance

Correlation tests (Pearson) were performed between each of the two coordination tasks and SM1/OCC neurometabolites to investigate the degree of association between performance scores and concentration levels of the six neurometabolites in the two aforementioned brain regions. The α-level of significance for Bonferroni correction was set at p ≤ 0.0021; herein correcting for 24 independent correlation tests (6 metabolites × 2 regions × 2 tasks). Subsequently, partial Pearson correlations were used to explore in which neurometabolites variation in the tissue-corrected concentration levels were related to bimanual performance above and beyond the effect of age.

Findings revealed significant positive associations between PPT performance and SM1 levels of NAA (r = 0.39, p < 0.001), Glx (r = 0.34, p = 0.001), Cr (r = 0.42, p < 0.001), and mI (r = 0.41, p < 0.001) (see **Figure 4A** and supplemental **Table S2**). Among these, the correlation between performance on the PPT and SM1 level of mI was robust to partial correlation with age (partial-r ≥ 0.34, ps = 0.003). This was not the case for NAA, Glx, and Cr (all partial-r ≤ 0.30, p > 0.005). However, Fisher r–to-z transformations showed no significant differences between correlation coefficients for any of the six metabolites in neither voxel locations (all | z | ≤ 1.28, p > 0.1), indicating similar relationships between concentrations and performance across the various neurometabolites.

For the BCT task, significant positive associations were observed between average accuracy scores across the four movement-trajectory conditions and SM1 levels of NAA (r = 0.37, p < 0.001) and Glx (r = 0.32, p = 0.002), and OCC levels of NAA (r = 0.33, p = 0.002) (see **Figure 4B**). These relationships were not robust to partial correlations with age as a covariate; all partial-r ≤ 0.31, ps > 0.005 (see supplemental **Table S2**). Significant differences between non-adjusted and age-adjusted correlation coefficients were found for SM1 NAA (non-

adjusted r = 0.37 versus age-corrected partial correlation r = 0.08; Fisher r–to-z transformations: z = 1.95, p = 0.026) and OCC NAA (non-adjusted r = 0.33 versus age-corrected partial correlation r = 0.02; Fisher r-to-z transformation: z = 2. 08, p = 0.019) but not for SM1 Glx (non-adjusted r = 0.32 versus age-corrected partial correlation r = 0.14; Fisher r-to-z transformation: z = 1.25, p > 0.1).
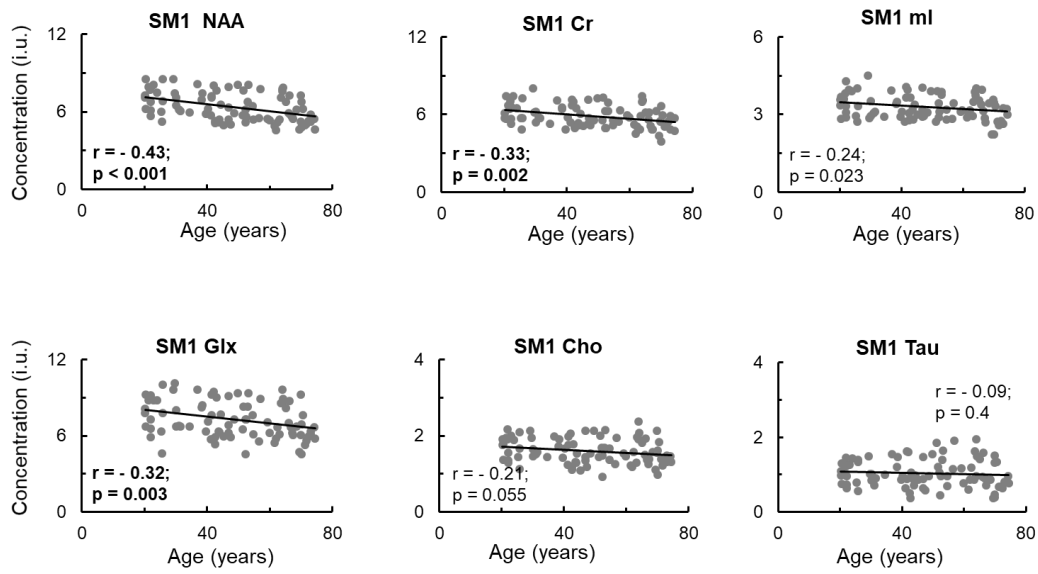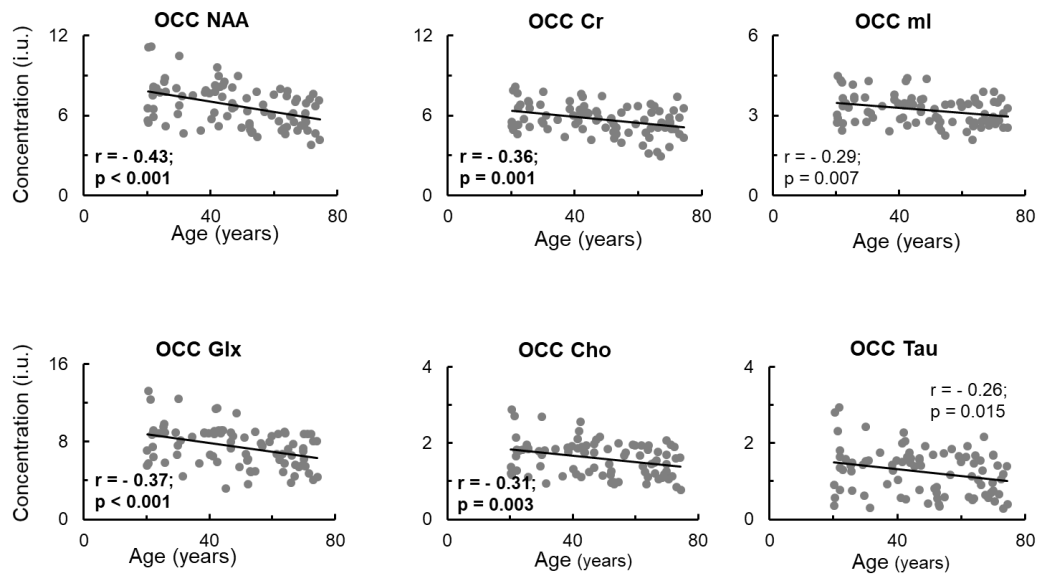
Figure 3.3. Linear-regression plots of metabolite levels by age in the primary sensorimotor (SM1) voxel positioning (A) or occipital cortex (OCC) voxel positioning (B). Abbreviations: i.u. = institutional units; N-acetylaspartate; Glx = glutamate-glutamine complex; Cr = creatine; Cho = choline; mI = myoinositol; Tau = Taurine. The correlation coefficients were considered significant when p-values were below the Bonferroni corrected threshold at $p < 0.0042$ (= 0.05/12), marginally significant when $p < 0.01$, and not significant when $p \geq 0.01$.
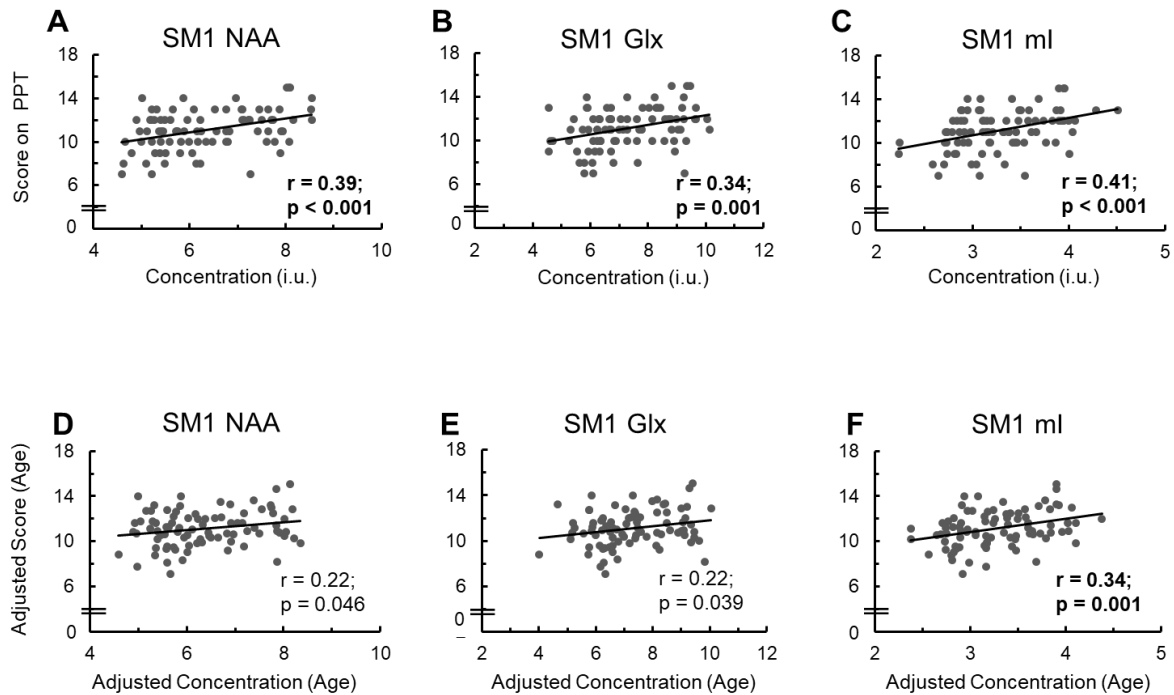
Figure 3.4. (A-C) Linear-regression plots showing the neurometabolite correlates of Purdue Pegboard Test (PTT) performance scores (i.e., average number of pairs inserted). Illustrations are shown for SM1 NAA, Glx, and mI (see supplemental Table S2 for correlations with the remaining SM1 and OCC neurometabolites). (D-F) Relationships between neurometabolite levels and performance after adjusting for the variance explained by age remained significant only for mI (p = 0.001). Abbreviations: i.u. = institutional units; N-acetylaspartate; Glx = glutamate-glutamine complex; Cr = creatine; mI = myoinositol. The correlation coefficients were considered significant when p-values were below the Bonferroni corrected threshold at p < 0.0021 (= 0.05/24), marginally significant when p < 0.01, and not significant when p ≥ 0.01.

3.4.3.2 Contribution of specific neurometabolites to performance

We used multiple regression analyses to examine the specific contribution of each neurometabolite to performance on the PPT and BCT tasks. For PTT performance, the regression model revealed that together the six metabolites in both SM1 and OCC contributed to 33.4% of the variance in performance, and that SM1 mI (t(73) = 2.01, p = 0.049) and SM1 Cho (t(73) = -2.92, p = 0.005) were independent predictors of performance to a greater extent than the contributions of the other metabolites (all ps ≥ 0.1; for details, see supplemental **Table S3**). However, only SM1 mI was a significant and independent predictor of PTT performance (t(84) = 4.10, p < 0.0001) when a stepwise regression model was applied, accounting for 16.7 % of the variance (**Table 3.2**; for details, see supplemental **Table S4**).

For BCT performance, the regression model revealed that together the six metabolites in both SM1 and OCC contributed to 27.4% of the variance in performance. However, none of the neurometabolites contributed independently to performance (all ps ≥ 0.077; for details, see supplemental **Table S5**). Using a stepwise regression model, only the SM1 NAA was a significant and independent predictor of BCT (t(84) = 3.64, p = 0.0005), contributing 13.6 % to the variance in performance. (**Table 3.2**; for details, see supplemental **Table S6**).
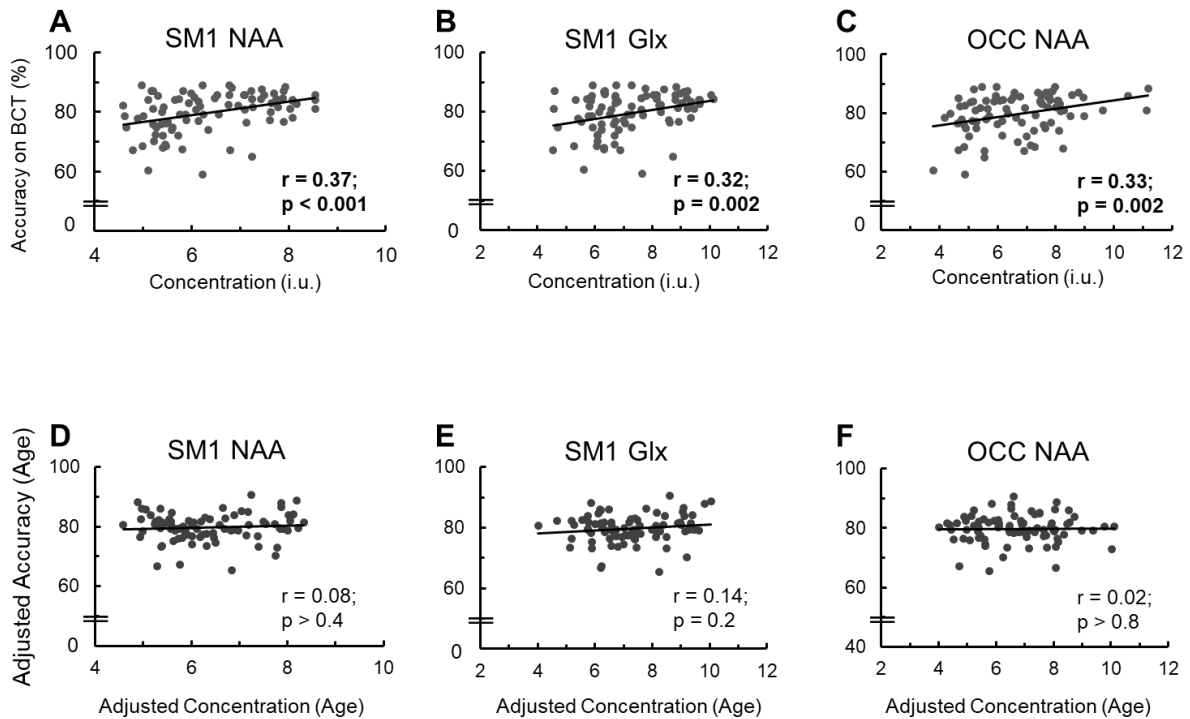
Figure 3.5. (A-C) Linear-regression plots showing the neurometabolite correlates of Bimanual Coordination Task (BCT) performance. Illustrations are shown SM1 NAA and Glx and OCC NAA (see supplemental Table S2 for correlations with the remaining SM1 and OCC neurometabolites). (D-F) Relationships between neurometabolite levels and performance after adjusting for the variance explained by age were not significant ($p \geq 0.068$). Abbreviations: i.u. = institutional units; N-acetylaspartate; Glx = glutamate-glutamine complex. The correlation coefficients were considered significant when p-values were below the Bonferroni corrected threshold at $p < 0.0021$ (= 0.05/24), marginally significant when $p < 0.01$, and not significant when $p \geq 0.01$.

3.5   DISCUSSION

Our findings provide novel evidence that neurometabolic changes in the aging left sensorimotor cortex (SM1) account for age-related decline of bimanual coordination skills in healthy older adults. A first major observation was that (tissue-corrected) levels of multiple neurometabolites in both the left sensorimotor and occipital regions of the healthy human brain decreased significantly with age. A second major observation was that lower NAA levels in the left SM1 corresponded to poorer levels of performance on the BCT, a visuomotor task that has shown associations with brain structural and functional connectivity measures in several studies of the aging brain (Fujiyama *et al.*, 2016; King *et al.*, 2017; Solesio-Jofre *et al.*, 2014). Finally, our observations indicated that superior performance on the Purdue Pegboard test was predicted by high levels of mI in the SM1.

Table 3.2: Main neurometabolic predictors of motor performance obtained by stepwise regression between behavioral motor measures on Purdue and BCT tasks and the putative neurometabolite predictors (NAA, Glx, Cr, Cho, mI, and Tau concentrations in the SM1 and OCC regions).

Task	Predictor†	R^2	R^2-Adj.	F	B ± SE	β ± SE	p-value
PPT		0.334[a]	0.225	3.06**			
	SM1 mI	0.167[b]	0.157	16.8***	1.603 ± 0.391	0.408 ± 0.100	< 0.0001
BCT		0.274[a]	0.154	2.29*			
	SM1 NAA	0.136[b]	0.126	13.2***	2.255 ± 0.620	0.369 ± 0.101	0.0005

†Significant contribution by an independent variable to the total explained variation in the stepwise multiple regression model (p < 0.01).

[a] Summary statistics for standard multiple regression model (Table S3 and Table S5 in supplementary materials).

[b] Summary statistics and regression summary for stepwise multiple regression model (Table S4 and Table S6 in supplementary materials).

PPT = Purdue pegboard test; BCT = Bimanual tracking task; SM1 = primary sensorimotor cortex; OCC = occipital cortex; NAA = N-acetylaspartate; Glx = glutamate-glutamine complex; Cr = creatine; Cho = choline; mI = myoinositol; Tau = Taurine; B = regression coefficient; β = standardized regression coefficient; SE = standard error; R2 = Multiple R2; R2-Adj = Adjusted R2; *p < 0.05; ** p < 0.01; *** p < 0.001.

3.5.1 Effects of age on neurometabolite levels in SM1 and OCC

Findings from the current MRS data showed an overall age-related decrease in the concentration of principal brain neurometabolites such as NAA, Cr, and Glutamate/Glutamine (Glx) in both voxel locations. Significant age-related decline in Cho level was observed only in the OCC voxel, whereas, for the remaining metabolites, only weak and/or moderate trends towards low levels in old age (mI and Cho in the SM1 voxel and mI and Tau in the OCC voxel) or no age-effects at all (SM1 Tau) were found. Overall, our findings point towards homogeneous age-related alterations of 1H-MRS neurometabolites within each region with the exception of SM1 Tau. Specifically, concentration levels of Cr, Glx, and NAA showed similar declines with age in both regions, whereas age-related changes in concentration levels of Cho and Tau were more prominent in the OCC than in the SM1. However, there were no statistically significant differences among the correlation coefficients (exception: SM1 NAA and SM1 Tau).

Given the aforementioned findings, it looks like age-related changes in neurometabolite concentration could be caused, partly, by region-specific structural neurodegenerative processes as previously proposed by Grachev and Apkarian (2001); for specific details see: Soares *et al*. (2009). Direct evidence

for this interpretation was provided in a recent study by Ding and colleagues (Ding *et al*., 2016), who applied whole brain ^{1}H-MR spectroscopic (wbMRS) imaging to study metabolite concentrations in the GM and WM of different brain regions. Specifically, Ding *et al* (2016) showed: (1) Age-dependent decrease of NAA content occurred predominantly in GM across all brain regions, whereas age-related decline of NAA content in WM occurred only in the right and left frontal lobes and the left temporal lobe. (2) Significant decline of Glx content in GM occurred for the main part more in the right frontal than in posterior brain regions. (3) Age-dependent changes in contents of Cho, total Cr (tCr) and mI occurred mostly in WM (irrespective of brain region examined). Interestingly, observations from our study showed that NAA, Glx, and Cr concentrations in the SM1 and OCC voxels were slightly more susceptible to aging as compared to mI, Cho and Tau (for SM1) or mI and Tau (for OCC) (see **Figure 3**). But again, with exception of the difference between SM1 NAA and SM1 Tau, we did not find statistical differences among all other correlation coefficients.   In addition, results from partial correlations showed that SM1 neurometabolites were more susceptible to changes in GM content within the voxel whereas this was not the case for the OCC neurometabolites (see supplemental **Table S1**). This may suggest, at first sight, that neurodegenerative changes associated with GM loss in the SM1 may have some (even though minor) impact on concentration levels of NAA within this voxel. However, we found no significant differences between correlation coefficients with and without control for within voxel tissue composition. Moreover, findings from the study of Ding *et al* (2016) suggest that while reduced brain NAA (and possibly Glx and Cr) in the aging human brain could be associated with a reduction of withe volume and neuronal density, age-related differences in WM microstructural organization may also be a contributing factor. Indeed, recent studies associated reduced levels of NAA with a decline in WM tract integrity in patients with a mild traumatic brain injury (Grossman *et al*, 2015) or schizophrenia (Chiappelli *et al*, 2015).

Significant negative correlations with age were also found for the Glx levels in both voxel locations, though the age-effect was slightly less pronounced than that observed for NAA. This finding is in line with previous studies reporting a declining trend of Glx levels with age across multiple cortical and subcortical regions, including the primary sensorimotor cortex (Kaiser, *et al*., 2005), striatum (Zahr *et al*., 2013), hippocampus (Harris *et al*, 2014), and the prefrontal lobe (Ding *et al*, 2016). Similarly to NAA, decreased Glx levels with age in the SM1 and OCC voxels may reflect age-related reduction in neuronal density and/or decrease of neuronal metabolic activity (Ding *et al*, 2016; Kaiser *et al*., 2005). Taken together, the findings that age-related changes in NAA and Glx concentrations occur in parallel could suggest that changes in brain tissue volume and brain metabolite concentrations with age may be triggered by shared neurodegenerative processes; albeit one should not preclude the possibility that the latter may be triggered by the former. This could indicate loss of neuronal integrity and demyelination (NAA), altered energy-metabolism (Cr) and/or shift in balance of neurotransmitter metabolism (Glx). Further studies combining whole brain ^{1}H-MRS and ^{13}C-MRS imaging methods will be required to either substantiate or disprove those interpretations. (Boumezbeur *et al*., 2009; Rothman *et al*., 2011).

Although minor, declining trends with age were also observed for levels of Cho and mI in both voxel locations and for levels of Tau in the OCC voxel location. However, these findings were inconsistent with findings of other ^{1}H-MRS studies involving healthy older adults, reporting increased levels of mI and Cho with age (e.g., Chiappelli *et al*, 2015; Ding *et al*, 2016; Schmitz *et al*., 2018 Zahr *et al*, 2013). For example, mI content, related to glial cell size/proliferation, has been reported to increase in WM (Chiappelli *et al*,

2015; Ding *et al*., 2016) whereas findings from ^{1}H-MRS data in our study showed decreased levels of mI in both SM1 and OCC voxels. Also contrary to our findings was the observed increased level of Cho (Ding *et al*, 2016; Schmitz *et al*., 2018 Zahr *et al*, 2013); however, see observations of Tumati and colleagues (Tumati *et al*., 2018) who reported reduced Cho and mI levels in elderly with mild cognitive impairments. This inconsistency could be attributed, partially, to differences in voxel's tissue composition across the selected regions of interest (Gussew *et al*, 2012), and/or susceptibility of the selected regions of interests to WM loss with aging (e.g., Ding *et al*, 2016). For example, observations from studies where increased Cho or mI levels with age were reported, came predominantly from prefrontal and temporal voxels that are more sensitive to WM loss than left SM1 or middle OCC (Ding *et al*, 2016). Importantly, increased concentrations of Cho and mI have been argued to signify progressive loss of myelin integrity which is expected to be more prominent in pathologies such as multiple sclerosis (MS), traumatic brain injury (TBI) or schizophrenia (e.g., Chiappelli *et al*, 2015; Klauser *et al*, 2018; Marshall *et al*., 2018; Zaaraoui *et al*., 2010) than in healthy aging.

3.5.2 Neurometabolic correlates of motor performance

In line with findings from previous studies, we observed a progressive decline in bimanual performance with age (Boisgontier *et al*, 2016; Fujiyama *et al*., 2012; Fujiyama *et al*, 2016; Heuninckx *et al*., 2004; King *et al*, 2017; Serrien *et al*., 2000; Swinnen *et al*., 1998). In general, young adults (i.e., participants in the 20-35 years old cohort) showed higher performance scores than older adults (i.e., participants in the 65-75 years old cohort) on both the PPT and the BCT. Previous work has attributed these declines to multiple factors, including loss of GM and WM volume (Boisgontier *et al*, 2016; Fling *et al*, 2011; Koppelmans *et al*., 2015; Serbruyns *et al*, 2015), breakdown in the brain's network segregation (King *et al*, 2017), and/or disruption of connectivity between motor and non-motor brain regions (Fujiyama *et al*., 2016). The observations from the current study suggest that, in addition to structural and functional changes (e.g., Fujiyama *et al*, 2016; Inano *et al*, 2013; King *et al*, 2017), neurometabolic changes across the lifespan may also be a contributing factor for the noted bimanual performance declines with increasing age.

Our findings corroborate, in part, observations from other studies highlighting the association between age-related changes in prefrontal or striatal concentrations of NAA or Glx and observed declines in motor or cognitive functioning in older healthy adults (e.g., Nikolaidis *et al*, 2017; Zahr *et al*, 2008; Zahr *et al*, 2013). Other evidence linking changes in the concentration levels of brain neurometabolites such as NAA to performance deficits or abnormalities emerged from studies on pathological populations or pathological aging (Chiappelli *et al*, 2015; Kantarci *et al*, 2002; Tumati *et al*, 2018); for review see Zanigni *et al* (2015). Importantly, decreases in concentration of NAA have previously been linked to reduced microstructural organization of WM or decreased axonal density in aging and pathological conditions (Bjartmar *et al*, 2000; Bonneville *et al*, 2002; Chiappelli *et al*., 2015; Grossman *et al*., 2015; Wijtenburg *et al*, 2013). As such, the present finding referring to the positive relationship between SM1 NAA levels and accuracy scores on the BCT suggests that a reduced NAA may reflect impaired functional integrity of brain networks that support bimanual control. This assertion is supported by evidence from some studies where both MRS and diffusion tensor imaging (DTI) were conducted on cohorts of healthy elderly and/or patients with neurodegenerative diseases, showing that reduced NAA concentrations were associated with degeneration of WM tracts (Chiappelli *et al*., 2015; Grossman *et al*, 2015; Wijtenburg *et al*., 2013). Future research investigating the role of NAA as a biomarker of brain network

integrity in healthy (as well as in pathological) aging should examine the extent by which declines in NAA levels are linked to reduced connectivity and disrupted neural network communication.

Finally, evidence from the current study showed that SM1 mI levels were positively associated with performance on the Purdue Pegboard Test (PPT). However, a careful examination of the current findings in relation to findings from previous studies require additional considerations. Specifically, evidence from multiple studies indicated that mI levels slightly increased with age (Chiappelli *et al.*, 2015; Raininko and Mattsson, 2010; Reyngoudt *et al*, 2012; Zahr *et al.*, 2013). This would suggest a negative association between cortical and/or subcortical levels of mI and performance, a finding that is in contrast to the observations of the present study, which revealed a positive significant correlation between mI levels in SM1 and performance. Further studies are necessary in order to conclude whether the positive association reported here between mI levels and performance on the PPT indeed arise from alterations in structural and functional integrity of SM1.

3.6   CONCLUSIONS

We have shown that levels of multiple neurometabolites in both SM1 and OCC regions of the healthy human brain decrease significantly with age and that lower NAA levels in the left SM1 are associated with age-related declines in bimanual performance. Given that NAA may reflect neurodegenerative processes related to alterations in WM microstructure, these findings highlight the necessity to make use of multimodal imaging approaches in order to reveal interactions between brain structure, neurochemicals and behavior. Neurometabolite concentrations in other brain regions are also important to consider because motor functions are orchestrated via interactions between the motor and other brain networks. Therefore, further research using 1H-MRS should be conducted to examine age-related changes in neurometabolite levels across multiple regions of the brain as plausible predictors of motor performance decline in healthy older adults.

3.7   SUPPLEMENTARY MATERIAL

Bimanual coordination task (BCT)

A customized nonferromagnetic apparatus was positioned above the participants' laps. The device contained 2 dials (5 cm diameter) to be rotated by the 2 hands in order to control the movement of a cursor. The left and right hands controlled movements along the vertical and horizontal axes, respectively. When the left-hand dial was rotated clockwise (CW), the cursor moved up, whereas the cursor moved down when the left-hand dial was rotated counterclockwise (CCW). CW and CCW movements of the right-hand dial resulted in movements to the right and left, respectively. Angular displacements of the dials were registered with nonferromagnetic high precision optical shaft encoders (HP, 2048 pulses per revolution, sampling frequency of 100 Hz), which were fixed to the movement axes of both dials. This enabled registration of kinematics as well as the display of online visual feedback. Visual information depicting task stimuli and feedback were shown on a LCD projector, visible via a mirror placed in front of the eyes. The goal of the BCT was to track a visual target presented on the screen by simultaneously rotating the 2 dials with the 2 hands. Each trial started by depicting a desired

behavioral trajectory (blue line), a target dot (white circle) as well as the cursor to be moved by the participants (see **supplementary Figure S1, panel A**). Prior to each trial, the cursor would be automatically shift to the appropriate starting position, after a 2s planning period the target dot would move along the trajectory at a constant speed for 10 s. The participants would then have 10s to mimic the trajectory as accurately as possible by rotating the dials after which the screen would turn black and following an interval of 3 s the next target would appear. Four different movement trajectories were included in order to modulate task complexity (see **supplemental Figure S1, panel B**). The first 2 trajectories required participants to follow a diagonal line on the screen but differed in terms of the slope of the line and thus the relative velocities (i.e., frequency ratios) the 2 hands had to rotate in order to appropriately perform the task. Participants moved the hands either at a 1:1 or 2:5 velocity ratio. Thus, the 2 hands needed to rotate at the same velocity for the Line 1:1 condition (with the direction of movement either from the screen's bottom-right to top-left or vice versa; equal number of trials per block). Conversely, for the Line 2:5 condition, the left hand had to rotate 2 units for every 5 units the right hand rotated (or vice versa; equal number of trials per block). The third condition required the 2 hands to move at a 1:1 frequency ratio, but the trajectory followed a V- or inverted-V shaped pattern (equal number of trials per block) in which participants had to change the direction or angle of their movement (herein referred to as the condition Angle). Last, participants again moved at a 1:1 frequency ratio, but the trajectory abruptly altered directions in a zigzag manner (herein referred to as condition Abrupt). This Abrupt pattern was either oriented horizontally or vertically (equal number of trials per block). Each BCT session contained 8 blocks, with each block consisting of 24 trials (6 per movement trajectory) and lasting approximately 6 min.
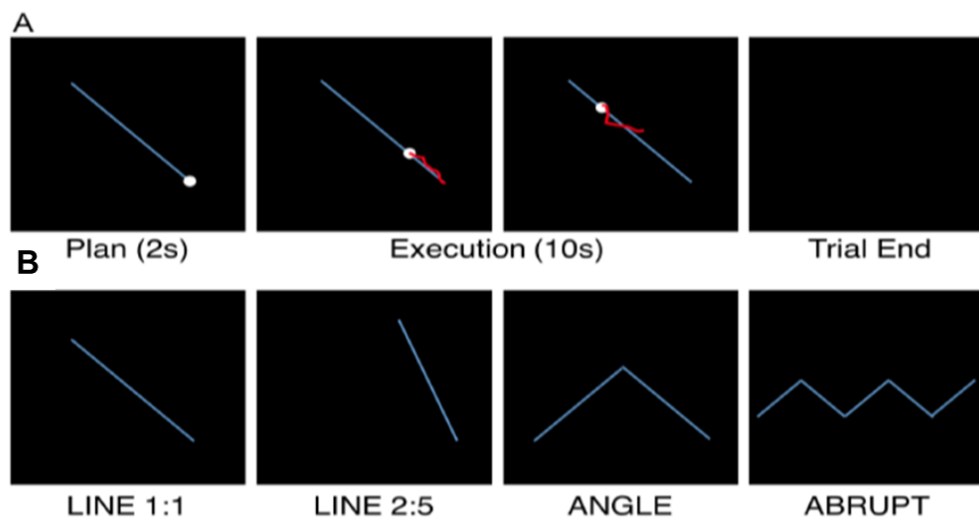
Supplemental Figure S1

Exemplar movement trajectories (one trial) for Line 25 (left panel) and Abrupt (right) movement trajectory conditions are depicted in **supplemental Figure S2**. The Blue line represents the ideal movement path and the Red line represents the participant's movement trajectory (axes are x and y coordinates in units of mm). Note that the dependent measure average deviation, defined as the average Euclidean distance between target and participant's cursor position, is similar in the two exemplar trials. However, in the Abrupt condition (right panel), the participant executed a vertical line through the middle of the desired movement trajectory. In such a case, the Euclidean distance between

cursor and target fluctuated – and sometimes reached a value of zero – based on the movement pattern of the desired target and not the participant's movement. Thus, the mean Euclidean distance for the trial was relatively small despite the participant failing to perform the task appropriately. Conversely, the accuracy measure defined in the main text highlights a clear difference between the two exemplar trials and thus is a more appropriate assessment of performance, particularly for the irregular (i.e., Angle and Abrupt) movement trajectories.
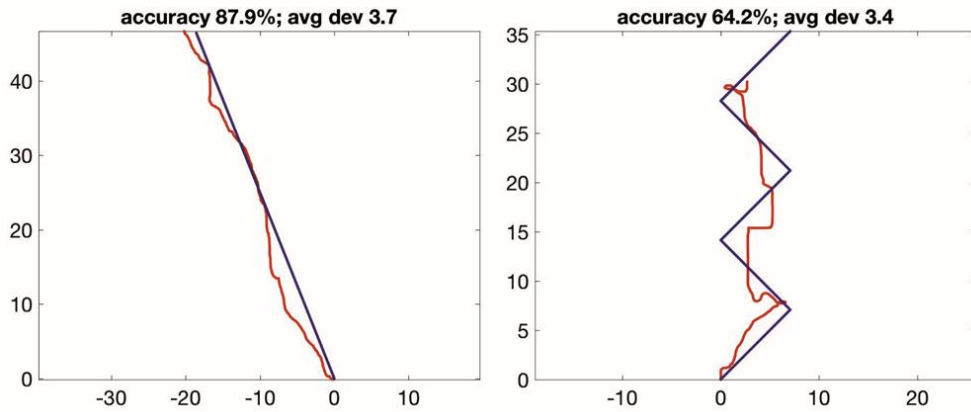
Supplemental Figure S2

The x and y positions of both the target circle and the participants' cursor were sampled at 100 Hz and recorded for subsequent offline processing conducted in MATLAB R2016b (The MathWorks, Natick, Massachusetts, USA). Movement accuracy was the primary measure and reflected the percentage of overlap between the target trajectory and the participant trajectory. The primary dependent measure, labeled as movement accuracy, reflected the percentage of the target line that was "covered" by the participants' movements. For each sample within a trial (i.e., every 10 ms), a line with the shortest distance between the participant's cursor and the ideal movement trajectory was projected. The projection point on the target line was marked as covered and then movement accuracy was quantified as the percentage of the ideal movement trajectory that was covered by the participant. No trials were labeled as statistical outliers for the accuracy dependent measure, defined as scores greater than 2SD from the mean for that particular individual block and movement trajectory. Outlier analyses were completed separately for each block to account for performance changes as a function of practice. The average accuracy scores obtained for each of the four trajectory condition are illustrated in **supplementary Figure S3** as function of age (n=86 participants). The dependent variable used in the current study was the average accuracy score collapsed over all BCT sessions and the four movement trajectories
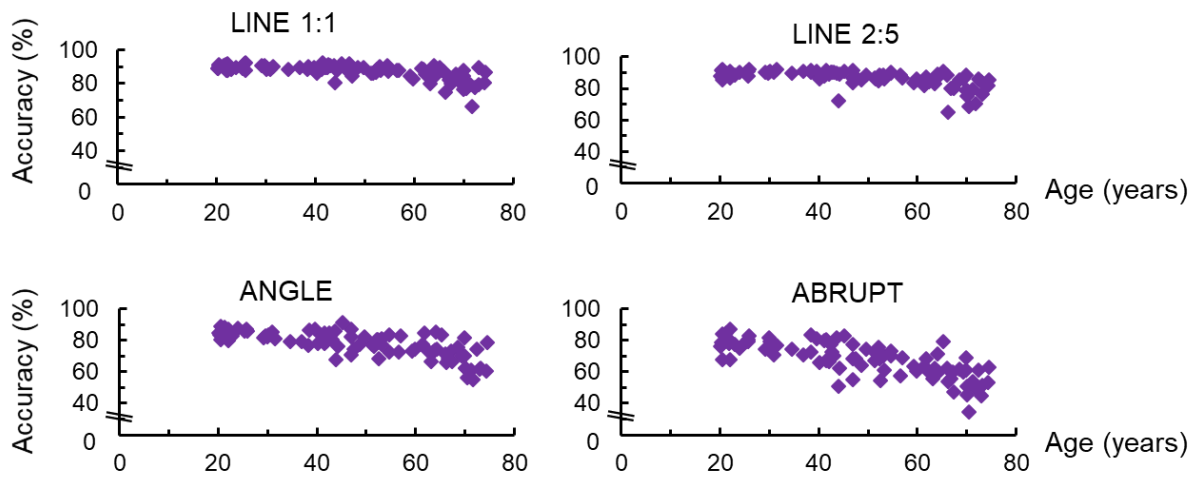
Supplemental Figure S3

Fractional tissue volumes

Supplemental **Figure S4** illustrates age-related changes in the fractional tissue volumes of gray matter (GM), white matte (WM), and cerebrospinal fluid (CSF) in the sensorimotor (SM1) and the occipital cortex (OCC) voxels (n=86 participants). Solid lines show the linear fits with age. A significant negative correlations with age was observed for SM1 fractional GM volume (r = -0.24, p = 0.026), suggesting that gray matter content in the sensorimotor voxel declined with age. No effects of age were found for the fractional tissue volumes of WM and CSF in SM1 voxel or fractional tissue volumes of GM, WM, and CSF in the OCC voxel (all r ≤ 0.12, p > 0.2).

SM1

OCC
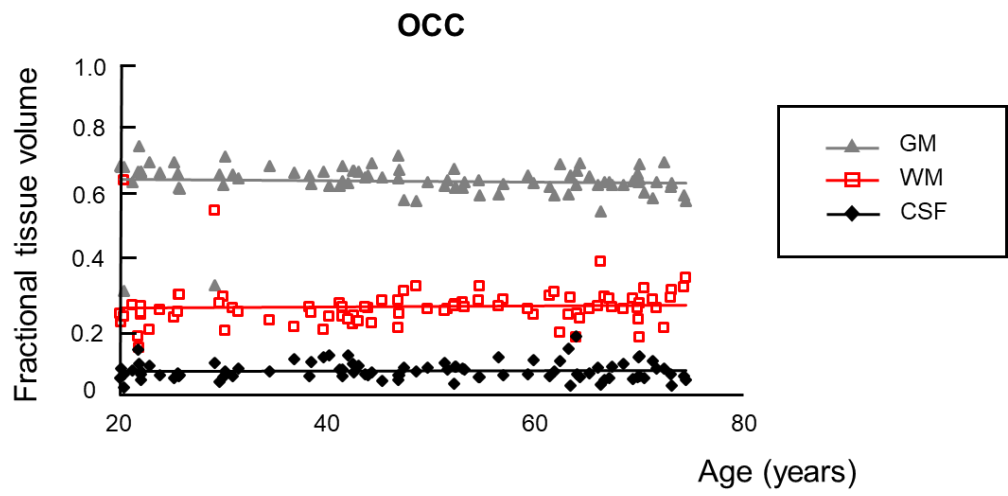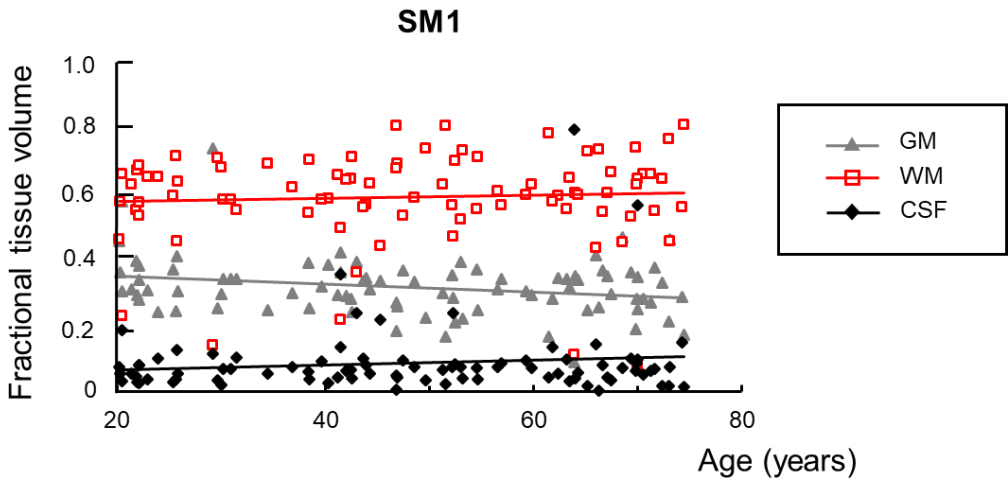
Supplemental Figure S4

Supplemental Table S1

Results of the Pearson correlations between neurometabolites levels and age and the partial correlation coefficients obtained after adjusting for structural tissue composition properties within voxel (n = 86 participants).

		SM1						OCC					
		NAA	Glx	Cr	mI	Cho	Tau	NAA	Glx	Cr	mI	Cho	Tau
r	AGE	**-0.43***	**-0.32***	**-0.33***	-0.24^{NS}	-0.21^{NS}	-0.09^{NS}	**-0.43***	**-0.37***	**-0.36***	-0.29†	**-0.31***	-0.26^{NS}
partial-r	fgm	**-0.40***	-0.29†	-0.29†	-0.21^{NS}	0.19^{NS}	-0.08^{NS}	**-0.44***	**-0.38***	**-0.37***	-0.30†	**-0.32***	-0.27^{NS}
partial-r	fwm	**-0.43***	**-0.31***	**-0.33***	-0.24^{NS}	-0.20^{NS}	-0.09^{NS}	**-0.44***	**-0.38***	**-0.36***	-0.29†	**-0.32***	-0.27^{NS}

SM1 = primary sensorimotor cortex; OCC = occipital cortex; NAA = N-acetylaspartate; Glx = glutamate-glutamine complex; Cr = creatine; Cho = choline; mI = myoinositol; Tau = Taurine. r = Pearson correlation coefficient; partial-r = Pearson partial correlation coefficient corrected for % fraction of grey matter (fgm) or white matter (fwm) utilized for tissue class segmentation within each voxel; The correlation coefficients were considered significant (*) when p-values were below the Bonferroni corrected threshold at $p < 0.0042$ (= 0.05/12), marginally significant (†) when $p < 0.01$, and not significant (NS) when $p \geq 0.01$. Significant correlations are highlighted in **bold text**.

Supplemental Table S2

Results of the Pearson correlations between neurometabolite measures and performance measures on the two motor tasks and the partial correlation coefficients obtained after adjusting for age (n=86 participants).

Task		SM1						OCC					
		NAA	Glx	Cr	mI	Cho	Tau	NAA	Glx	Cr	mI	Cho	Tau
PPT	r	**0.39***	**0.34***	**0.42***	**0.41***	0.27^{NS}	0.23^{NS}	$0.30†$	$0.29†$	$0.28†$	$0.28†$	0.27^{NS}	0.20^{NS}
	partial-r (age)	0.22^{NS}	0.22^{NS}	$0.30†$	**0.34***	0.19^{NS}	0.22^{NS}	0.11^{NS}	0.13^{NS}	0.12^{NS}	0.16^{NS}	0.13^{NS}	$<0.1^{NS}$
BCT	r	**0.37***	**0.32***	$0.29†$	$0.28†$	0.24^{NS}	0.20^{NS}	**0.33***	0.26^{NS}	0.26^{NS}	0.20^{NS}	0.25^{NS}	0.23^{NS}
	partial-r (age)	0.08^{NS}	0.14^{NS}	0.08^{NS}	0.16^{NS}	0.14^{NS}	0.20^{NS}	0.02^{NS}	-0.02^{NS}	0.00^{NS}	-0.02^{NS}	0.03^{NS}	0.06^{NS}

PPT = Purdue Pegboard Test; BCT = Bimanual Coordination Task; SM1 = primary sensorimotor cortex; OCC = occipital cortex; NAA = N-acetylaspartate; Glx = glutamate-glutamine complex; Cr = creatine; Cho = choline; mI = myoinositol; Tau = Taurine. r = Pearson correlation coefficient; partial-r = Pearson partial correlation coefficient corrected for age (age). The correlation coefficients were considered significant (*) when p-values were below the Bonferroni corrected threshold at $p < 0.0021$ (= 0.05/24), marginally significant (†) when $p < 0.01$, and not significant (NS) when $p \geq 0.01$. Significant correlations are highlighted in **bold text**.

Supplemental Table S3

Results of the multiple regression between performance measures on the Purdue Pegboard Test (PPT) and the putative neurometabolite predictors (NAA, Glx, Cr, Cho, mI, and Tau concentrations in the SM1 and OCC regions).

		R	R^2	R^2-Adj.	F(12,73)	B ± SE	β ± SE	p-value
		0.578	0.334	0.225	3.06**			
SM1	NAA					0.419 ± 0.622	0.253 ± 0.376	0.50
	Glx					0.538 ± 0.502	0.423 ± 0.395	0.29
	Cr					0.500 ± 0.630	0.230 ± 0.290	0.43
	Cho					-6.081 ± 2.085	-1.091 ± 0.374	0.005
	mI					1.932 ± 0.963	0.492 ± 0.245	0.049
	Tau					0.697 ± 0.909	0.142 ± 0.186	0.45
OCC	NAA					-0.144 ± 0.380	-0.123 ± 0.324	0.71
	Glx					0.082 ± 0.324	0.092 ± 0.367	0.80
	Cr					-0.210 ± 0.487	-0.128 ± 0.297	0.67
	Cho					2.342 ± 1.992	0.574 ± 0.488	0.24
	mI					0.453 ± 0.915	0.136 ± 0.274	0.62
	Tau					-1.442 ± 0.884	-0.468 ± 0.287	0.11

SM1 = primary sensorimotor cortex; OCC = occipital cortex; NAA = N-acetylaspartate; Glx = glutamate-glutamine complex; Cr = creatine; Cho = choline; mI = myoinositol; Tau = Taurine; B = regression coefficient; β = standardized regression coefficient; SE = standard error; R^2 = Multiple R^2; R^2-Adj = Adjusted R^2; *p < 0.05; ** p < 0.01; *** p < 0.001.

Supplemental Table S4

Summary of the stepwise (backward) regression between performance measures on the Purdue Pegboard Test (PPT) and the putative neurometabolite predictors (NAA, Glx, Cr, Cho, mI, and Tau concentrations in the SM1 and OCC regions). Predictors are sorted from first (OCC Glx) to last (OCC Cho) out in the order of removal.

Predictor	R	R^2	R^2-Adj.	$F_{(1,84)}$	Multiple R^2	R^2 - Change	F –to enter/remove	p-value
SM1 mI	0.408	0.167	0.157	16.81***				
OCC Glx					0.334	-0.001	0.063	0.80
OCC NAA					0.333	-0.001	0.117	0.73
OCC mI					0.331	-0.002	0.216	0.64
OCC Cr					0.330	-0.001	0.070	0.79
SM1 NAA					0.326	-0.004	0.497	0.48
SM1 Tau					0.322	-0.004	0.466	0.50
SM1 Cr					0.311	-0.011	1.327	0.25
SM1 Glx					0.272	-0.039	4.526	0.036
OCC Tau					0.244	-0.027	3.028	0.085
SM1 Cho					0.221	-0.023	2.531	0.12
OCC Cho					0.167	-0.054	5.778	0.018

SM1 = primary sensorimotor cortex; OCC = occipital cortex; NAA = N-acetylaspartate; Glx = glutamate-glutamine complex; Cr = creatine; Cho = choline; mI = myoinositol; Tau = Taurine; *$p < 0.05$; ** $p < 0.01$; *** $p < 0.001$.

Supplemental Table S5

Results of the multiple regression between performance measures on the Bimanual Coordination Task (BCT) and the putative neurometabolite predictors (NAA, Glx, Cr, Cho, mI, and Tau concentrations in the SM1 and OCC regions).

		R	R^2	R^2-Adj.	F(12,73)	B ± SE	β ± SE	p-value
		0.523	0.274	0.155	2.29*			
SM1	NAA					4.307 ± 2.400	0.705 ± 0.393	0.077
	Glx					1.351 ± 1.937	0.288 ± 0.412	0.49
	Cr					-2.760 ± 2.433	-0.344 ± 0.303	0.26
	Cho					-12.92 ± 8.049	-0.627 ± 0.391	0.11
	mI					3.096 ± 3.718	0.214 ± 0.256	0.41
	Tau					0.114 ± 3.509	0.006 ± 0.194	0.97
OCC	NAA					1.989 ± 1.467	0.459 ± 0.339	0.18
	Glx					-1.159 ± 1.252	-0.354 ± 0.383	0.36
	Cr					2.811 ± 1.880	0.464 ± 0.310	0.14
	Cho					2.326 ± 7.690	0.154 ± 0.510	0.76
	mI					-6.062 ± 3.532	-0.491 ± 0.286	0.090
	Tau					-0.283 ± 3.413	-0.025 ± 0.300	0.93

SM1 = primary sensorimotor cortex; OCC = occipital cortex; NAA = N-acetylaspartate; Glx = glutamate-glutamine complex; Cr = creatine; Cho = choline; mI = myoinositol; Tau = Taurine; B = regression coefficient; β = standardized regression coefficient; SE = standard error; R2 = Multiple R2; R2-Adj = Adjusted R2; *p < 0.05; ** p < 0.01; *** p < 0.001.

Supplemental Table S6

Summary of the stepwise (backward) regression between performance measures on the Bimanual Coordination Task (BCT) and the putative neurometabolite predictors (NAA, Glx, Cr, Cho, mI, and Tau concentrations in the SM1 and OCC regions). Predictors are sorted from first (SM1 Tau) to last (OCC NAA) out in the order of removal.

Predictor	R	R^2	R^2-Adj.	$F(1,84)$	Multiple R^2	R^2 - Change	F –to enter/remove	p-value
SM1 NAA	0.369	0.136	0.126	13.24***				
SM1 Tau					0.274	-0.0000	0.001	0.97
OCC Tau					0.274	-0.0001	0.006	0.93
OCC Cho					0.272	-0.0011	0.115	0.74
SM1 Glx					0.267	-0.0058	0.602	0.44
SM1 mI					0.258	-0.0082	0.861	0.36
SM1 Cr					0.250	-0.0089	0.933	0.33
OCC Glx					0.242	-0.0071	0.750	0.39
OCC Cr					0.233	-0.0090	0.952	0.33
OCC mI					0.218	-0.0150	1.589	0.21
SM1 Cho					0.196	-0.0222	2.333	0.13
OCC NAA					0.136	-0.0600	6.193	0.015

SM1 = primary sensorimotor cortex; OCC = occipital cortex; NAA = N-acetylaspartate; Glx = glutamate-glutamine complex; Cr = creatine; Cho = choline; mI = myoinositol; Tau = Taurine; $*p < 0.05$; $** p < 0.01$; $*** p < 0.001$.

3.8 REFERENCES

Beets, I.A.M., Gooijers, J., Boisgontier, M.P., Pauwels, L., Coxon, J.P., Wittenberg, G., Swinnen, S.P. Reduced neural differentiation between feedback conditions after bimanual coordination training with and without augmented visual feedback. *Cereb. Cortex*. 2015; 25: 1958–1969.

Ben Salem, D., Walker, P.M., Aho, S., Tavernier, B., Giroud, M., Tzourio, C., Ricolfi, F., Brunotte, F. Brain flexibility and balance and gait performances mark morphological and metabolic abnormalities in the elderly. *J. Clin. Neurosci*. 2008; 15: 1360–1365.

Bjartmar, C., Kidd, G., Mork, S., Rudick, R., Trapp, B.D. Neurological disability correlates with spinal cord axonal loss and reduced N-acetyl aspartate in chronic multiple sclerosis patients. *Ann Neurol. 2000*; 48: 893–901.

Block, W., Karitzky, J., Träber, F., Pohl, C., Keller, E., Mundegar, R.R., Lamerichs, R., Rink, H., Ries, F., Schild, H.H., Jerusalem, F., 1998. Proton magnetic resonance spectroscopy of the primary motor cortex in patients with motor neuron disease: subgroup analysis and follow-up measurements. *Arch. Neurol*. 55, 931–936.

Boisgontier, M.P., Cheval, B., van Ruitenbeek, P., Levin, O., Renaud, O., Chanal, J., Swinnen, S.P. Whole-brain grey matter density predicts balance stability irrespective of age and protects older adults from falling. *Gait & Posture*. 2016; 45: 143-150.

Boisgontier, M.P., van Ruitenbeek, P., Leunissen, I., Chalavi, S., Sunaert, S., Levin, O., Swinnen, S.P. Nucleus accumbens and caudate atrophy predicts longer action selection times in young and old adults. *Hum. Brain Mapp*. 2016;37: 4629–4639.

Bonneville, F., Moriarty, D.M., Li, B.S., Babb, J.S., Grossman, R.I., Gonen, O. Whole-brain N-acetylaspartate concentration: correlation with T2-weighted lesion volume and expanded disability status scale score in cases of relapsing-remitting multiple sclerosis. *AJNR, Am. J. Neuroradiol*. 2000; 23: 371–375.

Boumezbeur, F., Mason, G.F., de Graaf, R.A., Behar, K.L., Cline, G.W., Shulman, G.I., Rothman, D.L., Petersen, K.F. Altered brain mitochondrial metabolism in healthy aging as assessed by *in vivo* magnetic resonance spectroscopy. *J Cereb Blood Flow Metab*. 2010; 30: 211 – 221.

Chard DT, Griffin CM, McLean MA, Kapeller P, Kapoor R, Thompson AJ, Miller DH. Brain metabolite changes in cortical grey and normal-appearing white matter in clinically early relapsing-remitting multiple sclerosis. *Brain*. 2002 Oct;125(Pt10):2342-52.

Chiappelli, J., Hong, L.E., Wijtenburg, S.A., Du, X., Gaston, F., Kochunov, P., Rowland, L.M. Alterations in frontal white matter neurochemistry and microstructure in schizophrenia: implications for neuroinflammation. *Transl. Psychiatry*. 2015.

Cichocka, M., Bereś, A. From fetus to older age: A review of brain metabolic changes across the lifespan. Ageing Res. Rev. 2018; 46: 60 – 73.

Desrosiers, J., Hébert, R., Bravo, G., Dutil, E. The Purdue Pegboard Test: normative data for people aged 60 and over. Disabil. Rehabil. 1995;17: 217 – 224.

Ding, B., Chen, K.M., Ling, H.W., Zhang, H., Chai, W.M., Li, X., Wang, T. Diffusion tensor imaging correlates with proton magnetic resonance spectroscopy in posterior cingulate region of patients with alzheimer's disease. *Dement Geriatr Cogn Disord*. 2008; 25: 218 – 225.

Ding, X.Q., Maudsley, A.A., Sabati, M., Sheriff, S., Schmitz, B., Schütze, M., Bronzlik, P., Kahl, K.G., Lanfermann, H. Physiological neuronal decline in healthy aging human brain - An *in vivo* study with MRI and short echo-time whole-brain1H MR spectroscopic imaging. *NeuroImage*. 2016; 137: 45–51.

Duarte, J.M.N., Do, K.Q., Gruetter, R. Longitudinal neurochemical modifications in the aging mouse brain measured *in vivo* by ^{1}H magnetic resonance spectroscopy. *Neurobiol Aging*. 2014; 35: 1660 – 1668.

Duarte, J.M.N., Lei, H., Mlynárik, V., Gruetter, R. The neurochemical profile quantified by *in vivo* 1H NMR spectroscopy. *NeuroImage*. 2012; 61: 342–362.

Eylers, V. V., Maudsley, A.A., Bronzlik, P., Dellani, P.R., Lanfermann, H., Ding, X.Q. Detection of normal aging effects on human brain metabolite concentrations and microstructure with whole-brain MR spectroscopic imaging and quantitative MR imaging. *Am. J. Neuroradiol*. 2016;37: 447–454.

Fling, B.W., Seidler, R.D. Fundamental differences in callosal structure, neu-rophysiologic function, and bimanual control in young and older adults. *Cereb.Cortex*. 2012b; 22: 2643–2652.

Fling, B.W., Seidler, R.D. Task-dependent effects of interhemispheric inhibi-tion on motor control. Behav. Brain Res. 2012b; 226: 211–217.

Fling, B.W., Walsh, C.M., Bangert, A.S., Reuter-Lorenz, P.A., Welsh, R.C., Seidler, R.D. Differential callosal contributions to bimanual control in young and older adults. J. Cogn. Neurosci. 23, 2171–2185.

Fujiyama, H., Garry, M.I., Levin, O., Swinnen, S.P., Summers, J.J., 2009. Age-related dif-ferences in inhibitory processes during interlimb coordination. Brain Res. 2011; 1262: 38–47.

Fujiyama, H., Hinder, M.R., Schmidt, M.W., Garry, M.I., Summers, J.J. Age-related differences in corticospinal excitability and inhibition duringcoordination of upper and lower limbs. Neurobiol. Aging. 2012; 33: 1481-1484.

Fujiyama, H., Van Soom, J., Rens, G., Gooijers, J., Leunissen, I., Levin, O., Swinnen, S.P. Age-related changes in frontal network structural and functional connectivity in relation to bimanual movement control. *J. Neurosci*. 2016; 36: 1808–1822.

Gao, F., Edden, R.A.E., Li, M., Puts, N.A.J., Wang, G., Liu, C., Zhao, B., Wang, H., Bai, X., Zhao, C., Wang, X., Barker, P.B. Edited magnetic resonance spectroscopy detects an age-related decline in brain GABA levels. *NeuroImage*. 2013; 78: 75–82.

Gasparovic, C., Song, T., Devier, D., Bockholt, H.J., Caprihan, A., Mullins, P.G., Posse, S., Jung, R.E., Morrison, L.A. Use of tissue water as a concentration reference for proton spectroscopic imaging. *Magn. Reson. Med*. 2006; 55: 1219–1226.

Giorgio, A., Santelli, L., Tomassini, V., Bosnell, R., Smith, S., De Stefano, N., Johansen-Berg, H. Age-related changes in grey and white matter structure throughout adulthood. *NeuroImage*. 2010; 51: 943-951.

Greenhouse, I., Noah, S., Maddock, R.J., Ivry, R.B. Individual differences in GABA content are reliable but are not uniform across the human cortex. *NeuroImage*. 2016; 139: 1–7.

Grachev, I.D., Apkarian, A.V. Chemical network of the living human brain: Evidence of reorganization with aging. *Cogn. Brain Res*. 2001; 11: 185–197.

Grachev, I.D., Swarnkar, A., Szeverenyi, N.M., Ramachandran, T.S., Apkarian, A.V. Aging alters the multichemical networking profile of the human brain: an *in vivo* 1H-MRS study of young versus middle-aged subjects. J. Neurochem. 2001; 77: 292 – 303.

Grossman E.J., Kirov, I.I., Gonen, O., Novikov, D.S., Davitz, M.S., Lui, Y.W., Grossman, R.I., Inglese, M., Fieremans, E. N-acetyl-aspartate levels correlate with intra-axonal compartment parameters from diffusion MRI. *NeuroImage*. 2015; 118: 334 – 343.

Gussew, A., Erdtel, M., Hiepe, P., Rzanny, R., Reichenbach, J.R. Absolute quantitation of brain metabolites with respect to heterogeneous tissue compositions in 1H-MR spectroscopic volumes. Magn. Reson. Mater. *Physics, Biol. Med*. 2012; 25: 321–333.

Haga, K.K., Khor, Y.P., Farrall, A., Wardlaw, J.M. A systematic review of brain metabolite changes, measured with 1H magnetic resonance spectroscopy, in healthy aging. *Neurobiol. Aging*. 2009; 30, 353–363.

Harris, J.L., Yeh, H.W., Swerdlow, R.H., Choi, I.Y., Lee, P., Brooks, W.M. High-field proton magnetic resonance spectroscopy reveals metabolic effects of normal brain aging. *Neurobiol. Aging*. 2014; 35: 1686–1694.

Heise, K.F., Zimerman, M., Hoppe, J., Gerloff, C., Wegscheider, K., Hummel, F.C. The aging motor system as a model for plastic changes of GABA-mediated intracortical inhibition and their behavioral relevance. *J. Neurosci*. 2013; 33: 9039–9049.

Heuninckx, S., Debaere, F., Wenderoth, N., Verschueren, S., Swinnen, S.P. Ipsilateral coordination deficits and central processing requirements associatedwith coordination as a function of aging. J. Gerontol B. *Psychol. Sci. Soc. Sci*. 2004; 59, 225–232.

Hermans, L., Levin, O., Maes, C., van Ruitenbeek, P., Heise, K.F., Edden, R.A.E., Puts, N.A.J., Peeters, R., King, B.R., Meesen, R.L.J., Leunissen, I., Swinnen, S.P., Cuypers, K. GABA levels and measures of intracortical and interhemispheric excitability in healthy young and older adults: an MRS-TMS study. Neurobiol. Aging. 2018; 65: 168–177.

Hinder, M.R., Fujiyama, H., Summers, J.J. Premotor-motor interhemispheric inhibition is released during movement initiation in older but not young adults. *PLoS One*. 2012; 7.

Hu, Y., Chen, X., Gu, H., Yang, Y. Resting-State Glutamate and GABA concentrations predict task-induced deactivation in the default mode network. *J Neurosci*. 2013; 33: 18566 – 18573.

Inano, S., Takao, H., Hayashi, N., Yoshioka, N., Mori, H., Kunimatsu, A., Abe, O., Ohtomo, K., 2013. Effects of age and gender on neuroanatomical volumes. *J. Magn. Reson. Imaging.* 2013; 37: 1072–1076.

Kaiser, L.G., Schuff, N., Cashdollar, N., Weiner, M.W. Scyllo-inositol in normal aging human brain: 1H magnetic resonance spectroscopy study at 4 Tesla. *NMR Biomed*. 2005; 18: 51–55.

Kalra, S., Tai, P., Genge, A., Arnold, D.L. Rapid improvement in cortical neuronal integrity in amyotrophic lateral sclerosis detected by proton magnetic resonance spectroscopic imaging. *J. Neurol*. 2006; 253: 1060–1063.

Kantarci, K., Smith, G.E., Ivnik, R.J., Petersen, R.C., Boeve, B.F., Knopman, D.S., Tangalos, E.G., Jack, C.R. Jr. 1H magnetic resonance spectroscopy, cognitive function, and apolipoprotein e genotype in normal aging, mild cognitive impairment and Alzheimer's disease. *J. Int. Neuropsychol. Soc*. 2002; 8: 934 – 942.

Kantarci, K., Weigand, S.D., Petersen, R.C., Boeve, B.F., Knopman, D.S., Gunter, J., Reyes, D., Shiung, M., O'Brien, P.C., Smith, G.E., Ivnik, R.J., Tangalos, E.G., Jack, C.R. Jr. Longitudinal 1H MRS changes in mild cognitive impairment and Alzheimer's disease. *Neurobiol. Aging*. 2007; 28: 1330–1339.

Kapogiannis, D., Reiter, D.A., Willette, A.A., Mattson, M.P. Posteromedial cortex glutamate and GABA predict intrinsic functional connectivity of the default mode network. *NeuroImage*. 2013; 64: 112–119.

King, B.R., van Ruitenbeek, P., Leunissen, I., Cuypers, K., Heise, K.-F., Santos Monteiro, T., Hermans, L., Levin, O., Albouy, G., Mantini, D., Swinnen, S.P. Age-related declines in motor performance are associated with decreased segregation of large-scale resting state brain networks. Cereb. Cortex. 2017. (ahead of print); see https://doi.org/10.1093/cercor/bhx297

Klauser, A.M., Wiebenga, O.T., Eijlers, A.J.C., Schoonheim, M.M., Uitdehaag, B.M.J., Barkhof, F., Pouwels, P.J.W., Geurts, J.J.G. Metabolites predict lesion formation and severity in relapsing-remitting multiple sclerosis. *Mult. Scler. J*. 2018; 24: 491–500.

Koppelmans, V., Hirsiger, S., Mérillat, S., Jäncke, L., Seidler, R.D., 2015. Cerebellar gray and white matter volume and their relation with age and manual motor performance in healthy older adults. *Hum. Brain Mapp*. 2015; 36: 2352–2363.

Levin, O., Fujiyama, H., Boisgontier, M.P., Swinnen, S.P., Summers, J.J. Aging and motor inhibition: a converging perspective provided by brain stimulation and imaging approaches. *Neurosci. Biobehav. Rev*. 2014; 43: 100 - 117.

Lord, A.R., Li, M., Demenescu, L.R., van den Meer, J., Borchardt, V., Krause, A., Heinze, H.J., Breakspear, M., Walter, M1. richness in functional connectivity depends on the neuronal integrity within the posterior cingulate cortex. *Front Neurosci*. 2017;11: 184.

Maes, C., Hermans, L., Pauwels, L., Chalavi, S., Leunissen, I., Levin, O., Cuypers, K., Peeters, R., Sunaert, S. Mantini D., Puts, N.A.J., Edden, R.A.E., Swinnen, S.P., 2017. Age-related differences in GABA levels are driven by bulk tissue changes. Hum. Brain Mapp. (ahead of print); see https://doi.org/10.1002/hbm.24201

Marshall, I., Thrippleton, M.J., Bastin, M.E., Mollison, D., Dickie, D.A., Chappell, F.M., Semple, S.I.K., Cooper, A., Pavitt, S., Giovannoni, G., Wheeler-Kingshott, C.A.M.G., Solanky, B.S., Weir, C.J., Stallard, N., Hawkins, C., Sharrack, B., Chataway, J., Connick, P., Chandran, S. Characterisation of tissue-type metabolic content in secondary progressive multiple sclerosis: a magnetic resonance spectroscopic imaging study. *J. Neurol*. 2018; 265: 1795 – 1802.

Santos Monteiro, T., Beets, I.A.M, Boisgontier, M.P., Gooijers, J., Pauwels, L., Chalavi, S., King. B., Albouy, G., Swinnen, S.P. Relative cortico-subcortical shift in brain activity but preserved training-induced neural modulation in older adults during bimanual motor learning. Neurobiol Aging. 2017; 58: 54-67.

Nasreddine, Z.S., Phillips, N.A., Bédirian, V., Charbonneau, S., Whitehead, V., Collin, I., Cummings, J.L., Chertkow, H. The Montreal Cognitive Assessment, MoCA: a brief screening tool for mild cognitive impairment. *J Am Geriatr Soc*. 2005; 53: 695–699.

Nikolaidis, A., Baniqued, P.L., Kranz, M.B., Scavuzzo, C.J., Barbey, A.K., Kramer, A.F., Larsen R.J. Multivariate Associations of Fluid Intelligence and NAA. *Cereb. Cortex*. 2017; 27: 2607 – 2616.

Oldfield, R.C. The assessment and analysis of handedness: The Edinburgh inventory. *Neuropsychologia*. 1971; 9: 97–113.

Pears, M.R., Cooper, J.D., Mitchison, H.M., Mortishire-Smith, R.J., Pearce, D.A., Griffin, J.L. High resolution 1H NMR-based metabolomics indicates a neurotransmitter cycling deficit in cerebral tissue from a mouse model of Batten disease. J Biol Chem. 2005; 280: 42508 – 42514.

Porges, E.C., Woods, A.J., Edden, R.A.E., Puts, N.A.J., Harris, A.D., Chen, H., Garcia, A.M., Seider, T.R., Lamb, D.G., Williamson, J.B., Cohen, R.A. Frontal gamma-aminobutyric acid concentrations are associated with cognitive performance in older adults. Biol Psychiatry Cogn Neurosci *Neuroimaging*. 2017; 2: 38 – 44.

Poullet, J., Sima, D.M., Simonetti, A.W., De Neuter, B., Vanhamme, L., Lemmerling, P., Van Huffel, S., Neuter, B. De, Vanhamme, L. An automated quantitation of short echo time MRS spectra in an open source software environment: AQSES. *NMR Biomed*. 2007; 20: 493–504.

Raininko, R., Mattsson, P. Metabolite concentrations in supraventricular white matter from teenage to early old age: A short echo time ^{1}H magnetic resonance spectroscopy (MRS) study. *Acta Radiol*. 2010; 51: 309 – 315.

Reyngoudt, H., Claeys, T., Vlerick, L., Verleden, S., Acou, M., Deblaere, K., De Deene, Y., Audenaert, K., Goethals, I., Achten, E. Age-related differences in metabolites in the posterior cingulate cortex and hippocampus of normal ageing brain: a 1H-MRS study. *Eur. J. Radiol*. 2012; 81: e223 – e231.

Reis, J., Swayne, O.B., Vandermeeren, Y., Camus, M., Dimyan, M.A., Harris-love, M., Perez, M.A., Ragert, P., Rothwell, J.C., Cohen, L.G. Contribution of transcranial magnetic stimulation to the understanding of cortical mechanisms involved in motor control. J. Physiol. 2008; 586: 325-351.

Rothman, D.L., De Feyter, H.M., de Graaf, R.A., Mason, G.F., Behar, K.L. ^{13}C MRS studies of neuroenergetics and neurotransmitter cycling in humans. *NMR Biomed*. 2011; 24: 943–957.

Sanaei Nezhad, F., Anton, A., Parkes, L.M., Deakin, B., Williams, S.R. Quantification of glutathione in the human brain by MR spectroscopy at 3 Tesla: Comparison of PRESS and MEGA-PRESS. *Magn. Reson. Med*. 2017; 78:

1257 – 1266.

Savic, I., Thomas, A.M., Ke, Y., Curran, J., Fried, I., Engel, J. Jr. *In vivo* measurements of glutamine + glutamate (Glx) and N-acetyl aspartate (NAA) levels in human partial epilepsy. Acta Neurol. Scand. 2000; 102: 179 – 188.

Schmitz, B., Wang, X., Barker, P.B., Pilatus, U., Bronzlik, P., Dadak, M., Kahl, K.G., Lanfermann, H., Ding, X.Q., 2018. Effects of aging on the human brain: a proton and phosphorus MR spectroscopy study at 3T. J. Neuroimaging. 2018; 28: 416–421.

Serbruyns, L., Leunissen, I., Huysmans, T., Cuypers, K., Meesen, R.L., van Ruitenbeek, P., Sijbers, J., Swinnen, S.P. Subcortical volumetric changes across the adult lifespan: Subregional thalamic atrophy accounts for age-related sensorimotor performance declines. *Cortex*. 2015; 65: 128–138.

Serrien, D.J., Swinnen, S.P., Stelmach, G.E. Age-related deterioration of coor-dinated interlimb behavior. *J. Gerontol. B. Psychol. Sci. Soc. Sci*. 2000; 55B: 295–303.

Sisti, H.M., Geurts, M., Clerckx, R., Gooijers, J., Coxon, J.P., Heitger, M.H., Caeyenberghs, K., Beets, I.A.M., Serbruyns, L., Swinnen, S.P. Testing multiple coordination constraints with a novel bimanual visuomotor task. *PLoS One*. 2011; 6: e23619.

Soares, D.P., Law, M., 2009. Magnetic resonance spectroscopy of the brain: review of metabolites and clinical applications. *Clin. Radiol*. 2009; 64: 12 – 21.

Solesio-Jofre, E., Serbruyns, L., Woolley, D.G., Mantini, D., Beets, I.A.M., Swinnen, S.P. Aging effects on the resting state motor network and interlimb coordination. *Hum. Brain Mapp*. 2014; 35: 3945–3961.

Soeiro-de-Souza, M.G., Henning, A., Machado-Vieira, R., Moreno, R.A., Pastorello, B.F., da Costa Leite, C., Vallada, H., Otaduy, M.C. Anterior cingulate Glutamate-Glutamine cycle metabolites are altered in euthymic bipolar I disorder. *Eur. Neuropsychopharmacol*. 2015; 25: 2221–2229.

Stefan, D., Cesare, F. Di, Andrasescu, A., Popa, E., Lazariev, A., Vescovo, E., Strbak, O., Williams, S., Starcuk, Z., Cabanas, M., Van Ormondt, D., Graveron-Demilly, D. Quantitation of magnetic resonance spectroscopy signals: The jMRUI software package. Meas. Sci. Technol. 2009; 20. (see https://doi.org/10.1088/0957-0233/20/10/104035).

Stovell, M.G., Yan, J.L., Sleigh, A., Mada, M.O., Carpenter, T.A., Hutchinson, P.J.A., Carpenter, K.L.H. Assessing metabolism and injury in acute human traumatic brain injury with magnetic resonance spectroscopy: Current and future applications. *Front Neurol*. 2017; 8: 426.

Swinnen, S.P., Verschueren, S., Bogaerts, H., Dounskaia, N., Lee, T., Stelmach, G., Serrien, D. Age-related deficits in motor learning and differences in feedback processing during the production of a bimanual coordination pattern. *Cogn.Neuropsychol*. 2018; 15: 439–466.

Thielen, J.W., Hong, D., Rohani Rankouhi, S., Wiltfang, J., Fernández, G., Norris, D.G., Tendolkar, I. The increase in medial prefrontal glutamate/glutamine concentration during memory encoding is associated with better memory performance and stronger functional connectivity in the human medial prefrontal-thalamus-hippocampus network. *Hum. Brain Mapp*. 2018; 39: 2381 – 2390.

Tiffin, J., Asher, E.J., 1948. The Purdue pegboard; norms and studies of reliability and validity. *J. Appl. Psychol*. 1948; 32: 234 – 247.

Träber, F., Block, W., Lamerichs, R., Gieseke, J., Schild, H.H. 1H Metabolite relaxation times at 3.0 Tesla: Measurements of T1 and T2 values in normal brain and determination of regional differences in transverse relaxation. *J. Magn. Reson. Imaging*. 2004; 19: 537–545.

Tumati, S., Opmeer, E.M., Marsman, J.C., Martens, S., Reesink, F.E., De Deyn, P.P., Aleman, A. Lower choline and myo-inositol in temporo-parietal cortex is associated with apathy in amnestic MCI. *Front Aging Neurosci*. 2018; 10: 106.

Wansapura, J.P., Holland, S.K., Dunn, R.S., Ball, W.S. Jr. NMR relaxation times in the human brain at 3.0 tesla. *J. Magn. Reson. Imaging*. 1999; 531 – 538.

Weerasekera, A., Sima, D., Dresselaers, T., Van Huffel, S., Van Damme, P., Himmelreich, U. Noninvasive assessment of disease progression and neuroprotective effects of dietary coconut oil supplementation in the SOD1G93A mouse model:1H-magnetic resonance spectroscopic study. NeuroImage (Clinical): 2018. advanced online publication (see https://doi.org:10.1016/j.nicl.2018.09.011).

Wijtenburg, S.A., McGuire, S.A., Rowland, L.M., Sherman, P.M., Lancaster, J.L., Tate, D.F., Hardies, L.J., Patel, B., Glahn, D.C., Hong, L.E., Fox, P.T., Kochunov, P. Relationship between fractional anisotropy of cerebral white matter and metabolite concentrations measured using (1)H magnetic resonance spectroscopy in healthy adults. *NeuroImage*. 2013; 66, 161–168.

Yang, Z-Y., Yue, Q., Xing, H-Y., Tan, Q-Y., Sun, H-Q., Gong, Q-Y., Tan, Z.J., Quan, H. A quantitative analysis of 1H-MR spectroscopy at 3.0 T of three brain regions from childhood to middle age. Br. *J. Radiol*. 2015; 88: 20140693.

Yousry, T.A., Schmid, U.D., Alkadhi, H., Schmidt, D., Peraud, A., Buettner, A., Winkler, P. Localization of the motor hand area to a knob on the precentral gyrus. A new landmark. *Brain*. 1997; 120: 141–157.

Zaaraoui, W., Rico, A., Audoin, B., Reuter, F., Malikova, I., Soulier, E., Viout, P., Le Fur, Y., Confort-Gouny, S., Cozzone, P.J., Pelletier, J., Ranjeva, J.P. Unfolding the long-term pathophysiological processes following an acute inflammatory demyelinating lesion of multiple sclerosis. *Magn. Reson. Imaging*. 2010; 28: 477–486.

Zahr, N.M., Mayer, D., Pfefferbaum, A., Sullivan, E.V. Low striatal glutamate levels underlie cognitive decline in the elderly: evidence from *in vivo* molecular spectroscopy. *Cereb. Cortex*. 2008 8, 2241 – 2250.

Zahr, N.M., Mayer, D., Rohlfing, T., Chanraud, S., Gu, M., Sullivan, E.V., Pfefferbaum, A. *In vivo* glutamate measured with magnetic resonance spectroscopy: Behavioral correlates in aging. *Neurobiol. Aging*. 2013; 34: 1265–1276.

Zanigni, S., Testa, C., Calandra-Buonaura, G., Sambati, L., Guarino, M., Gabellini, A., Evangelisti, S., Cortelli, P., Lodi, R., Tonon, C. The contribution of cerebellar proton magnetic resonance spectroscopy in the differential diagnosis among parkinsonian syndromes. *Parkinsonism Relat. Disord*. 2015; 21: 929 – 937.

Zhu, H., Barker, P.B. MR spectroscopy and spectroscopic imaging of the brain. *Methods Mol. Biol*. 2011; 711: 203–226.

Chapter 4

Motor Cortex Metabolite Alterations in Amyotrophic Lateral Sclerosis Assessed *in vivo* Using Edited and Non-edited Magnetic Resonance Spectroscopy

A. Weerasekera[1], R. Peeters[3], D. Sima[2, 7] T. Dresselaers[3], S. Sunaert[3], J. De Vocht[4], K. Claeys, S[4]. Van Huffel[2], P. Van Damme[4,5,6], U. Himmelreich[1]

(1) Biomedical MRI unit/ MoSAIC, Department of Imaging and Pathology, KU Leuven, Leuven, Belgium.

(2) Department of Electrical Engineering (ESAT), STADIUS Center for Dynamical Systems, Signal Processing and Data Analytics, KU Leuven, Leuven, Belgium.

(3) Radiology, Department of Imaging and Pathology, UZ Leuven, Leuven, Belgium.

(4) University Hospitals Leuven, Department of Neurology, Leuven, Belgium

(5) KU Leuven – University of Leuven, Department of Neurosciences, Experimental Neurology, and Leuven Brain Institute (LBI), Leuven, Belgium.

(6) VIB, Center for Brain & Disease Research, Laboratory of Neurobiology, Leuven, Belgium

(7) icometrix, R&D department, Leuven, Belgium.

4. Motor Cortex metabolite alterations in Amyotrophic Lateral Sclerosis assessed *in vivo* using edited and non-edited magnetic resonance spectroscopy.

4.1 ABSTRACT

Previous MRI and proton spectroscopy (^{1}H-MRS) studies have revealed impaired neuronal integrity and altered neurometabolite concentrations in the motor cortex of patients with amyotrophic lateral sclerosis (ALS). Here, we aim to use MRI with conventional and novel MRS sequences to further investigate neurometabolic changes in the motor cortex of ALS patients and their relation to clinical parameters. We measured neurometabolic profiles using a regular PRESS MRS sequence in patients (n=20) and healthy controls (HC) (n=20). In addition, the novel HERMES (Hadamard Encoding and Reconstruction of MEGA-Edited Spectroscopy) MRS sequence was used to simultaneously quantify GABA and glutathione in patients (n=7) and HC (n=7). We observed an 11% decrease in *N*-acetylaspartate (NAA) (p = 0.025), 15% increase in glutamate + glutamine (Glx) (p = 0.0084) and a 21% increase in *myo*-inositol (mIns) (p = 0.0051) levels for ALS patients compared to HC. NAA levels in the bulbar-onset group were found to be significantly (p = 0.0097) lower compared to the limb-onset group. A strong correlation (p < 0.0001; Rρ = -0.8801) for mIns and a weak correlation (p = 0.0066; Rρ = -0.6673) for Glx was found for the disease progression, measured by declining of the ALS Functional Rating Scale-Revised criteria (ALSFRS-R). Concentrations of mIns and Glx also correlated with disease severity measured by forced vital capacity (FVC). A trend towards decreasing glutathione concentrations in ALS patients was observed (p = 0.0842). Results suggest that mean neurometabolite concentrations detected in the motor cortex may indicate clinical and pathological changes in ALS.

4.2 INTRODUCTION

Amyotrophic lateral sclerosis (ALS) is an idiopathic, progressive and a fatal neurodegenerative disease characterised by selective death of motor neurons in the motor cortex, brainstem and spinal cord (Hardiman *et al.*, 2017; van Es *et al.*, 2017). These neurons innervate facial and articulator muscles, regulate the swallowing and control upper and lower limbs. ALS symptoms include fasciculations, progressive atrophy of the skeletal muscles, weakness and paralysis of the upper and lower limbs (Cleveland *et al.*, 2001). In addition, loss of speech and partly degeneration of the respiratory muscles are present in most ALS patients dying of respiratory failure.

The pathophysiological mechanisms leading to the degeneration of motor neurons are still largely unknown and possibly multifactorial (Kiernan *et al.*, 2011). However, there are several hypotheses underlying the disease process including oxidative stress, glutamate excitotoxicity, impaired mitochondrial function, and aberrant protein folding (Turner *et al.*, 2008).

Localized *in vivo* proton magnetic resonance spectroscopy (^{1}H-MRS) is a non-invasive technique for measuring neurometabolites. MRS has been used to assess the progression of neurodegeneration in humans and animal models of diseases including Alzheimer's disease, Huntington's disease and ALS (Jenkins *et al.*, 2000; Andreassen *et al.*, 2001; Choi *et al* 2003a; Dedeoglu *et al.*, 2004; Jenkins *et al.*, 2005; Marjanska *et al.*, 2005, Weerasekera *et al.*, 2018). Neurometabolites detectable by ^{1}H-MRS include N-acetylaspartate (NAA), which is considered as an *in vivo* marker of neuronal activity; choline-containing compounds (Cho), which are markers for cell-membrane synthesis; creatine + phosphocreatine (Cr), markers for energy metabolism; *myo*-inositol (mIns), which is a maker for inflammation, and a range of other signals that might not be visible depending on type and quality of spectra as well as on the pathological condition (Verma *et al.*, 2016). Neurotransmitters such as the excitatory neurotransmitter glutamate (Glu), glutamine (Gln), the inhibitory neurotransmitter γ-aminobutyric acid (GABA) and the reduced and oxidized form of the peptide glutathione are also detectable by ^{1}H-MRS. Although the latter compounds are of considerable neuroscientific interest, their accurate quantification by *in vivo* MRS can represent a significant challenge due to their low concentrations, complex spin systems (signal pattern) and overlapping spectral resonances. Using advanced edited MRS sequences, low concentration metabolites such as GABA and glutathione can be accurately measured (Mullins *et al.*, 2014; Sanaei *et al.*, 2017; Raschke *et al.*, 2018). In this regard, the novel Hadamard Editing and Reconstruction of MEGA-edited Spectroscopy (HERMES) sequence allows the simultaneous detection of multiple metabolites with overlapping signals in the [1]H-MR spectrum. The HERMES sequence has demonstrated a two-fold reduction in scan time for GABA and GSH editing compared to successively acquired measurements using conventional editing methods (Chan *et al.*, 2016; Saleh *et al.*, 2016). Reduced scan time benefits the patient comfort and compliance, thus minimizes motion during scanning. In this study, we utilized conventional point-resolved spectroscopy (PRESS) and the novel edited HERMES MRS sequences to detect the neurometabolic profiles in ALS patients. We have examined the relationships between neurometabolite levels and clinical parameters, including ALS Functional Rating Scale-Revised (ALSFRS-R) score and Forced Vital Capacity (FVC).

4.3 MATERIALS AND METHODS

4.3.1 Ethical considerations

The research protocol was approved (S55312) by the local Ethics Committee from the University Hospital (UZ) Leuven. Written informed consent was obtained from all subjects included in the study.

4.3.2 Study Participants and Design

Twenty individuals with ALS were recruited for the Phenotype Research for ALS Modifier Discovery (PYRAMID) study conducted at UZ Leuven, Gasthuisberg campus (**Table 4.1**). The PYRAMID study was designed to create a detailed databank of clinical information and samples from ALS patients. Clinical parameters included the declining of the ALSFRS-R (Rooney *et al.*, 2017) and FVC (Czaplinski.*et al.*, 2006). ALSFRS-R (range 0 to 48, 48: normal) is a rating scale that determines patients' valuation of their competence and independence in 12 functional activities such as motor capability and respiratory performance. A score of 0 to 4 rates each question, where a score of 0 indicate no function while a score

of 4 would indicate normal function. (Cedarbaum *et al.*, 1999). FVC is measured with a spirometry test where function of the respiratory muscles is assessed in people with ALS (Kaplan *et al.*, 1994). In addition, twenty apparently healthy, age and gender-matched controls (HC) were recruited.

Table 4.1: Patient and healthy control group characteristics.

Clinical Parameters	ALS patient group		Healthy control group	
	Mean	±SD	Mean	±SD
Age (years)	56	10	57	8
Gender (male: female)	16:4		16:4	
Disease duration (months)	20	15		
ALSFRS-R score	30.2	9		
FVC (%)	86.3	29.5		
Riluzole use (yes: no)	16:4			
Onset locus (limb:bulbar)	12:8			

4.3.3   Magnetic Resonance Protocol and Data Acquisition

All MRI studies, which included structural MRI examination and single-voxel ^{1}H MRS of the motor cortex, were conducted on a 3T Philips Achieva (Philips Healthcare, Best, The Netherlands) scanner using a 32-channel receiver head coil system (Philips Healthcare, Best, The Netherlands). First, a three-dimensional anatomical T_1-weighted scan of seven minutes was performed to capture the structural characteristics of the brain (MPRAGE, repetition/time echo (TR/TE) = 9.6ms/4.6ms; inversion time = 900 ms, 0.98 x 0.98 x 1.2mm pixel size; field of view (FOV) = 192 x 250 x 250; 160 coronal slices of 1.2 mm thickness, flip angle, 8°). The anatomical scan was used to accurately position the volume of interest for MRS acquisition.

4.3.4   Non-edited Conventional MRS acquisition

Standard single voxel ^{1}H-MR spectra were acquired from the left motor cortex with a voxel size of 2x2x2 cm^3 (for voxel placement see **Figure 4.1A**), using a point resolved spectroscopy pulse sequence (PRESS, repetition time/echo time, TR/TE 2000/22 ms; receiver bandwidth 2 kHz, 128 averages, 1024 sample points. Water suppression method: MOIST (multiple optimizations insensitive suppression train). The total acquisition time was 5 min, 30s.

4.3.5   Edited MRS acquisition with HERMES sequence

Edited single voxel ^{1}H MR spectra were acquired also from the left motor cortex with a voxel size of 3x3x3 cm^3 (keeping the same voxel position as for the PRESS sequence but increasing the size by 1 cm), using the HERMES sequence (Saleh *et al*., 2016; Chan *et al*., 2016) with TR/TE, 2000/80 ms; 2 averages; 160 dynamic scans; 20ms pulse duration; water frequency was set to 4.68 ppm; 16 phase cycles. Water suppression method: MOIST. The total acquisition time was 10 min, 56s.

4.3.6 ^{1}H MRS data processing and quantification

Non-edited spectra were processed using jMRUI v6.0 (Stefan *et al*., 2009). Spectra were phase corrected. An HLSVD (Hankel Lanczos Singular Values Decomposition) filter was applied to remove the residual water signal (van den Boogaart *et al*., 1994). Metabolites were quantified with the QUEST algorithm in jMRUI using a simulated (nmrscopeb) basis set (Ratiney *et al*., 2004). Results are reported relative to the non-suppressed water signal. 16 neurometabolites (Alanine, Aspartic acid, total creatine, choline, GABA, glycine, glucose, glutamate, glutamine, NAA, *myo*-inositol, *Scyllo*-inositol, lactate, phosphoethanolamine, *scyllo*-inositol, taurine) were quantified. Only neurometabolites with a Cramer-Rao lower bound < 20% were considered for quantification. Edited spectra were processed by the Gannet toolkit v3.0, using water as a reference (Edden *et al*., 2014). Signal-to-noise ratio (SNR) measurements were determined by jMRUI QUEST, in time-domain (Maximum of FID/standard deviation of FID tail).

4.3.7   MRI Segmentation

The MPRAGE T$_1$-weighted MR images, acquired for the localization and placement of the MRS voxels were segmented with a statistical parametric mapping approach using spm8 (http://www.fil.ion.ucl.ac.uk/spm/). Voxel registration was performed using custom-made scripts developed in MATLAB (The MathWorks, Natick, Massachusetts, USA) by Dr. Nia Goulden (Bangor University Wales, UK), which can be accessed at http://biu.bangor.ac.uk/projects.php.en. Using the T$_1$-weighted MR image and the orientation and location information from the Philips SPAR files, the scripts generates a mask of the voxel location, which then is used to calculate the partial volumes of gray matter (GM), white matter (WM), and cerebrospinal fluid (CSF) percentages within the voxel.

4.3.8   Tissue Correction

The segmented tissue fractions were then used to correct for metabolite concentrations quantified by using jMRUI-QUEST for differences in cerebrospinal fluid content according to Gasparovic *et al*., 2006. T$_1$ and T$_2$ values for grey matter, white matter, and CSF used in this study were 1331, 832, and 3817 ms and 110, 79, and 503 ms, respectively. Metabolite relaxation times that were used for calculating the final corrected metabolite concentrations were taken from previously studies (Wansapura *et al*., 1999; Traber *et al*., 2004).

4.3.9   Statistical Analysis

Statistical analysis was performed using Prism GraphPad v5 (GraphPad, La Jolla, California) with unpaired, two-tailed Student t-tests on groups of patients with patients versus control subjects. A p-value of less than 0.05 was considered statistically significant in this study. Spearman's rank correlation coefficients were calculated to evaluate the correlations between neurometabolites and clinical parameters, e.g. ALSFRS-R score and FVC.

4.4   RESULTS

4.4.1   Subjects

Twenty patients with ALS (male = 16, female = 4; mean age, 56 ± 10 years) and 20 healthy controls (male = 16, female = 4; mean age, 57 ± 8 years) were studied using a 3T MR scanner. Out of 20 patients, 16 were on the ALS medication Riluzole. Comparison of localized PRESS ^{1}H-MR spectra from an ALS patient and a healthy control is shown in **Figure 4.1B** and a representative HERMES spectrum of an ALS patient is shown in **Figure 4.1C**.

4.4.2   Voxel segmentation

The 2x2x2 cm^3 voxel comprised on average 59%±12% white matter, 26%±15% gray mater, and 14%±10% CSF for the patient group and 55%±15% white matter, 33%±10% gray mater, and 12%±11% CSF for the control group, respectively. The gray, white matter and CSF content within the motor cortex was not significantly different between subjects with ALS and controls.
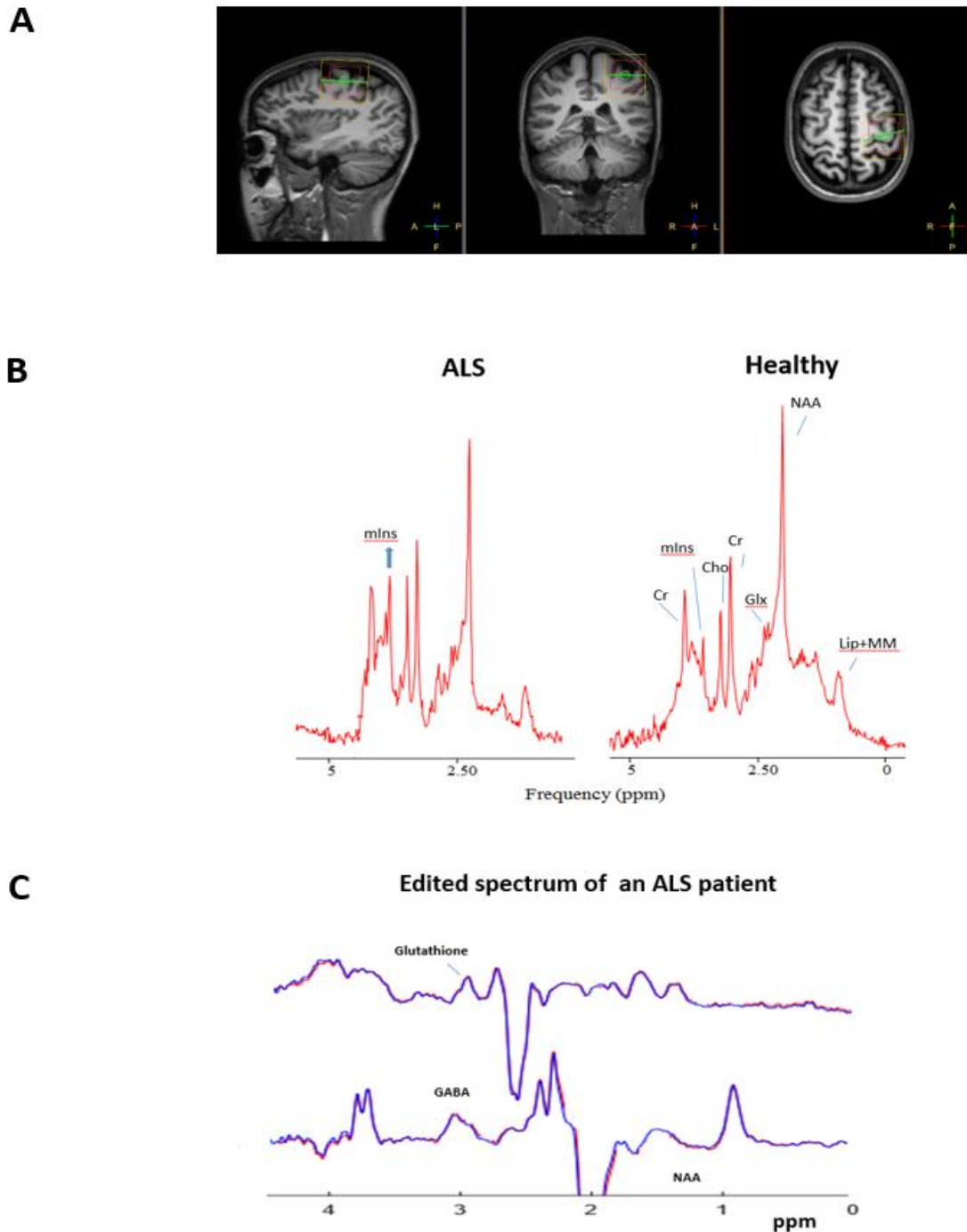
Figure 4.1. (A) 3x3x3 cm^3 voxel placement on precentral gyrus overlaid on a sagittal, coronal and axial T1 (MPRAGE) image. **(B)** Non-edited PRESS spectra from an ALS patient (left) and a healthy control (right). Blue arrow shows the increased *myo*-inositol resonance at 3.61 ppm. **(C)** Edited HERMES spectra of an ALS patient processed with GANNET. Top spectra: edited glutathione spectrum, bottom: edited GABA spectrum. *Abbreviations*: *Lip+MM, lipda+macromolecules; NAA, N-acetylaspartate; Glx, glutamate+glutamine; Cr, creatine; Cho, choline; mIns, myo-inositol.*

4.4.3 MRS quality parameters

No significant differences in spectral quality or amount of CSF in the voxel were apparent between the groups (**Table 4.2**).

Table 4.2: MRS Data Quality

MRS quality parameters	ALS patient group	Healthy control group
Signal-to-noise ratio	60±10	54±8
Water linewidth (Hz)	7±1	7±0.5
%CSF	10.3±6.1	12.1±3.2

4.4.4 Neurometabolites

Neurometabolite levels from the motor cortex of subjects with ALS and healthy controls were quantified using a standard non-edited PRESS sequence (ALS: n = 20, HC: n = 20) (**Figure 4.1B**) and an edited HERMES sequence (ALS: n = 7, HC: n = 7) (**Fig 4.1C**). Quality of the fitting for both acquisitions is shown in Figure 2 (**Fig 4.2A and B**).

4.4.5 Metabolite quantification using PRESS

The comparison between ALS patients and healthy controls (**Figure 4.3**) showed a decrease of 11% in NAA in subjects with ALS compared to healthy controls (p = 0.025). In addition, Glx and *myo*-inositol levels were found to be increased by 15% (p = 0.0084) and 21% (p = 0.0051) in ALS patients, respectively. No significant correlations were found for these metabolites (NAA-mIns: p = 0.1178, Rρ = -0.36; NAA-Glx: p = 0.2927, Rρ = 0.2476; Glx-*myo*-inositol: p = 0.1212, Rρ = 0.3580). No significant differences were found for other quantified metabolites.

A
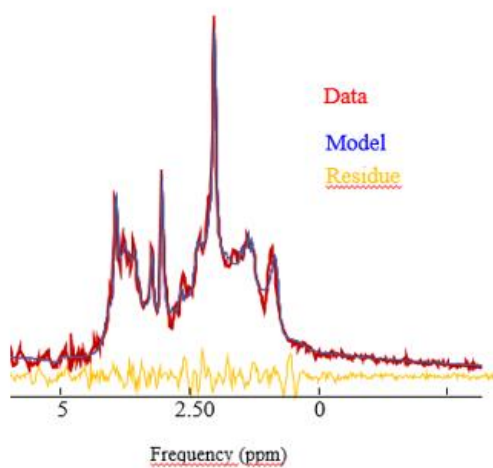
B
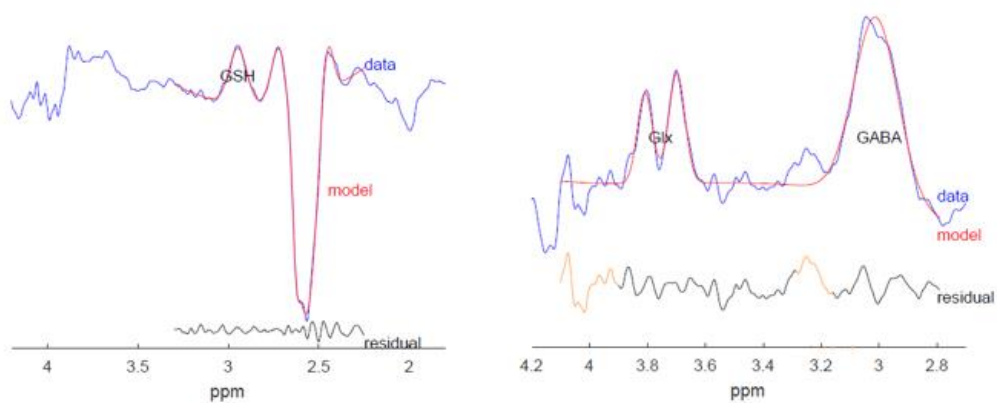
Figure 4.2. **(A)** Original non-edited PRESS spectrum (red) fitted using QUEST algorithm overlayed with estimated spectrum (blue), bottom; residue (green) after quantification. **(B)** Model fit of edited HERMES spectrum of glutathione (left, blue) with estimated overlayed (red). Right: corresponding GABA spectrum. Note the very good fitting quality (excellent overlay of aqcuired and model data).
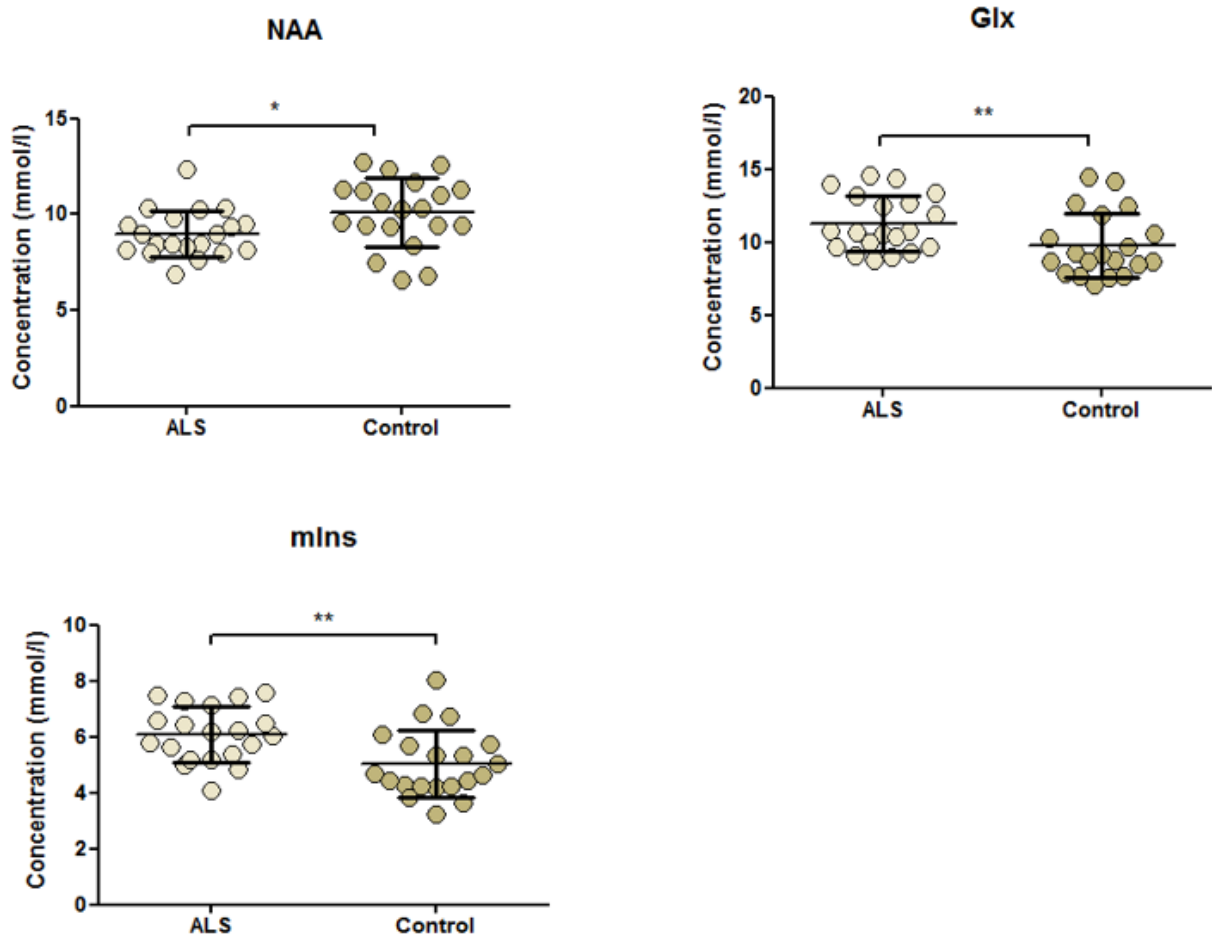
Figure 4.3. Absolute concentrations of NAA, Glx and *myo*-inositol in the motor cortex of ALS patients (n = 20) and age-matched healthy controls (n = 20). Statistical significances between the two groups and mean concentrations within each group are shown. Concentration values are given as mean ± SD; *$P < 0.05$, **$P < 0.01$

Regarding metabolite ratios, several metabolite ratios revealed significant differences between patients and healthy controls (**Figure 4.4**). Namely, mIns/Cr ($p = 0.0011$), and mIns/NAA ($p = 0.0009$) showed significant increases compared to healthy controls. Significant decreases were found for NAA/Cr ($p = 0.0014$), NAA/Glx ($p = 0.0042$, NAA/Cho ($p = 0.0056$) and NAA/mIns ($p = 0.0011$) ratios.

The comparison of the limb-ons*et* ALS patient group (n = 12) with the bulbar-onset patient group (n = 8) showed significantly ($p= 0.0097$) lower NAA concentrations in the motor cortex of bulbar-onset patients than in the limb-onset group (**Figure 4.5**).
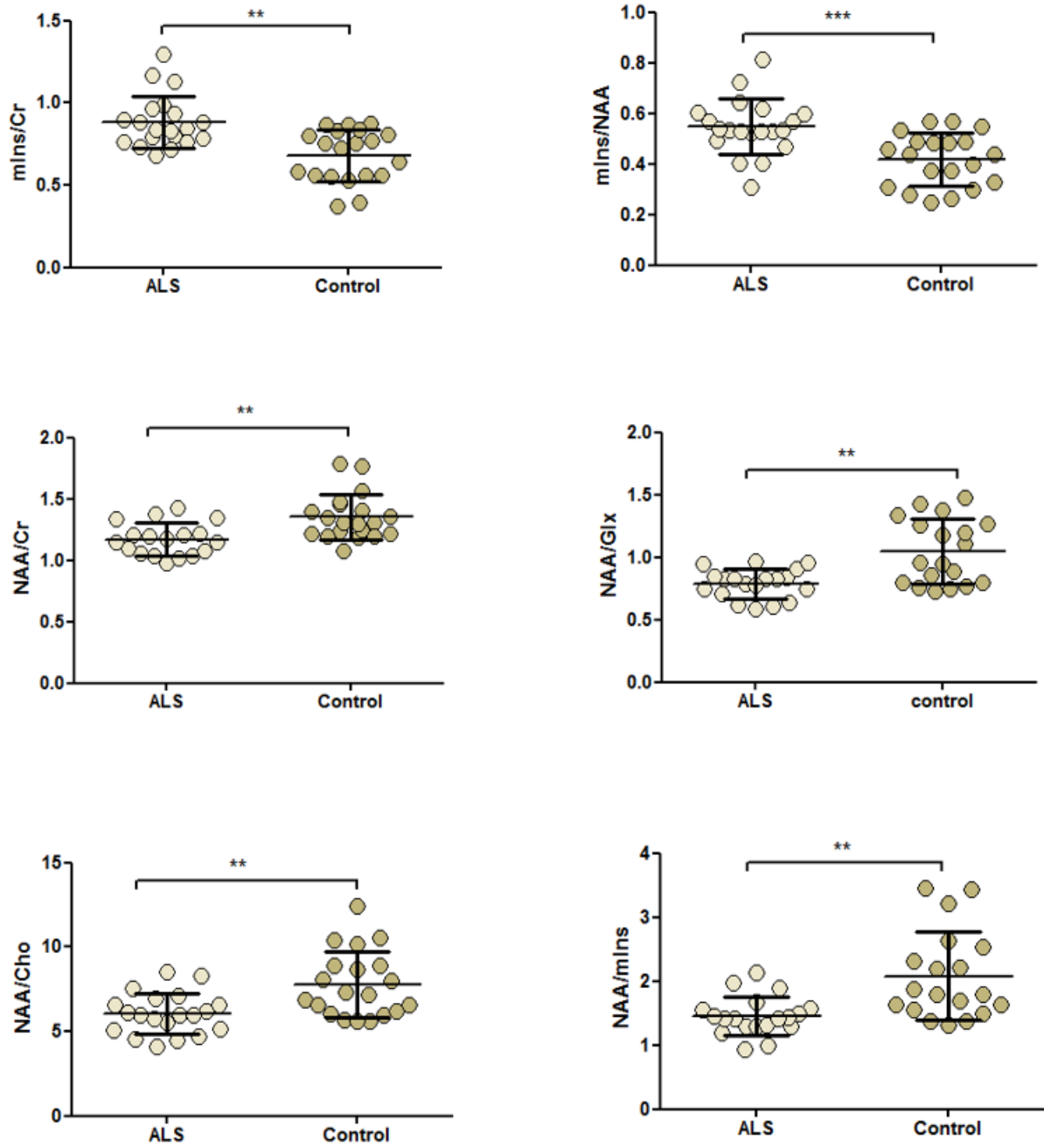
Figure 4.4. Ratios of mIns/Cr, mIns/NAA, NAA/Cr, NAA/Glx, NAA/Cho and NAA/mIns in the motor cortex of ALS patients (n = 20) and age-matched healthy controls (n = 20). Statistical significances between the two groups and mean concentrations within each group are shown. Concentration values are given as mean ± SD; *$P < 0.05$, **$P < 0.01$, ***$P < 0.001$
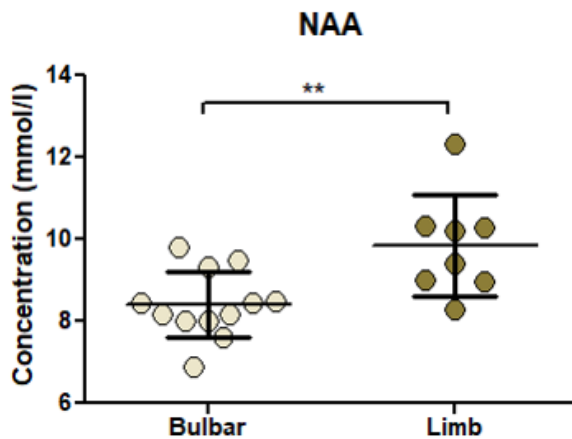
Figure 4.5. NAA concentrations in the motor cortex of bulbar-on*set* ALS patient group (n = 8) and limb-on*set* ALS patient group (n = 12). Concentration values are given as mean ± SD; **$P < 0.01$

4.4.6 Metabolite quantification using HERMES

In addition to the conventional PRESS acquisition, we utilized the novel Hadamard-encoded spectral editing scheme to simultaneously quantifying low concentration glutathione and GABA at a field strength of 3T. The comparison between ALS patients and healthy controls (**Figure 4.6**) showed a trend towards a decrease of glutathione in patients with ALS compared to healthy controls ($p = 0.0842$). No changes in GABA were observed between the two groups ($p= 0.48$).

4.4.7 Correlations of neurometabolites with ALSFRS-R and FVC scores

Neurometabolite concentrations and ratios were correlated with the clinical parameters ALSFRS-R scores and FVC (**Figures 4.7 & 4.8**). Only neurometabolites/ neurometabolite ratios that showed a significant difference or a trend between patients with ALS and healthy controls were selected. Correlations are summarized in **Table 4.3**.
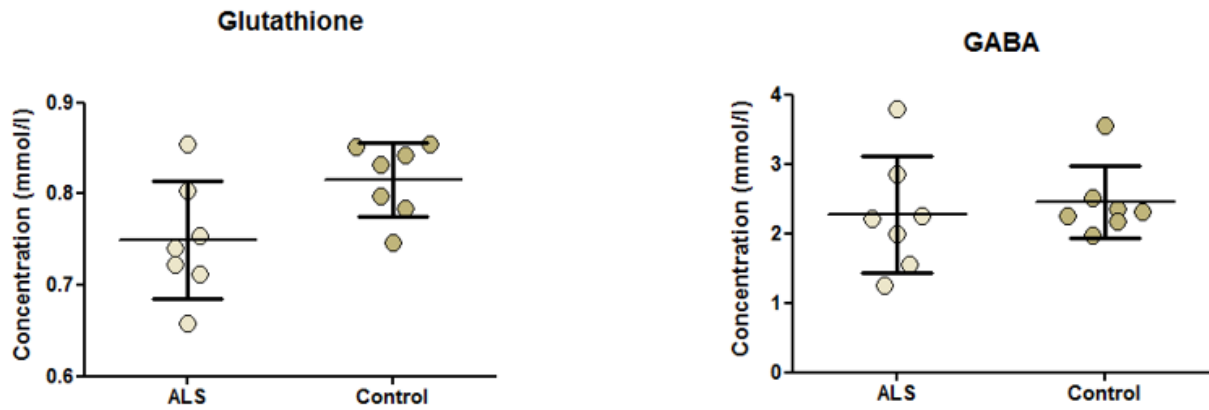
Figure 4.6. Absolute concentrations of glutathione and GABA in the motor cortex of ALS patients (n = 7) and age-matched healthy controls (n = 7). Statistical significances between the two groups and mean concentrations within each group are shown. Concentration values are given as mean ± SD;

Table 4.3: Correlations between absolute metabolic concentrations (mM) and functional parameters

Metabolite	ALS-FRS-R		FVC	
	Spearman, Rρ	*p*-value	Spearman, Rρ	*p*-value
mIns	-0.8801	< 0.0001	-0.6357	0.0109
Glx	-0.6673	0.0066	-0.688	0.0046
NAA	0.4705	0.0767	0.2373	0.3945
NAA/Cr	0.7091	0.0182	-0.08242	0.789
NAA/Glx	0.8104	0,0002	0.7	0.0037
NAA/mIns	0.8062	0.0005	0.5253	0.0537
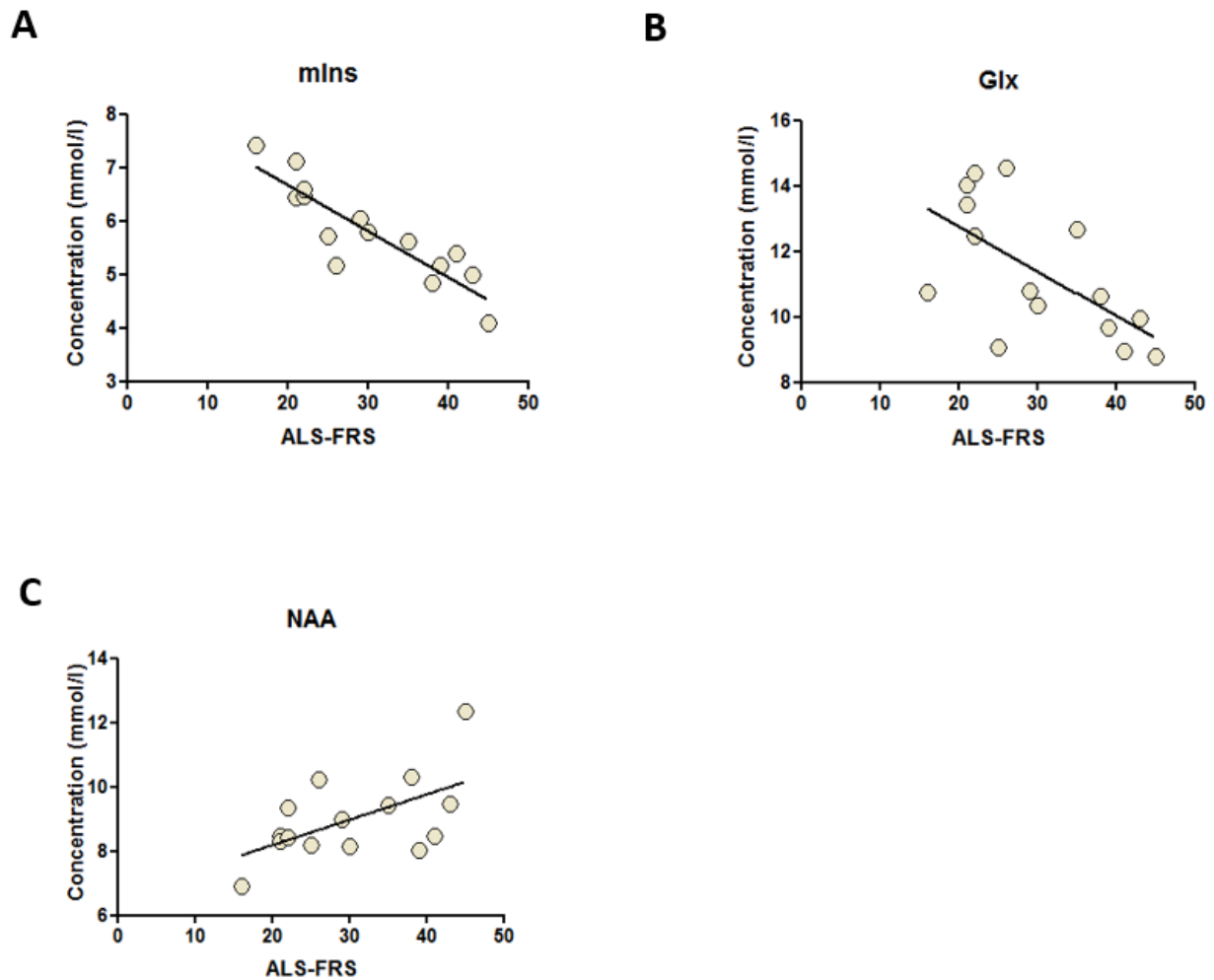
Figure 4.7. Correlation between neurometabolite concentrations and the disease progression measured with ALSFRS-R. **(A)** Demonstrates the correlation of regional mIns and ALSFRS-R. The resulting slope in linear fit is represented by the solid black line (Rρ = -0.8801, *P* < 0.0001). **(B)** Glx vs ALSFRS-R (Rρ = 0.-0.6673, *P* = 0.0066). **(C)** NAA vs ALSFRS-R (Rρ = 0.4705, *P* = 0.0767). *Abbreviation: NAA, N-acetylaspartate; mIns, myo-inositol; Glx, glutamate+glutamine*
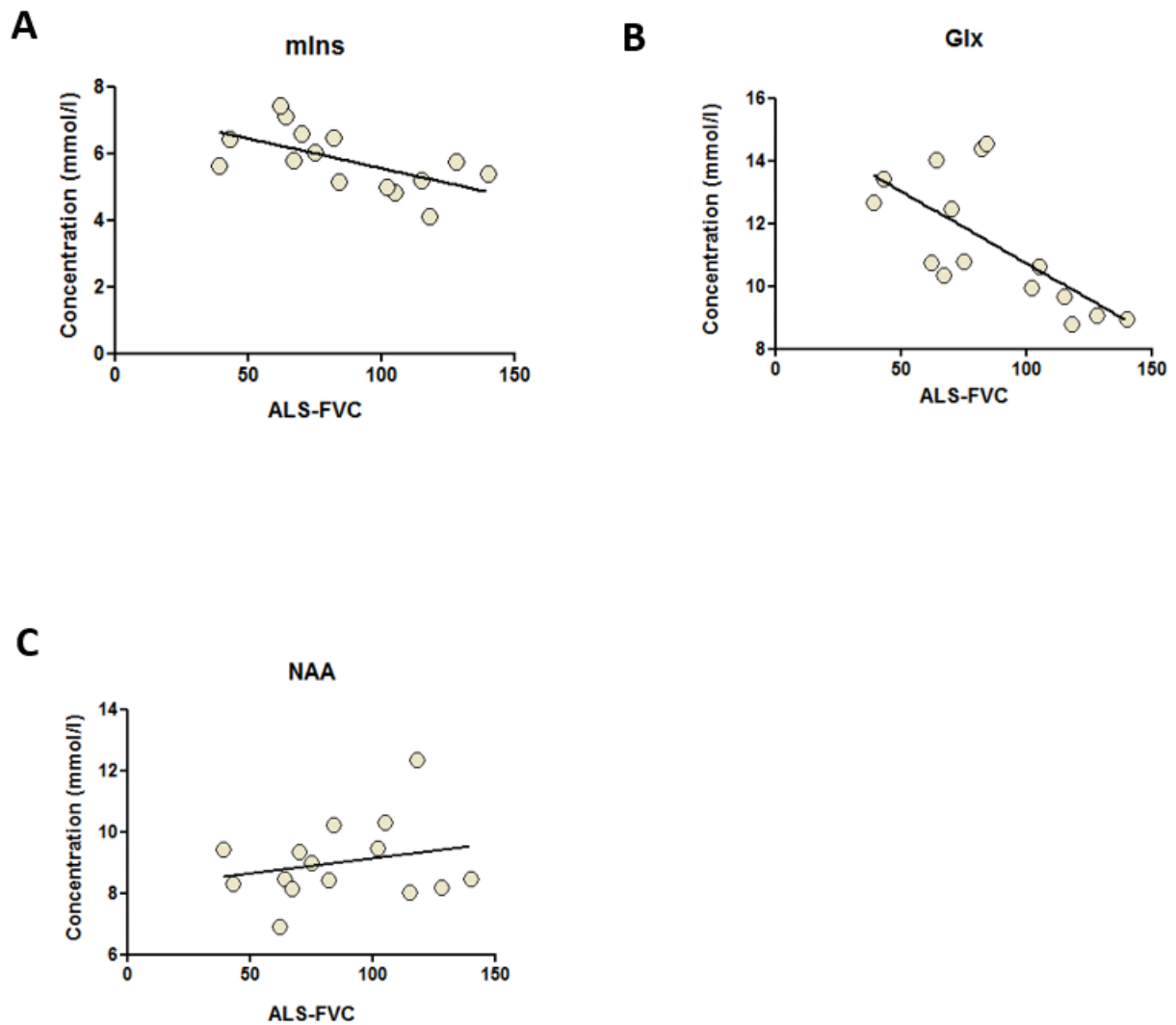
Figure 4.8. Correlation between neurometabolite concentrations and the disease progression measured with FVC. **(A)** mIns vs FVC (Rρ = -0.0.6357, *P* = 0.0109). **(B)** Glx vs ALSFRS-R (Rρ = -0.688, *P* = 0.0046). **(C)** NAA vs FVC (Rρ = 0.2373, *P* = 0.3945). *Abbreviation: NAA, N-acetylaspartate; mIns, myo-inositol; Glx, glutamate+glutamine*

4.5 DISCUSSION

The value of *in vivo* MR spectroscopy in evaluating upper motor neuron integrity in ALS has been previously demonstrated (Pioro *et el*., 1994; Jones *et al*., 1995; Kalra *et al*., 1999; Han *et al*., 2010; Foerster *et al*., 2014; Liu *et al*., 2015; Grolez *et al*., 2016). To the best of our knowledge, this is the first study to apply conventional PRESS and novel edited HERMES sequences at 3T in an ALS study. The use of robust editing techniques enable access to neurometabolic data that was previously inaccessible to conventional MRS due to the heavy overlap with signals of metabolites with higher concentrations.

4.5.1 Decreased motor cortex N-acetylaspartate

In the brain, NAA is generally considered exclusively of neuronal origin. Therefore, it is regarded as a marker for neuronal density and integrity. MRS results from this study showed a significant decrease in the levels of NAA in the motor cortex of ALS patients compared to healthy controls. Moreover, the lower NAA levels observed in the bulbar-onset patient group may imply a more severe upper motor neuron involvement in the bulbar-onset group. In addition, significant decreases in the NAA/Cr, NAA/Cho, NAA/Glx and NAA/mIns ratios were also observed.

Jones *et al* (Jones *et al.*, 1995) first applied MRS on ALS patients and reported reduced NAA and NAA/Cho levels in the motor cortex. Other groups confirmed these findings using high-field MR scanners (Cwik *et al.*, 1998; Block *et al.*, 1998; Rule *et al.*, 2004; de Graaff *et al.*, 2010; Stagg *et al.*, 2013; Atassi *et al.*, 2017; Cheong *et al.*, 2017). Therefore, reduced NAA levels in the motor cortex is the most frequently reported in MRS studies of ALS. This reduction is usually attributed to neuronal loss. However, if NAA was indeed an exclusive neuronal marker, one would expect that the motor cortex NAA levels would correlate with disease severity. Even though a significant decrease in the NAA levels in ALS patients was observed in this study, no correlation was found for NAA concentration and the ALSFRS-R score (Rρ = 0.4705, *P* = 0.0767). Furthermore, in above-mentioned studies, most did not report such correlations or they reported correlations with respect to disease diagnosis (definite, probable and possible) but not with the disease severity (ALSFRS-R).

4.5.2 Increased motor cortex *myo*-inositol

We have found significant elevation *myo*-inositol, a glial marker, in ALS patients compared to healthy controls. This finding is consistent with previous studies. Elevated *myo*-inositol levels have been previously reported for numerous neurodegenerative diseases, including Alzheimer's disease (Voevodskaya *et al.*, 2016), Huntington's disease (Sturrock *et al.*, 2015) and ALS (Kalra *et al.*, 2006; Foerster *et al.*, 2013; Cheong *et al.*, 2017). Furthermore, we found a significant (Rρ = -0.8801, *P*< 0.0001) negative correlation between *myo*-inositol levels of ALS patients with the ALSFRS-R score (ALSFRS-R mean ± SD = 30.2 ± 9). This indicates that the significant group difference is primarily driven by the higher *myo*-inositol levels in those who are severely affected by the disease. The increase of *myo*-inositol levels with the ALS progression is further supported by two previous studies that enrolled patients at an early disease stage (ALSFRS-R mean ± SD = 40.1 ± 4.3, van der Graaff *et al.*, 2010; ALSFRS-R mean ± SD = 38.2 ± 4.7, Atassi *et al.*, 2017) where the authors found no differences in *myo*-inositol levels.

4.5.3 Increased motor cortex Glx

Glutamate is the most abundant neurotransmitter in the brain, as well as a structural component of proteins, a component of intermediate energy metabolism and a precursor for glutamine, GABA and glutathione (Erecinska *et al.*, 1990; Bak *et al.*, 2006). In ALS, excitotoxicity of glutamate is assumed to be one of the leading contributors to ALS pathogenesis (Van Den Bosch *et al.*, 2006). *In vivo* high-field ^{1}H-MR spectroscopy studies in humans and animal models of ALS suggest changes in glutamate concentrations in the motor cortex (Choi *et al* 2009, Attassi *et at.*, 2017). However, due to the molecular structural similarity of glutamate and glutamine, conventional MRS at clinically used magnetic field

strengths of 1.5 and 3 T is challenging for reliable quantification of the two molecules. Therefore, the combined signal Glx is often reported and considered to be more reliable. We have found a 15% increase in Glx concentrations in the ALS group compared to healthy controls. Higher glutamate levels in plasma and CSF of ALS patients was previously reported (Camu *et al.*, 1993; Plaitakis *et al.*, 1993). Previous MRS studies on ALS patients also reported significantly higher Glx levels and a negative correlation with ALSFRS score (Piorro *et al.*, 1999; Hans *et al.*, 2010). However, it should be noted that out of the 20 patients recruited in our study, 16 were taking Riluzole. Riluzole has been shown to decrease glutamatergic neurotransmission by acting as an antagonist of presynaptic NMDA and AMDA glutamate receptors, as well as by increasing glutamate transporter uptake (Albo *et al.*, 2004; Lamanauskas *et al.*, 2008; Fumagalli *et al.*, 2008). Foerster *et al* reported higher levels of Glx in the motor cortex of untreated patients compared to Riluzole-treated patients (Foerster *et al.*, 2013).

4.5.4   Motor cortex GABA and glutathione

Changes in low concentration GABA and glutathione has shown to play an important role in ALS pathology (Foerster *et al.*, 2013; Diana el al., 2017; Di LAzzaro *et al.*, 2017; Chiò *et al.*, 1998; Vargas *et al.*, 2012; Weiduschat *et al.*, 2014). Since edited MRS allows reliable detection of J-coupled, low-concentration metabolites such as the inhibitory neurotransmitter GABA and the redox compound glutathione, we simultaneously measured the GABA and glutathione levels using the edited-HERMES MRS sequence. For the edited MRS study, 7 patients and 7 healthy controls were used (all 7 patients were taking Riluzole). Our data show no difference in GABA levels between the ALS group and the healthy controls. However, since Riluzole also acts on GABAergic systems (Foerster *et al.*, 2013) the interpretation of GABA levels in the two groups becomes challenging. As for glutathione levels, a decreasing trend was observed for the ALS group compared to healthy controls. A recent study by Weiduschat *et al* using a *J*-edited PRESS sequence reported lower levels of glutathione in the motor cortex of ALS patients (n=11) compared to healthy controls (n=13) (Weiduschat *et al.*, 2014). However, further studies using edited MRS and a larger sample size is necessary to confirm these findings.

4.6   CONCLUSIONS

In conclusion, the combined use of non-edited and edited MRS could be a powerful and non-invasive tool to study molecular changes of neurodegeneration in ALS. Previously, low concentration metabolites were deemed impractical to acquire for diagnostic MRS due to time considerations and patient discomfort. However, simultaneous editing of these metabolites using sequences such as HERMES, enable the reduction of total scan time considerably, increase the diagnostic accuracy and enhance the patient comfort. The diagnostic value is demonstrated by the significant neurometabolic changes in the motor cortex of ALS patients that are reported in this study. Some of the observed neurometabolic changes also showed significant correlations with clinical measures. Our results also agrees well with previous findings which may indicate the robustness of quantitative MRS.

4.7 REFERENCES

Andreassen OA, Jenkins BG, Dedeoglu A, Ferrante KL, Bogdanov MB, Kaddurah-Daouk R, Beal MF. Increases in cortical glutamate concentrations in transgenic amyotrophic lateral sclerosis mice are attenuated by creatine supplementation. *J Neurochem*. 2001; **77**:383–390.

Albo F, Pieri M, Zona C. Modulation of AMPA receptors in spinal motor neurons by the neuroprotective agent riluzole. *J Neurosci Res*. 2004; 78(2):200–207.

Atassi N, Xu M, Triantafyllou C, Keil B, Lawson R, Cernasov P, Ratti E, Long CJ, Paganoni S, Murphy A, Salibi N, Seethamraju R, Rosen B, Ratai EM. Ultra high-field (7tesla) magnetic resonance spectroscopy in Amyotrophic Lateral Sclerosis. *PLoS One*. 2017; 12(5).

Bak LK, Schousboe A, Waagepetersen HS. The glutamate/GABA-glutamine cycle: aspects of transport, neurotransmitter homeostasis and ammonia transfer. *J Neurochem*. 2006; 98(3):641–653.

Baslow MH. The Vertebrate Brain, Evidence of Its Modular Organization and Operating System: Insights into the Brain's Basic Units of Structure, Function, and Operation and How They Influence Neuronal Signaling and Behavior. *Frontiers in Behavioral Neuroscience*. 2011; 5:5.

Bede P, Bokde A, Elamin M, Byrne S, McLaughlin RL, Jordan N, Hampel H, Gallagher L, Lynch C, Fagan AJ, Pender N, Hardiman O. Grey matter correlates of clinical variables in amyotrophic lateral sclerosis (ALS): a neuroimaging study of ALS motor phenotype heterogeneity and cortical focality. *J Neurol Neurosurg Psychiatry*. 2013; 84(7):766-73.

Block W, Karitzky J, Träber F, Pohl C, Keller E, Mundegar RR, Lamerichs R, Rink H, Ries F, Schild HH, Jerusalem F. Proton magnetic resonance spectroscopy of the primary motor cortex in patients with motor neuron disease: subgroup analysis and follow-up measurements. *Arch Neurol*. 1998; 55(7):931-6.

Branco LM, De Albuquerque M, De Andrade HM, Bergo FP, Nucci A, França MC Jr. Spinal cord atrophy correlates with disease duration and severity in amyotrophic lateral sclerosis. *Amyotroph Lateral Scler Frontotemporal Degener*. 2014; 15(1-2):93-7.

Camu W, Billiard M, Baldy-Moulinier M. Fasting plasma and CSF amino acid levels in amyotrophic lateral sclerosis: a subtype analysis. *Acta Neurol Scand*. 1993; 88(1):51-5.

Cedarbaum JM, Stambler N, Malta E, Fuller C, Hilt D, Thurmond B, *et al*. The ALSFRS-R: a revised ALS functional rating scale that incorporates assessments of respiratory function. BDNF ALS Study Group (Phase III). *J Neurol Sci*. 1999; 169(1–2):13–21.

Chan KL, Puts NAJ, Schär M, Barker PB, Edden RAE. HERMES: Hadamard Encoding and Reconstruction of MEGA-Edited Spectroscopy. *Magnetic resonance in medicine*. 2016; 76(1):11-19.

Chiò A, Cucatto A, Terreni AA, Schiffer D. Reduced glutathione in amyotrophic lateral sclerosis: an open, crossover, randomized trial. *Ital J Neurol Sci*. 1998; 19(6):363-6.

Choi IY, Lee SP, Guilfoyle DN, Helpern JA. *In vivo* NMR studies of neurodegenerative diseases in transgenic and rodent models. *Neurochem Res* 2003a; 28:987–1001.

Choi, J., Kustermann, E., Dedeoglu, A., & Jenkins, B. G. Magnetic Resonance Spectroscopy of Regional Brain Metabolite Markers in FALS Mice and the Effects of Dietary Creatine Supplementation. *The European Journal of Neuroscience*. 2009; 30 (11), 2143–2150.

Cleveland, D.W., Rothstein, J.D. From Charcot to Lou Gehrig: deciphering selective motor neuron death in ALS. *Nat. Rev. Neurosci*. 2001; 2: 806–819.

Cwik VA, Hanstock CC, Allen PS, Martin WR. Estimation of brainstem neuronal loss in amyotrophic lateral sclerosis with *in vivo* proton magnetic resonance spectroscopy. *Neurology*. 1998; 50(1):72-7.

Czaplinski A, Yen AA, Appel SH. Forced vital capacity (FVC) as an indicator of survival and disease progression in an ALS clinic population. *Journal of Neurology, Neurosurgery, and Psychiatry*. 2006; 77(3):390-392.

Dedeoglu A, Choi JK, Cormier K, Kowall NW, Jenkins BG. Magnetic resonance spectroscopic analysis of Alzheimer's disease mouse brain that express mutant human APP shows altered neurochemical profile. *Brain Res.* 2004; 1012:60–65.

Diana A, Pillai R, Bongioanni P, O'Keeffe AG, Miller RG, Moore DH. Gamma aminobutyric acid (GABA) modulators for amyotrophic lateral sclerosis/motor neuron disease. *Cochrane Database Syst Rev*. 2017;1.

Di Lazzaro V, Pellegrino G, Ranieri F, Florio L, Musumeci G, Caulo M, Ferretti A, Capone F. Effects of repetitive TMS of the motor cortex on disease progression and on glutamate and GABA levels in ALS: A proof of principle study. *Brain Stimul*. 2017; 10(5):1003-1005.

Erecinska M, Silver IA. Metabolism and role of glutamate in mammalian brain. *Prog Neurobiol*. 1990; 35(4):245–296.

Foerster BR, Pomper MG, Callaghan BC, Petrou M, Edden RA, Mohamed MA, Welsh RC, Carlos RC, Barker PB, Feldman EL. An imbalance between excitatory and inhibitory neurotransmitters in amyotrophic lateral sclerosis revealed by use of 3-T proton magnetic resonance spectroscopy. *JAMA Neurol*. 2013; 70(8):1009-16.

Foerster BR, Carlos RC, Dwamena BA, *et al*. Multimodal MRI as a diagnostic biomarker for amyotrophic lateral sclerosis. *Annals of Clinical and Translational Neurology*. 2014; 1(2):107-114.

Fumagalli E, Funicello M, Rauen T, Gobbi M, Mennini T. Riluzole enhances the activity of glutamate transporters GLAST, GLT1 and EAAC1. *Eur J Pharmacol*. 2008; 14; 578(2–3):171–176.

Gasparovic C, Song T, Devier D, Bockholt HJ, Caprihan A, Mullins PG, Posse S, Jung RE, Morrison LA. Use of tissue water as a concentration reference for proton spectroscopic imaging. *Magn Reson Med*. 2006; 55(6):1219-26.

Grolez G, Moreau C, Danel-Brunaud V, *et al*. The value of magnetic resonance imaging as a biomarker for amyotrophic lateral sclerosis: a systematic review. *BMC Neurology*. 2016; 16(1):155.

Han J, Ma L. Study of the features of proton MR spectroscopy ((1)H-MRS) on amyotrophic lateral sclerosis. *J Magn Reson Imaging*. 2010; 31(2):305-8.

Hardiman O, Al-Chalabi A, Chio A, Corr EM, Logroscino G, Robberecht W, ShawPJ, Simmons Z, van den Berg LH. Amyotrophic lateral sclerosis. *Nat Rev DisPrimers*. 2017; 3:17085.

Hersch SM, Gevorkian S, Marder K, Moskowitz C, Feigin A, Cox M, Como P, Zimmerman C, Lin M, Zhang L, Ulug AM, Beal MF, Matson W, Bogdanov M, Ebbel E, Zaleta A, Kaneko Y, Jenkins B, Hevelone N, Zhang H, Yu H, Schoenfeld D, Ferrante R, Rosas HD. Creatine in Huntington disease is safe, tolerable, bioavailable in brain and reduces serum 8OH2′dG. *Neurology*. 2006; 66:250–252.

Jenkins BG, Andreassen OA, Dedeoglu A, Leavitt B, Hayden M, Borchelt D, Ross CA, Ferrante RJ, Beal MF. Effects of CAG repeat length, HTT protein length and protein context on cerebral metabolism measured using magnetic resonance spectroscopy in transgenic mouse models of Huntington's disease. *J Neurochem*. 2005; 95:553–562.

Jenkins BG, Klivenyi P, Kustermann E, Andreassen OA, Ferrante RJ, Rosen BR, Beal MF. Nonlinear decrease over time in N-acetyl aspartate levels in the absence of neuronal loss and increases in glutamine and glucose in transgenic Huntington's disease mice. *J Neurochem* 2000; 74: 2108–2119.

Jones AP, Gunawardena WJ, Coutinho CM, Gatt JA, Shaw IC, Mitchell JD. Preliminary results of proton magnetic resonance spectroscopy in motor neuron disease (amyotrophic lateral sclerosis). *J Neurol Sci* 1995; 129 (suppl):85–89.

Kalra S, Arnold DL, Cashman NR. Biological markers in the diagnosis and treatment of ALS. *J Neurol Sci* 1999; 165: S27–32.

Kalra S, Hanstock CC, Martin WR, Allen PS, Johnston WS. Detection of cerebral degeneration in amyotrophic lateral sclerosis using high-field magnetic resonance spectroscopy. *Arch Neurol*. 2006; 63(8):1144-8.

Kamada K, Takeuchi F, Houkin K, Kitagawa M, Kuriki S, Ogata A, Tashiro K,Koyanagi I, Mitsumori K, Iwasaki Y. Reversible brain dysfunction in MELAS: MEG, and (1)H MRS analysis. *J Neurol Neurosurg Psychiatry*. 2001; 70(5):675-8.

Kaplan LM, Hollander D. Respiratory dysfunction in amyotrophic lateral sclerosis. *Clin Chest Med*. 1994; 15(4):675-81.

Kiernan MC, Vucic S, Cheah BC, Turner MR, Eisen A, Hardiman O, Burrell JR,Zoing MC. Amyotrophic lateral sclerosis. *Lancet*. 2011; 377(9769):942-55.

Kim HJ, de Leon M, Wang X, Kim HY, Lee YJ, Kim YH, Kim SH. Relationship between Clinical Parameters and Brain Structure in Sporadic Amyotrophic Lateral Sclerosis Patients According to Onset Type: A Voxel-Based Morphometric Study. *PLoS One*. 2017; *12(*1).

Kwan JY, Meoded A, Danielian LE, Wu T, Floeter MK. Structural imaging differences and longitudinal changes in primary lateral sclerosis and amyotrophic lateral sclerosis. *NeuroImage : Clinical*. 2013;2:151-160.

Lamanauskas N, Nistri A. Riluzole blocks persistent Na+ and Ca2+ currents and modulates release of glutamate via presynaptic NMDA receptors on neonatal rat hypoglossal motoneurons in vitro. *Eur J Neurosci*. 2008; 27(10):2501–2514.

Liu C, Jiang R, Yi X, Zhu W, Bu B. Role of diffusion tensor imaging or magnetic resonance spectroscopy in the diagnosis and disability assessment of amyotrophic lateral sclerosis. *J Neurol Sci*. 2015; 348(1-2):206-10.

Marjanska M, Curran GL, Wengenack TM, Henry PG, Bliss RL, Poduslo JF, Jack CR Jr, Ugurbil K, Garwood M. Monitoring disease progression in transgenic mouse models of Alzheimer's disease with proton magnetic resonance spectroscopy. *Proc Natl Acad Sci* U S A. 2005; 102:11906–11910.

Mullins PG, McGonigle DJ, O'Gorman RL, Puts NA, Vidyasagar R, Evans CJ; Cardiff Symposium on MRS of GABA, Edden RA. Current practice in the use of MEGA-PRESS spectroscopy for the detection of GABA. *Neuroimage*. 2014; 86:43-52.

Pioro EP, Antel JP, Cashman NR, Arnold DL. Detection of cortical neuron loss in motor neuron disease by proton magnetic resonance spectroscopic imaging *in vivo*. *Neurology* 1994; 44:1933–1938.

Pioro EP, Majors AW, Mitsumoto H, Nelson DR, Ng TC. 1H-MRS evidence of neurodegeneration and excess glutamate + glutamine in ALS medulla. *Neurology*. 1999; 53:71–79.

Plaitakis A, Constantakakis E. Altered metabolism of excitatory amino acids, N-acetyl-aspartate and N-acetyl-aspartyl-glutamate in amyotrophic lateral sclerosis. *Brain Res Bull*. 1993; 30(3-4):381-6.

Provencher SW. Estimation of metabolite concentrations from localized *in vivo* proton NMR spectra. *Magn Reson Med* 1993; 30:672–9. Raschke F, Noeske R, Dineen RA, Auer DP. Measuring Cerebral and CerebellarGlutathione in Children Using (1)H MEGA-PRESS MRS. *AJNR Am J Neuroradiol*. 2018; 39(2):375-379.

Rooney J, Burke T, Vajda A, Heverin M, Hardiman O. What does the ALSFRS-Rreally measure? A longitudinal and survival analysis of functional dimensionsubscores in amyotrophic lateral sclerosis. *J Neurol Neurosurg Psychiatry*. 2017; 88(5):381-385.

Saleh MG, Oeltzschner G, Chan KL, Puts NAJ, Mikkelsen M, Schär M, Harris AD, Edden RAE. Simultaneous edited MRS of GABA and glutathione. Neuroimage. 2016; 142:576-582.

Sanaei Nezhad F, Anton A, Parkes LM, Deakin B, Williams SR. Quantification ofglutathione in the human brain by MR spectroscopy at 3 Tesla: Comparison of PRESS and MEGA-PRESS. *Magn Reson Med*. 2017; 78(4):1257-1266.

Smith EF, Shaw PJ, De Vos KJ. The role of mitochondria in amyotrophic lateralsclerosis. *Neurosci Lett*. 2017; S0304-3940(17)30544-X.

Stagg CJ, Knight S, Talbot K, Jenkinson M, Maudsley AA, Turner MR. Whole-brain magnetic resonance spectroscopic imaging measures are related to disability in ALS. *Neurology*. 2013; 80(7):610-5.

Sturrock A, Laule C, Wyper K, Milner RA, Decolongon J, Dar Santos R, ColemanAJ, Carter K, Creighton S, Bechtel N, Bohlen S, Reilmann R, Johnson HJ, Hayden MR, Tabrizi SJ, Mackay AL, Leavitt BR. A longitudinal study of magnetic resonance spectroscopy Huntington's disease biomarkers. *Mov Disord*. 2015; 30(3):393-401.

Traber F, Block W, Lamerichs R, *et al*. 1H metabolite relaxation times at 3.0 Tesla: Measurements of T1 and T2 values in normal brain and determination of regional differences in transverse relaxation. *J Magn Reson Imaging*. 2004; 19:537–45.

Turner BJ, Talbot K. Transgenics, toxicity and therapeutics in rodent models of mutant SOD1-mediated familial ALS. *Prog Neurobiol*. 2008; 85:94–134.

Turner MR, Agosta F, Bede P, Govind V, Lulé D, Verstraete E. Neuroimaging in amyotrophic lateral sclerosis. *Biomark Med*. 2012; 6(3):319-37.

Van Den Bosch L, Van Damme P, Bogaert E, Robberecht W. The role of excitotoxicity in the pathogenesis of amyotrophic lateral sclerosis. *Biochim Biophys Acta*. 2006; 1762(11-12):1068-82.

van der Graaff MM, Lavini C, Akkerman EM, Majoie ChB, Nederveen AJ, Zwinderman AH, Brugman F, van den Berg LH, de Jong JM, de Visser M. MR spectroscopy findings in early stages of motor neuron disease. *AJNR Am J Neuroradiol*. 2010; 31(10):1799-806.

van Es MA, Hardiman O, Chio A, Al-Chalabi A, Pasterkamp RJ, Veldink JH, vanden Berg LH. Amyotrophic lateral sclerosis. *Lancet*. 2017; 390(10107):2084-2098.

Vargas, Marcelo R., Delinda A. Johnson, and Jeffrey A. Johnson. "Decreased Glutathione Accelerates Neurological Deficit and Mitochondrial Pathology in Familial ALS-Linked hSOD1^{G93A} Mice Model." *Neurobiology of disease.* 2011; 543–551.

Verma A, Kumar I, Verma N, Aggarwal P, Ojha R. Magnetic resonance spectroscopy — Revisiting the biochemical and molecular milieu of brain tumors. *BBA Clinical*. 2016; 5:170-178.

Voevodskaya O, Sundgren PC, Strandberg O, Zetterberg H, Minthon L, Blennow K, Wahlund LO, Westman E, Hansson O; Swedish BioFINDER study group. Myo-inositol changes precede amyloid pathology and relate to APOE genotype in Alzheimer disease. *Neurology*. 2016; 86(19):1754-61.

Wansapura JP, Holland SK, Dunn RS, *et al*. NMR relaxation times in the human brain at 3.0 Tesla. *J Magn Reson Imaging*. 1999; 9:531–38.

Weiduschat N, Mao X, Hupf J, Armstrong N, Kang G, Lange DJ, Mitsumoto H, Shungu DC. Motor cortex glutathione deficit in ALS measured *in vivo* with the J-editing technique. *Neurosci Lett*. 2014; 570:102-7.

Weerasekera A, Sima D, Dresselaers T, Van Huffel S, Van Damme P, Himmelreich U. Non-invasive Assessment of Disease Progression and Neuroprotective Effects of Dietary Coconut Oil Supplementation in the SOD1^{G93A}

Mouse Model:1H-Magnetic Resonance Spectroscopic Study. Neuroimage: Clinical. Advanced online publication.

Chapter 5

Comparison of GABA and Glutamate/Glutamine Quantification from Edited and Unedited MR Spectra – Assessment of Age Effects.

Akila Weerasekera[1], Diana Sima[2,5], Ronald Peeters[3] Tom Dresselaers[3], Oron Levin[4], Stephan Swinnen[4], Sabine Van Huffel[2], Uwe Himmelreich[1]

(1) Biomedical MRI unit/ MoSAIC, Department of Imaging and Pathology, KU Leuven, Leuven, Belgium.

(2) Department of Electrical Engineering (ESAT), STADIUS Center for Dynamical Systems, Signal Processing and Data Analytics, KU Leuven, Leuven, Belgium and Imec Leuven, Belgium.

(3) Radiology, Department of Imaging and Pathology, UZ Leuven, Leuven, Belgium. Movement Control & Neuroplasticity Research Group, KU Leuven, Leuven, Belgium.

(4) Department of Imaging and Pathology, UZ Leuven, Leuven, Belgium. Movement Control & Neuroplasticity Research Group, KU Leuven, Leuven, Belgium.

(5) icometrix, R&D department, Leuven, Belgium.

5. Comparison of GABA and glutamate/glutamine quantification from edited and unedited MR spectra – assessment of age effects.

5.1 ABSTRACT

Purpose Here we compare currently available spectral fitting methods to assess the in vivo concentrations for GABA and glutamate + glutamine (Glx) derived from J-edited (MEGA-PRESS) and unedited (MEGA-PRESS-OFF) magnetic resonance (MR) spectra. In addition, we tested the approach to assess the inter-subject variability in neurotransmitter levels arising from age effects.

Materials and Methods Single voxel MEGA-edited PRESS MR spectra were acquired from a 27 cm^3 voxel placed in the left sensorimotor cortex (SM1) of 10 young adults (YA) and 10 older adults (OA) using an 3T Philips Achieva clinical MR scanner. MEGA-edited spectra were quantified using the Gannet 3.0 toolbox and jMRUI v6.0-AMARES algorithm. MEGA-edit-OFF (unedited) spectra were quantified with the jMRUI v6.0-QUEST algorithm. Quantification methods were compared using two-tailed unpaired t-tests. Age-differences in concentrations using the three methods were assessed using two-way ANOVA with Bonferroni post-hoc test.

Results GABA levels estimated using Gannet and QUEST showed very good agreement. Significant positive correlation was found for GABA values estimated with Gannet-QUEST (R^2 = 0.95) and Gannet-AMARES (R^2 = 0.69) and for Glx estimated with Gannet-AMARES (R^2 = 0.69). Edited GABA estimated with AMARES showed significantly lower levels for the older adults. Likewise, GABA estimated with Gannet and QUEST (MEGA-edit-OFF) had a trend towards decreasing GABA levels in older adults (P = 0.028, P = 0.067 and P = 0.057, respectively).

Conclusion There is a good agreement between GABA values estimated with Gannet (edited) and QUEST (MEGA-OFF) spectral fitting methods. The strong correlation between the Gannet (edited) and QUEST (MEGA-OFF) methods may suggest that conventional MRS (PRESS or STEAM) with an echo time TE=68ms may be used to measure GABA levels accurately in the absence of advanced MRS sequences like MEGA-PRESS. Furthermore, our results indicate that within the SM1 voxel GABA levels were lower in older as compared to young adults.

5.2 INTRODUCTION

Imbalances in neurotransmitters glutamate and glutamine (Glx) as well as γ-aminobutyric acid (GABA) have been implicated aging as well as in various neurodegenerative and neuropsychiatric disorders including Alzheimer's disease, Parkinson's disease, Amyotrophic Lateral Sclerosis (ALS), epilepsy and schizophrenia (Helms et al., 2006; Martin 2007; Stone et al., 2007). Proton magnetic resonance spectroscopy (^{1}H-MRS) is a validated method for assessing gamma-aminobutyric acid (GABA) and Glx concentrations *in vivo* for various conditions (Shungu et al., 2016). GABA is becoming the focus of interest in functional neuroimaging, as resting in vivo GABA levels derived from ^{1}H-MRS have been linked to changes in cerebral blood volume and blood oxygen level dependent (BOLD) fMRI signal during visual stimulation (Donahue et al., 2010; Muthukumaraswamy et al., 2009), as well as the negative BOLD response in the default mode network (Northoff et al., 2007). Changes in GABA have also been observed with motor task activity (Floyer-Lea et al., 2006). Changes in glutamate and glutamine have been detected following acute pain stimulation (Siddall et al., 2006; Gussew et al., 2010). Those studies suggest that MR spectroscopic measurements of GABA and glutamate are sensitive not only to baseline neurotransmitter levels but also to rapid regional modulations of neurotransmitter activity.

However, *in vivo* GABA and Glx detection by ^{1}H MRS presents significant challenges due to their complex signal pattern (J-coupling), their partly low concentration, overlap with other resonances and contamination by macromolecule (MM) signals. There is a growing interest in the application of advanced spectral editing methods to measure GABA and Glx in the human brain. Spectral editing methods such as the MEshcher–GArwood Point RESolved Spectroscopy (MEGA-PRESS) sequence (Mescher, et al., 1998; Edden et al., 2006) provide a promising approach for the separation of GABA from glutamate and glutamine. The technique is based on the J-coupling modulation of the compounds of interest (Mullins et al., 2014; Puts et al., 2012).

Currently there are various software-tools available for quantification of GABA concentration from edited spectra. The Gannet toolbox is such a software that is specifically designed to quantify GABA and Glx (Edden et al., 2014). The AMARES fitting algorithm in jMRUI is a semi-automated tool where prior knowledge is used to fit metabolite signals using single Gaussian or Lorentzian peaks (Vanhamme et al., 1997). Quantification methods that use simulated or experimental metabolite basis sets, such as QUEST in jMRUI (Naressi et al., 2001; Stefan et al., 2009), LC Model (Provencher 1993) and TARQUIN (Wilson et al., 2011) are mainly designed for unedited spectra, however, one can also use these methods to quantify edited spectra with appropriate adjustments to the metabolite basis sets and processing parameters.

To date no comparison was made of GABA concentrations derived from edited (MEGA-PRESS) and unedited (MEGA-OFF) spectra. Here we compare currently available spectral fitting methods, Gannet, AMARES and QUEST to assess the in vivo concentration values for GABA and Glx derived from edited (MEGA-PRESS) and unedited (MEGA-PRESS-OFF) spectra.

Spectral editing methods like the MEGA-PRESS technique provide a promising approach for the discrimination of GABA from glutamate and glutamine, but only very few studies have investigated the possible changes of GABA levels with advancing age (Sanacora et al., 1999; Chang et al., 2009) and relatively little is known about the inter-subject variability in neurotransmitter levels arising from age

effects. In the present study, we quantify the GABA and Glx concentrations derived with edited/unedited MEGA-PRESS using three different spectral fitting methods and investigated age related differences in neurotransmitter levels in a group of healthy young and old adults.

5.3 MATERIALS AND METHODS

5.3.1 Subjects

The subject group for this proof-of-principle study consisted of 10 healthy young adults (YA) (5 female and 5 male; mean age, 38.2 ± 8.43 years; range, 18–45 years) and 10 healthy older adults (OA) (5 female and 5 male; mean age, 62.8 ± 6.26 years; range 60-70 years) with no history of neurological or psychiatric illness, illegal substance abuse or use of psychotropic medication. All subjects were right handed. The protocol was in accordance with the Declaration of Helsinki (1964) and the study was approved by the local medical ethics committee (University Hospital Leuven; MEC reference S58441). All participants gave written informed consent before being included in the study.

5.3.2 MR Data Acquisition

MR imaging and spectroscopy studies were performed with a 3 Tesla (T) Philips Achieva Magnetic Resonance scanner (Philips Healthcare, The Netherlands) using a 32-channel receiver head coil. The scanning protocol included a three-dimensional (3D) fast inversion-recovery prepared gradient echo acquisition (number of slices = 160, slice thickness = 1.2 mm, repetition time (TR) = 9.6 ms, echo time (TE) = 4.6 ms, field of view = 256 mm × 256 mm, flip angle = 20 dgr, matrix = 256 × 192, spatial resolution = 0.98 × 0.98 × 1.2 mm), used for placing of the spectroscopic volume of interest. Single voxel edited ^{1}H-MR spectra were acquired from a $3 \times 3 \times 3$ cm^3 volume of interest (VOI) positioned in the left sensorimotor using the MEGA-PRESS sequence (Mescher et al., 1996; Mescher et al., 1998). The sensorimotor voxel (**Figure 5.1**) was centered over the left hand-knob (Yousry et al., 1997), parallel to the anterior and posterior axis. One surface was parallel to the cortical surface in the coronal and axial views (as shown in Hermans et al., 2018). A total of 320 averages were acquired for each spectrum (number of signal averages (NSA) = 160, dynamic scans = 2) with a TR of 2000 ms, a TE of 68 ms, and 16 phase cycles, water suppression performed with MOIST (Ogg et al., 1994) resulting in an acquisition time of 10 min 56 sec. MEGA-editing was achieved with 20-ms Gaussian editing pulses applied at 1.9 ppm and 7.5 ppm in alternate spectral lines.

5.3.3 Data Pre-processing

After loading the raw data, apodization (3Hz), frequency correction, water removal and calculation of the edited spectrum was performed automatically without any user input using the Gannet software (Edden et al., 2014). For AMARES and QUEST, spectra were frequency and phase corrected and the water peak was removed manually prior to quantification (Vanhamme et al., 1997; Ratiney et al., 2005) Difference spectra from edited and non-edited spectra were derived using a custom made jMRUI plugin. Data were not apodized for AMARES and QUEST.

5.3.4 Data Processing and Analysis

Edited spectra were quantified using the Gannet 3.0 toolbox (Edden et al., 2014) and the jMRUI v6.0-AMARES algorithm (Vanhamme et al., 1997). Spectral fitting in AMARES was performed after manually defining the center frequency and linewidth of the GABA and Glx peaks, and modeling the GABA peak at 3.0 ppm as a singlet and the co-edited glutamate + glutamine (Glx) peak at 3.75 ppm as a doublet. MEGA-PRESS-OFF spectra were quantified with the jMRUI v6.0-QUEST algorithm (Ratiney et al., 2005). A metabolite basis set for QUEST was simulated using a PRESS protocol (TE = 68ms) in NMRScopeB (Starčuk et al., 2017). An unsuppressed water signal was acquired from the same voxels, such that data is reported as the water-normalized ratios: GABA/H2O and Glx/H2O. Corrections were applied for relaxation effects using published values for the metabolite relaxation times (Mlynarik et al., 2001; Ethofer et al., 2003; Traber et al., 2004). In this study, concentrations were not corrected for partial volume CSF contamination.

Water-referenced GABA and Glx concentrations were estimated in institutional units from metabolite amplitudes according to the following formula (Mullins *et al.*, 2014):

$$[\text{GABA}] = \frac{S_{\text{GABA}}}{S_{\text{H2O}}} * [\text{H2O}] * \text{VIS}_{\text{H2O}} \frac{1 - e^{\left(\frac{-\text{TR}}{\text{T1}_{\text{H2O}}}\right)}}{1 - e^{\left(\frac{-\text{TR}}{\text{T1}_{\text{GABA}}}\right)}} * \frac{e^{\left(\frac{-\text{TE}}{\text{T2}_{\text{H2O}}}\right)}}{e^{\left(\frac{-\text{TE}}{\text{T2}_{\text{GABA}}}\right)}} \qquad (1)$$

where S_{GABA} and S_{H2O} are the averaged raw GABA and water signals, $[H_2O]$ is the brain water concentration (e.g. 55,550 mmol/l), VIS_{H2O} is the water visibility (e.g. 0.65 in white matter, TR is the repetition time, $T_{1\text{H2O}}$ is the T_1 of water (1.1 s) (Wansapura *et al.*, 1999), $T_{2\text{H2O}}$ is the T_2 of water (0.095 s) (Wansapura *et al.*, 1999), $T_{1\text{GABA}}$ is the T_1 of GABA (0.8 s), $T_{2\text{GABA}}$ is the T_2 of GABA (0.13 s) (Träber *et al.*, 2004),

Statistical analysis was done using Prism GraphPad v5 (GraphPad, La Jolla, California). Quantification methods were compared using two-tailed unpaired t-tests. Age-difference concentration values of the three methods were assessed using two-way ANOVA with Bonferroni post-hoc test. Pearson correlation coefficients were calculated to evaluate the correlations between the methods. A *P*-value less than 0.05 was considered statistically significant in this study.

5.4   RESULTS

A representative MEGA-PRESS spectrum and non-edited spectrum of a participant is shown in **Figure 5.1**. The GABA peak at 3.0 ppm and the Glx peak at 3.75 ppm from edited MEGA-PRESS spectra were

visualized for all spectra with high signal-to-noise ratio. The average linewidth of the non-suppressed water spectra was 6.8±2.1 and average signal-to-noise ratio of spectra was 58.3±8. **Figure 5.2** shows the fitting of the data from the three methods. Glutamate, glutamine and GABA estimated using QUEST had a Cramér—Rao lower bounds of less than 15%. **Figure 5.3** depicts the GABA and Glx concentrations estimated with Gannet, AMARES, and QUEST for the 20 subjects. The differences between concentration values measured using Gannet, AMARES and QUEST across all subjects are presented in **Table 5.1**. GABA levels estimated with Gannet and QUEST showed similar values. Significant positive correlations were found for GABA and Glx values estimated with Gannet, AMARES and QUEST, where strongest correlation was seen between Gannet and QUEST (**Table 5.2**).
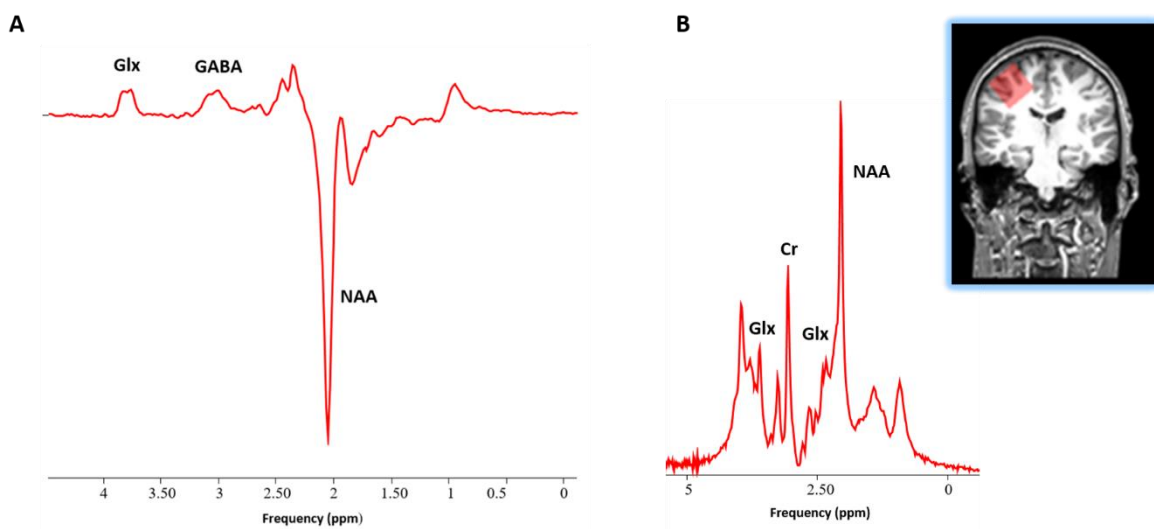
Figure 5.1: Representative processed MEGA-PRESS spectrum (A) and processed non-edited PRESS spectrum (B) acquired from the left sensory motor cortex of one participant visualized by jMRUI.
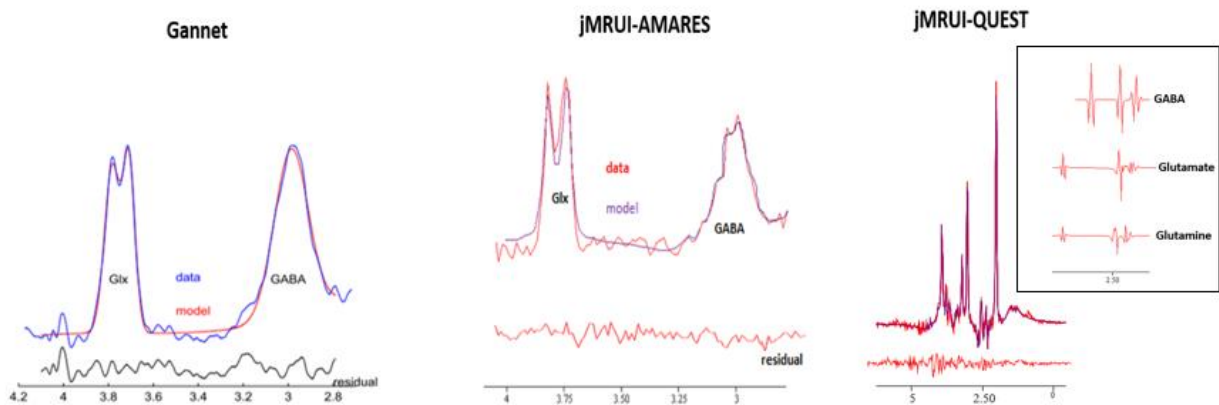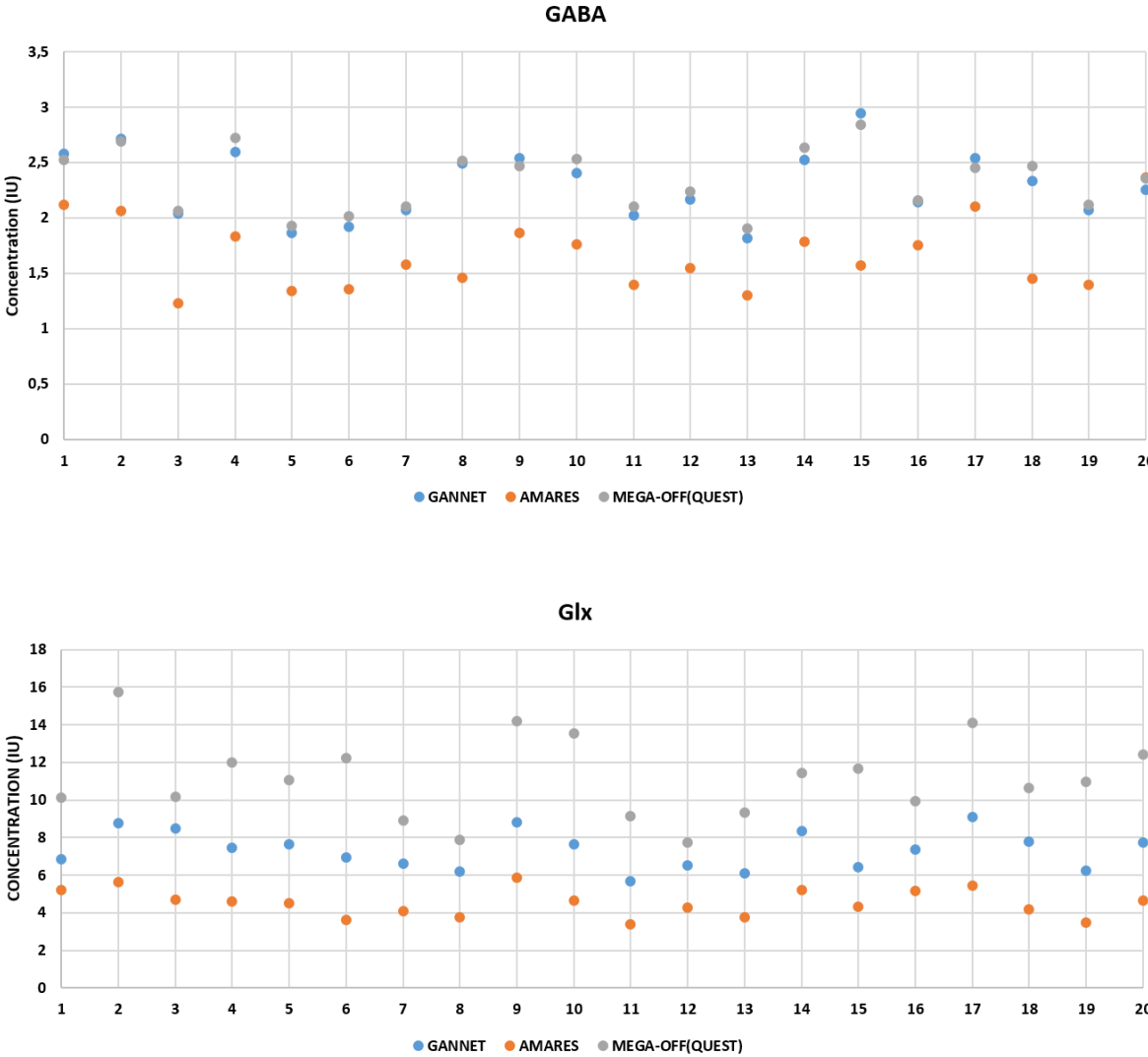
Figure 5.3: GABA and Glx concentrations estimated with Gannet, AMARES, and QUEST for the 20 subjects. Note the GABA estimated by Gannet and QUEST is almost identical. In addition, all three methods show a lower inter-subject variability for GABA compared to Glx.

Table 5.1: Mean ± SD GABA and Glx concentrations estimated with Gannet, AMARES, and QUEST for the 20 subjects.

Method	GABA	Glx
Gannet	2.3±0.3	7.3±0.9
AMARES	1.7±0.3	4.5±0.7
% difference	-30	-47
T-test (p-value)	<0.0001	<0.0001

Method	GABA	Glx
Gannet	2.3±0.3	7.3±0.9
QUEST	2.3±0.3	6.0±1.1
% difference	~0	-20
T-test (p-value)	0.67	0.001

Method	GABA	Glx
QUEST	2.3±0.3	6.0±1.1
AMARES	1.7±0.3	4.5±0.7
% difference	-30	-29
T-test (p-value)	<0.0001	<0.0001

Table 5.2: Correlation information comparison of GABA and Glx estimated with Gannet, AMARES, and QUEST.

Gannet vs QUEST	GABA	Glx
Pearson r	0,9744	0,7311
R^2	0.9495	0,5346
P-value	<0.0001	0,0002

Gannet vs AMARES	GABA	Glx
Pearson r	0,8314	0,8316
R^2	0,6979	0,6915
P-value	<0,0001	<0,0001

QUEST vs AMARES	GABA	Glx
Pearson r	0,7511	0,6178
R^2	0,5642	0,3817
P-value	0,0003	0,0037

MEGA-PRESS edited GABA estimated with AMARES showed significantly lower levels for the older adults (**Figure 5.4**). Likewise GABA estimated with Gannet and QUEST (MEGA-OFF) showed a trend towards decreasing GABA levels in older adults ($P = 0.028$, $P = 0.067$ and $P = 0.057$ respectively).

GABA

Glx
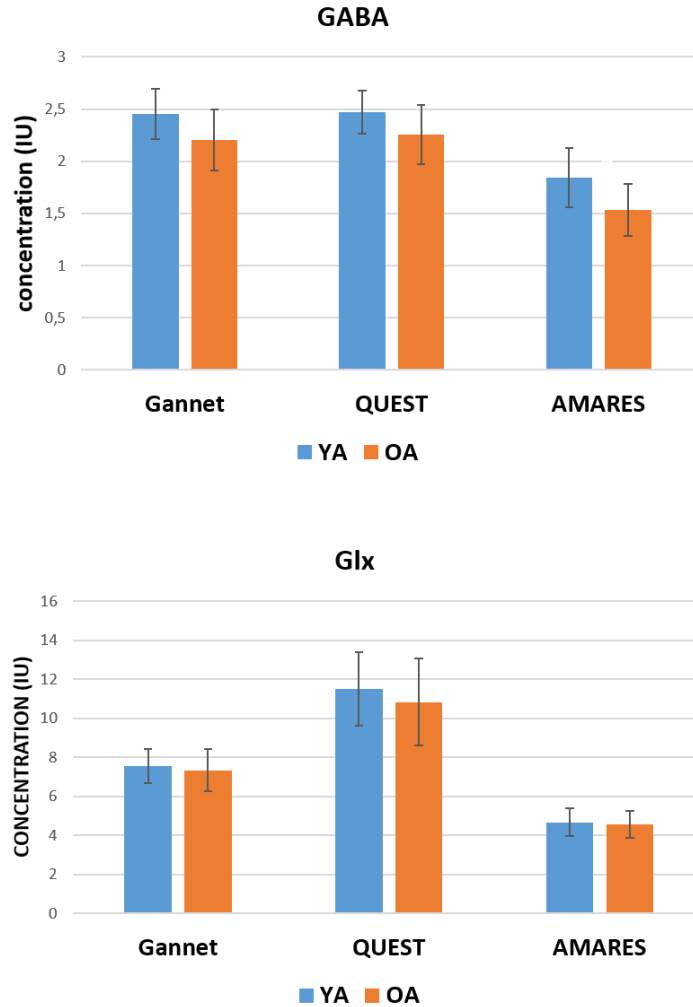
Figure 5.4. GABA concentrations for young (n = 10) and old (n = 10) adults estimated with Gannet, QUEST and AMARES.

5.5 DISCUSSION

The high spectral quality and high sensitivity to GABA seen for all the spectra in this study indicate that the MEGA-PRESS method provides a robust tool for the in vivo detection of especially GABA in the sensory motor cortex. However, it should be mentioned that the GABA concentrations reported in this study (both edited and unedited) also contain contributions from co-edited macromolecule signals. Therefore, fitting of the edited peak at 3.0 ppm as either a singlet or a doublet will yield an estimate for GABA that should be indicated as having a substantial contribution from macromolecules, this is often referred to as GABA+ in the literature [Harris et al., 2017; Porges et al., 2017]. Results from metabolite nulling studies suggest that the MM resonances can account for nearly half the apparent GABA concentration, although the relative contribution of the MM to the GABA+ peak is thought to remain relatively stable across brain regions and subjects (Kegeles et al., 2007).

Direct comparison of the three spectral fitting methods using comparable metrics is not feasible due to several reasons. Errors in fit determined using jMRUI-QUEST reflect a statistical model that fits all metabolites simultaneously, while the errors generated from the fit by using GANNET do not consider errors propagated in preprocessing (frequency alignment, subtraction etc.). Also, time and signal-to-noise penalties were not considered in this study. We mainly looked for consistency in the data generated by the acquisition and three fitting methods.

The inter-subject variability for GABA levels was lower than that of Glx for all three fitting methods. Almost no difference in concentration values was found for GABA estimated with Gannet (edited) and QUEST (unedited). A 30% difference in GABA concentrations was found for AMARES compared to the other two methods. For Glx, a 20% difference in values was found between Gannet-QUEST and 29% difference was seen between AMARES-QUEST. The largest Glx difference of 47% was found between Gannet and AMARES. The variability in concentration values obtained by all three methods could be due to several factors such as the differences in water visibility values (% of water in brain tissue), apodization and editing efficiency values used in each processing tool in estimating the absolute concentration. A strong positive correlation between Gannet and QUEST suggest that the two methods are in good agreement for quantifying GABA acquired by edited and unedited MEGA-PRESS spectra. Due to the good agreement of the Gannet and QUEST derived GABA values, a next step could be to acquire GABA using a regular PRESS sequence with a TE = 68ms and compare the data with those acquired with MEGA-PRESS. Such a study could confirm if a regular PRESS sequence with a TE = 68ms could replace the MEGA-PRESS sequence for reliable GABA quantification.

In this study, we also investigated the changes of neurotransmitters GABA and Glx levels in the sensorimotor cortex of young and old adults. Even though not many studies reported GABA changes with advancing age, a recent study from Porges and co-workers observed a decrease in GABA levels with advancing age within frontal and parietal locations (Porges et al., 2017). Our observation of lower GABA in older adults as compared to young adults needs further analysis with tissue corrections since the distribution of GABA varies across neural tissue fractions (Olsen et al., 2009). The age-related differences in GABA levels we observed may be driven by the gray matter loss rather than altered GABA levels within the gray and white matter tissues. However, we did not observe any significant changes in the Glx levels of the two groups. An alternative interpretation of the GABA+ concentrations could be a decreased MM contribution with old age. However, some preliminar studies have reported increased MM in the aging brain (Hofmann et al., 2001; Mader et al., 2002; Marjańska et al., 2018).

In conclusion, there is a good agreement between GABA values estimated with Gannet (edited) and QUEST (MEGA-OFF) spectral fitting methods. The strong correlation between the Gannet (edited) and QUEST (MEGA-OFF) may suggest that conventional MRS (PRESS) with a TE=68ms may be used to measure GABA levels accurately in the absence of advanced MRS sequences. Furthermore, our results indicate that within the SM1 voxel GABA levels were lower in older as compared to young adults.

5.6 REFERENCES

Chang L, Jiang CS, Ernst T. Effects of age and sex on brain glutamate and other metabolites. *Magn Reson Imaging*. 2009; 27(1):142-5.

Donahue MJ, Near J, Blicher JU, Jezzard P. Baseline GABA concentration and fMRI response. *Neuroimage*. 2010; 53:392–398.

Edden RA, Puts NA, Harris AD, Barker PB, Evans CJ. Gannet: A batch-processing tool for the quantitative analysis of gamma-aminobutyric acid–edited MR spectroscopy spectra. *J Magn Reson Imaging*. 2014; 40(6):1445-52.

Ethofer T, Mader I, Seeger U, *et al*. Comparison of longitudinal metabolite relaxation times in different regions of the human brain at 1. 5 and 3 Tesla. *Magn Reson Med*. 2003; 50:1296–1301.

Floyer-Lea A, Wylezinska M, Kincses T, Matthews PM. Rapid modulation of GABA concentration in human sensorimotor cortex during motor learning. *J Neurophysiol*. 2006; 95:1639–1644.

Gussew A, Rzanny R, Erdtel M, *et al*. Time-resolved functional H-1 MR spectroscopic detection of glutamate concentration changes in the brain during acute heat pain stimulation. *Neuroimage*. 2010; 49:1895–1902.

Harris AD, Puts NAJ, Wijtenburg SA, et al. Normalizing data from GABA-edited MEGA-PRESS implementations at 3 Tesla. *Magn Reson Imaging*. 2017; 42:8-15.

Helms G, Ciumas C, Kyaga S, Savic I. Increased thalamus levels of glutamate and glutamine (Glx) in patients with idiopathic generalised epilepsy. *J Neurol Neurosurg Psychiatry*. 2006; 77:489–494.

Hofmann L, Slotboom J, Boesch C, Kreis R. Characterization of the macromolecule baseline in localized (1)H-MR spectra of human brain. *Magn Reson Med*. 2001; 46(5):855-63.

Kegeles L, Mao X, Gonsalez R, Shungu DC. Evaluation of anatomic variation in macromolecule contribution to the GABA signal using metabolite nulling and the J-editing technique at 3T. Proceedings of the 15th Annual Meeting of ISMRM; Berlin, Germany. 2007. p. abstract 391.

Mader I, Seeger U, Karitzky J, Erb M, Schick F, Klose U. Proton magnetic resonance spectroscopy with metabolite nulling reveals regional differences of macromolecules in normal human brain. *J Magn Reson Imaging*. 2002; 16(5):538-46.

Marjańska M, Deelchand DK, Hodges JS, McCarten JR, Hemmy LS, Grant A, Terpstra M. Altered macromolecular pattern and content in the aging human brain. *NMR Biomed*. 2018; 31(2).

Martin WRW. MR Spectroscopy in neurodegenerative disease. *Mol Imaging Biol*. 2007; 9:196–203.

Mescher M, Tannus A, Johnson MO, Garwood M. Solvent suppression using selective echo dephasing. *J Magn Reson Ser A*. 1996; 123(2):226–229.

Mescher M, Merkle H, Kirsch *J, Garwood M, Gruetter R NMR Biomed. 1998; 11(6):266-72.*

Mlynarik V, Gruber S, Moser E. Proton T-1 and T-2 relaxation times of human brain metabolites at 3 Tesla. *NMR Biomed*. 2001; 14:325–331

Mullins PG, Mc Gonigle DJ, O'Gorman RL. Current practice in the use of MEGA-PRESS spectroscopy for the detection of GABA. *Neuroimage*. 2014; 86:43-52.

Muthukumaraswamy SD, Edden RAE, Jones DK, Swettenham JB, Singh KD. Resting GABA concentration predicts peak gamma frequency and fMRI amplitude in response to visual stimulation in humans. *Proc Natl Acad Sci U S A*. 2009; 106:8356–8361.

Naressi A, Couturier C, Devos JM, Janssen M, Mangeat C, de Beer R, Graveron-Demilly D. Java-based graphical user interface for the MRUI quantitation package. *MAGMA*. 2001; 12(2-3):141-52.

Northoff G, Walter M, Schulte RF, *et al*. GABA concentrations in the human anterior cingulate cortex predict negative BOLD responses in fMRI. *Nat Neurosci*. 2007; 10:1515–1517.

Ogg RJ, Kingsley PB, Taylor JS. WET, a T1- and B1-insensitive water-suppression method for in vivo localized 1H NMR spectroscopy. J Magn Reson B. 1994; 104(1):1-10.

Olsen RW, Sieghart W. GABA A receptors: subtypes provide diversity of function and pharmacology. *Neuropharmacology*. 2009; 56(1):141-8.

Porges EC, Woods AJ, Lamb DG, Williamson JB, Cohen RA, Edden RAE, Harris AD. Impact of tissue correction strategy on GABA-edited MRS findings. Neuroimage. 2017; 162:249-256.

Porges EC, Woods AJ, Edden RA, Puts NA, Harris AD, Chen H, Garcia AM, Seider TR, Lamb DG, Williamson JB, ohen RA. Frontal Gamma-Aminobutyric Acid Concentrations Are Associated With Cognitive Performance in Older Adults. *Biol Psychiatry Cogn Neurosci Neuroimaging*. 2017: 2(1):38-44.

Provencher SW. Estimation of metabolite concentrations from localized *in vivo* proton NMR spectra. *Magn Reson Med*. 1993; 30(6):672-9.

Puts NA, Edden RA. *In vivo* magnetic resonance spectroscopy of GABA: a methodological review. *Prog Nucl Magn Reson Spectrosc*. 2012; 60:29-41.

Ratiney H, Sdika M, Coenradie Y, Cavassila S, van Ormondt D, Graveron-Demilly D. Time-domain semi-parametric estimation based on a metabolite basis set. *NMR Biomed*. 2005; 18:1–13.

Sanacora G, Mason GF, Rothman DL, Behar KL, Hyder F, Petroff OA, Berman RM, Charney DS, Krystal JH. Reduced cortical gamma-aminobutyric acid levels in depressed patients determined by proton magnetic resonance spectroscopy. *Arch Gen Psychiatry*. 1999; 56(11):1043-7.

Siddall PJ, Stanwell P, Woodhouse A, Somorjai RL, Dolenko B, Nikulin A, Bourne R, Himmelreich U, Lean C, Cousins MJ, Mountford CE. Magnetic resonance spectroscopy detects biochemical changes in the brain associated with chronic low back pain: a preliminary report. Anesth Analg. 2006; 102(4):1164-8.

Shungu DC, Mao X, Gonzales R. Brain GABA Detection *in vivo* with the J-editing ^{1}H MRS Technique: A Comprehensive Methodological Evaluation of Sensitivity Enhancement, Macromolecule Contamination and Test-Retest Reliability. *NMR in biomedicine*. 2016; 29(7):932-942.

Starčuk Z Jr, Starčuková J. Quantum-mechanical simulations for *in vivo* MR spectroscopy: Principles and possibilities demonstrated with the program NMRScopeB. *Anal Biochem*. 2017; 15; 529:79-97.

Stefan D, Cesare FD, Andrasescu A, Popa E, Lazariev A, Vescovo E, Strbak O, *et al*. Quantitation of magnetic resonance spectroscopy signals: the jMRUI software package. *Meas Sci Technol*. 2009; 20(10):104035.

Stone JM, Morrison PD, Pilowsky LS. Glutamate and dopamine dysregulation in schizophrenia - A synthesis and selective review. *J Psychopharmacol (Oxf)*. 2007; 21:440–452.

Traber F, Block W, Lamerichs R, Gieseke J, Schild HH. H-1 metabolite relaxation times at 3. 0 tesla: measurements of T1 and T2 values in normal brain and determination of regional differences in transverse relaxation. *J Magn Reson Imaging*. 2004; 19:537–545.

Vanhamme L, van den Boogaart A, Van Huffel S. Improved method for accurate and efficient quantification of MRS data with use of prior knowledge. *J Magn Reson*. 1997; 129(1):35-43.

Wansapura JP, Holland SK, Dunn RS, Ball WS Jr. *J Magn Reson Imaging*. 1999; 9(4):531-8.

Wilson M, Reynolds G, Kauppinen RA, Arvanitis TN, Peet AC. A constrained least-squares approach to the automated quantitation of *in vivo* [1]H magnetic resonance spectroscopy data. *Magn Reson Med*. 2011; 65(1):1-12.

Chapter 6

Non-Invasive Assessment of Disease Progression and Neuroprotective Effects of Dietary Coconut Oil Supplementation in the ALS SOD1[G93A] Mouse Model: a [1]H-Magnetic Resonance Spectroscopic Study.

A. Weerasekera[1], D.M. Sima[2,5], T. Dresselaers[3], S. Van Huffel[2], P. Van Damme[4], U. Himmelreich[1*]

(1) Biomedical MRI unit/ MoSAIC, Department of Imaging and Pathology, KU Leuven, Leuven, Belgium.

(2) Department of Electrical Engineering (ESAT), STADIUS Center for Dynamical Systems, Signal Processing and Data Analytics, KU Leuven, Leuven, Belgium.

(3) Radiology, Department of Imaging and Pathology, UZ Leuven, Leuven, Belgium.

(4) Department of Neurology, University Hospitals Leuven and Laboratory of Neurobiology, Department of Neurosciences, KU Leuven and Center for Brain & Disease Research, VIB , Leuven, Belgium.

(5) icometrix, R&D department, Leuven, Belgium.

6. Non-Invasive Assessment of Disease Progression and Neuroprotective Effects of Dietary Coconut Oil Supplementation in the ALS SOD1^{G93A} Mouse Model: a ^{1}H-Magnetic Resonance Spectroscopic Study.

6.1 ABSTRACT

Amyotrophic Lateral Sclerosis (ALS) is an incurable neurodegenerative disease primarily characterized by progressive degeneration of motor neurons in the motor cortex, brainstem and spinal cord. Due to relatively fast progression of ALS, early diagnosis is essential for possible therapeutic intervention and disease management. To identify potential diagnostic markers, we investigated age-dependent effects of disease onset and progression on regional neurochemistry in the SOD1^{G93A} ALS mouse model using localized *in vivo* magnetic resonance spectroscopy (MRS). We focused mainly on the brainstem region since brainstem motor nuclei are the primarily affected regions in SOD1^{G93A} mice and ALS patients. In addition, metabolite profiles of the motor cortex were also assessed. In the brainstem, a gradual decrease in creatine levels were detected starting from the pre-symptomatic age of 70 days postpartum. During the early symptomatic phase (day 90), a significant increase in the levels of the inhibitory neurotransmitter γ- aminobutyric acid (GABA) was measured. At later time points, alterations in the form of decreased NAA, glutamate, glutamine and increased myo-inositol were observed. Also, decreased glutamate, NAA and increased taurine levels were seen at late stages in the motor cortex. A proof-of-concept (PoC) study was conducted to assess the effects of coconut oil supplementation in SOD^{G93A} mice. The PoC revealed that the coconut oil supplementation together with the regular diet delayed disease symptoms, enhanced motor performance, and prolonged survival in the SOD1^{G93A} mouse model. Furthermore, MRS data showed stable metabolic profile at day 120 in the coconut oil diet group compared to the group receiving a standard diet without coconut oil supplementation. In addition, a positive correlation between survival and the neuronal marker NAA was found. To the best of our knowledge, this is the first study that reports metabolic changes in the brainstem using *in vivo* MRS and effects of coconut oil supplementation as a prophylactic treatment in SOD1^{G93A} mice.

6.2 INTRODUCTION

Amyotrophic lateral sclerosis (ALS) is an idiopathic, progressive and a fatal neurodegenerative disease characterized by selective death of motor neurons in the motor cortex, brainstem and spinal cord. The bulbar neurons regulate the swallowing and spinal motor neurons innervate limb muscles. ALS symptoms and signs include fasciculations, progressive atrophy of the skeletal muscles, weakness and paralysis of the upper and lower limbs (Cleveland *et al.*, 2001). In addition, loss of speech and denervation of the respiratory muscles occurs with most ALS patients dying of respiratory failure.

The pathophysiological mechanisms leading to the degeneration of motor neurons are still largely unknown and possibly multifactorial. However, there are several hypotheses underlying the disease process including oxidative stress, glutamate excitotoxicity, impaired mitochondrial function, aberrant protein folding, disturbances in RNA metabolism and impaired axonal transport (Turner *et al*., 2008; Wang *et al*., 2015; De Vos *et al*., 2017; *Liu et al*., 2017).

While approximately 10% of ALS cases have familial causes (fALS), in 90% the disease is considered sporadic (sALS). The etiology of sALS is largely unknown; however, about 20% of fALS is associated with a dominantly inherited mutation in the gene that encodes the Cu/Zn-superoxide dismutase 1 (SOD1). A key pathology observed in SOD1 mutation is the abnormal build-up of misfolded-dysfunctional mutant SOD1 protein aggregates in affected motor neurons (Bruijn *et al*., 1998). However, since most mutant SOD1 proteins are able to function normally, a toxic gain of function is more likely as a cause for pathogenesis of SOD-related ALS (Boillée *et al*., 2006; Sau *et al*., 2007; Bunton-Stasyshyn *et al*., 2015; Bastow *et al*., 2016).

The SOD1^{G93A} transgenic mouse, which over-expresses a mutated form of the human SOD1 gene (Gurney *et al*., 1994) has been studied as an experimental model for fALS. This model presents with clinical symptoms and neuropathological features that mimic those characteristic of fALS (Rosen *et al*., 1993; Van Damme *et al*., 2017), such as severe hind limb paralysis with atrophy of skeletal muscles (Tu *et al*., 1996). In SOD1^{G93A} mice, atrophy of the diaphragm muscles leads to respiratory failure and subsequent death (Tankersley *et al*., 2007). At the moment there is a strong urgency to find predictive biomarkers in the progression of ALS since early diagnosis is the key for possible disease management methods (Karitzky *et al*., 2001). Magnetic resonance imaging (MRI) and spectroscopy (MRS) have become essential in the diagnosis of various neurological diseases mainly because of their non-invasive nature, high soft tissue contrast and multi-parametric readouts. In human ALS patients, both T2-weighted and fluid-attenuated inversion recovery (FLAIR) MR images have shown non-specific hyperintense alterations in the primary motor cortex and corticospinal tract (Lee *et al*., 2003; Hecht *et al*., 2003). Also, it is well established that T2-weighted MRI is sensitive to tissue changes around the time of symptom onset in SOD1^{G93A} mice (Zang *et al*., 2004; Niessen *et al*., 2006; Bucher *et al*., 2007; Evans *et al*., 2014). These studies reported that T2-weighted MRI revealed an early and progressive degeneration in the SOD1^{G93A} hindbrain motor nuclei, including motor nuclei V (trigeminal), VII (facial), and XII (hypoglossal).

In vivo ^{1}H-MRS) is a non-invasive method for measuring brain metabolites. It has been used to assess the progression of neurodegeneration in humans and mouse models of diseases including ALS, Alzheimer's, Huntington's and Parkinson's disease (Jenkins *et al*., 2000; Andreassen *et al*., 2001; Choi *et al* 2003a; Dedeoglu *et al*., 2004; Jenkins *et al*., 2005; Marjanska *et al*., 2005; Van der Perren *et al* 2015). There are a number of neurometabolites that can be identified and quantified from *in vivo* MRS. N-acetyl aspartate (NAA), a known marker of neuronal health and function has been observed to decrease in motor cortex and then increase with Riluzole therapy (Kalra *et al*., 1999). A longitudinal study showed a decline of NAA in the motor cortex but not in other cortical regions of ALS (Choi *et al*., 2009). Increases in the neurotransmitters glutamate and glutamine have also been observed in ALS medulla (Pioro *et al*., 1999). Other molecules such as taurine and myo-inositol, that are related to both osmotic regulation/ neurotransmitter modulator as well as glial cell proliferation can be measured *in vivo*. ^{1}H-MRS also has the advantage of being able to measure changes in total creatine (the sum of creatine and phosphor-

creatine), which is a marker for the energy metabolism in cells with dietary supplementation (Andreassen *et al.*, 2001; Hersch *et al.*, 2006; Choi *et al.*, 2009).

There is considerable evidence to indicate that the ALS pathology arise due to impaired energy metabolism in motor neurons (Dupuis *et al.*, 2011). In ALS, a lower body mass index (BMI) is linked with higher risk of developing the disease and poor prognosis. Therefore, maintaining a higher BMI is proven to be beneficial in ALS (Gallow *et al.*, 2013; O'Reilly *et al.*, 2013). Previous studies have shown that a ketogenic diet or caprylic triglyceride halts the impairment of motor function and reduces death of motor neurons in the spinal cord of SOD1^{G93A} mice by restoring energy metabolism through ketone body utilization (Zhao *et al.*, 2006; Zhao *et al.*, 2012). In normal circumstances glucose acts as the main energy source for the cells. However, alternative energy sources such as ketone bodies or TCA cycle intermediates can potentially bypass the rate limiting steps associated with impaired neuronal glucose metabolism and restore mitochondrial adenosine triphosphate (ATP) production (Ari *et al.*, 2014). Recently, metabolic-targeted therapies such as therapeutic ketosis have been used in the disease management process in several neurological disorders (Hartman *et al.*, 2012; Hartman *et al.*, 2013). In addition, coenzyme Q (Beal *et al.*, 2002), creatine (Andreassen *et al.*, 2001), high-fat diet (Lupuis *et al.*, 2004), and ketogenic-medium chain triglyceride diet (Zhao *et al.*, 2006) were found to be effective against neuronal damage induced by excitotoxicity and mitochondrial inhibition. Furthermore, coconut oil which contains high levels of medium chain triglycerides (MCT) could act as a natural ketogenic supplement in ALS. However, we were unable to find any published clinical or preclinical trials of coconut oil, although sporadic reports exist on patient platforms (Gupta *et al.*, 2011). Therefore, we designed a proof-of-concept (PoC) study to assess the effects of coconut oil in the SOD1^{G93A} mouse model.

The goals in this study were to monitor the onset and progression of the disease by observing alterations in regional brain metabolism of SOD1^{G93A} mice using *in vivo* MR spectroscopy and to examine the potential neuroprotective effects of coconut oil dietary supplement in this model.

6.3 MATERIALS AND METHODS

6.3.1 Transgenic Mice

All animal experiments were performed according to the European Communities Council Directive of September 22nd 2010 (2010/63/EU) and approved by the local Animal Ethics Committee of the KU Leuven. Male transgenic mice carrying a high copy number of a mutant allele human superoxide dismutase 1 (SOD1) [B6SJL-TgN (SOD1-G93A) 1Gur, Stock #: 002726] were purchased and bred locally with female B6SJL mice (Jackson Laboratory, Bar Harbor, ME). The progeny were genotyped by tail DNA polymerase chain reaction (PCR).

In a first experiment, we used localized *in vivo* ^{1}H-MRS to evaluate metabolic changes associated with disease onset and progression in SOD1^{G93A} mice (n = 10). Metabolic profiles were assessed in the hindbrain and motor cortex in comparison to age-matched wild type (WT) mice (n = 10) of 30, 60, 70, 90, 110, 120 and 140 days postpartum (P30, P60... *etc*). In the second experiment, *in vivo* ^{1}H-MRS was used to assess the effects of coconut oil supplementation versus standard diet, tested in additional

cohorts of SOD1^{G93A} (n = 6) and control mice (n = 6). Also, body weight, motor performance and survival was assessed.

Time-points were selected to reflect disease stages either long before the onset of clinical symptoms (P30), right before the disease onset (P60-P70), at the average disease onset (P90-P110) and at the terminal stage of ALS (P120 and P140). Since sex could possibly be a factor for variations in the survival in SOD1^{G93A} model only males were used.

6.3.2   *In vivo* MRI and MR spectroscopy

All MR-based experiments were performed using a small-animal 9.4 Tesla MR scanner (Biospec 94/20, Bruker Biospin, Ettlingen, Germany) with a horizontal bore of 20 cm and equipped with an actively shielded gradient set (600 mT m^{-1}, inner diameter 11.7 cm). Single-voxel ^{1}H-MR spectra were acquired using a linear polarized resonator (7 cm diameter) for transmission, combined with a mouse brain surface coil for receiving (both Bruker Biospin, Ettlingen, Germany).

6.3.3   Animal preparation and monitoring

Mice were fixed in an animal-bed by placing the nose of the mouse in a nose cone, restraining it with a bite bar and custom made outer ear-inserts. The mouse head was lifted and gently stretched a few millimeters forward. By lining up the midline of the head and the spine produces an angle between the brainstem and the rest of the mouse body. This alignment decreases the distance between the surface coil and the brainstem region and allows acquisition of high quality data.

Throughout scanning, mice were anaesthetized with 1-2 % isoflurane in 100 % oxygen. Respiration and body temperature were continuously monitored and maintained at 60-100 min^{-1} and 37±1°C, respectively. Vidisic Eye Gel (Bausch & Lomb, Brussels, Belgium) was used to avoid the drying of eyes during scanning.

6.3.4   Magnetic Resonance Imaging

In order to visualize signal intensity changes, a T2-weighted 3D TurboRARE protocol was acquired with the following acquisition parameters: repetition time (TR) 1000 ms, echo time (TE) 12 ms, FOV 24×15×8.3 mm, matrix size 256×160×88, RARE factor 10, number of averages = 1. For the placement of the spectroscopy voxel, T2-weighted 2D RARE images (effective TE 50ms; matrix 256x256; 300um slice thickness) were acquired. For T2 relaxometry, a multi-slice multi-echo (MSME) sequence was used with ten echoes collected at intervals of 12 ms from TE = 12 ms to TE = 120 ms, with TR = 3000 ms and with NA = 1, FOV 25x25 mm, 19 slices, slice thickness of 0.5 mm and a matrix of 256 × 256. T2 maps were produced using the imageJ software (NIH, USA). T2 values were calculated using ITKSNAP (Penn Image Computing and Science Laboratory, USA) and an in-house python scripts.

6.3.5 ^{1}H-Magnetic Resonance Spectroscopy

MR spectra were acquired for volumes in the motor cortex and the hindbrain with a voxel size of 2x2.5.x1.5 mm^3 (see Figure 2). The hindbrain voxel covered the following nuclei: hypoglossal, medial vestibular nucleus, and the dorsal motor nucleus of the vagus nerve. MR spectra were acquired with a PRESS pulse sequence using the following parameters: TR = 1800 ms, TE = 20 ms, and number of averages 320 for motor cortex and 640 for hindbrain. Water suppression was optimized using VAPOR (Griffey *et al.*, 1990). An unsuppressed water spectrum (TE = 20 ms, TR = 1400 ms, number of averages = 4) was acquired before each ^{1}H-MRS spectrum (water suppressed) for quantification/ referencing. Shimming was performed using FASTMAP (Gruetter 1993), resulting in a final water line width at half height < 16 Hz. Spectra were processed using jMRUI v6.0 (Stefan *et al.*, 2009). Spectra were phase corrected and an HLSVD (Hankel Lanczos Singular Values Decomposition) filter was applied to remove the residual water signal (van den Boogaart *et al.*, 1994). Only metabolites with a Cramer-Rao lower bound < 25% were considered for quantification. Metabolites were quantified with the QUEST algorithm (Ratiney *et al.*, 2004) in jMRUI using a simulated (NMRScopeB) basis set (Starčuk Jr *et al.*, 2009). Results are reported in reference to the non-suppressed water signal. A total of 16 brain metabolites (Alanine, Aspartic acid, total creatine, choline, GABA, glycine, glucose, glutamate, glutamine, NAA, myo-inositol, Scyllo-inositol, lactate, phosphoethanolamine, scyllo-inositol, taurine) was quantified.

6.3.6   Diet Preparation

Extra virgin coconut oil (**supplementary Figure S1 (A)**), Royal Green, Frenchtop Natural Care Products BV, AL Hoornm Netherlands) was mixed with the standard rodent food (ssniff DIO D12450B, 4ml with 15-20g). Food was dispensed in a petri dish and placed inside the cage daily. Treatment started at 72 days after birth. At 70 days of age, animals underwent baseline MR spectroscopy, and the same animals were re-scanned at 120 days. Mice were followed up until end stage for behavior and survival studies. Control animals received standard rodent food (D12450B Rodent Diet with 10 kcal% fat from Ssniff laboratories).

6.3.7   Behavioral Assessments

Muscle strength and endurance was assessed by the paw grip endurance (PaGE) test (**supplementary Figure S1 (B)**) (Weydt *et al.*, 2003). Mice were placed on the center of a custom made metal grid and grid was turned upside down over a cage and the latency to fall (time in seconds) was recorded (Crawley 2007). Longest hanging-time was recorded after two attempts were given for each mouse.

6.3.8   Survival and End-Point

Survival endpoint criteria were defined as unable to return to the normal, upright position within 10s following push over, this was tested daily from P130 (Ari *et al.*, 2014). When the mice reached the end-stage, mice were euthanized by IP injection of Sodium pentobarbital (50 mg/kg, Butler Schein, NDC #11695-4829-1).

6.3.9 Statistical Analysis

All statistical tests were performed using GraphPad PRISM version 5 (GraphPad, San Diego). Two-way analysis of variance (ANOVA) tests were performed for each neurometabolite in hindbrain and motor cortex to evaluate the significance of the group (SOD1^{G93A} and WT) and postpartum age (P30, P60, P70, P90, P110, P120 and P140) as fixed factors. Subsequently, those neurometabolites, which had a significant effect were further analyzed for age-dependent effects within each group with a one-way ANOVA. One-way ANOVA and t-tests were used to assess significant differences in mean concentrations within each group and between the two groups. Comparisons between coconut oil treated and standard diet animals were made using by t-tests or ANOVA with post hoc analyses and effect of coconut oil diet on survival was assessed by the Kaplan-Meier survival analysis. The threshold for statistical significance was set at $P < 0.05$. P-values were Bonferroni corrected for multiple comparisons. Pearson correlation coefficient, r, was used for correlation analysis.

6.4   RESULTS

6.4.1   T$_2$-Weighted Magnetic Resonance Imaging

T$_2$-weighted MR images revealed increased hyperintense contrast in SOD1^{G93A} brainstem motor nuclei V (trigeminal), VII (facial), and XII (hypoglossal) (**Figure 6.1**). Contrast of the motor nuclei within the brainstem starts to increase relative to surrounding tissue around P90, parallel to the observation of first clinical symptoms such as tremors and gait abnormalities.

6.4.2   Magnetic Resonance Spectroscopy

In order to assess neurometabolic alterations, we acquired MR spectra (motor cortex: signal to noise ratio > 14; line-width 9 ± 2 Hz, hindbrain: SNR > 10, line-width 12 ± 3 Hz, water/lipid/artifact suppressed). Typical MR spectra obtained from the motor cortex and hindbrain of a SOD1^{G93A} mouse at P30 are shown in **Figure 6.2**. MR spectra of the time-evolution of neurometabolites in the hindbrain of SOD1^{G93A} mice is presented in **Figure 6.3**.

Two-way ANOVA tests for each 16 neurometabolites showed significant interactions in the motor cortex and the hindbrain of the SOD1^{G93A} mice. The neurometabolic changes observed in SOD1^{G93A} mice and the comparison to WT mice are shown in **Figure 6.4** (hindbrain) and **Figure 6.5** (motor cortex). In the motor cortex, significant interactions were found for glutamate ($F = 3.0$, $P < 0.01$), taurine ($F = 4.7$, $P = 0.0002$) and NAA ($F = 6.4$, $P < 0.0001$). As for the hindbrain, significant interaction of the two factors were found for creatine ($F = 13.6$, $P < 0.001$), GABA, ($F = 3.3$, $P = 0.0044$), glutamate ($F = 4.1$, $P = 0.0009$), glutamine ($F = 4.2$, $P < 0.001$), mIns ($F = 4.1$, $P < 0.001$), and NAA ($F = 4.2$, $P = 0.0008$). For the metabolites, which showed significant interaction, data were further analyzed by one-way ANOVAs separately in SOD1^{G93A} mice and WT mice to evaluate influences of animal age for each brain region.
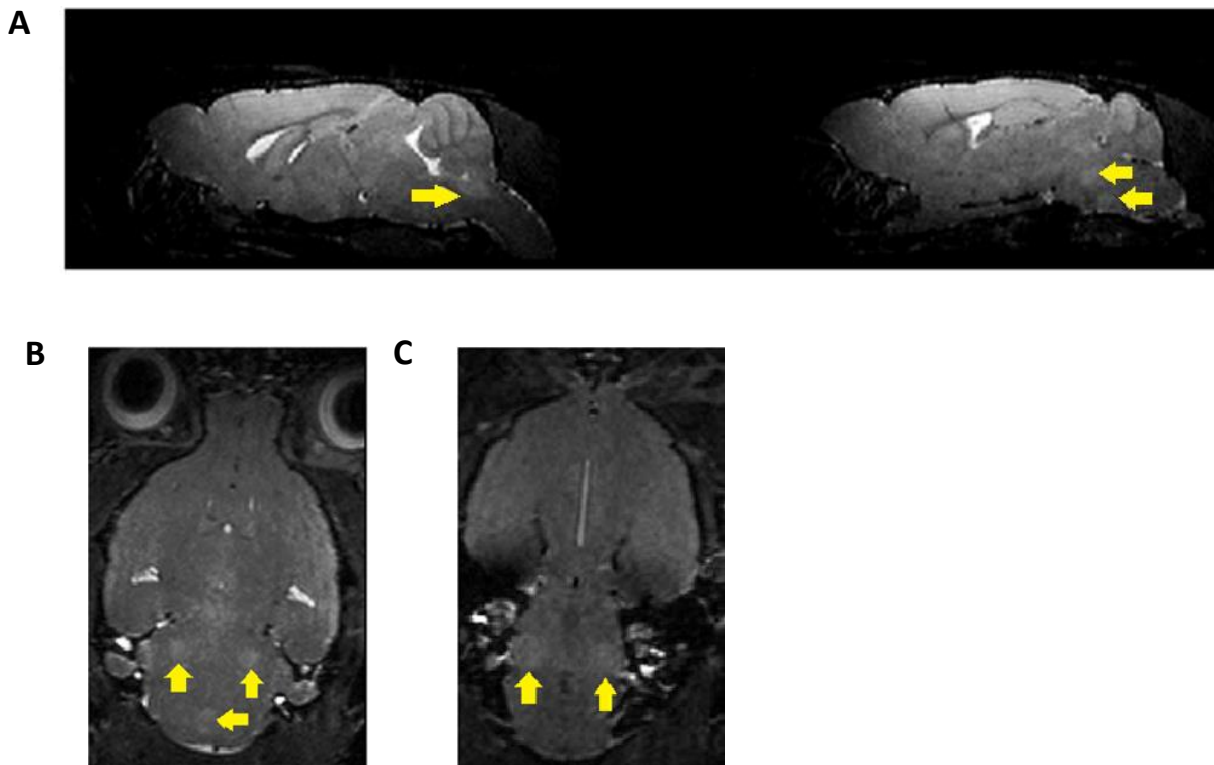
Figure 6.1 T2-weighted MRI Sections showing hyperintense regions in SOD1^{G93A} miceT2-weighted MRI showing hyperintense contrast in the brainstem region compared to surrounding regions in a 140 day old SOD1^{G93A} mouse. (**A**) Left: Sagittal sections: arrow shows hyperintensity in the brainstem nucleus Nc. XII (hypoglossal). Right: Sagittal sections: arrows show hyperintensities in the brainstem nuclei Nc V (trigeminal), Nc VII. (**B**) Coronal section: white arrows show bilateral hyperintensities in Nc V (trigeminal). Yellow arrow: hyperintensity in Nc XII (hypoglossal). (**C**) Coronal section: arrows show bilateral hyperintensities in Nc VII (facial).

In the motor cortex of SOD1^{G93A} mice, age-dependent effects were found for the excitatory neurotransmitter glutamate, neuronal marker NAA and the neurotransmitter modulator taurine. Decreases in glutamate ($P < 0.05$) and NAA ($P < 0.0001$) concentrations around P120 as well as a continuous increase in taurine from P90 ($P < 0.05$) were found. The increase in taurine concentration was significant ($P < 0.001$) between the two groups at P110 (**Figure 6.5**). In the hindbrain of SOD1^{G93A} mice, a significant ($P = 0.001$) age dependent decrease in creatine levels were found at P110. However, the levels of creatine were significantly ($P < 0.0001$) different between SOD1^{G93A} and WT around P70. A significant ($P < 0.0001$) decrease of glutamine was observed at early-symptomatic stage (P110). For the inhibitory neurotransmitter GABA, a significant ($P < 0.0001$) increase was found at P90 and a significant ($P = 0.0110$) decrease of NAA concentration was detected at P120. Also, a significant ($P < 0.0001$) decrease in the glutamate and an increase of the inflammation/glial marker myo-inositol ($P < 0.0001$) were found at P140. The mean concentrations of glutamate and taurine were significantly higher (41.2%, 118.5%, respectively) in the motor cortex than in the hindbrain for both groups (**Figure 6.6**). A 3-time point summary of the significant neurometabolite concentrations in both regions for SOD1^{G93A} and WT is presented in **Table 6.1**. To further analyze the dependence between the altered neurometabolite concentrations in the motor cortex and hindbrain, Pearson correlation coefficients (r) were calculated using all seven time points for SOD1^{G93A} mice (**Figure 6.7** and **Figure 6.8**). Strong

correlations were observed for NAA and glutamate in the motor cortex and brainstem ($r = 0.968$, $P = 0.0003$; $r = 0.915$, $P = 0.0038$, respectively). Also in the motor cortex, significant negative correlations were found between NAA and taurine ($r = -0.785$, $P = 0.036$) and between glutamate and taurine ($r = -0.758$, $P = 0.048$). In the hindbrain, strong correlation was seen between NAA and creatine ($r = 0.983$, $P < 0.0001$), NAA-glutamate ($r = 0.947$, $P = 0.0041$), between NAA and myo-inositol ($r = -0.905$, $P = 0.0050$), and between glutamate and creatine ($r = 0.889$, $P = 0.0074$).
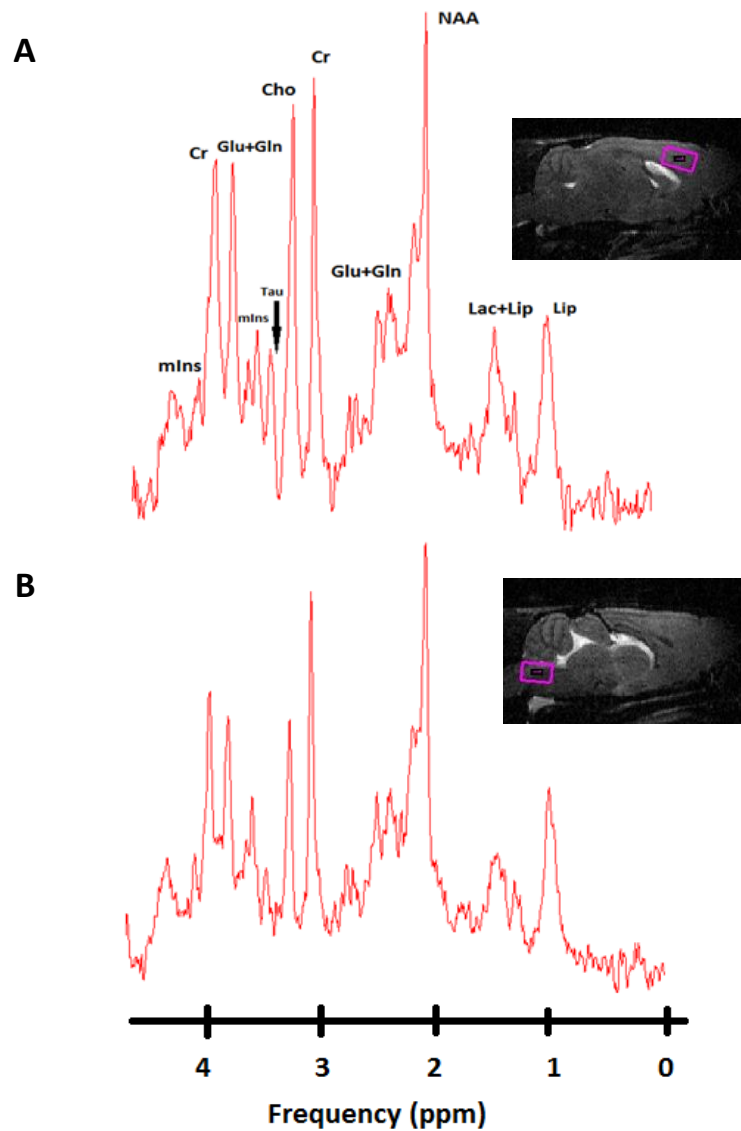
Figure 6.2. [1]H-MR spectra of the motor cortex and hindbrain of a SOD1[G93A] mouse 30 days postpartum acquired at 9.4 Tesla. (**A**) *In vivo* [1]H-MR spectra acquired from the motor cortex and (**B**) hindbrain of a SOD1[G93A] mouse with labelled visible neurometabolite peaks. Right images show the voxel localization in both regions (2x2.5.x1.5 mm[3]). *Abbreviations*: *Lip, lipid; Lac, lactate; NAA, N-acetylaspartate; Glu, glutamate; Gln, glutamine; Cr, creatine; Cho, choline; Tau, taurine; mIns, myo-inositol.*
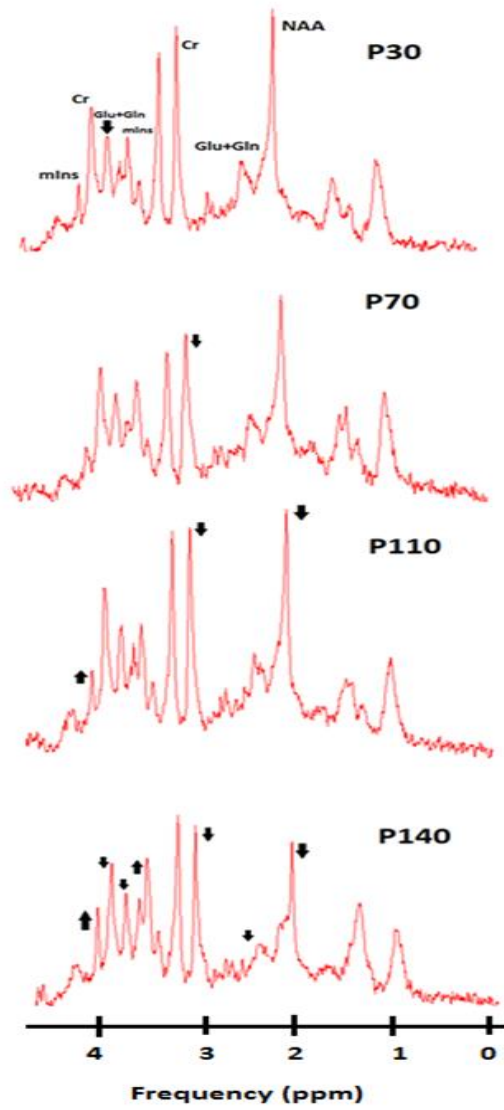
Figure 6.3. MR spectra illustrating the evolution of neurometabolites in the hindbrain of SOD1[G93A] mice. Hindbrain [1]H-MR spectra of postpartum day 30, 70, 110, and 140 of a single SOD1[G93A] mouse are shown. Arrows depict changes in signal intensities during the four time-points.
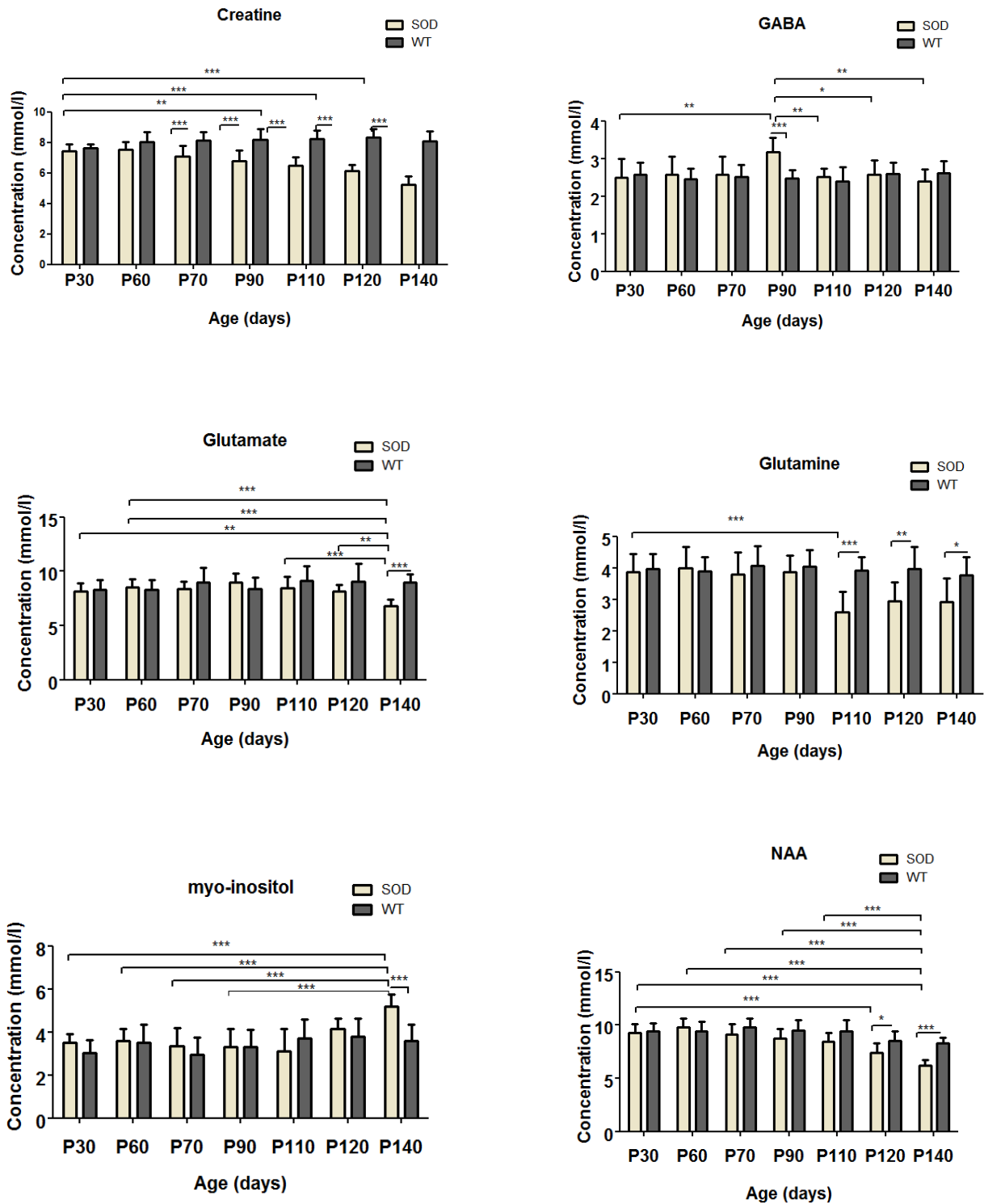
Figure 6.4. Absolute Concentrations of creatine, γ-aminobutyric acid (GABA), glutamate, glutamine, myo-inositol, and N-acetyl aspartate (NAA) in the hindbrain of SOD1[G93A] and WT mice. Concentrations of creatine, γ-aminobutyric acid (GABA), glutamate, glutamine, myo-inositol, and N-acetyl aspartate (NAA) in the hindbrain of SOD1[G93A] (n = 10) and age-matched wild-type mice (n = 10) at 30, 60, 70, 90, 110, 120, 140 days postpartum were determined relative to the unsuppressed water signal from the same voxel. Statistical significances between the two groups and mean concentrations within each group are shown. Concentration values are presented as mean ± SD; *$P < 0.05$, **$P < 0.01$, ***$P < 0.001$
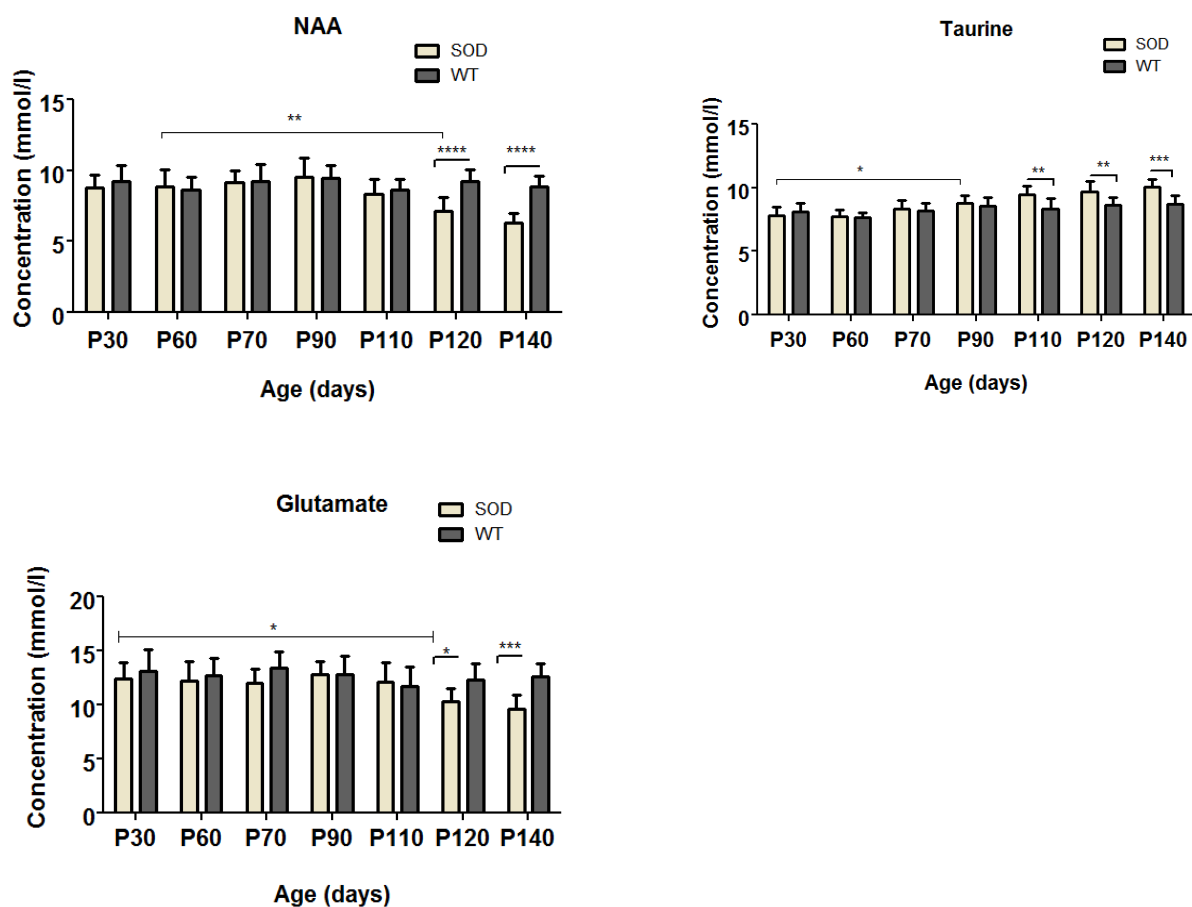
Figure 6.5. Absolute Concentrations of NAA, taurine and glutamate in the motor cortex of SOD1[G93A] and WT mice. Concentrations of NAA, taurine and glutamate in the motor cortex of SOD1[G93A] (n = 10) and age-matched wild-type mice (n = 10) at 30, 60, 70, 90, 110, 120, 140 days postpartum were determined relative to the unsuppressed water signal from the same voxel. Statistical significances between the two groups and mean concentrations within each group are shown. Concentration values are presented as mean ± SD; *P < 0.05, **P < 0.01, ***P < 0.001

Table 6.1: Summary of metabolite concentrations of SOD and WT mice

| | | | Metabolite Concentration (mean±S.D in mmol/l) | | | | | | |
Model	Age	Location	NAA	tCr	Glu	Gln	mIns	Taurine
SOD	P30	Hindbrain	9.27±0.79	7.45±0.43	8.15±0.73	3.87±0.57	3.50±0.39	2.23±0.32
		Motor cortex	8.77±0.88	6.68±0.79	12.38±1.50	3.01±0.44	2.02±0.47	7.82±0.65
WT		Hindbrain	9.42±0.74	7.40±0.20	8.30±0.87	3.97±0.47	3.04±0.57	1.89±0.85
		Motor cortex	9.21±1.12	7.21±0.72	13.14±1.98	3.54±0.32	2.15±0.76	8.12±0.57
SOD	P110	Hindbrain	8.48±0.81	6.47±0.61	8.47±1.05	2.59±0.64	3.10±1.03	2.50±023
		Motor cortex	8.93±0.78	7.11±0.65	13.05±0.87	3.23±0.35	2.24±0.36	9.45±0.70
WT		Hindbrain	9.43±1.02	8.22±0.59	9.13±1.29	3.54±0.36	3.24±0.59	2.45±0.14
		Motor cortex	8.84±0.92	7.68±0.53	11.68±1.80	3.10±0.42	1.97±0.89	8.35±0.84
SOD	P140	Hindbrain	6.22±0.49	5.23±0.57	6.77±0.61	2.91±0.75	5.20±0.55	2.36±0.13
		Motor cortex	6.29±0.73	6.68±0.79	9.62±1.26	3.21±0.33	2.32±0.61	10.03±0.63
WT		Hindbrain	10.05±0.58	7.89±0.78	9.24±0.74	3.34±0.42	3.45±0.72	2.01±0.35
		Motor cortex	9.21±0.47	7.45±0.87	12.85±0.84	3.12±0.25	2.04±0.63	8.73±0.65
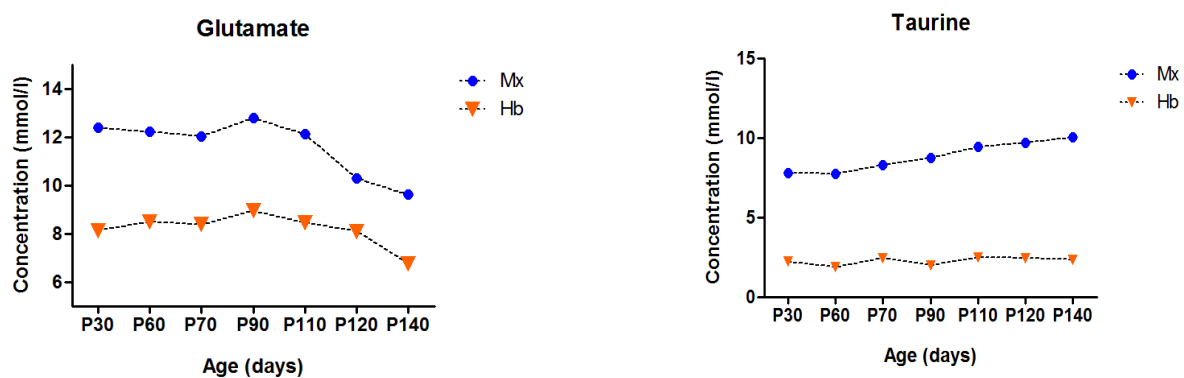
Figure 6.6. Absolute concentrations of glutamate, taurine in hindbrain and motor cortex of SOD[G93A] mice. Comparison of mean concentrations of glutamate, taurine in hindbrain and motor cortex of SOD1[G93A] (n = 10) at 30, 60, 70, 90, 110, 120, 140 days postpartum. *Abbreviations: Mx. Motor cortex; Hb, hindbrain.*
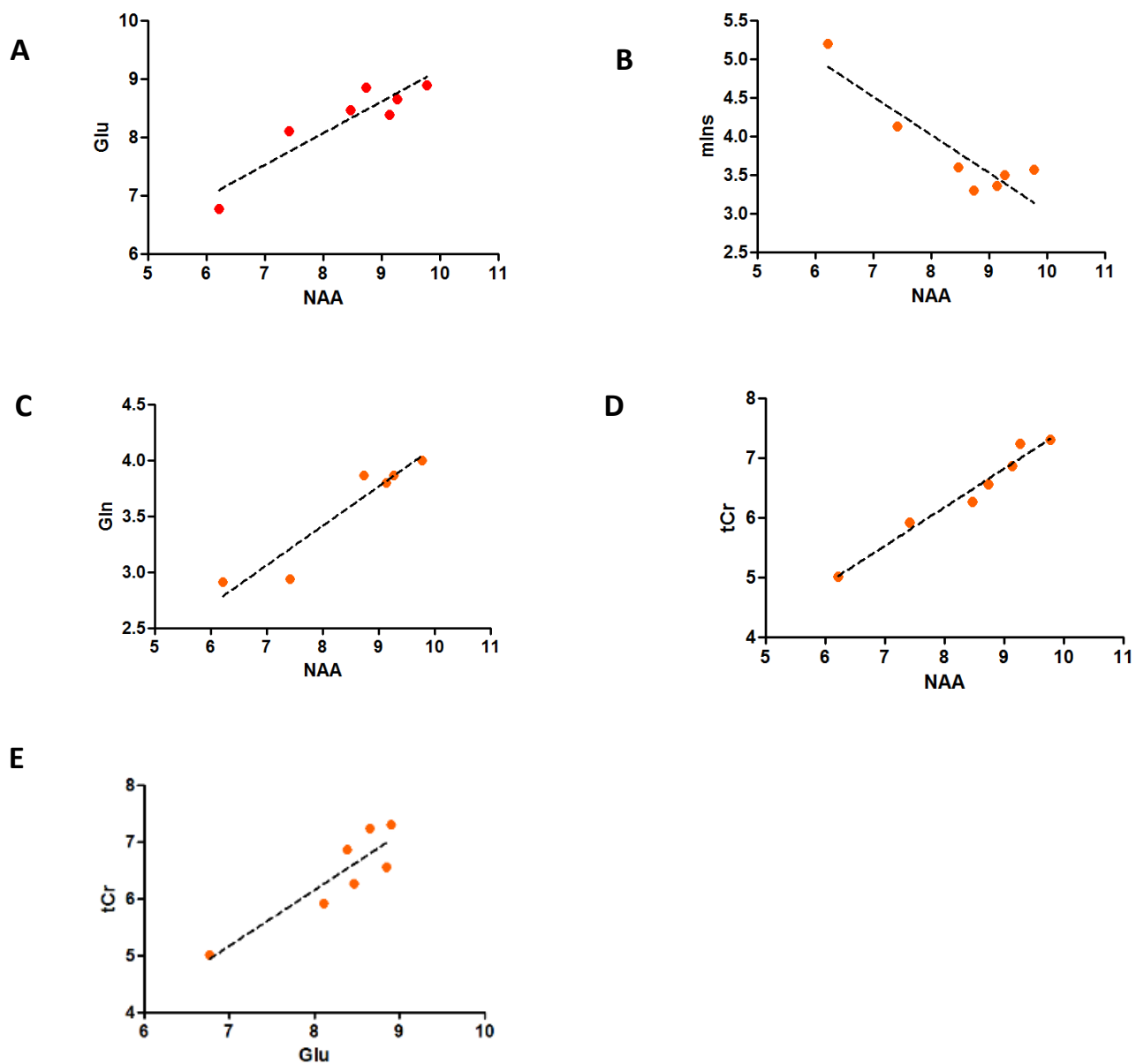
Figure 6.7. Correlation between neurometabolite concentrations in SOD1^{G93A} hindbrain. Correlation between neurometabolite concentrations in the hindbrain of SOD1^{G93A} mice for all time-points (30, 60, 70, 90, 110, 120, 140 days postpartum). **(A)** Correlation of glutamate and NAA concentrations through life-span. The slope in linear fit is shown by the dashed black line (R^2 = 0.837). **(B)** Correlation between myo-Inositol versus NAA concentrations (R^2 = 0.819). **(C)** Relation between glutamine and NAA concentrations (R^2 = 0.898). **(D)** Correlation between creatine and NAA concentrations (R^2 = 0.965). **(E)** Correlation between creatine and glutamate (R^2 = 0.791) concentrations. *Abbreviation: NAA, N-acetylaspartate; tCr, total creatine; mIns, myo-inositol; Glu, glutamate;*
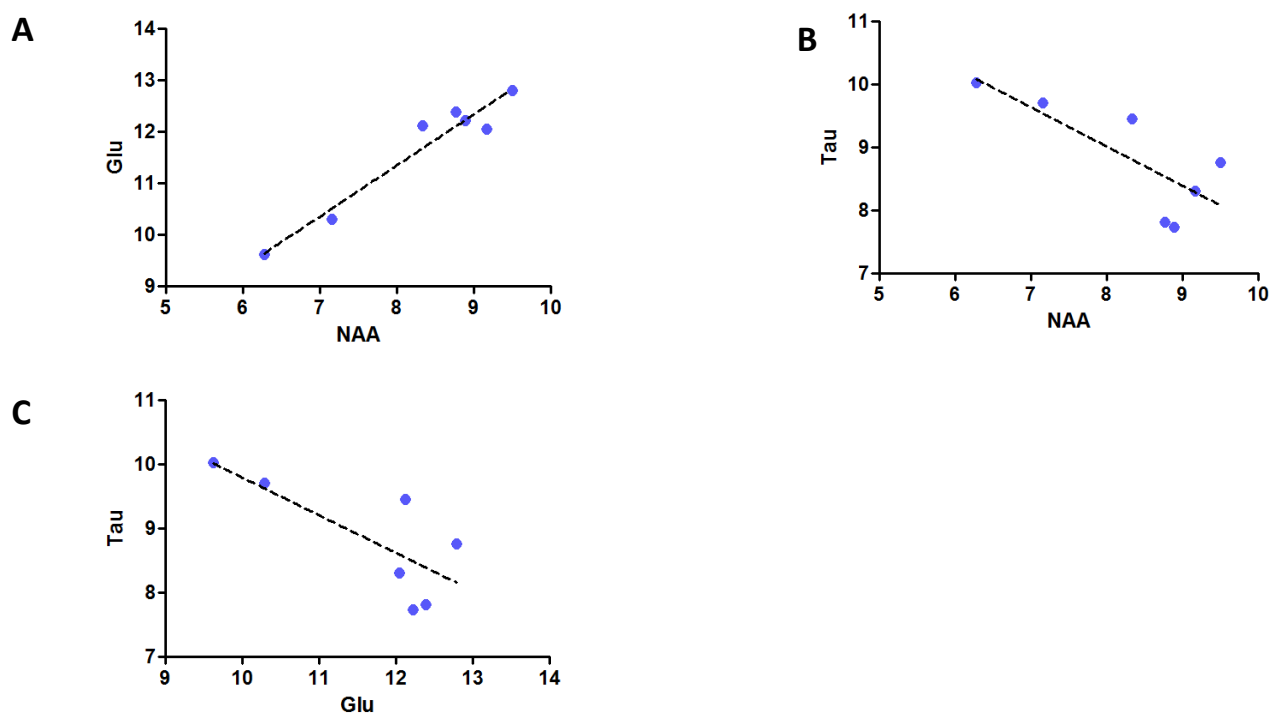
Figure 6.8. Correlation between neurometabolite concentrations in SOD1^G93A motor córtex. Correlation between neurometabolite concentrations in SOD1^{G93A} motor cortex for all time-points (30, 60, 70, 90, 110, 120, 140 days postpartum). (**A**) Correlation between glutamate and NAA (R^2 = 0.938). (**B**) Correlation between taurine and NAA (R^2 = 0.616). (**C**) Correlation between taurine and glutamate (R^2 = 0.575). *Abbreviation: NAA, N-acetylaspartate; Glu, glutamate; Tau, taurine.*

6.4.3   Development of Symptoms

In this first experiment, SOD1^{G93A} mice developed tremors in the hind-limbs between P90 and P100, and gait impairment around P115. Interestingly, in all animals an early and increasingly pronounced effect on left hind-limb tremors and dysfunction was detected. Total paralysis of both hind-limbs were detected between P140 and P150, reaching the endpoint of the disease.

6.4.4   Effect of Coconut oil diet on motor performance in SOD1^{G93A} Mice

In a second experiment, animals were treated with a virgin coconut oil diet starting from 72 days of age. These animals were compared with animals receiving standard food. The diet had the following effects on SOD mice:

I. Body weight: Coconut oil diet had a significant net positive effect on retention of body weight at 90 (*P* < 0.001), 110 (*P* < 0.0001) and 130 (*P* < 0.0001) days of age compared to the mice fed with a normal diet (**Figure 6.9 A**).

II. Motor performance: Better motor performance was recorded in the treated group on week 14, 15 and 16 (P = 0.001, P = 0.0001, P = 0.0001) when compared to normal diet group (**Figure 6.9 B**).

III. Survival: Coconut oil diet extended the mean survival by 11% (164.7 ± 5.4 days for coconut oil-fed versus 147.2 ± 3.3 days for normal fed, P < 0.0001, n=6) (**Figure 6.9 C**).
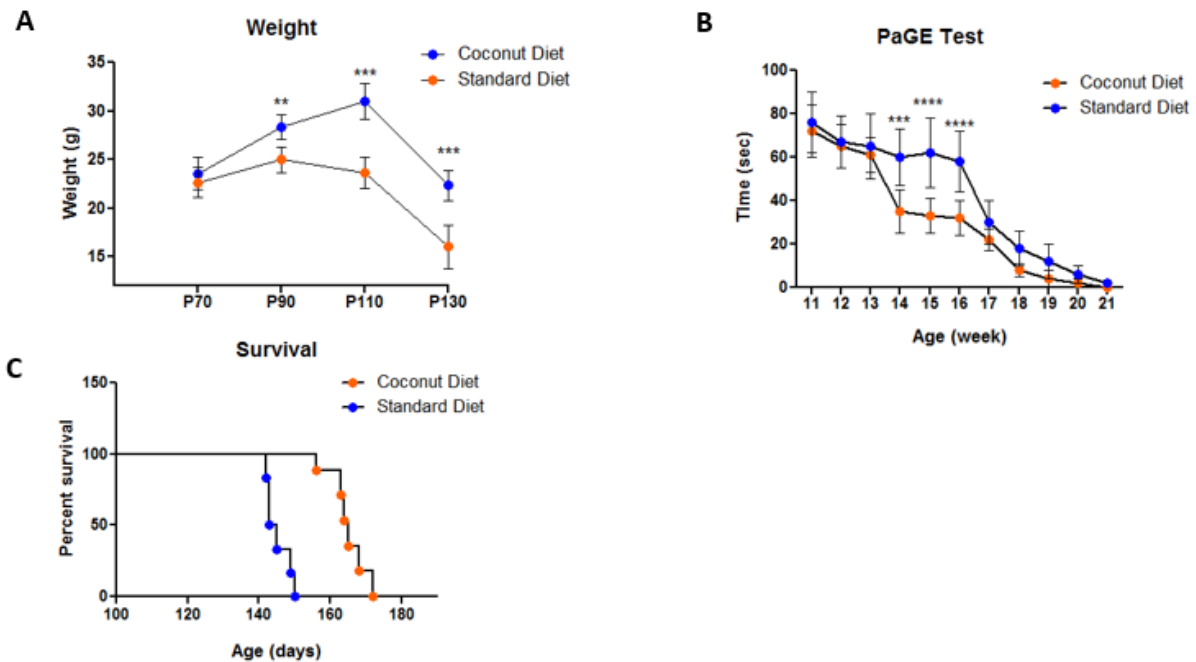
Figure 6.9. Effect of the coconut oil diet on SOD1^{G93A} mice. (**A**) The effect of the coconut oil diet on weight in SOD1^{G93A} mice at the beginning of treatment (Day 70), day 90, day 110 and day 130 of the study. Coconut oil fed group had significant net positive effect on retention of body weight during P90 ($P < 90$), P110 ($P < 0.001$) and P130 ($P < 0.0001$). (**B**) The PaGE test showed better motor performance in the coconut oil diet group on week 14, 15 and 16 ($P < 0.001$, $P < 0.0001$, $P < 0.0001$, respectively), compared to the standard diet group. (**C**) Kaplan-Meier survival plot of the study groups. SOD1^{G93A} mice on coconut oil diet displayed significantly prolonged survival (13.6%) compared to standard diet animals (p < 0.0001). Data = mean ± SD; Coconut oil diet group: n = 6, standard diet group: n = 6. **$P < 0.01$, ***$P < 0.001$, **** $P < 0.0001$

6.4.5   Effects of Coconut Oil diet on Neurometabolites and MRI

MR spectra were acquired at baseline (P70) and P120 for both coconut oil and standard diet groups. We examined the changes in neurometabolite concentrations in the hindbrain within and among the two groups. Compared to the baseline, stable (no significant changes) metabolite levels were estimated at the late time point (P120) for the coconut oil fed group (**Figure 6.10 A**). In contrast, the previously observed pattern of changes in neurometabolite levels (see first experiment) were observed for creatine ($P < 0.05$) and NAA ($P < 0.05$) in the standard diet group (**Figure 6.10 B**). Even though the neurometabolite concentration for NAA was not significantly different when comparing the coconut oil treated group with the standard diet mice at P120 (**Figure 6.10 C**), the levels were higher on average (8.6±2.2 for coconut oil treated group vs. 7.6±1.2 for standard diet group, respectively). Creatine

concentrations for the treated group were significantly higher ($P < 0.05$) at P120 compared to the standard group (7.1±1.3 vs. 5.60±1.2 respectively).
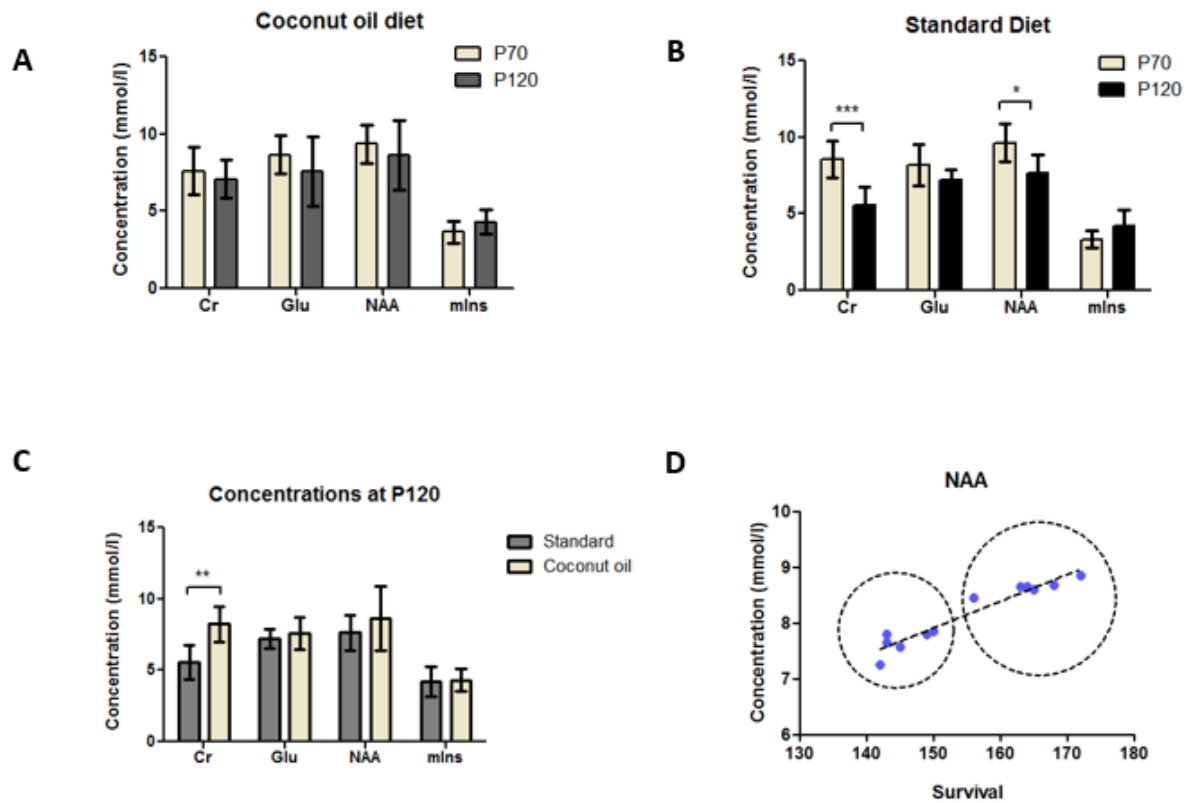
Figure 6.10. The effects of coconut oil supplementation on hindbrain neurometabolite levels of SOD1[G93A] mice assessed with ^{1}H-MRS. (**A-B**) *In vivo* MRS neurometabolite profiles of standard diet group and coconut oil diet group at day 70 and day 120. Significant decrease in creatine and NAA was found for the standard diet group between 70 and 120 days ($P < 0.001$, $P < 0.005$ respectively). No significant changes in neurometabolites were found for the coconut oil diet group between day 70 and day 120. (**C**) Comparison of the two groups at P120. Significant decrease in creatine was found for the standard diet group ($P < 0.01$) compared to the coconut oil diet group. (**D**) A highly significant ($P < 0.0001$) correlation ($R^2 = 0.922$) between the survival and the hindbrain NAA levels was seen for the two groups. Dotted circles highlight the standard diet and coconut oil diet groups.

6.5 DISCUSSION

MRI and MRS have been applied to monitor ALS progression and treatment response in both humans as well as transgenic ALS mouse models (Wang *et al.*, 2011; Kumar *et al.*, 2013; Verstraete *et al* 2015). In the present study, we employed *in vivo* MRI and MRS to monitor the disease onset and progression

in the SOD1[G93A] mouse model. Furthermore, we conducted a small-scale PoC study to assess the potential neuroprotective effect of coconut oil diet in SOD1[G93A] mice.

To the best of our knowledge, only three studies have examined the SOD1[G93A] neurometabolic changes utilizing *in vivo* MRS and/or *ex vivo* high resolution NMR spectroscopy (Andreassen *et al.*, 2001; Choi *et al.*, 2010; Niessen *et al.*, 2007). Two of the studies also examined the possible beneficial effects of dietary creatine supplementation in the same mouse model. The set up and results of the above mentioned studies are summarized in the (**Supplementary Table 1**). Our study revealed significant changes in the hindbrain and motor cortex of SOD1[G93A] mice. While some observations are consistent with previous studies, our findings also indicate some dissimilar patterns.

6.5.1   T2-weighted MRI and SOD1[G93A] brainstem pathology

Previously it was shown that in SOD1[G93A] mice, spinal cord motor neurons and lower motor nuclei are the most vulnerable structures for degeneration (Niessen *et al.*, 2006; Niessen *et al.*, 2007). Consequently, it is reasonable to assume that neurometabolic changes occurring in those motor nuclei during the life-span of this mouse model (Kong *et al.*, 1998). Using T2-weighted MR imaging Niessen *et al* (Niessen *et al.*, 2004) showed clear signal intensity enhancement compared with surrounding tissue in various motor nuclei within the brainstem of SOD1[G93A] mice, including the hypoglossal nucleus (Nc. Nv XII), nucleus ambiguus (Nc. Nv IX, X), facial nucleus (Nc. Nv VII), and trigeminal nucleus (Nc. Nv V). Using T2-weighted MR images, we observed similar increased contrast in the SOD1[G93A] brainstem motor nuclei V (trigeminal), VII (facial), and XII (hypoglossal) compared to WT mice. Trigeminal and hypoglossal nuclei are shown to be two key motor components involved in mastication (chewing) and licking behaviors of mice (Hillel *et al.*, 1989; Zang *et al.*, 2004).

In our previous studies with this model, we observed impaired chewing and licking behavior through the progressive decline in body weight and food consumption of SOD1[G93A] mice. Caron *et al* demonstrated that the hyperintensities in T2-weighted MRI of the brainstem region are associated with the formation of vacuoles rather than the loss of motor neurons (Caron *et al.*, 2015). In fact, vacuolization is one of the initial signs of motor neuron changes in SOD1[G93A] (Higgins *et al.*, 2013). Vacuolization, which is primarily due to abnormal and swollen mitochondria, has been observed as early as one month of age in dendrites and proximal axons of spinal motor neurons (Kong *et al.*, 1998; Bendotti *et al.*, 2001), before the loss of motor nuclei and the appearance of a glial reaction (Bendotti *et al.*, 2005).

6.5.2   [1]H-MR spectroscopy

Our study implies MR detectable involvement of the hindbrain and motor cortex in the course of the disease seen as significant changes in SOD1[G93A] neurometabolite concentrations. Some of these significant changes in the hindbrain region of SOD1[G93A] mice are in accordance with previous observations by Niessen *et al.* (Niessen *et al.*, 2007) and Choi *et al.* (Choi *et al.*, 2010) using the same mouse model. Niessen *et al.* observed a decrease in glutamine at P90, a decrease in NAA and glutamate at P120. Choi *et al.* also reported a decrease in NAA at P142 as well as a trend towards decreasing glutamate. Furthermore, they reported an increase in inflammation/glial marker myo-inositol between

P110 and P142. We observed a decrease in glutamine at P110 and a decrease in NAA, glutamate at P120 and P140, respectively. Similar to Choi *et al.*, we also observed an increase in myo-inositol around P140. However, our results show somewhat different patterns from those observed in those previous studies. For instance, unlike Andreassen *et al.* and Choi *et al.* (Andreassen *et al.*, 2001; Choi *et al.*, 2010), we did not observe neither an increase in glutamate and glutamine at the early disease stages nor an increase in glutamine at end stage. Concerning the neuronal marker NAA, we were unable to confirm the early decrease of NAA in the brainstem at P75 as was reported by Niessen *et al.* Apart from the above mentioned differences, we were able to find significant neurometabolite changes in both the motor cortex and hindbrain regions that were not previously described in the SOD1[G93A] animal model.

6.5.3 Decreased NAA and glutamate in the motor cortex of SOD1[G93A] mice

Reductions in the neuronal marker NAA have been reported in the motor cortex of individuals with ALS (Block *et al.*, 1998; Bradley *et al.*, 1999; Gredal *et al.*, 1997). The most common finding reported in *in vivo* MRS studies of ALS patients is also the reduction of the neuronal marker NAA in the motor cortex, which is generally interpreted as neuronal loss (Agosta *et al.*, 2010; Rule *et al.*, 2004). Our results show decreased NAA levels at the end stages between P120 and P140. However, since NAA is synthesized in neuronal mitochondria, changes in NAA levels could also reveal mitochondrial dysfunction (Clark *et al.*, 1998; Vielhaber *et al.*, 2001). Furthermore, our study shows decreased glutamate levels in the motor cortex of SOD1[G93A] mice around P120 and P140, which was not previously reported for this model.

Glutamate is the main excitatory neurotransmitter in the brain, though higher extracellular glutamate is associated with several neurodegenerative diseases including ALS. Previous MRS studies in patients, using low magnetic field strengths (1.5 or 3 Tesla) have reported variable results on glutamate concentrations in patients with ALS (Bradley *et al.*, 1999; Bowen *et al.*, 2000; Block *et al.*, 1998; Han *et al.*, 2010). However, a recent study by Atassi *et al* (Atassi *et al.*, 2017), using a higher magnetic field (7 Tesla) reported decreased glutamate levels in the motor cortex of ALS patients compared to healthy controls.

6.5.4 Increased taurine in the motor cortex of SOD1[G93A] mice

In the motor cortex, age-dependent concentration changes were found for taurine in SOD1[G93A] mice. An age-dependent increase in taurine started at around P90 and became significant at P110 compared to WT mice. Niessen *et al.* also reported increased taurine levels in the motor cortex at P90, however, the changes were similar in both SOD1[G93A] mice and control mice (Niessen *et al.*, 2007). Our finding of increased taurine levels is in agreement with studies in postmortem ALS patients, where higher levels of taurine were detected in the brain and spinal cord (Yoshino *et al.*, 1979; Perry *et al.*, 1987; Malessa *et al.*, 1991). Taurine is a non-essential amino acid whose exact function is unclear. However, it has been proposed as a modulator of neurotransmitter action, where it is shown to exert an inhibitory effect (Curtis *et al.*, 1965). Jung *et al.* reported that SOD1[G93A] mice have higher levels of brain taurine and higher expression of the taurine transporter, TauT (Jung *et al.*, 2013). Evidently, expression of this transporter increases under oxidative stress and is controlled by the heat shock factor 1 protein.

Increased expression of taurine transporters and uptake of taurine in motor neurons in ALS could be a compensatory mechanism (Jung *et al.*, 2013).

6.5.5   Increased GABA in the hindbrain of SOD1[G93A] mice

Around P90, or in the early symptomatic stage we observed an increase in GABA levels in the hindbrain which normalized thereafter and remains stable. Imbalance of GABA has been implicated to play an important role in the pathogenesis of ALS. GABA is produced by decarboxylation of glutamic acid, catalyzed by the glutamic acid decarboxylase enzyme (Petroff *et al*, 2002). Therefore, an increase in GABA could have a pathological implication in reversing glutamate excitotoxicity and thereby act as a protective mechanism against cell damage. Along this mechanism, pharmacological agents that increase the levels of GABA such as baclofen and gabapentin have been suspected to be beneficial in treating ALS. The reason for our observation of GABA levels normalizing after P90 and remaining stable until P140 is currently unclear. Although the continuous reduction of glutamate and glutamate levels starting at around P110 may trigger a compensatory GABA level increase which longitudinally appears stable compared to other metabolites. However, *in vivo* GABA detection by ^{1}H-MRS, even at higher magnetic field strengths, presents significant challenges arising from the low brain concentration, overlap with more intense resonances and contamination by mobile macromolecule signals (Pfeuffer *et al.*, 1999). Therefore, caution must be taken in interpreting MRS-GABA results.

6.5.6   Gradual decrease in total creatine levels in the hindbrain of pre-symptomatic SOD1[G93A] mice

^{1}H-MRS detectable creatine constitutes of creatine and phosphocreatine (total creatine), which are indistinguishable at magnetic field strengths of 9.4 T and below (Sartoriua *et al.*, 2008). Creatine plays a major role in maintaining ATP levels constant in cells with high and unstable energy demands (Rae *et al.*, 2015; Gasparovic *et al.*, 2009). In MRS, creatine is frequently used as an internal reference since it is considered stable even under most pathological conditions. However, clinical MR spectroscopic studies reported that early and progressive reduction of total creatine levels in the striatum is associated with the onset and progression of Huntington's disease (Sanchez-Pernaute *et al.*, 1999; Reynolds *et al.*, 2005). In our study, we observed a gradual decrease in creatine levels in the SOD1[G93A] hindbrain starting between P60 and P90. The decrease was clearly evident in all ten SOD1[G93A] mice (**Supplementary Figure S3**). Our finding of decreased creatine level in the hindbrain of SOD1[G93A] mice may indicate a hyper-metabolic environment in the motor nuclei region. In a recent publication, Atassi *et al.* (Atassi *et al.*, 2017) observed a decrease in creatine in the left precentral gyrus of ALS patients compared to healthy controls. In ALS, a hyper-metabolic state in the hindbrain may possibly occur due to the imbalance of glutamate-glutamine cycle. Increased glutamate/glutamine levels have been reported in the medulla of ALS patients (*Pioro et al.*, 1997). Therefore, a possible pathway could be that enhanced excitatory neurotransmitter release leads to the hyper-metabolism of the hindbrain of SOD1[G93A] mice, which results in an overconsumption of creatine. An imbalance in supply-demand in creatine levels may threaten the viability of the neuronal cells and hence make them susceptible to degeneration. However, further investigations are needed to support this hypothesis. On the contrary, *in vitro* NMR studies using

brainstem extracts from SOD1^{G93A} mice, reported stable creatine levels (Niessen *et al*., 2007; Choi *et al*., 2010). One reason for this disagreement could be the brain extracts used in the *ex vivo* experiments covered a larger volume compared to the smaller voxel size (7.5 mm^3) used in our *in vivo* MRS experiments. Since mainly the motor nuclei are affected in the brainstem, homogenization of brain extracts from a larger region may mask the detection of subtle changes in neurometabolites in those affected areas. In addition, biological variability, sample preparation technique and signal acquisition/ processing parameters might also influence the precision and accuracy of *ex vivo* measurement of neurometabolites.

6.5.7 Increased myo-inositol in the hindbrain of SOD1^{G93A} mice

We were able to detect a significant increase in the glial marker myo-inositol in the hindbrain of SOD1^{G93A} mice from around P140. This finding is consistent with the observation of Choi *et al.* where they observed an increase in myo-inositol in the medulla between 110-142 days (Choi *et al*., 2010). Furthermore, similarly MRS studies with ALS patients have also shown increased myo-inositol (Block *et al*., 1998; Bowen *et al*., 2000; Kalra *et al*., 2006; Foerster *et al*., 2014; Atassi *et al*., 2017).

Correlation analyses between the neurometabolites in the hindbrain and motor cortex indicate that the factors regulating the levels of these metabolites may be interrelated. However, definite interpretations of the biological significance of these interrelations remain to be elucidated.

6.5.8 Coconut Oil Diet Improved Motor Performance and Increased Survival in SOD1^{G93A} mice

The influence of dietary factors in ALS progression has been a focus of previous research (Cacabelos *et al*., 2014). It is well accepted that malnutrition is indeed a negative prognostic factor in ALS (Greenwood *et al*., 2013). Furthermore, the 'ALS Untangled' study reported that saturated fatty acids, such as those present in coconut oil, could alleviate the disease progression by means of increasing energy bioavailability towards mitochondrial pathways (ALS Untangled 2012). Extracted from the meat of coconuts, coconut oil comprises 2.5% of world vegetable oil production (Hamid *et al*., 2011; ALS Untangled 2012). It is available in a basic "virgin" form, and also as an "RBD" (refined, bleached and deodorized) form, which has no coconut aroma or taste. Coconut oil can be fractionated into different medium-chain fatty acids; fractionated coconut oil is sometimes referred to as medium chain triglyceride (MCT) oil (ALS Untangled 2012).

6.5.9 Coconut oil as compensation for mitochondrial dysfunction in ALS

Mitochondrial dysfunction is likely to play an important role in ALS pathophysiology (Martin *et al.,* 2011). Among the mitochondrial dysfunctions identified, cells extracted from patients with ALS show decreased complex-I activity, which contribute to impaired energy production (Swerdlow *et al*., 1998). MCT in coconut oil are converted in the liver into ketone bodies. In cultured neurons treated with drugs impairing complex 1 function, the addition of ketone bodies can restore complex 1 function (Tieu *et al*., 2003). Therefore, consumption of coconut oil and thereby raising ketone body levels may help

compensate for mitochondrial dysfunction and impaired energy production in patients with ALS. Alternatively, there is growing evidence suggesting that nutritional status (Desport *et al.*, 1999) and lipid metabolism (Dorst *et al.*, 2011) are important prognostic factors in patients with ALS. In that context, coconut oil could possibly slow the disease progression by acting as a high caloric reservoir that increases circulating lipids.

6.5.10 Proof of concept study: coconut oil as a dietary treatment for SOD1[G93A] mice

One major finding of our study is that coconut oil supplemented diet demonstrated improved motor function in SOD mice on PaGE test compared to animals receiving standard diet during weeks 14 to 16. The coconut oil diet group showed 13.5% extended survival compared to the standard diet group. T2-weighted MR images acquired at P120 showed typical hyperintensities in the hypoglossal nucleus for animals receiving standard diet, which is less pronounced for animals of the coconut oil group (**Supplementary Figure S2 A**). T2-relaxometry maps from the hypoglossal nucleus confirmed increased T2-values for the standard diet group compared to the coconut oil group (**Supplementary Figure S2 B, C**). MRS data showed a stable neurometabolic profile in mice receiving a coconut oil supplemented diet compared to mice receiving standard diet at P120. Also we observed a significant ($P < 0.0001$) positive correlation ($r = 0.88$) between survival and NAA concentrations (**Figure 6.9D**), where the coconut oil group showed higher levels of NAA and extended survival. Kalra *et al.* showed that impaired neuronal integrity (decreased NAA) in the motor cortex negatively correlates with survival in ALS (Kalra *et al.*, 2006). Therefore, improved NAA levels are a possible biological marker for vital prognosis in ALS. However, we cannot exclude the fact that a general improvement of the dietary state (instead of ketone bodies supplemented with the coconut oil) can also contribute to the improved survival and motor function.

6.6   CONCLUSION

In conclusion, MR images of SOD1[G93A] mice between 90 and 140 days revealed clear signal intensity enhancements compared to surrounding tissue in specific motor nuclei within the hindbrain, which are not detectable in age-matched WT mice. MRS evaluation of neurometabolic profiles revealed biochemical alterations in the motor cortex and hindbrain of transgenic ALS SOD1[G93A] mice. In a PoC study, we have demonstrated that coconut oil supplementation added to a standard rodent diet improved motor function, delayed neurological deficits, extended survival and was reflected by the absence of neurochemical changes otherwise seen in age matched animals of the SOD1[G93A] mouse model. Thus the study provides experimental evidence that prophylactic treatment with coconut oil diet may slow motor deterioration and protect motor neurons in SOD1[G93A] mice. Our initial results suggest that the neuroprotective effect by coconut oil may provide beneficial effects in ALS through a dietary intervention. Although promising, it is important to note that this was a pilot study, and more research is needed to validate these preliminary results. Finally, our study confirms that degeneration of neurons in the brainstem may indeed contribute significantly to the onset and overall disease progression in the SOD1[G93A] ALS model. Therefore, therapeutic trials in this mouse model should evaluate the beneficial effects to brainstem motor neurons. Furthermore, we confirm that ^{1}H-MRS technique has the potential to be a used as diagnostic and a therapy monitoring tool in the SOD1[G93A] ALS mouse model.

6.7 SUPPLEMENTARY MATERIAL

Supplementary Fig1: PoC study: Coconut oil dietary supplementation. (A) Nutritional facts of Royal Green Coconut Oil. Right image shows standard food mixed with coconut oil in a petri dish. **(B)** Paw grip endurance (PaGE) test, a mouse hanging upside down on a metal grid and latency to fall is recorded.
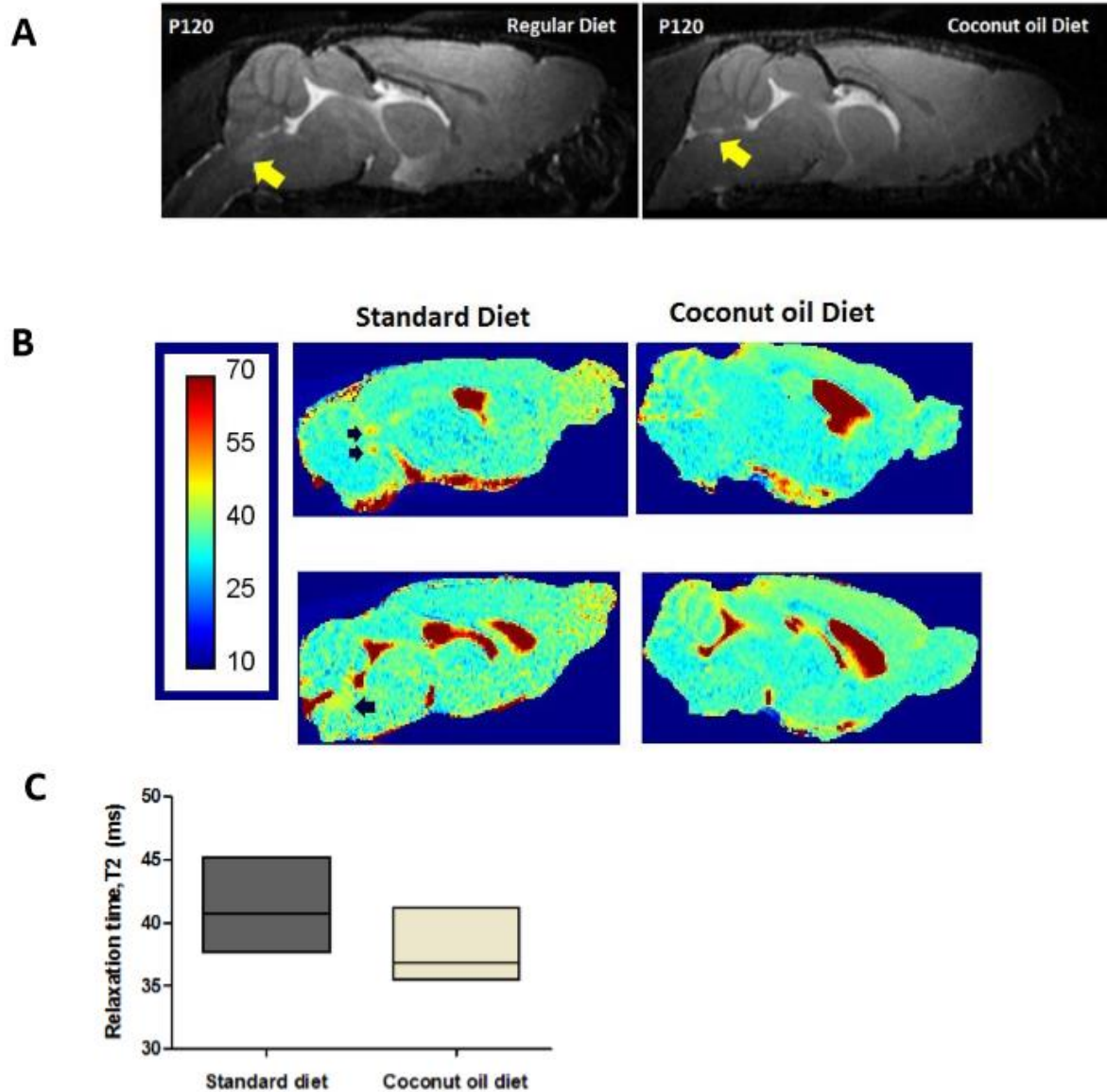
Supplementary Fig2: PoC study: Relaxometry. (A) Sagittal T2-weighted MR section of SOD1[G93A] mouse on standard diet (left) showing pronounced hyperintensity in the hypoglossal nucleus (arrow) compared to standard diet mouse (right) at age 120 days. (B) T2 maps of SOD1[G93A] animals receiving standard and coconut oil diet. Arrows indicate the hypoglossal and trigeminal nuclei in the sagittal T2 maps. (C) T2 relaxation values (in milliseconds) from the hypoglossal nucleus for the two groups at 120 days ($P = 0.054$), n = 6.

SOD1-G93A

CONCENTRATION (MMOL/L) — AGE (DAYS)

WT

CONCENTRATION (MMOL/L) — AGE (DAYS)
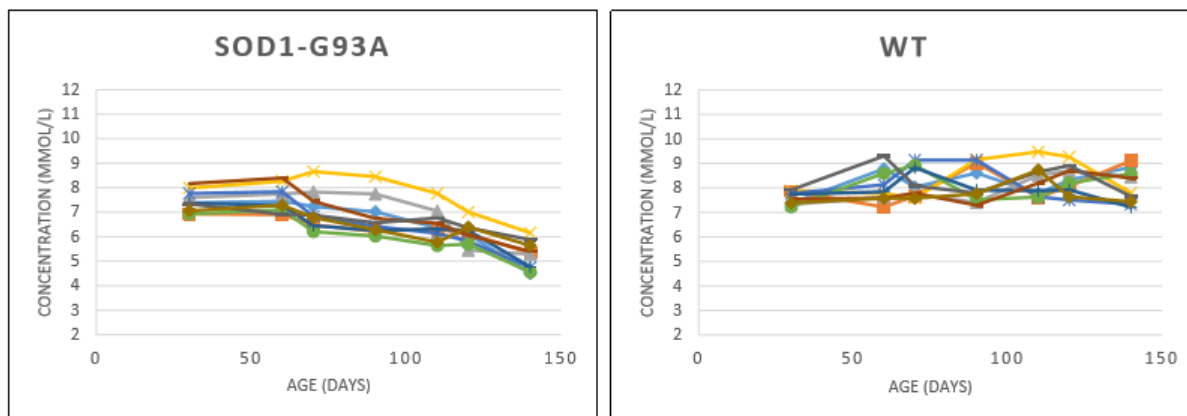
Supplementary Fig3: Evolution of creatine levels in SOD1^{G93A} and WT mice. Creatine levels of the 10 SOD^{G93A} and wild-type mice at 30, 60, 70, 90, 110, 120, 140 days postpartum.

Supplementary Table 1: ^{1}H-MRS Studies of ALS SOD1^{G93A} mice

Publication	MRS	NMR	Regions	Metabolic differences SOD1-G93A vs WT
Andreassen et al, 2001	-4.7T GE Omega -PRESS TE/TR 136ms/2s		sensorimotor cortex bilaterally, voxel 6.5x1.8x3 mm	-Increase Glutamate+Glutamine at P75
Niessen et al, 2007		-600 MHz Bruker -TR = 10s -8.5µs pulse length	brainstem, cerebellum, cortex, spinal cord	-Decrease NAA spinal cord at P34 -Decrease NAA, GABA, Glutamine spinal cord at P75 -Decrease NAA brainstem at P75 -Increase Taurine cerebellum at P75 -Decrease NAA,GABA, Glutamine Aspartate spinal cord at P90 -Decrease NAA, Glutamine brainstem at P90 -Increase Lactate, Succinate spinal cord at P90 -Increase Taurine cortex and cerebellum at P90 -Decrease NAA, GABA, Glutamate, Glutamine, Aspartate, Inositol spinal cord at P120 -Decrease NAA, Glutamate, Glutamine brainstem at P120 -Increase Lactate, Succinate spinal cord-brainstem at P120 -Increased Taurine cortex, cerebellum at P120
Choi et al, 2009	-9.4T Bruker -home built elliptical surface coil - PRESS TE/TR 146ms2.2s/2.2s NA 600-700	-600 MHz Bruker - TR = 12s -12 µs pulse length	*In-vivo* motor and cingulate cortex voxel 6.5×1.35×2.5mm *In-vitro* sensorimotor cortex, cerebellum, medulla spinal cord	-Decrease in NAA in mice with four limbs affected versus those with no limbs affected – irrespective of age -Increase Glutamate sensorimotor cortex at P84 -Increase Glutamine sensorimotor cortex at P141 -Increase Glutamate+Glutamine medulla at P114+P142 -Decrease NAA medulla at P142 -Increased glutamate, inositols and taurine spinal cord-medulla between P112-P142 -Decreased NAA and NAAG spinal cord at P112

140

6.8 REFERENCES

Achilli, F., Boyle, S., Kieran, D., Chia, R., Hafezparast, M., Martin, J.E., Schiavo, G., Greensmith, L., Bickmore, W., Fisher, E.M., 2005. The SOD1 transgene in the G93A mouse model of amyotrophic lateral sclerosis lies on distal mouse chromosome 12. Amyotroph Lateral Scler Other Motor Neuron Disord. 6(2), 111-4.

Adhihetty, P.J., Irrcher, I., Joseph, A.M., Ljubicic, V., Hood, D.A., 2003. Plasticity of skeletal muscle mitochondria in response to contractile activity. Exp Physiol. 88(1), 99-107.

Agosta, F., Chiò, A., Cosottini, M., De Stefano, N., Falini, A., Mascalchi, M., Rocca, M.A., Silani, V., Tedeschi, G., Filippi, M., 2010. The present and the future of neuroimaging in amyotrophic lateral sclerosis. AJNR Am J Neuroradiol. 31(10), 1769-77.

Horská, A., Barker, P.B., 2010. Imaging of Brain Tumors: MR Spectroscopy and Metabolic Imaging. Neuroimaging clinics of North America. 20(3), 293-310.

ALSUntangled Group. ALSUntangled 15, 2012. Coconut oil. Amyotrophic Lateral Sclerosis: Official Publication of the World Federation of Neurology Research Group on Motor Neuron Diseases. 13(3), 328–330.

Andreassen, O.A., Jenkins, B.G., Dedeoglu, A., Ferrante, K.L., Bogdanov, M.B., Kaddurah-Daouk, R., Beal, M.F., 2001. Increases in cortical glutamate concentrations in transgenic amyotrophic lateral sclerosis mice are attenuated by creatine supplementation. J Neurochem. 77, 383–390.

Ari, C., Poff, A.M., Held, H.E., Landon, C.S., Goldhagen, C.R., Mavromates, N., D'Agostino, D.P., 2014. Metabolic therapy with Deanna Protocol supplementation delays disease progression and extends survival in amyotrophic lateral sclerosis (ALS) mouse model. PLoS One. 9(7), e103526.

Atassi, N., Xu, M., Triantafyllou, C., Keil, B., Lawson, R., Cernasov, P., Ratti, E., Long, C.J., Paganoni, S., Murphy, A., Salibi, N., Seethamraju, R., Rosen, B., Ratai, E.M., 2017. Ultra high-field (7tesla) magnetic resonance spectroscopy in Amyotrophic Lateral Sclerosis. PLoS One. 12(5), e0177680.

Bastow, E.L., Peswani, A.R., Tarrant, D.S., Pentland, D.R., Chen, X., Morgan, A., Staniforth, G.L., Tullet, J.M., Rowe, M.L., Howard, M.J., Tuite, M.F., Gourlay, C.W., 2016. New links between SOD1 and metabolic dysfunction from a yeast model of amyotrophic lateral sclerosis. J Cell Sci. 129(21), 4118-4129.

Beal, M.F., 2002. Coenzyme Q10 as a possible treatment for neurodegenerative diseases. Free Radic Res. 36(4), 455-60.

Bendotti, C., Calvaresi, N., Chiveri, L., Prelle, A., Moggio, M., Braga, M., Silani, V., De Beasi, S., 2001. Early vacuolization and mitochondrial damage in motor neurons of FALS mice are not associated with apoptosis or with changes in cytochrome oxidase histochemical reactivity. Journal of the neurological sciences. 191(1–2), 25–33.

Bendotti, C., Carri, M.T., 2004. Lessons from models of SOD1-linked familial ALS. Trends Mol Med. 10(8), 393–400.

Boillée, S., Vande Velde, C., Cleveland, D.W., 2006. ALS: a disease of motor neurons and their nonneuronal neighbors. Neuron. 52(1), 39-59. Review.

Bruijn, L. I., Houseweart, M. K., Kato, S., Anderson, K. L., Anderson, S. D., Ohama, E., Reaume, A. G., Scott, R. W., and Cleveland, D. W., 1998. Aggregation and motor neuron toxicity of an ALS-linked SOD1 mutant independent from wild-type SOD1. Science. 281, 1851–1854.

Bucher, S., Braunstein, K.E, Niessen, H.G., Kaulisch, T., Neumaier, M., Boeckers, T.M., Stiller, D., Ludolph, A.D., 2007. Vacuolization correlates with spin-spin relaxation time in motor brainstem nuclei and behavioral tests in the transgenic G93A-SOD1 mouse model of ALS. Eur J Neurosci. 26, 1895–1901.

Bunton-Stasyshyn, R.K., Saccon, R.A., Fratta, P., Fisher, E.M., 2015. SOD1 Function and Its Implications for Amyotrophic Lateral Sclerosis Pathology: New and Renascent Themes. *Neuroscientist*. 21(5), 519-29.

Cacabelos, D., Ayala, V., Ramírez-Nunez, O., Granado-Serrano, A.B., Boada, J., Serrano, J.C., Cabré, R., Nadal-Rey, G., Bellmunt, M.J., Ferrer, I., Pamplona, R., Portero-Otin, M., 2014. Dietary lipid unsaturation influences survival and oxidative modifications of an amyotrophic lateral sclerosis model in a gender-specific manner. Neuromolecular Med. 16(4), 669-85.

Caron, I., Micotti, E., Paladini, A., Merlino, G., Plebani, L., Forloni, G., Modo, M., Bendotti, C., 2015. Comparative Magnetic Resonance Imaging and Histopathological Correlates in Two SOD1 Transgenic Mouse Models of Amyotrophic Lateral Sclerosis. *PLoS One*. 10(7), e0132159.

Choi, I.Y., Lee, S.P., Guilfoyle, D.N., Helpern, J.A., 2003a. *In vivo* NMR studies of neurodegenerative diseases in transgenic and rodent models. *Neurochem Res*. 28, 987–1001.

Choi, J., Kustermann, E., Dedeoglu, A., & Jenkins, B. G., 2009. Magnetic Resonance Spectroscopy of Regional Brain Metabolite Markers in FALS Mice and the Effects of Dietary Creatine Supplementation. The European Journal of Neuroscience. 30(11), 2143–2150.

Clark, J.B., 1998. N-acetyl aspartate: a marker for neuronal loss or mitochondrial dysfunction. Dev. Neurosci. 20, 271–276.

Cleveland, D.W., Rothstein, J.D., 2001. From Charcot to Lou Gehrig: deciphering selective motor neuron death in ALS. *Nat. Rev. Neurosci*. 2, 806–819.

Crawley, M. J., 2007. Data Input, in The R Book, John Wiley & Sons, Ltd, Chichester, UK.

Curtis, D.R., Watkins, J.C., 1965. The pharmacology of amino acids related to gamma-aminobutyric acid. *Pharmacol Rev*. 17(4),347-391.

Dedeoglu, A., Choi, J.K., Cormier, K., Kowall, N.W., Jenkins, B.G., 2004. Magnetic resonance spectroscopic analysis of Alzheimer's disease mouse brain that express mutant human APP shows altered neurochemical profile. *Brain Res*. 1012, 60–65.

Desport, J.C., Preux, P.M., Truong, T.C., Vallat, J.M., Sautereau, D., Couratier, P., 1999. Nutritional status is a prognostic factor for survival in ALS patients. Neurology. 53(5), 1059-63.

De Vos, K.J., Hafezparast, M., 2017. Neurobiology of axonal transport defects in motor neuron diseases: Opportunities for translational research? Neurobiol Dis. 105, 283-299.

Dietz, V., 2010. Behavior of spinal neurons deprived of supraspinal input. Nat Rev Neurol. 6(3), 167-74.

Dorst, J., Kühnlein, P., Hendrich, C., Kassubek, J., Sperfeld, A.D., Ludolph, A.C., 2011. Patients with elevated triglyceride and cholesterol serum levels have a prolonged survivalin amyotrophic lateral sclerosis. J Neurol. 258(4), 613-7.

Dupuis, L., Pradat, P.F., Ludolph, A.C., Loeffler, J.P., 2011. Energy metabolism in amyotrophic lateral sclerosis. Lancet Neurol. 10(1), 75-82.

Eidelberg, E., 1981. Consequences of spinal cord lesions upon motor function, with special reference to locomotor activity. Prog Neurobiol. 17(3), 185-202.

Foerster, B. R., Carlos, R. C., Dwamena, B. A., Callaghan, B. C., Petrou, M., Edden, R. A. E., … Pomper, M. G. 2014. Multimodal MRI as a diagnostic biomarker for amyotrophic lateral sclerosis. Annals of Clinical and Translational Neurology, 1(2), 107–114.

Gallo, V., Wark, P.A., Jenab, M., Pearce, N., Brayne, C., Vermeulen, R., Andersen, P.M., Hallmans, G., Kyrozis, A., Vanacore, N., Vahdaninia, M., Grote, V., Kaaks, R., Mattiello, A., Bueno-de-Mesquita, H.B., Peeters, P.H., Travis, R.C., Petersson, J., Hansson, O., Arriola, L., Jimenez-Martin, J.M., Tjønneland, A., Halkjær, J., Agnoli, C., Sacerdote, C., Bonet, C., Trichopoulou, A., Gavrila, D., Overvad, K., Weiderpass, E., Palli, D., Quirós, J.R., Tumino, R., Khaw, K.T., Wareham, N., Barricante-Gurrea, A., Fedirko, V., Ferrari, P., Clavel-Chapelon, F., Boutron-Ruault, M.C., Boeing, H., Vigl, M., Middleton, L., Riboli, E., Vineis, P., 2013. Prediagnostic body fat and risk of death from amyotrophic lateral sclerosis: the EPIC cohort. Neurology. 26, 80(9):829-38.

Gasparovic, C., Yeo, R., Mannell, M., Ling, J., Elgie, R., Phillips, J., Doezema, D., Mayer, A.R., 2009. Neurometabolite concentrations in gray and white matter in mild traumatic brain injury: a 1H-magnetic resonance spectroscopy study. J Neurotrauma. 26(10), 1635-43.

Greenwood, D.I., 2013. Nutrition management of amyotrophic lateral sclerosis. Nutr Clin Pract. 28(3), 392-9.

Griffey, R. H., Flamig, D. P., 1990. VAPOR for Solvent -Supressed, Short -Echo, Volume -Localized Proton Spectroscopy. Journal of Magnetic Resonance. 88, 161-166.

Gruetter, R., 1993. Automatic, localized *in vivo* adjustment of all first- and second-order shim coils. Magn Reson Med. 29(6), 804-11.

Gupta, Sunil & Jason Riis. "PatientsLikeMe: An Online Community of Patients." Harvard Business School Case 511-03, February 2011. (Revised Novem 2012).

Gurney, M.E., Pu, H., Chiu, A.Y., Dal Canto, M.C., Polchow, C.Y., Alexander, D.D., Caliendo, J., Hentati, A., Kwon, Y.W., Deng, H.X., *et al*., 1994. Motor neuron degeneration in mice that express a human Cu, Zn superoxide dismutase mutation. Science. 17, 264(5166), 1772-5.

Hartman, A.L., 2012. Neuroprotection in metabolism-based therapy. Epilepsy Res. 100(3), 286-94.

Hartman, A.L., 2013. Stafstrom CE. Harnessing the power of metabolism for seizure prevention: focus on dietary treatments. Epilepsy Behav. 26(3), 266-72.

Hecht, M.J., Fellner, F., Fellner, C., Hilz, M.J., Neundorfer, B., Heuss, D., 2002. Hyperintense and hypointense MRI signals of the precentral gyrus and corticospinal tract in ALS: a follow-up examination including FLAIR images. J Neurol Sci. 199, 59–65.

Hersch, S.M., Gevorkian, S., Marder, K., Moskowitz, C., Feigin, A., Cox, M., Como, P., Zimmerman, C., Lin, M., Zhang, L., Ulug, A.M., Beal, M.F., Matson, W., Bogdanov, M., Ebbel, E., Zaleta, A., Kaneko, Y., Jenkins, B., Hevelone, N., Zhang, H., Yu, H., Schoenfeld, D., Ferrante, R., Rosas, H.D., 2006. Creatine in Huntington disease is safe, tolerable, bioavailable in brain and reduces serum 8OH2′dG. Neurology.66, 250–252.

Hillel, A.D., Miller, R., 1989. Bulbar amyotrophic lateral sclerosis: patterns of progression and clinical management. Head Neck. 11(1), 51-9.

Higgins, C.M., Jung, C., Xu, Z., 2003. ALS-associated mutant SOD1^{G93A}causes mitochondrial vacuolation by expansion of the intermembrane space and by involvement of SOD1 aggregation and peroxisomes. BMC Neuroscience. 4, 16.

Jenkins, B.G., Andreassen, O.A., Dedeoglu, A., Leavitt, B., Hayden, M., Borchelt, D., Ross, C.A., Ferrante, R.J., Beal, M.F., 2005. Effects of CAG repeat length, HTT protein length and protein context on cerebral metabolism measured using magnetic resonance spectroscopy in transgenic mouse models of Huntington's disease. J Neurochem. 95, 553–562.

Jenkins, B.G., Klivenyi, P., Kustermann, E., Andreassen, O.A., Ferrante, R.J., Rosen, B.R., Beal, M.F., 2000. Nonlinear decrease over time in N-acetyl aspartate levels in the absence of neuronal loss and increases in glutamine and glucose in transgenic Huntington's disease mice. J Neurochem.74, 2108–2119.

Jung, M.K., Kim, K.Y., Lee, N.Y., Kang, Y.S., Hwang, Y.J., Kim, Y., Sung, J.J., McKee, A., Kowall, N., Lee, J., Ryu, H., 2013. Expression of taurine transporter (TauT) is modulated by heat shock factor 1 (HSF1) in motor neurons of ALS. Mol Neurobiol. 47(2), 699-710.

Kalra, S., Arnold, D.L., Cashman, N.R., 1999. Biological markers in the diagnosis and treatment of ALS. J Neurol Sci. 165, S27–32.

Kalra, S., Vitale, A., Cashman, N.R., Genge, A., Arnold, D.L., 2006. Cerebral degeneration predicts survival in amyotrophic lateral sclerosis. Journal of Neurology, Neurosurgery, and Psychiatry. **77**(11), 1253-1255.

Karitzky, J., Ludolph, A.C., 2001. Imaging and neurochemical markers for diagnosis and disease progression in ALS. J. Neurol. Sci. 191, 35–41.

Kong, J., Xu, Z., 1998. Massive mitochondrial degeneration in motor neurons triggers the onset of amyotrophic lateral sclerosis in mice expressing a mutant SOD1. J Neurosci. 18(9), 3241-50.

Kumar, A., Ghosh, D., Singh, R.L., 2013. Amyotrophic Lateral Sclerosis and Metabolomics: Clinical Implication and Therapeutic Approach. J Biomark. 2013:538765.

Lee, Y.C., Markus, R., Hughes, A., 2003. MRI in ALS: corticospinal tract hyperintensity. Neurology. 61, 1600.

Liu, Y.J., Tsai, P.Y., 2017. Chern Y. Energy Homeostasis and Abnormal RNA Metabolism in Amyotrophic Lateral Sclerosis. Front Cell Neurosci. 11,126.

Malessa, S., Leigh, P.N., Bertel, O., Sluga, E., Hornykiewicz, O., 1991. Amyotrophic lateral sclerosis: glutamate dehydrogenase and transmitter amino acids in the spinal cord. J Neurol Neurosurg Psychiatry. 54(11), 984-8.

Marjanska, M., Curran, G.L,, Wengenack, T.M., Henry, P.G., Bliss, R.L., Poduslo, J.F., Jack, C.R Jr., Ugurbil, K., Garwood, M., 2005. Monitoring disease progression in transgenic mouse models of Alzheimer's disease with proton magnetic resonance spectroscopy. Proc Natl Acad Sci U S A. 102, 11906–11910.

Martin, L.J., 2011. Mitochondrial pathobiology in ALS. J Bioenerg Biomembr. 43(6), 569-79.

Morris, M.E., Perry, A., Bilney, B., Curran, A., Dodd, K., Wittwer, J.E., Dalton, G.W., 2006. Outcomes of physical therapy, speech pathology, and occupational therapy for people with motor neuron disease: a systematic review. Neurorehabil Neural Repair. 20(3):424-34.

Niessen, H.G., Angenstein, F., Sander, K., Kunz, W.S., Teuchert, M., Ludolph, A.C *et al*., 2006. *In vivo* quantification of spinal and bulbar motor neuron degeneration in the G93A-SOD1 transgenic mouse model of ALS by T2 relaxation time and apparent diffusion coefficient. Exp Neurol. 201, 293–300.

Niessen, H.G., Debska-Vielhaber, G., Sander, K., Angenstein, F., Ludolph, A.C., Hilfert, L., Willker, W., Leibfritz, D., Heinze, H.J., Kunz, W.S., Vielhaber, S., 2007. Metabolic progression markers of neurodegeneration in the transgenic G93A-SOD1 mouse model of amyotrophic lateral sclerosis. Eur J Neurosci. 25(6),1669-77.

O'Reilly, É.J., Wang, H., Weisskopf, M.G., Fitzgerald, K.C., Falcone, G., McCullough, M.L., Thun, M., Park, Y., Kolonel, L.N., Ascherio, A., 2013. Premorbid body mass index and risk of amyotrophic lateral sclerosis. Amyotroph Lateral Scler Frontotemporal Degener. 14(3), 205-11.

Perry, T.L., Hansen, S. & Jones, K., 1987. Brain glutamate deficiency in amyotrophic lateral sclerosis. Neurology. 37, 1845–1848.

Petroff, O.A., 2002. GABA and glutamate in the human brain. Neuroscientist. 8(6), 562-73.

Pfeuffer, J., Tkác, I., Provencher, S.W., Gruetter, R., 1999. Toward an *in vivo* neurochemical profile: quantification of 18 metabolites in short-echo-time (1)H NMR spectra of the rat brain. J Magn Reson. 141(1), 104-20.

Pioro, E.P., Majors, A.W., Mitsumoto, H., Nelson, D.R., Ng, T.C., 1999. 1H-MRS evidence of neurodegeneration and excess glutamate + glutamine in ALS medulla. Neurology. 53, 71–79.

Rae, C.D., Bröer, S., 2015. Creatine as a booster for human brain function. How might it work? Neurochem Int. 89, 249-59.

Ratiney, H., Coenradie, Y., Cavassila, S., van Ormondt, D., Graveron-Demilly, D., 2004. Time-domain quantitation of 1H short echo-time signals: background accommodation. MAGMA. 16(6), 284-96.

Reynolds, N.C Jr., Prost, R.W., Mark, L.P., 2005. Heterogeneity in 1H-MRS profiles of presymptomatic and early manifest Huntington's disease. Brain Res. 1031(1), 82-9.

Rosen, D.R., Siddique, T., Patterson, D., Figlewicz, D.A., Sapp, P., Hentati, A., Donaldson, D., Goto, J., O'Regan, J.P., Deng, H.X., *et al.*, 1993. Mutations in Cu/Zn superoxide dismutase gene are associated with familial amyotrophic lateral sclerosis. Nature. 362(6415), 59-62.

Rule, R.R., Suhy, J., Schuff, N., Gelinas, D.F., Miller, R.G., Weiner, M.W., 2004. Reduced NAA in motor and non-motor brain regions in amyotrophic lateral sclerosis: a cross-sectional and longitudinal study. Amyotroph Lateral Scler Other Motor Neuron Disord. 141-9.

Sánchez-Pernaute, R., García-Segura, J.M., del Barrio, Alba, A., Viaño, J., de Yébenes, J.G., 1999. Clinical correlation of striatal 1H MRS changes in Huntington's disease. Neurology. 11, 53(4), 806-12.

Sau, D., De Biasi, S., Vitellaro-Zuccarello, L., Riso, P., Guarnieri, S., Porrini, M., Simeoni, S., Crippa, V., 2007. Onesto E, Palazzolo I, Rusmini P, Bolzoni E, Bendotti C, Poletti A. Mutation of SOD1 in ALS: a gain of a loss of function. Hum Mol Genet. 1, 16(13), 1604-18.

Starcuk, Z.O., Strbak, J., Starcukova, Graveron-Demilly., 2008. Simulation of steady state free precession acquisition mode in coupled spin systems for fast MR spectroscopic imaging. *IEEE International Workshop on Imaging Systems and Techniques.* 302-306.

Stefan, D., Di Cesare, F., Andrasescu, A., Popa, E., Lazariev, A., Vescovo, E., Strbak, O., Williams, S., Starcuk, Z., Cabanas, M., van Ormondt, D., Graveron-Demilly. D., 2009. Quantitation of magnetic resonance spectroscopy signals: the jMRUI software package. *Measurement Science and Technology.* 20, 104035 (9pp).

Swerdlow, R.H., Parks, J.K., Cassarino, D.S., Trimmer, P.A., Miller, S.W., Maguire, D.J., Sheehan, J.P., Maguire, R.S., Pattee, G., Juel, V.C., Phillips, L.H., Tuttle, J.B., Bennett JP., Jr,Davi, R.E., Parker, W.D Jr., 1998. Mitochondria in sporadic amyotrophic lateral sclerosis. Exp Neurol. 153(1):135-42.

Tankersley, C.G., Haenggeli, C., Rothstein, J.D., 2007. Respiratory impairment in a mouse model of amyotrophic lateral sclerosis. *J. Appl. Physiol*. 102, 926–932.

Tieu, K., Perier, C., Caspersen, C., Teismann, P., Wu, D.C., Yan, S.D., Naini, A., Vila, M., Jackson-Lewis, V., Ramasamy, R., Przedborski, S., 2003. D-beta-hydroxybutyrate rescues mitochondrial respiration and mitigates features of Parkinson disease. J Clin Invest. 112(6), 892-901.

Tu, P.H., Raju, P., Robinson, K.A., Gurney, M.E., Trojanowski, J.Q., Lee, V.M., 1996. Transgenic mice carrying a human mutant superoxide dismutase transgene develop neuronal cytoskeletal pathology resembling human amyotrophic lateral sclerosis lesions. Proc. Natl. Acad. Sci. U. S. A. 93, 3155–3160.

Turner, B.J., Talbot, K., 2008. Transgenics, toxicity and therapeutics in rodent models of mutant SOD1-mediated familial ALS. Prog Neurobiol. 85, 94–134.

Van Damme, P., Robberecht, W., Van Den Bosch, L., 2017. Modelling amyotrophic lateral sclerosis: progress and possibilities. Dis Model Mech. 10(5),537-549.

Van der Perren, A., Toelen, J., Casteels, C., Macchi, F., Van Rompuy, A.S., Sarre, S., Casadei, N., Nuber, S., Himmelreich, U., Osorio Garcia, M.I., Michotte, Y., D'Hooge, R., Bormans, G., Van Laere, K., Gijsbers, R., Van den Haute, C., Debyser, Z., Baekelandt, V., 2015. Longitudinal follow-up and characterization of a robust rat model for Parkinson's disease based on overexpression of alpha-synuclein with adeno-associated viral vectors. Neurobiol Aging. 36(3), 1543-58.

Van den Boogaart, A., van Ormondt, D., Pijnappel, W. W. F., de Beer, R. and Ala Korpel, M., 1994. Removal of the residual water resonance from 1H magnetic resonance spectra. Mathematics of Signal Processing III, Clarendon Press: Oxford. 175-195.

Verstraete, E., Foerster, B.R., 2015. Neuroimaging as a New Diagnostic Modality in Amyotrophic Lateral Sclerosis. Neurotherapeutics. 12(2), 403-416.

Vielhaber, S., Kaufmann, J., Kanowski, M., Sailer, M., Feistner, H., Tempelmann, C., Elger, C.E., Heinze, H.-J. & Kunz, W.S., 2001. Effect of creatine supplementation on metabolite levels in ALS motor cortices. Exp. Neurol. 172, 377–382.

Wang, S., Melhem, E.R., Poptani, H., Woo, J.H., 2011. Neuroimaging in Amyotrophic Lateral Sclerosis. Neurotherapeutics. The journal of the American Society for Experimental NeuroTherapeutics. 8(1), 63-71.

Wang, W., Zhang, F., Li, L., Tang, F., Siedlak, S.L., Fujioka, H., Liu, Y., Su, B., Pi, Y., Wang, X., 2015. MFN2 couples glutamate excitotoxicity and mitochondrial dysfunction in motorneurons. J Biol Chem. 290(1), 168-82.

Yoshino, Y., Koike, H. & Akai, K., 1979. Free amino acids in motor cortex of amyotrophic lateral sclerosis. Experientia. 35**,** 219–220.

Zang, D.W., Yang, Q., Wang, H.X., Egan, G., Lopes, E.C., Cheema, S.S., 2004. Magnetic resonance imaging reveals neuronal degeneration in the brainstem of the superoxide dismutase 1 transgenic mouse model of amyotrophic lateral sclerosis. Eur J Neurosci. 20(7), 1745-51.

Zhao, W., Varghese, M., Vempati, P., Dzhun, A., Cheng, A., Wang, J., Lange, D., Bilski, A., Faravelli, I., Pasinetti, G.M, 2012. Caprylic triglyceride as a novel therapeutic approach to effectively improve the performance and attenuate the symptoms due to the motor neuron loss in ALS disease. PLoS One. 7(11).

Zhao, Z., Lange, D.J., Voustianiouk, A., MacGrogan, D., Ho, L., Suh, J., Humala, N., Thiyagarajan, M., Wang, J., Pasinetti, G.M., 2006. A ketogenic diet as a potential novel therapeutic intervention in amyotrophic lateral sclerosis. BMC Neurosci.7, 29.

Chapter 7

Molecular Changes Observed by Positron Emission Tomography and Magnetic Resonance Imaging Precede Nuclear Clearance and Aggregation of Transactive-Response DNA-binding Protein TDP-43 in hTDP-43^{A315T} Transgenic mice

Akila Weerasekera[1†], Melissa Crabbé[2†], Sandra Tomé[3], Willy Gsell[1], Diana Sima[4,6], Cindy Casteels[2],Tom Dresselaers[5], Christophe Deroose[2], Sabine Van Huffel[6], Dietmar Rudolf Thal[3,7], Philip Van Damme[8,9], Uwe Himmelreich[1]

(†) both authors contributed equally to this study

(1) Biomedical MRI unit/ MoSAIC, Department of Imaging and Pathology, KU Leuven, Leuven, Belgium.

(2) Division of Nuclear Medicine, Department of Imaging and Pathology, KU Leuven, Belgium; MoSAIC - Molecular Small Animal Imaging Centre, KU Leuven, Leuven, Belgium.

(3) Laboratory for Neuropathology, Department of Neurosciences, KU Leuven, Leuven Belgium.

(4) Icometrix, R&D department, Leuven, Belgium.

(5) Radiology, Department of Imaging and Pathology, UZ Leuven, Leuven, Belgium.

(6) Department of Electrical Engineering (ESAT), STADIUS Center for Dynamical Systems, Signal Processing and Data Analytics, KU Leuven, and imec, Leuven, Belgium.

(7) Department of Pathology, UZ-Leuven, Leuven, Belgium

(8) Laboratory of Neurobiology, Department of Neurosciences, KU Leuven, Leuven, Belgium and Center for Brain & Disease Research, VIB, Leuven, Belgium.

(9) Neurology Department, University Hospitals, Leuven, Belgium

7. Molecular changes observed by positron emission tomography and magnetic resonance imaging precede nuclear clearance and aggregation of transactive-response DNA-binding protein TDP-43 in hTDP-43^{A315T} transgenic mice

7.1 ABSTRACT

Currently TAR DNA binding protein 43 (TDP-43) pathology underlying Amyotrophic Lateral Sclerosis (ALS) remains poorly understood, which hinders both clinical diagnosis and drug discovery efforts. To better understand the disease pathophysiology, positron emission tomography (PET) and multiparametric magnetic resonance imaging (mp-MRI) provide a non-invasive mode to investigate metabolic, structural, and neurochemical abnormalities *in vivo*. For the first time, we report the findings of a longitudinal PET-MR study in the hTDP-43^{A315T} ALS mouse model, investigating disease-related changes in the mouse brain. ^{18}F-FDG PET showed significantly lowered glucose metabolism in the motor and somatosensory cortices of hTDP-43^{A315T} mice whereas metabolism was elevated in the region covering the bilateral substantia nigra, reticular and amygdaloid nucleus between 3 and 7 months of age, as compared to controls. Magnetic resonance spectroscopy data showed significant changes in glutamate+glutamine (Glx) and choline levels in motor cortex and hindbrain of hTDP-43^{A315T} mice compared to controls. Cerebral blood flow (CBF) measurements using arterial spin labelling technique showed no significant age- or group-dependent changes in brain perfusion. Diffusion MRI indices indicated transient changes in different motor areas of the brain in hTDP-43^{A315T} mice around 14 months of age. Nuclear clearance of TDP-43 and cytoplasmic TDP-43 proteinaceous inclusions were observed in the brains of symptomatic, 18-month-old mice, *i.e.* following the changes detected by *in vivo* [^{18}F]FDG PET imaging. Our results reveal that disease- and age-related functional neurochemical alterations, together with limited structural changes, occur in hTDP-43^{A315T} mice as compared to their healthy counterparts. These changes preceded nuclear clearance of TDP-43 and its aggregation in the cytoplasm of frontocentral neurons.

7.2 INTRODUCTION

Amyotrophic lateral sclerosis (ALS) is a fatal progressive neurodegenerative disorder in which loss of upper and lower motor neurons leads to paralysis with a typical disease course of 1 to 5 years. Most forms of ALS are sporadic (sALS), however about 10% of patients have an inherited familial form of the disease (fALS) and a clear family history (Chia *et al.*, 2018). Understanding of ALS genetics began with

the discovery of dominant causative mutations in the gene encoding copper/zinc superoxide dismutase 1 (SOD1) in about 20% of fALS cases and in about 1% of sporadic cases (Hardiman and van den Berg, 2017). Subsequently, other even more rare familial form of ALS with atypical disease features were linked to mutations in several other genes including C9orf72, FUS, TDP-43 (Lagier-Tourenne and Cleveland, 2009). One of the neuropathological hallmarks of ALS is the presence of ubiquitylated neuronal cytoplasmic inclusions (NCIs) in upper and lower motor neurons (Leigh *et al.*, 1991). In 2006, the 43kDa TDP-43 protein has been identified as the major component of NCIs in sALS and SOD1–negative fALS, as well as sporadic and familial frontotemporal lobar dementia (FTLD) (Neumann *et al.*, 2006). TDP-43 is a highly conserved ubiquitously expressed nuclear protein with two RNA recognition motifs (Krecic and Swanson, 1999). Under normal conditions, TDP-43 shuttles between the nucleus and the cytoplasm and is involved in gene splicing and micro RNA biogenesis. Furthermore, mutant fragments of TDP-43 were detected in post-mortem ALS neuronal tissues suggesting that abnormal molecular-weighted TDP-43 could be a causative protein in these disorders (Neumann *et al.*, 2006). Albeit TDP-43 proteinopathy is a common pathological feature in human ALS, the mechanism related to pathogenesis is poorly understood. The missense mutation, Ala-315-Thr (A315T) was identified as a candidate gene in familial ALS through the sequencing of the TDP-43 gene, thereby establishing a connection between mutant TDP-43 proteinopathy and neurodegeneration (Gitcho *et al.*, 2008). Although TDP-43 mutations are not a common feature in familial ALS, similar pathological observations were made in sporadic ALS (Kabashi *et al.*, 2008). In 2010, Wegorzewska and colleagues reported on the first published transgenic model of TDP-43 proteinopathy, describing the prnp-hTDP-43A315T overexpression mouse model created on a hybrid C57BL/6 and CBA genetic background (Wegorzewska *et al.*, 2009). These mice were reported to develop gait abnormalities starting from about three months onwards. However, the TDP-43A315T mouse model, now available on a 100% C57BL6/J congenic genetic background from The Jackson laboratory (stock number 010700), was reported to develop an early intestinal blockage that prevents the disease phenotype progression and leads to premature sudden death (Guo *et al.*, 2012; Esmaeili *et al.*, 2013). Herdewyn *et al.* also showed that by replacing the standard rodent food pellets with an easily digestible gel diet, one can by-pass the gastrointestinal dysfunction and allow time for pathology to develop in the brain and spinal cord in these mice (Herdewyn *et al.*, 2014). Both male and female TDP-43A315T mice develop significant motor impairment, with deficits appearing earlier and progressing faster in males.

Discovering biomarkers of ALS pathology has the potential to diagnose patients at the early disease onset stage, which is essential to provide optimal patient care (disease management) and categorize patients for clinical trials. Preclinical research based on the use of transgenic ALS mouse models has become an essential part of biomarker discovery and novel preclinical drug evaluation in ALS (Perrin, 2014). *In vivo* imaging such as positron emission tomography (PET), magnetic resonance imaging and spectroscopy (MRI-MRS) have shown to provide unique insights into complex biological processes. These techniques also allow the temporal study of individual animals over time, enabling the assessment of disease progression in transgenic animal models. In this regard, non-invasive imaging of the TDP-43 A315T transgenic mouse model may help us elucidate the pathophysiology and identify disease-related metabolic and structural changes that may be translated into clinical research. Therefore, we investigated, for the first time, the effect of hTDP-43^{A315T} expression on the mouse cerebrum through *in vivo* PET-MR imaging, combining ^{18}F-fluorodeoxyglucose (FDG) PET, diffusion tensor imaging (DTI), arterial spin labeling (ASL) perfusion MR imaging and MR spectroscopy (MRS).

7.3 MATERIALS AND METHODS

7.3.1 Experimental design

PET-MR imaging time points were chosen to non-invasively investigate physiological changes in the mouse cerebrum associated with hTDP-43^{A315T} overexpression from early- to late-stage pathology, in accordance with previous studies (Herdewyn *et al.*, 2014; Beel *et al.*, 2018). ^{18}F-FDG-PET images acquired simultaneously with high-resolution MR images (section 7.3.4) were obtained in a separate scan session from more time-consuming MRS, DTI, and ASL perfusion MR scans (section 7.3.5). A total of 36 transgenic and 14 non-transgenic mice were included in this study. A detailed description of the cohort characteristics and experimental timeline are shown in **Figure 7.1**.

Figure 7.1. Experiment timeline. T_1-T_5 indicate all time points where molecular imaging was performed, including magnetic resonance spectroscopy (MRS), diffusion tensor imaging (DTI), and perfusion MR imaging with arterial spin labeling (top panel). ^{18}F-fluorodeoxyglucose (FDG) positron emission tomography (PET) combined with anatomical MRI was performed in the same cohort, but in separate scan sessions (bottom panel). Each panel describes the age (mean ± standard deviation) and amount of animals in the respective hTDP-43^{A315T} transgenic and control groups. Abbreviation: hTDP-43^{A315T}: human TAR DNA binding protein 43 carrying the A315T mutation; ctrl: non-transgenic control mice.

7.3.2 Transgenic Mice

All experiments were performed in accordance with institutional guidelines and compliant with the national and European Communities Council Directive of November 24, 1986 (86/609/EEC). The Animal Research Committee of the KU Leuven University, Belgium approved the study protocol (P075/2016). Prp-hTDP-43A315T transgenic mice were purchased from Jackson Laboratory (stock number 010700, Bar Harbor, ME, USA), and back-crossed for 10 generations into a congenic C57BL/6 J background, leading to a pure C57BL/6 J background. All animals were housed in a conventional animal facility in regular mouse cages. Mice were given gel food (DietGel®31M, ClearH20, Maine, USA) from 60 days *postpartum*. Food and water were made available *ad libitum*. Body weight, body appearance and motor performance were monitored weekly. Onset of gait abnormalities was defined by the appearance of a swimming gait. Mice were classified as end stage (ES) when presenting with following symptoms:

immobility, lethargy, or absence of righting reflex, and were euthanized accordingly. A number of mice developed ulcerative dermatitis in the rostral back region which is a common effect in ageing C57BL/6 mice (Hampton *et al.*, 2012). Mice were treated with dermal cream (20 mg/g fusidic acid + 1mg/g betamethasone, topical administration) for a maximum of 14 days and their nails were clipped. In case mice lost more than 20% of their initial body weight, mice were also sacrificed. Only female mice were used in this study to avoid any influence of gender.

7.3.3 Animal procedures

Before and during imaging procedures, mice were anaesthetized with 1-2% isoflurane in 100% oxygen. Mice were then placed in an MRI-compatible animal bed by placing the nose of the mouse in a nose cone, restraining it with a bite bar and custom-made outer ear-inserts. Respiration and body temperature were continuously monitored and maintained at 60-100 breaths min^{-1} and 37±1 °C, respectively. Prior to tracer injection, blood glucose was measured in each individual animal.

7.3.4 Simultaneous *in vivo* ^{18}F-FDG PET – MR imaging

Simultaneous ^{18}F-FDG PET-MR imaging was performed on an Albira Si PET insert (Bruker, Ettlingen, Germany) in combination with a 7 Tesla (T) MR scanner (Biospec 70/30, Bruker Biospin, Ettlingen, Germany). The PET insert has a 0.7 mm spatial resolution, 12% sensitivity, and 80x148 mm field of view. The ^{18}F-FDG radiotracer was prepared using an IBA 18/9 cyclotron (Ion Beam Applications, Louvain-La-Neuve, Belgium) and FDG synthesis module. After overnight fasting, mice were injected with approximately 10.4±1.8 MBq of ^{18}F-FDG into in the tail vein. If necessary the solution was diluted to a maximum volume of 200 μL using a 0.9% saline solution. Mice remained anaesthetized throughout the 30 min uptake period whereafter a 30 min static scan was initiated (Wong *et al.*, 2011; Casteels *et al.*, 2013). List-mode data were reconstructed in a single frame using the Maximum-Likelihood Expectation-Maximization algorithm (MLEM; 12 iterations). Scans were randoms and scatter corrected. Data were collected in a 32x32 mm matrix with 0.5 mm isotropic resolution.

To visualize signal intensity changes and for co-registration of PET images, a T2-weighted 3D TurboRARE protocol was acquired simultaneously with the following acquisition parameters: repetition time (TR) 1000 ms, echo time (TE) 12 ms, FOV 24×15×8.3 mm, matrix size 256×160×88, RARE factor 10, number of averages = 1.

First, PET and T2-weighted MR images were co-registered in the mouse native space. Following, T2-MR images of the cerebrum of each individual mice were co-registered to the Mirrione mouse brain atlas whereafter the same rigid transformation was applied to the PET scans using PMOD version 3.8 software (PMOD Technologies, Zurich, Switzerland). Standard uptake values (SUV) were calculated (=activity concentration (MBq/ml)/injected dose (MBq)), as a measure of absolute FDG uptake. Relative glucose metabolism was determined by normalizing the regional ^{18}F-FDG uptake to the whole-brain uptake. Volume-of-interest (VOI)-based analysis was executed using a predefined VOI map including 20 anatomical regions of mice with a C57BL/6 J background. Voxel-wise analysis was performed using Statistical Parametric Mapping 12 (SPM12, Wellcome Department of Cognitive Neurology, London, United Kingdom). Spatially normalized images were masked to exclude extra-cerebral signal. We used a 2 sample t-test for cross-sectional comparisons and a flexible factorial design taking into account factors

'time point' and 'group'. SPM analysis was performed using a 0.8 relative threshold of mean image intensity, with and without global normalization. T-maps were interrogated at a $p_{height}\leq0.005$ (uncorrected) peak level and extend threshold of $k_E>200$ voxels (1.6 mm^3). Only significant clusters with $p_{height}<0.05$ (corrected for multiple comparisons) were retained. Exceptions on $p_{cluster}$ were accepted for clusters with a plausible neurobiological basis and in light of previous ALS research.

7.3.5   *In vivo* MR imaging

MRS, DTI and perfusion MR acquisitions were performed using a small-animal 9.4 T MR scanner (Biospec 94/20, Bruker Biospin) with a horizontal bore of 20 cm and equipped with an actively shielded gradient set (600 mT m^{-1}, inner diameter 11.7 cm). MR data was acquired using a linear polarized resonator (7.2 cm diameter) for transmission, combined with a quadrature shaped mouse brain surface coil for receiving (both Bruker Biospin).

7.3.6 ^{1}H-Magnetic Resonance Spectroscopy

MR spectra were acquired for volumes in the motor cortex and the hindbrain with a voxel size of 2x2.5x1.5 mm^3. The hindbrain voxel covered the following nuclei: hypoglossal, medial vestibular nucleus, and the dorsal motor nucleus of the vagus nerve. MR spectra were acquired with a PRESS pulse sequence as previously reported (Weerasekera *et al.*, 2018) and using the following parameters: TR=1800 ms, TE=20 ms, and number of averages 320 for motor cortex and 640 for hindbrain. Water suppression was optimized using VAPOR. An unsuppressed water spectrum (TE=20 ms, TR=1400 ms, number of averages = 4) was acquired before each ^{1}H-MR spectrum (water suppressed) for quantification/ referencing. Shimming was performed using FASTMAP, resulting in a final water line width at half height of less than 16 Hz. Spectra were processed using jMRUI v6.0 (Stefan *et al.*, 2009). Spectra were phase corrected and an HLSVD (Hankel Lanczos Singular Values Decomposition) filter was applied to remove the residual water signal. Only metabolites with a Cramer-Rao lower bound <25% were considered for quantification. Metabolites were quantified with the QUEST algorithm in jMRUI using a simulated (NMRScopeB) metabolite basis set (Ratiney *et al.*, 2004; Starcuk *et al.*, 2009). Results are reported in reference to the non-suppressed water signal. A total of 16 brain metabolites (alanine, aspartic acid, total creatine, choline, GABA, glycine, glucose, glutamate, glutamine, NAA, myo-inositol, Scyllo-inositol, lactate, phosphoethanolamine, scyllo-inositol, taurine) were quantified. The sum of glutamate and glutamine concentrations was reported as Glx.

7.3.7   Arterial Spin labeling, Diffusion Tensor Imaging and T2-weighted MRI

Perfusion maps were recorded from a single 1mm thick axial forebrain slice covering the motor cortex, striatum and nucleus accumbens using a flow-sensitive alternating inversion recovery (FAIR) approach (Kim and Tsekos, 1997). ASL MR image acquisition was as previously reported [Oosterlinck *et al.*, 2011; Govaerts *et al.*, 2019]. In brief, a rapid acquisition with relaxation enhancement (RARE) readout was used with the following specific parameters: TR=18s, TE=5.2ms, FOV 2.5×2.5cm, matrix 128×128 with partial Fourier acceleration to 128×72, 14 inversion times from 20 to 8000ms, and using an inversion hyperbolic secant pulse of 14ms with a slab thickness of 1.6mm. Fractional anisotropy (FA) and mean

diffusivity (MD) were determined using a two-dimensional single shot echo planar spin echo acquisition with the following specific parameters: 13 slices of 0.6 mm thick with 0.12 mm gap, TR/TE = 7000/52 ms, acquisition matrix 128×128 zero filled to 256×256 resulting in a spatial resolution of 98×98 μm, fat suppression and diffusion parameters: δ/Δ = 6/14 ms, 15 non-co-linear directions, 6 b-values (250 500 750 1000 1500 3000).

For the placement of the spectroscopy voxel, T2-weighted 2D RARE images (effective TE 50 ms; matrix 256x256; 300 μm slice thickness) were acquired. Perfusion MR images were processed using the Paravison 5.1 software (Bruker Biospin). Absolute cerebral blood flow (CBF) values were calculated using the T1 difference method and assuming an arterial T1 of 2.4s. Diffusion data was analyzed using region-based analysis in DSI Studio (http://dsi-studio.labsolver.org); fractional anisotropy (FA), radial diffusivity (RD) and mean diffusivity (MD) were calculated for the following anatomical regions: striatum, motor cortex and hindbrain.

7.3.8   Immunohistochemistry

After perfusion with 4% paraformaldehyde, the brains were fixed in 4% paraformaldehyde for at least 1 week, dehydrated overnight, and embedded in paraffin blocks. Sections of 5 μm were cut and dried overnight.

The TDP-43 cytoplasmic aggregates and nuclear TDP-43 were labeled using an antibody against phosphorylated TDP-43 (pTDP), clone 1D3 (MABN14, rat monoclonal, 1/100, Merck Millipore, MA, USA) or with anti-TDP-43 (12892-1-AP, rabbit polyclonal, 1/1000, ProteinTech, IL, USA) with a Dako autostainer Link 48, according to the manufacturer's protocol (Dako, Belgium). Briefly, after pre-treatment (pH=6) for antigen retrieval and deparaffinization, the sections were treated with peroxidase blocking reagent (Envision Flex Peroxidase-Blocking Reagent, Dako) for 5 min. Afterwards, a biotinylated anti-rat secondary antibody was used, followed by an ABC reaction to increase the detected signal (Vectastain Elite ABC HRP Kit, Vector labs, CA, USA). 3,3'-diaminobenzidine (Liquid DAB+ Substrate Chromogen System, Dako) was used as a chromogen to yield brown reaction products. Counterstaining with hematoxylin was performed. The slides were microscopically analyzed with a Leica DM2000 LED microscope and images were taken with a Leica DFC7000 T camera, at 200 or 400x magnification.

7.3.9   Statistical Analysis

Reported values are described as mean ± standard deviation unless indicated otherwise. All statistical analyses were performed using JMP and PRISM software (SAS Institute Inc., NC, USA; GraphPad Software, Inc., CA, USA). Body weight was analyzed using the Mann-Whitney U test with Bonferroni multiple testing correction. PET VOI-based data, MRS, DTI and perfusion MR data were analyzed using the standard least squares model, employing REML (restricted maximum likelihood estimation) with Tukey-Kramer post-hoc adjustments. Fixed effects included: pathology ('group'), time point ('time') and the group*time intercept. The term 'Subject' was added as a random effect. Survival analysis was performed using the Mantel-Cow method. A p-value < 0.05 was accepted as statistically significant.

7.4 RESULTS

7.4.1 ^{18}F-FDG PET imaging

To assess the effect of hTDP-43^{A315T} expression on cerebral glucose metabolism, we performed longitudinal *in vivo* ^{18}F-FDG-PET imaging. VOI- and voxel-wise analysis did not indicate significant changes in regional SUV values over time. Voxel-wise analysis did show decreased relative ^{18}F-FDG uptake (*i.e.* normalized to whole-brain ^{18}F-FDG uptake) in the unilateral motor- and somatosensory cortex of transgenic mice, as compared to controls (-15.8%; T_1 vs. T_2; **Figure 7.2A**). In the same time period, glucose metabolism significantly increased (+8%) in a cluster covering the substantia nigra, amygdaloid and reticular nucleus, extending towards the brain stem, in transgenic hTDP-43^{A315T} mice (**Figure 7.2B**). Between T_1 and T_3, transgenic mice also developed hypometabolism in the left lateral striatum (**Figure 7.2 C**). A detailed description of the cluster peak anatomical location and p-values are shown in **Table 7.1**.
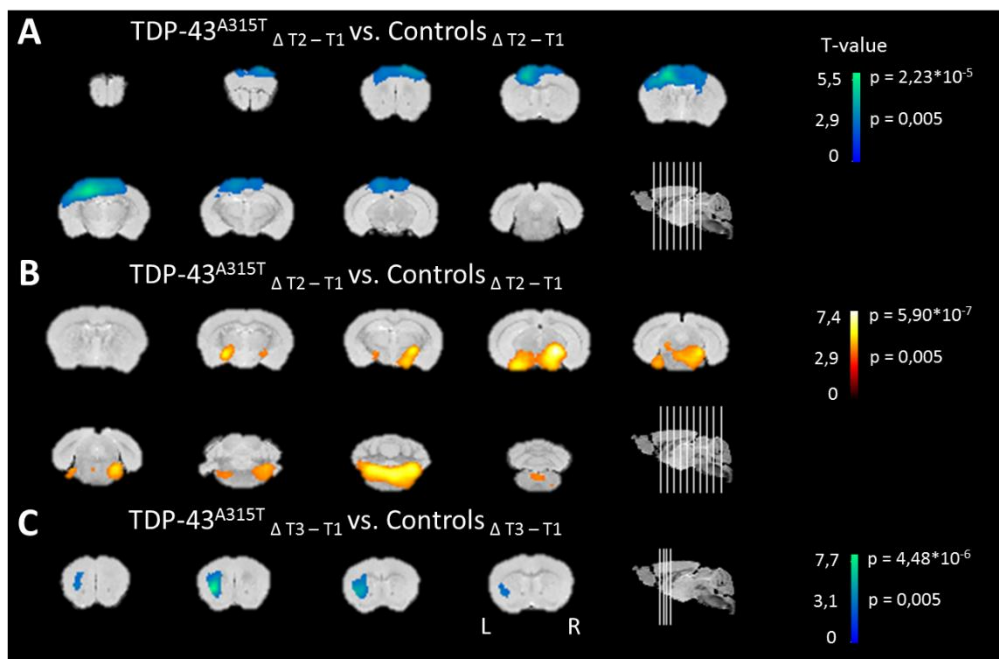
Figure 7.2. Relative ^{18}F-FDG uptake in hTDP-43^{A315T} transgenic mice. Functional T-maps are overlaid on coronal brain sections at p_{height}<0.005. Brain sections showing significantly **(A)** decreased glucose metabolism in a cluster comprising the left motor and somatosensory cortex and **(B)** elevated glucose uptake in the region of the substantia nigra, amygdaloid and reticular nucleus, in transgenic mice between time point 1 and 2 (T_1 vs. T_2), as compared with non-transgenic mice. **(C)** From T_1 to T_3, FDG uptake decreased in transgenic mice in a cluster covering the unilateral striatum, as compared to non-transgenic mice. The T-statistic color scale indicates the significance at the voxel level. The approximate age of the mice at the mentioned time points is: T_1: 3.5 months, T_2: 7 months, T_3: 11.5 months. Abbreviations: L, left; R, right; TDP-43^{A315T}, TAR DNA binding protein 43 carrying the A315T mutation.

	Cluster level		Voxel level		Intensity difference (%)	Structure
	p_{corr}	K_E	T	p_{uncorr}		Name
Controls Δ(t2-t1) < TDP-43^{A315T} Δ(t2-t1)	$8,26*10^{-5}$	6720	5,43	<0,001	+ 8,0 ± 5,5 %	Bilateral substantia nigra, amygdaloid nucleus and reticular nucleus
			4,71	<0,001		
			4,60	<0,001		
Controls Δ(t2-t1) > TDP-43^{A315T} Δ(t2-t1)	$9,29*10^{-5}$	8941	7,33	<0,001	- 15,8 ± 3,3 %	Unilateral motor and somatosensory cortex
			4,42	<0,001		
			3,24	0,002		
Controls Δ(t3-t1) > TDP-43^{A315T} Δ(t3-t1)	0,105	483	7,74	<0,001	- 9,0 ± 5,1 %	Unilateral striatum

Table 7.1. Voxel-wise ^{18}F-FDG PET analysis. Peak locations for the clusters in the group comparison at pheight<0.005 uncorrected and cluster extent > 200. Pcorr at cluster level, p-value corrected for the search volume; KE cluster extent; T, indication of statistical significance; puncorr, p-value uncorrected for the search volume. The age of the mice at T1-T3 scan sessions are: T1: 3.5 months, T2: 7 months, T3: 11.5 months. Intensity difference values are indicated as mean ± standard deviation.

7.4.2   Magnetic Resonance Spectroscopy

To assess potential neurometabolic alterations of the TDP mice, we acquired MR spectra (motor cortex: signal to noise ratio >15; line-width 10±3 Hz, hindbrain: SNR >11, line-width 12±3 Hz, water/lipid/artifact suppressed). Typical MR spectra obtained from the motor cortex of a hTDP-43^{A315T} mouse and non-transgenic control at T_1 are shown in **Figure 7.3**.

Of the metabolites, Glx and choline demonstrated time- and group-dependent differences in the motor cortex. Glx levels were significantly higher at early-stage acquisitions (T_1-T_2), in comparison with non-transgenic controls ($F_{[group \times time]}4.74=6.32$; p=0.0002; T_1: p=0,0018; T_2: p=0.0003). Choline levels depicted a gradual increase in hTDP-43^{A315T} mice, with significance at T_3 and T_5 ($F_{[group \times time]}4.74=6.32$; p=0.0006; T_3: p=0.03; T_5: p=0.0004). It should be noted that choline levels visualized by short-echo time MRS contain contributions from unbound free choline, glycerophosphorylcholine (GPC), phosphorylcholine (PC) and are often referred to as 'total choline' (tCho) or just choline.

In the hindbrain, Glx, creatine and choline levels depicted significant alterations. Glx concentrations showed both early- and late-stage group-dependent differences ($F_{[group \times time]}4.86=8.57$; p<0.0001). With respect to controls, we found Glx levels significantly increased at T_1 (p=0.0018), and subsequently decreased at T_4 (p<0.0001). Both groups showed an age-dependent drop in Glx concentrations between T_3 and T_5 ($F_{[time]}4.86=11.79$; p<0,0001; T_3-T_5: p<0,0001 in both groups). Creatine levels were influenced by the age of the animals, but not by pathology ($F_{[time]}4.86=5.43$; p=0,0006). By contrast, TDP-43^{A315T} mutant overexpression had a modest, but significant, effect on choline levels at late-stage time point T_5 ($F_{[group]}4.86=7.18$; p<0,0001; T_5: p=0.02), though time and interaction effects were not significant (p>0.05).
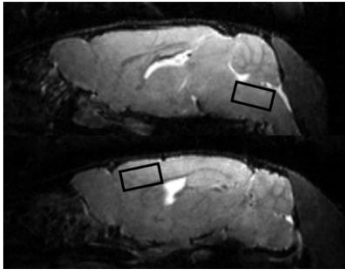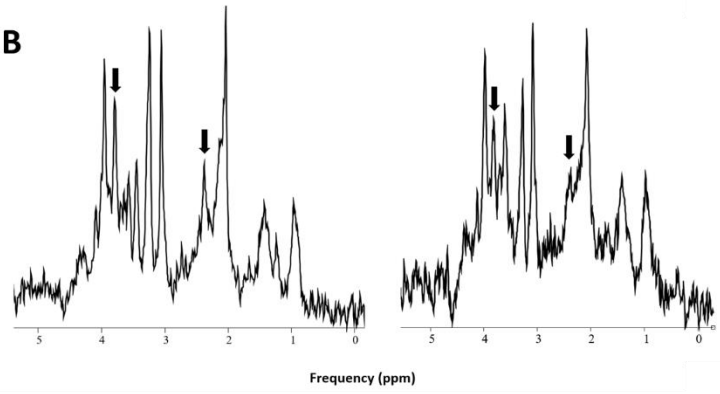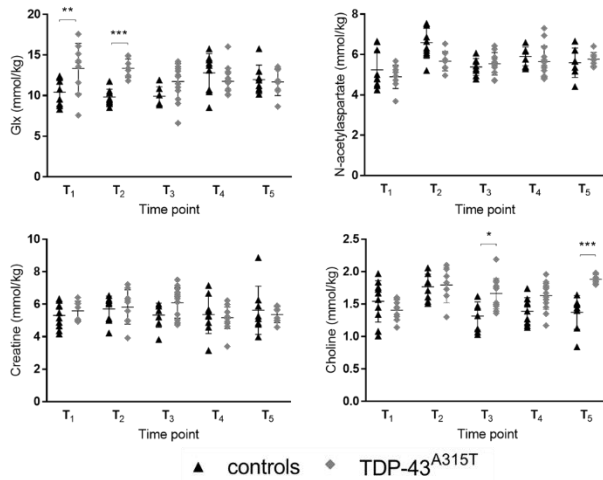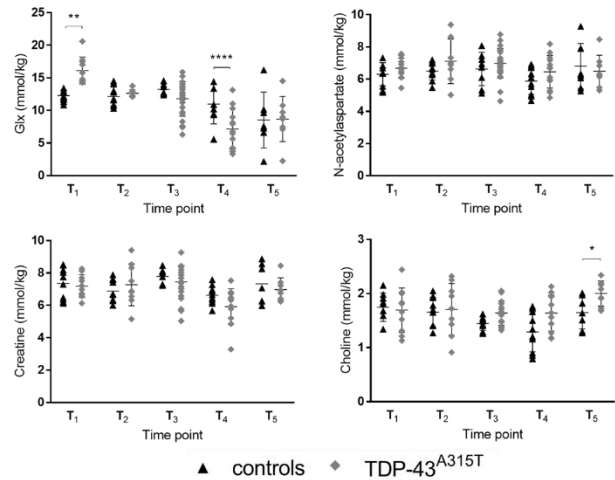
Figure 7.3. Evaluation of the metabolite profile in the motor cortex and hindbrain using MRI-guided ^{1}H-MRS. (A) Placement of the MRS voxel covering the hindbrain (top) and motor cortex (bottom), overlaid on a T_2-weighted MR image. (B) ^{1}H-MRS spectrum of the left motor cortex in a hTDP-43^{A315T} (left) and control mouse (right). Black arrows indicate the significantly different Glx (glutamate + glutamine) concentrations, as can be visually appreciated. (C-D) Overview of the 4 main neurometabolite concentrations, including Glx (glutamate + glutamine), N-acetylaspartate, creatine and choline. Concentrations measured in the motor cortex (C) and hindbrain (D) of hTDP-43^{A315T} and non-transgenic controls are displayed over time, visualized in dot plots. Time points mentioned in this figure are in correspondence with following approximate age of the animals: T_1: 2 months, T_2: 6 months, T_3: 9 months, T_4: 13,5 months, T_5: 16 months. Restricted maximum likelihood estimation. * p<0.05, ** p<0.01, *** p<0.001.

7.4.3 Perfusion MRI

Regional CBF values, obtained from ROIs in the motor cortex and striatum are represented in **Figure 7.4**. No significant changes in CBF was observed between the two groups in motor cortices and striatal ROIs.
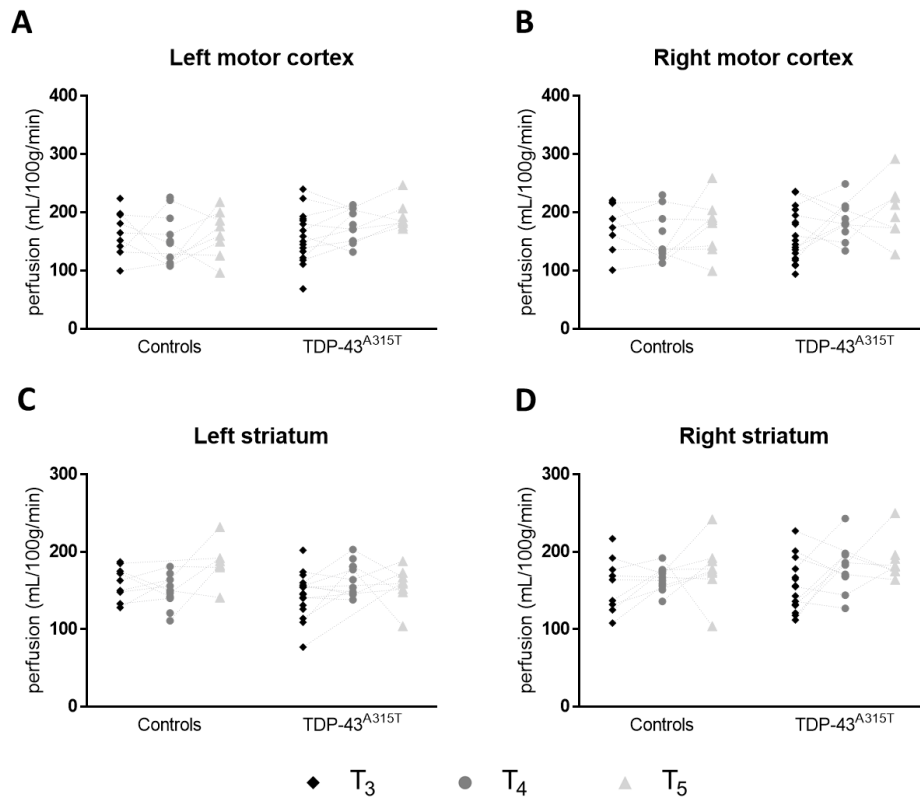
Figure 7.4. Cerebral blood perfusion in motor areas of the mouse cerebrum. Dot plots display perfusion values for the bilateral motor cortex **(A-B)** and striatum **(C-D)** of TDP-43^{A315T} mice and respective controls. ALS mice did not present with any significantly different perfusion values. Time points mentioned in this figure are in correspondence with following approximate age of the animals: T_3: 9 months, T_4: 13.5 months, T_5: 16 months.

7.4.4 Diffusion Tensor Imaging Measures

A summary of regional DTI metrics for the two groups are listed in **Table 7.2.** Significant differences in the DTI-based fractional anisotropy (FA), mean diffusivity (MD) and radial diffusivity (RD) between hTDP-43^{A315T} and WT mice were observed at T_4. In the striatum, a significant increase in FA ($F_{[group \times time]}2.48=4.62$; p=0.01; T_4: p=0.006) and decrease in RD ($F_{[group \times time]}2.48=6.80$; p=0.003; T_4: p=0.0001) were present. Of note, the group effect was non-significant for FA (p>0.05). In addition, a significant decrease in RD was present in the left motor cortex, which was not affected by the group*time interaction effect ($F_{[group]}1.17=8.74$; p=0.009; $F_{[time]}2.28=7.65$; p=0.002; T_4: p=0.03). A significant increase in MD in the brainstem region of both groups was also observed ($F_{[group \times time]}2.40=6.05$; p=0.005; $F_{[time]}2.40=14.80$; p<0.0001; T_4: p=0.03).

		Motor cortex		Striatum		Hindbrain	
		Controls	TDP-43^{A315T}	Controls	TDP-43^{A315T}	Controls	TDP-43^{A315T}
FA	T_3	$0{,}25 \pm 0{,}03$	$0{,}22 \pm 0{,}03$	$0{,}22 \pm 0{,}02$	$0{,}22 \pm 0{,}02$	$0{,}35 \pm 0{,}05$	$0{,}32 \pm 0{,}05$
	T_4	$0{,}24 \pm 0{,}03$	$0{,}20 \pm 0{,}05$	**$0{,}27 \pm 0{,}04$**	**$0{,}22 \pm 0{,}03^{\Omega}$**	$0{,}32 \pm 0{,}04$	$0{,}30 \pm 0{,}05$
	T_5	$0{,}21 \pm 0{,}02$	$0{,}20 \pm 0{,}03$	$0{,}20 \pm 0{,}02$	$0{,}21 \pm 0{,}04$	$0{,}24 \pm 0{,}03$	$0{,}26 \pm 0{,}03$
AD (10^{-3} mm^2/sec)	T_3	$0{,}77 \pm 0{,}03$	$0{,}76 \pm 0{,}02$	$0{,}75 \pm 0{,}03$	$0{,}75 \pm 0{,}03$	$0{,}74 \pm 0{,}09$	$0{,}72 \pm 0{,}09$
	T_4	$0{,}76 \pm 0{,}02$	$0{,}76 \pm 0{,}04$	$0{,}77 \pm 0{,}03$	$0{,}80 \pm 0{,}05$	$0{,}90 \pm 0{,}13$	$0{,}80 \pm 0{,}09$
	T_5	$0{,}75 \pm 0{,}02$	$0{,}75 \pm 0{,}05$	$0{,}76 \pm 0{,}02$	$0{,}77 \pm 0{,}02$	$0{,}70 \pm 0{,}06$	$0{,}72 \pm 0{,}04$
RD (10^{-3} mm^2/sec)	T_3	$0{,}53 \pm 0{,}02$	$0{,}55 \pm 0{,}03$	$0{,}54 \pm 0{,}02$	$0{,}55 \pm 0{,}03$	$0{,}45 \pm 0{,}07$	$0{,}45 \pm 0{,}08$
	T_4	**$0{,}53 \pm 0{,}02$**	**$0{,}56 \pm 0{,}03^{\Delta}$**	**$0{,}52 \pm 0{,}03$**	**$0{,}59 \pm 0{,}06^{\Theta}$**	$0{,}61 \pm 0{,}13$	$0{,}51 \pm 0{,}11$
	T_5	$0{,}55 \pm 0{,}01$	$0{,}56 \pm 0{,}02$	$0{,}56 \pm 0{,}01$	$0{,}56 \pm 0{,}02$	$0{,}48 \pm 0{,}04$	$0{,}49 \pm 0{,}02$
MD (10^{-3} mm^2/sec)	T_3	$0{,}61 \pm 0{,}02$	$0{,}62 \pm 0{,}03$	$0{,}61 \pm 0{,}02$	$0{,}61 \pm 0{,}02$	$0{,}55 \pm 0{,}08$	$0{,}54 \pm 0{,}08$
	T_4	$0{,}61 \pm 0{,}02$	$0{,}61 \pm 0{,}03$	$0{,}60 \pm 0{,}03$	$0{,}64 \pm 0{,}05$	**$0{,}71 \pm 0{,}13$**	**$0{,}60 \pm 0{,}01^{\Sigma}$**
	T_5	$0{,}61 \pm 0{,}02$	$0{,}63 \pm 0{,}020$	$0{,}63 \pm 0{,}01$	$0{,}63 \pm 0{,}01$	$0{,}55 \pm 0{,}05$	$0{,}56 \pm 0{,}02$

Table 7.2. Assessment of microstructural changes using diffusion tensor imaging. ROI analysis of fractional anisotropy (FA), axial diffusion (AD), radial diffusion (RD) and mean diffusion (MD) measured in the region of the motor cortex, striatum, and hindbrain of hTDP-43^{A315T} transgenic ALS mice and non-transgenic controls. Time points mentioned in this figure are in correspondence with following approximate age of the animals: T_3: 9 months, T_4: 13.5 months, T_5: 16 months. Values represent mean ± standard deviation. Significant alterations in MR diffusion were obtained by using the restricted maximum likelihood estimation model. Δ p<0.05, Ω and Σ p<0.01, Θ p<0.001.

7.4.5 Survival analysis and neuropathology

As expected, hTDP-43^{A315T} mice portrayed a significantly lower survival, as compared to non-transgenic mice, with a median survival of 480 days (X^2=12.94, p=0.0003; **Figure 7.5 A**). As previously described, disease onset and duration were highly variable. Mean age at symptom development was 310 ± 172 days and mice survived on average 78 ± 83 days following onset of symptoms. The weight of the mice significantly increased with age, but did not differ between groups ($F_{[time]}$ 14.413=23.67; p<0.0001; **Figure 7.5B**).

Interestingly, we observed an increased nuclear clearance of normal TDP-43 in aged, symptomatic TDP-43 mice (18 months of age) when compared to WT mice at 18 months of age, as well as compared to 10- and 21-months-old non-symptomatic TDP-43 mice, respectively (**Figure 7.6 A-D**). Cytoplasmic aggregates that are positive for phosphorylated TDP-43 (pTDP-43), were found in pyramidal neurons of layer V in the frontal cortex in symptomatic, 18 months old mice (pS409/pS410), although these inclusions were relatively rare (**Figure 7.6 E-H**).
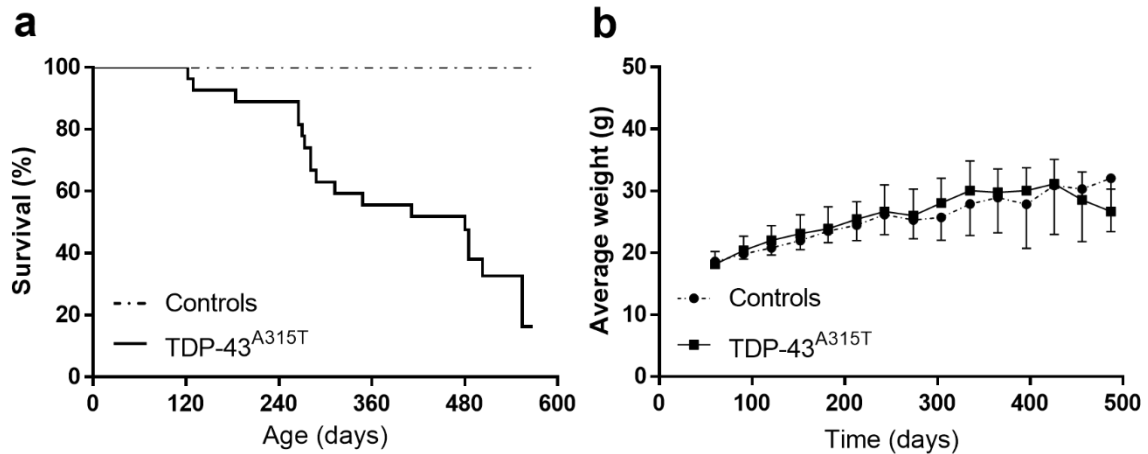
Figure 7.5. Life span and weight analysis in hTDP-43[A315T] transgenic mice. (a) Transgenic mice showed high variability regarding life span ranging from 122-554 days. (b) hTDP-43[A315T] did not have a significantly altered body weight in comparison with non-transgenic mice.
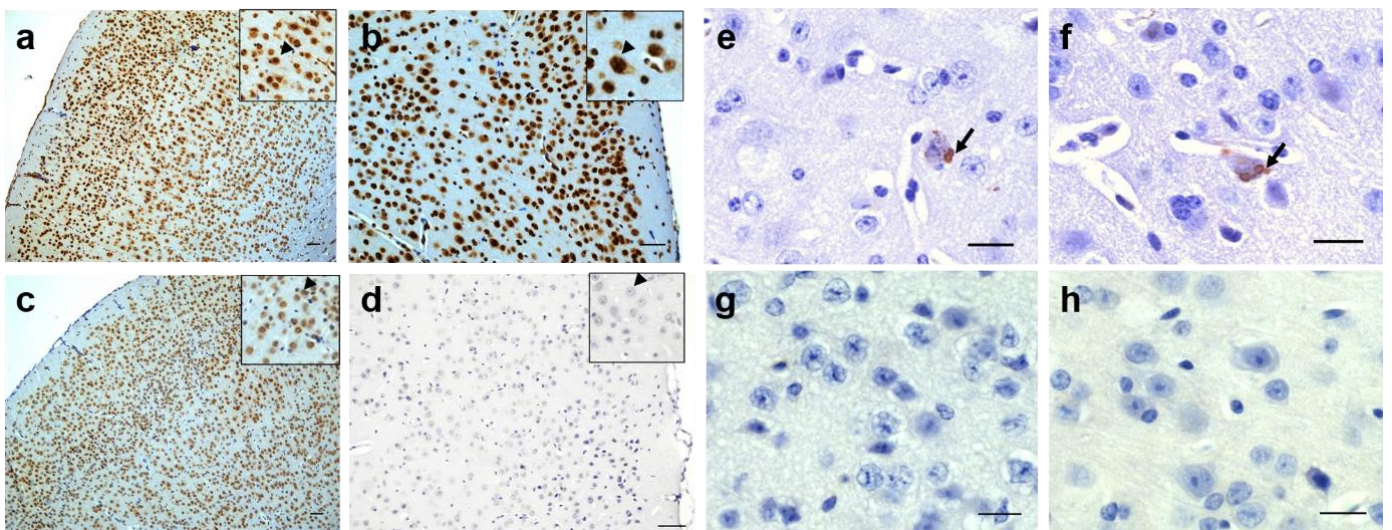
Figure 7.6. Nuclear clearance (A-D) and phosphorylated TDP-43 aggregates (E-H) associated with hTDP-43[A315T] expression. TDP-43 neuronal nuclear depletion assessment in the frontal cortex of (a) aged WT littermates (18 months), (b) younger, non-symptomatic hTDP-43[A315T] mice (10 months), (c) aged, but asymptomatic hTDP-43[A315T] mice (21 months) and (d) aged, symptomatic hTDP-43[A315T] mice (18 months). Nuclear clearance of TDP-43 was restricted to symptomatic 18-month-old hTDP-43A315T mice (d) but not seen in younger symptomatic animals or asymptomatic mice at the same age or older. Scale bars = 50µm. Phosphorylated TDP-43-immunoreactive cytoplasmic inclusions present in layer 5 of the frontal cortex of symptomatic 18-month-old hTDP-43[A315T] mice (e-f, arrows,) but not in aged WT littermates (18 months) (g) or in aged, asymptomatic hTDP-43[A315T] mice (21 months) (h). Scale bars = 20µm.

7.5 DISCUSSION

In this study, we systematically and non-invasively characterized the evolution of brain microstructural and metabolic alterations that occur in the hTDP-43^{A315T} mouse model using a multi-parametric *in vivo* PET-MRI-MRS approach.

The main finding of this study is that metabolic and functional imaging abnormalities observed by FDG-PET, MR spectroscopy (metabolite profiles for choline and glutamate+glutamine) and diffusion MRI preceded nuclear clearance of TDP-43 in neurons and the cytoplasmic aggregation of TDP-43 in neurons of the frontocentral cortex in the hTDP-43^{A315T} mouse. This finding may have impact on the interpretation of TDP-43 in ALS patients, probably representing just the "tombstone" of the underlying functional alterations of the neurons as indicated by the reduction of glucose metabolism and the changes in neurotransmitter levels. Since in our mouse model these changes occur in the areas which are typically affected in ALS such as the motor cortex, it is tempting to speculate whether such changes can be used for the early clinical diagnosis of ALS. Hypometabolism in the motor cortex has been demonstrated in ALS patients (Endo et al., 2017, D'hulst-Van Damme et al., 2018) and may be combined with imaging markers to identify ALS patients as early as possible.

Our longitudinal ^{18}F-FDG PET imaging study showed significantly lowered glucose metabolism in the motor and somatosensory cortices unilaterally, in parallel with an increase in the midbrain region, covering the bilateral substantia nigra, reticular and amygdaloid nucleus, and spreading towards the brain stem between three and seven months of age. By approximately one year of age, we also found decreased glucose utilization in the unilateral striatum in transgenic mice, as compared to non-transgenic controls.

These findings are in line with common metabolic patterns in ALS patients, where hypometabolism is generally found in the frontal and occipital lobes and relative hypermetabolism is present in the brainstem, amygdalae, cerebellum and medial temporal lobe (Agosta *et al.*, 2018). To our knowledge, no previous data have been presented, examining disease-related changes in cerebral glucose metabolism in TDP-43 transgenic mice models. Due to differences in transgene, symptom development and life span, it remains difficult to compare these findings to those in other commonly used rodent models of ALS, such as the SOD1. In this mouse model, carrying the SOD1^{G93A} mutation, research reported no significant effect on glucose utilization in motor-related regions (Lei *et al.*, 2018).

All metabolically altered regions (including cortex, striatum and midbrain regions) were shown to express the mutant transgene in neurons and glia (Wegorzewska *et al.*, 2009), and could therefore be affected by TDP-43 pathology. Also in ALS patients, TDP-43 immunoreactive lesions were found in the previously mentioned regions (Cykowski *et al.*, 2017). Given that 18F-FDG PET is an indicator of synaptic dysfunction and neurodegeneration, it is plausible that reduced FDG uptake in the motor cortex represents the pronounced neuronal loss and ubiquitin aggregate pathology in layer V, as previously shown by histological analysis (Wegorzewska *et al.*, 2009).

Of note, decreased FDG uptake has been associated with mitochondrial dysfunction, and subsequent neuronal loss in several disorders (Herrero-Mendez *et al.*, 2009; Tenney *et al.*, 2014). Mutant TDP-43 was shown to accumulate in the mitochondria of neurons, impair respiratory complex I subunits, directly

causing disrupted cellular bioenergetics (Wang *et al.*, 2016). This altered metabolic state may further explain the altered glucose metabolism we observed in several motor-related cerebral regions in TDP-43 transgenic mice.

On the other hand, hypermetabolic patterns in the mid- and hindbrain may correspond to inflammation involving microglial activation. In the SOD1[G93A] model, Gargiulo *et al.* reported "microgliopathy" in this region surrounding several motor nuclei, using ^{18}F-DPA-714 PET imaging of the translocator protein (TSPO), a well-known marker for neuroinflammation (Gargiulo *et al.*, 2016).

We examined the evolution of the neurochemical profile in the motor cortex and hindbrain of hTDP-43[A315T] and control mice using ^{1}H-MRS. Our results showed significant changes in Glx and choline levels in the motor cortex and hindbrain of hTDP-43[A315T] mice compared to controls. Elevations in the Glx levels at the 2- and 6-month time points suggest an alteration in glutamatergic transmission creating an imbalance between the excitatory and inhibitory neuronal activity in both regions. In correspondence with our findings, Lei and colleagues showed increased levels of glutamate in the motor cortex of pre-symptomatic hSOD1[G93A] transgenic animals (Lei *et al.*, 2018; Weerasekera *et al.*, 2018). The glutamate-glutamine cycling in the glia and neurons is a complex process, where the enzyme glutamine synthetase plays a vital role. Impairment of this enzyme, which is highly susceptible to oxidative damage, can lead to a decreased metabolism of glutamate to glutamine (Oliver *et al.*, 1990). Thereby, an increase in tissue levels of glutamate/glutamine could also reflect impaired energy metabolism, similar to observations in transgenic mice of Huntington's disease (Jenkins *et al.*, 2000).

In this study, a time- and group-dependent increase in total choline was observed in the motor cortex of transgenic mice at nine months. In the hindbrain, this increase was also present in 16-month-old mice. Choline-containing compounds are involved in pathways of phospholipid synthesis but also degradation as well as biosynthesis of neurotransmitter acetylcholine (Duarte *et al.*, 2012). Elevated choline levels have been systematically observed in neurodegenerative diseases such as Alzheimer's disease, Parkinson's disease and multiple sclerosis (Firbank *et al.*, 2002; Gonzalez-Toledo *et al.*, 2006; Narayanan *et al.*, 2006). Moreover, Duarte and colleagues reported brain choline levels to gradually increase as part of the normal ageing process and that this increase may be attributed to an increased release of water-soluble choline-compounds from cellular membranes (Duarte *et al.*, 2014).

Previous studies have reported that a decrease in glutamatergic transmission activity may activate a compensatory mechanism such as regulation of a secondary messenger system (Belousov *et al.*, 2001; Liu *et al.*, 2008). Interestingly, in the hindbrain, one such mechanism may cause a late-stage increase in the expression of acetylcholine. The MRS signal of choline has been used to assess the alteration of acetylcholine level in the brain (Lindner *et al.*, 2017). Therefore, the observed upregulation of choline levels at a later stage may be due to an upregulation of acetylcholine signaling following a decrease glutamate-mediated neurotransmission activity, as indicated by Glx measurements.

Assessing changes in cerebral blood flow (CBF) yields important information on the onset and progression of various pathological conditions (Yonas *et al.*, 2005; Struys *et al.*, 2017; Govaerts *et al.*, 2019). However, up to date, perfusion MRI in animal models of ALS has not been implemented. CBF is tightly coupled to neuronal activity of the brain, and is often considered as an indirect measurement of the energy demands of the brain, similar to FDG-PET. An increase in CBF is suggested to enhance the delivery of oxygen and substrates to the high-energy demand regions, and to facilitate the elimination

of toxic byproducts of cerebral metabolism (Peterson *et al.*, 2011). A previous arterial spin labeled MR study demonstrated hypoperfusion in ALS patients compared to healthy subjects in the frontal, medial, middle cingulate cortices, and precuneus (Rule *et al.*, 2010). In correspondence with clinical findings, spinal blood flow was progressively decreased at pre- and post-symptomatic stages in SOD1^{G93A} mice, as detected by in vivo capillary imaging (Miyazaki *et al* 2012). In this study, no significant age or group-related differences in basal CBF were observed in cerebral motor regions. It should be noted that anesthetics have a strong impact on cardiac function, brain function or microvascular hemodynamics, and the combination of all these effects could lead to modifications of CBF (Hendrich *et al.*, 2001). Isoflurane anesthesia tends to increase CBF (Govaerts *et al.*, 2019), which may have masked observations of subtle differences in perfusion values in the groups studied. Therefore, barbiturates such as a ketamine/xylazine combination may have been be a better choice of anesthetics. Alternatively, TDP pathology may not be responsible for the perfusion changes seen in ALS patients. Diffusion MRI-based measures such as the FA, MD, RD and AD were used to evaluate axonal and myelin integrity in the mouse cerebrum (Madden *et al.*, 2013; Ontaneda *et al.*, 2017). Although no age-related changes in diffusion parameters were found for both groups, disease-associated changes were detected, but only in mice at approximately 14 months of age, suggesting that hTDP-43^{A315T} expression is associated with limited microstructural changes in motor-related regions of the mouse brain.

In the apparently healthy bran, TDP-43 is predominantly located in the nucleus where it is involved in RNA metabolism. Within TDP-43 proteinopathies, abnormal cleavage and phosphorylation (pS409/pS140) of the protein has been associated with nuclear depletion and formation of pathological cytoplasmic inclusions (NCIs) (Arai *et al.*, 2006). A positive correlation was found between cytoplasmic aggregate formation and neurotoxicity *in vitro*, linking TDP-43 pathology to neurodegeneration (Barmada *et al.*, 2010). Thereby it has been hypothesized that in models of overexpressed human TDP-43, the loss of endogenous nuclear TDP-43 is the mechanism responsible for toxicity, rather than the toxic gain of function in the cytoplasm (Vanden Broeck *et al.*, 2014). This nuclear depletion, and subsequent loss of function, might constitute an early event in the disease pathology and might become more pronounced as the disease progresses (Neumann *et al.*, 2006). The differences in the nuclear clearance of non-phosphorylated TDP-43 between symptomatic 18 month-old TDP-43 mice, but not younger TDP-43 mice, corroborates this hypothesis. This becomes important, considering that we did not observe this nuclear depletion in aged WT littermates or non-symptomatic TDP-43 mice, which suggests an association of normal, nuclear TDP-43 depletion with the development of the disease, specifically the development of symptoms.

Several studies using *in vitro* and animal models have tried to address these mechanisms of degeneration. A study using primary rat cortical neuronal cultures showed that overexpression of A315T mutation is positively correlated with neurotoxicity and is associated with cytoplasmic aggregate formation (Barmada *et al.*, 2010). Abnormally phosphorylated TDP-43 (pS409/pS410) has been detected in the spinal cord of mutant TDP-43 mouse models, but less frequently in the brain (Xu *et al.*, 2011; White *et al.*, 2018). Despite the fact that ubiquitin-positive aggregates have been previously detected in this model, cytoplasmic inclusions positive for phosphorylated TDP-43 have not been described (Wegorzewska *et al.*, 2009). In our study, we observed the presence of phosphorylated TDP-43 aggregates in the cortex of symptomatic, 18-month old mice, but not in the brains of younger animals. Taking the highly variable life span and symptom onset in this cohort into account, the group-based acquisition protocol that was employed in our study is a main limitations. To improve the detection of

disease-related changes, one might opt for a dynamic acquisition protocol based on each animals' individual disease progression. However, this strategy may be challenging concerning logistics and statistical analysis.

Together, the presented longitudinal *in vivo* PET-MR data, reveal several important neurochemical and neuropathological alterations in the hTDP-43^{A315T} ALS mouse model, indicating that, multimodal imaging modalities such as PET and MR can form a powerful tool for longitudinal non-invasive follow-up of disease progression in preclinical animal models.

7.6 REFERENCES

Agosta F, Altomare D, Festari C, Orini S, Gandolfo F, Boccardi M, Arbizu J, Bouwman F, Drzezga A, Nestor P, Nobili F, Walker Z, Pagani M, Disorders E-ETFftPoF-PfDN (2018) Clinical utility of FDG-PET in amyotrophic lateral sclerosis and Huntington's disease. *Eur J Nucl Med Mol Imaging* 45:1546-1556.

Arai T, Hasegawa M, Akiyama H, Ikeda K, Nonaka T, Mori H, Mann D, Tsuchiya K, Yoshida M, Hashizume Y, Oda T. TDP-43 is a component of ubiquitin-positive tau-negative inclusions in frontotemporal lobar degeneration and amyotrophic lateral sclerosis. *Biochem Biophys Res Commun*. 2006: 351:602-611.

Barmada SJ, Skibinski G, Korb E, Rao EJ, Wu JY, Finkbeiner S. Cytoplasmic mislocalization of TDP-43 is toxic to neurons and enhanced by a mutation associated with familial amyotrophic lateral sclerosis. J Neurosci. 2010: 30:639-649.

Beel S, Herdewyn S, Fazal R, De Decker M, Moisse M, Robberecht W, Van Den Bosch L, Van Damme P. Progranulin reduces insoluble TDP-43 levels, slows down axonal degeneration and prolongs survival in mutant TDP-43 mice. *Mol Neurodegener*. 2018 13:55.

Belousov AB, O'Hara BF, Denisova JV. Acetylcholine becomes the major excitatory neurotransmitter in the hypothalamus in vitro in the absence of glutamate excitation. *J Neurosci*. 2001: 21:2015-2027.

Casteels C, Vunckx K, Aelvoet SA, Baekelandt V, Bormans G, Van Laere K, Koole M. Construction and evaluation of quantitative small-animal PET probabilistic atlases for [(1)(8)F]FDG and [(1)(8)F]FECT functional mapping of the mouse brain. PLoS One. 2013: 8.

Chia R, Chio A, Traynor BJ. Novel genes associated with amyotrophic lateral sclerosis: diagnostic and clinical implications. *Lancet Neurol*. 2018: 17:94-102.

Cykowski MD, Powell SZ, Peterson LE, Appel JW, Rivera AL, Takei H, Chang E, Appel SH. Clinical Significance of TDP-43 Neuropathology in Amyotrophic Lateral Sclerosis. *J Neuropathol Exp Neurol*. 2017: 76:402-413.

Duarte JM, Do KQ, Gruetter R. Longitudinal neurochemical modifications in the aging mouse brain measured *in vivo* by 1H magnetic resonance spectroscopy. Neurobiol Aging. 2014: 35:1660-1668.

Duarte JM, Lei H, Mlynarik V, Gruetter R. The neurochemical profile quantified by *in vivo* 1H NMR spectroscopy. Neuroimage. 2012: 61:342-362.

Esmaeili MA, Panahi M, Yadav S, Hennings L, Kiaei M. Premature death of TDP-43 (A315T) transgenic mice due to gastrointestinal complications prior to development of full neurological symptoms of amyotrophic lateral sclerosis. Int J Exp Pathol. 2013: 94:56-64.

Firbank MJ, Harrison RM, O'Brien JT. A comprehensive review of proton magnetic resonance spectroscopy studies in dementia and Parkinson's disease. Dement Geriatr Cogn Disord. 2002: 14:64-76.

Gargiulo S, Anzilotti S, Coda AR, Gramanzini M, Greco A, Panico M, Vinciguerra A, Zannetti A, Vicidomini C, Dolle F, Pignataro G, Quarantelli M, Annunziato L, Brunetti A, Salvatore M, Pappata S. Imaging of brain TSPO expression in a mouse model of amyotrophic lateral sclerosis with (18)F-DPA-714 and micro-PET/CT. *Eur J Nucl Med Mol Imaging*. 2016: 43:1348-1359.

Govaerts K, Lechat B, Struys T, Kremer A, Borghgraef P, Van Leuven F, Himmelreich U, Dresselaers T. NMR Biomed. 2019;32(2).

Gitcho MA, Baloh RH, Chakraverty S, Mayo K, Norton JB, Levitch D, Hatanpaa KJ, White CL, 3rd, Bigio EH, Caselli R, Baker M, Al-Lozi MT, Morris JC, Pestronk A, Rademakers R, Goate AM, Cairns NJ. TDP-43 A315T mutation in familial motor neuron disease. *Ann Neurol*. 2008: 63:535-538.

Gonzalez-Toledo E, Kelley RE, Minagar A. Role of magnetic resonance spectroscopy in diagnosis and management of multiple sclerosis. Neurol Res. 2006: 28:280-283.

Guo Y, Wang Q, Zhang K, An T, Shi P, Li Z, Duan W, Li C. HO-1 induction in motor cortex and intestinal dysfunction in TDP-43 A315T transgenic mice. *Brain Res*. 2012: 1460:88-95.

Hampton AL, Hish GA, Aslam MN, Rothman ED, Bergin IL, Patterson KA, Naik M, Paruchuri T, Varani J, Rush HG. Progression of ulcerative dermatitis lesions in C57BL/6Crl mice and the development of a scoring system for dermatitis lesions. *J Am Assoc Lab Anim Sci*. 2012: 51:586-593.

Hardiman O, van den Berg LH. Edaravone: a new treatment for ALS on the horizon? *Lancet Neurol*. 2017: 16:490-491.

Hendrich KS, Kochanek PM, Melick JA, Schiding JK, Statler KD, Williams DS, Marion DW, Ho C. Cerebral perfusion during anesthesia with fentanyl, isoflurane, or pentobarbital in normal rats studied by arterial spin-labeled MRI. *Magn Reson Med*. 2001: 46:202-206.

Herdewyn S, Cirillo C, Van Den Bosch L, Robberecht W, Vanden Berghe P, Van Damme P. Prevention of intestinal obstruction reveals progressive neurodegeneration in mutant TDP-43 (A315T) mice. *Mol Neurodegener* . 2014: 9:24.

Herrero-Mendez A, Almeida A, Fernandez E, Maestre C, Moncada S, Bolanos JP. The bioenergetic and antioxidant status of neurons is controlled by continuous degradation of a key glycolytic enzyme by APC/C-Cdh1. *Nat Cell Biol*. 2009: 11:747-752.

Jenkins BG, Klivenyi P, Kustermann E, Andreassen OA, Ferrante RJ, Rosen BR, Beal MF. Nonlinear decrease over time in N-acetyl aspartate levels in the absence of neuronal loss and increases in glutamine and glucose in transgenic Huntington's disease mice. *J Neurochem*. 2000: 74:2108-2119.

Kim SG, Tsekos NV. Perfusion imaging by a flow-sensitive alternating inversion recovery (FAIR) technique: Application to functional brain imaging. *Magnet Reson Med*. 1997: 37:675-675.

Krecic AM, Swanson MS. hnRNP complexes: composition, structure, and function. *Curr Opin Cell Biol*. 1999: 11:363-371.

Lagier-Tourenne C, Cleveland DW. Rethinking ALS: the FUS about TDP-43. *Cell*. 2009: 136:1001-1004.

Lei H, Dirren E, Poitry-Yamate C, Schneider BL, Gruetter R, Aebischer P. Evolution of the neurochemical profiles in the G93A-SOD1 mouse model of amyotrophic lateral sclerosis. *J Cereb Blood Flow Metab*. 2018.

Leigh PN, Whitwell H, Garofalo O, Buller J, Swash M, Martin JE, Gallo JM, Weller RO, Anderton BH. Ubiquitin-immunoreactive intraneuronal inclusions in amyotrophic lateral sclerosis. Morphology, distribution, and specificity. *Brain*. 1991. 114 (Pt 2):775-788.

Madden DJ, Bennett IJ, Burzynska A, Potter GG, Chen NK, Song AW. Diffusion tensor imaging of cerebral white matter integrity in cognitive aging. *Biochim Biophys Acta*. 2011;1822(3):386-400.

Lindner M, Bell T, Iqbal S, Mullins PG, Christakou A (2017) *In vivo* functional neurochemistry of human cortical cholinergic function during visuospatial attention. *PLoS One.* 12;

Narayanan S, Francis SJ, Sled JG, Santos AC, Antel S, Levesque I, Brass S, Lapierre Y, Sappey-Marinier D, Pike GB, Arnold DL. Axonal injury in the cerebral normal-appearing white matter of patients with multiple sclerosis is related to concurrent demyelination in lesions but not to concurrent demyelination in normal-appearing white matter. *Neuroimage*. 2006; 29:637-642.

Neumann M, Sampathu DM, Kwong LK, Truax AC, Micsenyi MC, Chou TT, Bruce J, Schuck T, Grossman M, Clark CM, McCluskey LF, Miller BL, Masliah E, Mackenzie IR, Feldman H, Feiden W, Kretzschmar HA, Trojanowski JQ, Lee VM. Ubiquitinated TDP-43 in frontotemporal lobar degeneration and amyotrophic lateral sclerosis. *Science*. 2006; 314:130-133.

Niessen HG, Debska-Vielhaber G, Sander K, Angenstein F, Ludolph AC, Hilfert L, Willker W, Leibfritz D, Heinze HJ, Kunz WS, Vielhaber S. Metabolic progression markers of neurodegeneration in the transgenic G93A-SOD1 mouse model of amyotrophic lateral sclerosis. *Eur J Neurosci*. 2007; 25:1669-1677.

Oliver CN, Starke-Reed PE, Stadtman ER, Liu GJ, Carney JM, Floyd RA. Oxidative damage to brain proteins, loss of glutamine synthetase activity, and production of free radicals during ischemia/reperfusion-induced injury to gerbil brain. *Proc Natl Acad Sci*. 1999; 87:5144-5147.

Ontaneda D, Sakaie K, Lin J, Wang XF, Lowe MJ, Phillips MD, Fox RJ. Measuring Brain Tissue Integrity during 4 Years Using Diffusion Tensor Imaging. *AJNR Am J Neuroradiol*. 2017; 38(1):31-38.

Perrin S (2014) Preclinical research: Make mouse studies work. *Nature*; 507:423-425.

Peterson EC, Wang Z, Britz G. Regulation of cerebral blood flow. *Int J Vasc Med*. 2011; 823525.

Ratiney H, Coenradie Y, Cavassila S, van Ormondt D, Graveron-Demilly D. Time-domain quantitation of 1H short echo-time signals: background accommodation. *MAGMA*. 2004; 16:284-296.

Rule RR, Schuff N, Miller RG, Weiner MW. Gray matter perfusion correlates with disease severity in ALS. Neurology. 2010; 74:821-827.

Starcuk Z, Starcukova J, Strbak O, Graveron-Demilly D. Simulation of coupled-spin systems in the steady-state free-precession acquisition mode for fast magnetic resonance (MR) spectroscopic imaging. Meas Sci Technol. 2009; 20.

Stefan D, Di Cesare F, Andrasescu A, Popa E, Lazariev A, Vescovo E, Strbak O, Williams S, Starcuk Z, Cabanas M, van Ormondt D, Graveron-Demilly D. Quantitation of magnetic resonance spectroscopy signals: the jMRUI software package. Meas Sci Technol. 2009; 20.

Struys T, Govaerts K, Oosterlinck W, Casteels C, Bronckaers A, Koole M, Van Laere K, Herijgers P, Lambrichts I, Himmelreich U, Dresselaers T. *J Cereb Blood Flow Metab*. 2017;37(2):726-739.

Tenney JR, Rozhkov L, Horn P, Miles L, Miles MV. Cerebral glucose hypometabolism is associated with mitochondrial dysfunction in patients with intractable epilepsy and cortical dysplasia. *Epilepsia*. 2014; 55:1415-1422.

Vanden Broeck L, Callaerts P, Dermaut B. TDP-43-mediated neurodegeneration: towards a loss-of-function hypothesis? *Trends Mol Med*. 2014; 20:66-71.

Wang W, Wang L, Lu J, Siedlak SL, Fujioka H, Liang J, Jiang S, Ma X, Jiang Z, da Rocha EL, Sheng M, Choi H, Lerou PH, Li H, Wang X. The inhibition of TDP-43 mitochondrial localization blocks its neuronal toxicity. *Nat Med*. 2016; 22:869-878.

Weerasekera A, Sima DM, Dresselaers T, Van Huffel S, Van Damme P, Himmelreich U. Non-invasive assessment of disease progression and neuroprotective effects of dietary coconut oil supplementation in the ALS SOD1(G93A) mouse model: A (1)H-magnetic resonance spectroscopic study. *Neuroimage Clin*. 2018; 20:1092-1105.

Wegorzewska I, Bell S, Cairns NJ, Miller TM, Baloh RH. TDP-43 mutant transgenic mice develop features of ALS and frontotemporal lobar degeneration. *Proc Natl Acad Sci*. 2009; 106:18809-18814.

White MA *et al*. TDP-43 gains function due to perturbed autoregulation in a Tardbp knock-in mouse model of ALS-FTD. *Nat Neurosci*. 2018; 21:552-563.

Wong KP, Sha W, Zhang X, Huang SC. Effects of administration route, dietary condition, and blood glucose level on kinetics and uptake of 18F-FDG in mice. *J Nucl Med*. 2011; 52:800-807.

Xu YF, Zhang YJ, Lin WL, Cao X, Stetler C, Dickson DW, Lewis J, Petrucelli L. Expression of mutant TDP-43 induces neuronal dysfunction in transgenic mice. *Mol Neurodegener*. 2011; 6:73.

Yonas H, Sesay M, Calli C, Liu HM, Lomena F, Nasel C, Meyer JS, Yunten N, Anckarsater H, Wintermark M. The goal is quantitative cerebral blood flow. *J Neuroradiol*. 2005; 32:291-293.

8. |General Discussion, Limitations and Future Perspectives

8.1 General conclusion

In this thesis, *in vivo* magnetic resonance imaging and spectroscopy in combination with other experimental procedures were used in clinical and pre-clinical settings. In the clinical setting, the primary focus was to investigate the changes in neurochemical profiles of healthy subjects due to normal aging and of patients with neurodegenerative disease states, specifically amyotrophic lateral sclerosis. As for the pre-clinical setting, imaging techniques were used as a tool to non-invasively monitor disease onset, progression and for monitoring therapy. In general, this work aimed in particular to further develop and apply quantitative *in vivo* neurochemical profiling by MRS in the investigation of ALS as an adjunct to standard neuroimaging, biochemical analyses and clinical assessment. Limitation of the techniques employed in this thesis are discussed and future perspectives are outlines in the next sections.

The analyses of trends in Europe and the USA show clearly that ALS incidence is rapidly increasing. One explanation for this trend could be the increased life-span in those developed countries. Aging is found to be a major risk factor for both, familial and sporadic neurodegenerative disorders. However, how the link between aging and ALS can be proven is still a major question in contemporary neuroscience. This prompts us to ask questions such as, what neurostructurual and neurometabolic changes occur in normal aging, and where/how does normal aging evolve into pathological neurodegeneration? ALS is characterized by progressive muscle weakness which mainly affects the motor performance. In order to elucidate the link between normal aging and ALS, it is essential to understand the relationship between neurometabolic changes in normal aging in connection with motor performance. While many studies focused mainly on the contribution of neurometabolite alterations to cognitive abilities (Kant arci *et al*., 2002; Ross *et al*., 2006; Mondego *et al*., 2011; Purges *et al*., 2017; Tomato *et al*., 2018), studies examining the neurometabolic changes in relation to motor performance in 'normal' aging are limited. In **chapter 3**, we examined the associations between age-related neurometabolite alterations in the motor and occipital cortices with motor performance.

MRS results from the aging study showed an overall decrease in the concentration of many MRS-detectable brain neurometabolites such as NAA, Cr, and Glx in both regions of interest with increasing age. Overall, our findings from this study pointed towards heterogeneous alterations of neurometabolites, which could be caused by region-specific neurodegenerative processes as previously proposed by Grace & Apiarian (Grace & Apiarian *et al*., 2001). Direct evidence for this hypothesis was provided in a recent study by Ding *et al* (Ding *et al*., 2016), who applied whole brain ^{1}H-MR spectroscopic (wbMRS) imaging to study metabolite concentrations in the gray matter and white matter of different brain regions. They showed that age-dependent decrease of NAA content occurred predominantly in gray matter, whereas age-related decline of NAA content in white matter occurred only in the right and left frontal lobes and the left temporal lobe. Based on these findings, we assume that age-related decrease of cerebral NAA observed in our study occurred predominantly due to a reduction in white matter volume and loss of neuronal density. The fact that within voxel brain matter and global brain

matter contents positively correlate with a neurometabolite decrease as found in our study further adds validity to this assumption. Interestingly, observations from our study showed that NAA concentrations in the motor cortex are slightly more susceptible to aging compared to other neurometabolites. Furthermore, Ding's study suggest that neurodegenerative changes associated with gray matter loss may have greater consequences on NAA content than on the content of other gray neruometabolites such as Glx. These findings suggest that a reduction in the concentration of NAA may be driven by age-related neurodegenerative processes in both gray and white matter substructures whereas age-related changes in the levels of the remaining metabolites were likely subject to tissue-specific alterations either in gray matter (Glx) or white matter (choline, myo-Inositol). Therefore, we can conclude that these structural and neurometabolic changes are an inevitable part of the normal aging process, and not necessarily related to neurodegenerative disease. It is likely that the vulnerability of these areas to normal age-related changes contributes to their vulnerability to pathological processes involved in neurodegenerative diseases such as ALS.

Over the past decades, MRI and MRS techniques have proven to be powerful investigation tools for non-invasive studies in ALS patients (Turner *et al.*, 2009). Despite the availability of functional rating scales and various diagnostic routines, both early diagnosis and prognosis remain a difficult task in ALS (Brooks *et al.*, 2000; Costa *et al.*, 2012). In order to improve this shortcoming, the identification and validation of disease-specific biomarkers for disease onset and monitoring is critical. Discovering biomarkers will also have a strong impact on the development of promising pharmacological agents and designing cost effective randomized clinical trials (RCT) in ALS. Even though neurochemical biomarkers have started to show the potential to monitor and assess disease progression in ALS, they have not been able yet to have a real impact on the accuracy of diagnosis. Neuroimaging offers a noninvasive approach to identify biomarkers and to monitor disease state in ALS. Major developments in neuroimaging have been the application of multiparametric MRI to exclude diseases that mimic ALS (Filippi *et al.*, 2010) and innovations in novel acquisition protocols and processing tools, which have led this technique to the forefront of biomarker discovery (Turner *et al.*, 2010). In our study of ALS patients, described in **chapter 4**, we applied conventional and advanced edited MRS sequences to further investigate neurometabolic changes in the motor cortex of ALS patients and their relation to clinical parameters. Conventional PRESS MRS data showed a decrease in NAA, increase in Glx and an increase in *myo*-inositol levels in the motor cortex of ALS patients compared to healthy, age-matched controls. NAA levels in the bulbar-onset group were found to be significantly lower compared to the limb-onset group. We also showed correlations for mIns and Glx with disease progression measured by the ALSFRS-R score. In line with our results are previous studies that have reported changes mainly in the motor cortex of ALS patients (Pohl *et al.*, 2001; Kalra *et al.*, 2006; Unrath *et al.*, 2007; Lombardo *et al.*, 2009; Verma *et al.*, 2013; Foerster *et al* 2014; Cervo *et al.*, 2015; Atassi *et al.*, 2017; Cheong *et al.*, 2017). Numerous contradictory reports have shown either higher or lower levels of Glx in the motor cortex of ALS patients (Bowen *et al.*, 2002; Han *et al.*, 2010; Kalra *et al.*, 2013). However, a recent study by Cheong *et al* (Cheong *et al.*, 2017) suggests that motor cortex glutamate levels depend on the disease stage in ALS. Our finding of Glx levels correlating with disease progression supports this view.

A major limitation of using conventional MRS sequences to acquire low-concentration metabolites such as GABA and glutathione using low field clinical MR scanners is the rather poor spectral resolution/ overlap of signals and the low SNR, which imposes for the latter a lower limit on the scan time for a given region of interest (Puts *et al.*, 2012; Mullins *et al.*, 2014). Successive acquisition of MRS sequences

to determine GABA and glutathione concentrations would generally take about 20 minutes per volume of interest using MEGA-PRESS editing techniques. Therefore, not many studies measure both compounds due to these time constrains. In this study, we have demonstrated for the first time the simultaneous acquisition of GABA and glutathione in half the scan time in ALS patients using the novel HERMES editing sequence. Our data showed no difference in GABA levels between the ALS group and healthy controls. However, since all patients participated in this study were taking Riluzole and since Riluzole is known to act on GABAergic systems (Foerster *et al.*, 2013), the interpretation of GABA levels in the two groups becomes challenging. Future studies should focus on newly recruited patients that are not yet under medication. As for glutathione levels, a trend of decreased concentrations was observed for the ALS group compared to healthy controls. Using spectral editing methods, a study by Weiduschat *et al* (Weiduschat *et al.*, 2014) reported lower levels of glutathione in the motor cortex of ALS patient, while a recent study by Cheong *et al* (Cheong *et al.*, 2017) reported no differences in glutathione levels. One explanation for this incongruity would be the difference between the patient cohorts' disease stages, where one study recruited more early stage patients and the other more severe stage patients.

In our study as well as in other ^{1}H-MRS studies performed on ALS patients, reduced NAA levels in the motor cortex is the most frequently reported metabolic alteration. Significantly lower NAA levels in the motor cortex is also widely reported in normal aging and other neurodegenerative disease ^{1}H-MRS studies. The reduction of NAA in the cortex with 'normal aging' is consistent with histological evidence of neuronal loss (Simic *et al.* 1997) and volumetric MR imaging measurements of decreased gray matter (Matsumae *et al.*, 1996; Lim *et al.*, 1997). Moreover, diminishing NAA levels reported during the middle age period correlates with brain volume decrease found in subjects older than fifty years (Double *et al.*, 1996). Therefore, our findings from both clinical studies are in overall agreement with previous histological, anatomical, and MR spectroscopic results.

As mentioned earlier, spectral editing methods such as the MEGA-PRESS technique provide a promising approach for the discrimination of GABA from overlapping highly concentrated neurometabolites. As with conventional MR spectroscopy, there are a number of software tools available for fitting and quantification of GABA concentration from edited spectra. Quantification methods that use prior knowledge models - simulated or acquired *in vivo* metabolite basis sets - such as LCModel, AMARES and QUEST in jMRUI can be applied to edited spectra with proper modifications to basis sets and control parameters. In contrast, GABA-analysis specific tools such as the Gannet software (Edden *et al.*, 2013) are custom-written to perform both preprocessing and quantification of MEGA-PRESS data. However, no comparison of the main software tools currently available has been published to date. Furthermore, to date no comparison was made of GABA concentrations derived from edited (MEGA-PRESS) and unedited (MEGA-OFF) spectra. In **chapter 5**, we compare currently available spectral fitting methods, Gannet, AMARES and QUEST to assess the *in vivo* concentration values for GABA and Glx derived from edited (MEGA-PRESS) and unedited (MEGA-PRESS-OFF) spectra. We tested the approach to assess the inter-subject variability in neurotransmitter levels arising from age effects. We found a strong positive correlation between Gannet and QUEST quantification methods, suggesting that the two methods are in good agreement in quantifying GABA acquired by edited and unedited MEGA-PRESS spectra. Due to the good agreement of the Gannet and QUEST derived GABA values, a next step could be to acquire GABA using a regular PRESS sequence with a TE = 68ms and compare the data with MEGA-PRESS acquired data. Such a study could confirm if a regular PRESS sequence with a TE = 68ms could replace

the MEGA-PRESS sequence for reliable GABA quantification. Future studies should also recruit larger numbers of subjects than in our preliminary proof-of-concept study.

Transgenic mouse models have become a vital part of basic research and drug development when it comes to assessing disease stages, disease progression and potential of current and novel treatments. Apart from very few in vitro high resolution NMR spectroscopy studies of transgenic ALS models (Niessen *et al.*, 2007; Choi *et al.*, 2009), *in vivo* ^{1}H-MRS studies of mouse models of ALS remain limited (Lei *et al.*, 2018). Furthermore, previous *in vivo* MRS studies on transgenic ALS mouse models have not consider the age-dependent neurometabolic alterations in various motor regions associated with ALS pathology. In addition, these studies suffer from sensitivity and quantification issues innate to all *in vivo* MRS applications. In **chapter 6**, we have monitored metabolic alterations in the motor cortex and hindbrain of SOD1^{G93A} mice at seven time points postpartum.

Using T2-weighted MRI, we were able to visualize the previously reported hyperintensities observed in multiple brainstem nuclei of these mice (Evans *et al*, 2014; Caron *et al.*, 2015). We confirmed the intensity changes with increased T2 relaxation values in brainstem motor nuclei V, VII and XII. The observed hyperintensities in these motor nuclei are associated with the formation of vacuoles rather than motoneuronal loss (Caron *et al.*, 2015). In fact, vacuolization, which is primarily due to abnormal and swollen mitochondria, has been detected as early as 30 days postpartum in dendrites and proximal axons of spinal motor-neurons (Kong *et al.*, 1998; Bendotti *et al.*, 2001) before the loss of motor neurons cell bodies and the appearance of a glial reaction [Belndotti *et al.*, 2004]. However, Evans *et al* suggest that another possibility for the T2 hyperintensities may be increased astrocytosis and microgliosis (Evans *et al.*, 2014). Similar MRI findings have been reported in human ALS patients, with hypointensities evident on T1-weighted MR images and hyperintensities on T2-weighted MRI along the cortico-spinal tract (Ellis *et al.*, 1999; Waragai *et al.*, 1997). However, in patients the basis of this signal change is not entirely clear at present.

Notably, neurometabolic changes specific to SOD1^{G93A} mice were detected in both the motor cortex and brainstem before the onset of motor symptoms. With the progression of the disease, other neurometabolic alterations further evolved with the appearance of motor symptoms originating from the brainstem and motor cortex of these mice. The neurometabolic alterations observed in our study are mostly consistent with the underlying cellular responses of ALS that evolve with disease progression. Despite the complexity of disease progression changes were seen for NAA, Glx, GABA, Cr, myo-inositol and Tau concentrations.

The most significant finding from this study was the detection of gradual decrease in creatine levels in the hindbrain starting from the pre-symptomatic age of 70 days postpartum. This finding was not previously reported in this mouse model using ^{1}H-MRS. Using High Performance Liquid Chromatography (HPLC), Browne *et al* reported normal creatine levels in 30-day postpartum SOD1^{G93A} mice but observed a 47% decreased creatine in the spinal cord at late presymptomatic stages. They further reported reduction in ADP and ATP levels in the 60 day postpartum SOD1^{G93A} spinal cords. Such changes in the brain of asymptomatic SOD1^{G93A} mice may reflect impaired energy metabolism, which could possibly be due to several causes:

1. Depletion of adenosine triphosphate (ATP); previously observed in SOD1^{G93A} mice (Browne *et al.*, 2006).
2. Depletion of cortical and subcortical glucose metabolism; observed in ALS patients (Ludolph *et al.*, 1992).
3. Hypermetabolism; FDG-PET showed increased metabolism in the brainstem of ALS patients (Cistaro *et al.*, 2012).

Therefore, our finding of decreased creatine level in the hindbrain of SOD1^{G93A} mice may be due to above mentioned causes. In a recent publication, Atassi *et al.* observed a decrease in creatine in the left precentral gyrus of ALS patients compared to healthy controls (Atassi *et al.*, 2017). Beneficial effects of ketogenic diet through improvements in mitochondrial energy production has previously been shown in SOD1^{G93A} mice (Zhao *et al.*, 2006). They observed that ketogenic diet fed SOD1^{G93A} mice maintained motor function longer than mice fed a standard rodent diet and had more intact motor neurons in the lumbar spinal cord. They further reported the restoration of rotenone inflicted inhibition of the mitochondrial Complex I by ketone bodies. Our observation and the available evidence indicating that ALS pathology is also related to impaired energy metabolism in motor neurons, prompted us to assess the efficacy of using coconut oil as a natural ketogenic supplement in SOD^{G93A} mice' diet. Results revealed that coconut oil supplementation together with the regular diet delayed disease symptoms (including MR-detectable biomarkers), enhanced motor performance, and prolonged survival in the SOD1^{G93A} mouse model. A recent study by Blasco *et al.* reported that higher caloric intake improves survival and low cholesterol levels might be harmful in ALS patients (Blasco *et al.*, 2017). In this regard, our results may ecourage to initiate a clinical trial to evaluate if coconut oil is effective in the treatment of ALS and use MRI/MRS as a monitoring tool.

In this study, we demonstrated that non-invasive *in vivo* ^{1}H-MRS detection of neurometabolic changes in motor neuron abundant regions (i.e. hindbrain and motor cortex) of the ALS SOD1^{G93A} mouse model is possible at magnetic high-field strength (≥ 7T). Such neurometabolic changes preceding symptom-onset in the SOD1^{G93A} mouse model can provide insights into disease onset, progression, identify early diagnostics biomarkers and ultimately assist in discovering targets for therapy.

TDP-43 was discovered as the major component of the ubiquitinated protein aggregates localized in the brain and spinal cord of most patients suffering from ALS and fronto-temporal lobar degeneration. Several mouse models were developed to study TDP-43 pathology with a range of phenotypes and histopathological features mimicking ALS. One of the first mouse models created to mimic TDP-43 pathology expresses the ALS-associated mutation A315T controlled by mouse prion promoter. However, up to date this mouse mode was not characterized by any neuroimaging modalities neither at single time points nor longitudinally. In **chapter 7**, we describe the non–invasive characterization of the hTDP-43^{A315T} mouse model for the first time using PET and MR imaging modalities. **Figure 8.1** summarizes the main findings.

Glucose Uptake FDG-PET	**Lowered glucose metabolism: motor cortex, striatum. Increased glucose metabolism: Midbrain region.**
Neurometablites ^{1}H-MRS	**Early-stage elevated glutamate + glutamine and choline levels in motor and hindbrain regions.**
Diffusion/Perfusion MRI	**Striatum: increase in FA, decrease in RD. decrease in RD was present in the left motor cortex. significant increase in MD in the brainstem region. No significant changes in perfusion.**
Cytoplasmic inclusions	**Increased nuclear clearance of normal TDP-43 in older, symptomatic mice (18 m). Cytoplasmic aggregates positive for phosphorylated TDP-43 in the cortex of symptomatic 18 month mice.**
Body Weight	**The weight of the mice significantly increased with age, but did not differ compared to controls.**
Motor symptoms and Survival	**Disease onset and duration highly variable. Mean age at symptom development was 310 ± 172 days and mice survived on average 78 ± 83 days following onset of symptoms. In general, the median survival increased to 480 days when mice were on a gel diet.**

Figure 8.1. Multimodal phenotype characterization: TDP-43-^{A315T} mice. Summary of major findings from the study. Abbrev: FA: fractional anisotropy, RD: radial diffusion, MD: mean diffusion.

^{18}F-FDG PET showed significantly lowered glucose metabolism in the motor and somatosensory cortices of hTDP-43^{A315T} mice whereas metabolism was elevated in the region covering the bilateral substantia nigra, reticular and amygdaloid nucleus between 3 and 7 months of age, as compared to controls. MRS results showed significant changes in Glx and choline levels in the motor cortex and hindbrain of hTDP-43^{A315T} mice compared to controls. Diffusion MRI indices indicated transient changes in different motor areas of the brain in hTDP-43^{A315T} mice around 14 months of age.

Ubiquitin positive cytoplasmic inclusions are a key pathological feature of ALS. The TDP-43 protein has been implicated in the sporadic form of ALS since ubiquitin inclusions co-localized with immunoreactive TDP-43 have been shown to alter nuclear/cytoplasmic localization in sporadic ALS autopsy specimens (Arai *et al.*, 2006, Neumann *et al.*, 2006). In the hTDP-43^{A315T} model, ubiquitin positive cytoplasmic inclusions were reported to be found in neurons of the spinal cord and brainstem but not in the cortex. Up to now, no ubiquitin positive TDP-43 aggregates were observed in the hTDP-43^{A315T} motor cortex. In collaboration with Dr. Dietmar Thal, we were able to show the presence of cytoplasmic TDP-43 proteinaceous inclusions in the cortex of symptomatic, late stage hTDP-43^{A315T} mice. This observation further confirms that the symptomatic phenotype in hTDP-43^{A315T} mice is related to altered TDP-43 function and has important implications for understanding ALS pathogenesis.

A summary of the MRS data from ALS patients and transgenic mouse models from this thesis is shown in **Table 8.1**. Patient MRS data are from a crossectional study compared to healthy volunteers.

Transgenic mice data are from longitudinal studies compared to their non-transgenic littermates. Decreased NAA and increased myo-inositol was observed in motor cortices of both patients and SOD1^{G93A} mice. Glx on the other hand was increased in patients and decreased in SOD1^{G93A} mice, while TDP-43^{A315T} mice also showed an increase at early time points. Increased choline was also detected at two distinct time point for the TDP^{A315T} mice.

Table 8.1: Clinical and preclinical MRS results

Group	MRS Observations
ALS Patients	Region: Motor cortex: NAA↓, Glx↑, mIns↑
SOD1^{G93A} mice	Region: Motor cortex: NAA↓, Glx↓, Tau↑ Region: Hindbrain: NAA↓, Glx↓, mIns↑, GABA↑(P70)
hTDP43^{A315T} mice	Region: Motor cortex: Glx↑, Cho↑ Region: Hindbrain: Glx↑(2 month), Glx↓(14 month), Cho↑

Imaging of the brainstem and spinal cord is especially difficult both in humans and in animal models. MR spectroscopy of the brainstem is a challenging task especially in the hindbrain due to its deep brain placement, small size of the area of interest and close proximity to bone structures. However, it has a large potential interest especially in the study of degenerative processes and tumors involving this brain area. Even though brainstem region structures are mainly affected in ALS mouse models, most *in vivo* MRS studies so far have not examined the longitudinal evolution of neurometabolites in this region. The use of a two-coil system; linearly polarized resonator for transmission combined with a mouse brain surface coil for receiving, acquisition with high number of averages and proper positioning of the mouse head enabled us to acquire high quality MR spectra from the brainstem region. Further improvements might be possible due to the development of new hardware components like cryogen-cooled surface coils.

8.2   Limitations and Future Perspectives

Studies presented in this thesis have a few limitations which needs to be discussed. In ALS, degeneration of motor neurons in the motor cortex leads to upper motor neuron abnormalities. Loss of motor neurons in the brain stem and spinal cord causes muscle atrophy, weakness, and fasciculation. In our study, we investigated the neurometabolic profiles from only the motor cortex, mainly due to time restrictions. Furthermore, in our clinical study, only the left motor cortex was selected. However, investigators should consider that motor neuron dysfunction in ALS may be asymmetrical and MRS findings can be unilateral or, if bilateral they can be more severe on a given brain hemisphere. Therefore, future MRS studies should preferentially be conducted bilaterally.

In addition, the question of data reproducibility needs to be addressed, particularly as the alterations in metabolites in neurodegeneration have been shown to be often subtle, and the detection of early neurometabolic alterations requires greater sensitivity. The conventional single voxel MRS technique presented in our clinical studies samples a volume of about 8 cm^3, in which presumably millions of neurons and glial cells are present. The neurometabolite signal is therefore an average across the whole-volume, and is not capable of detecting alterations in the distribution of metabolites across cell types or small anatomical structures. These partial volume effects must be taken into consideration when interpreting the data.

A common observation made in this thesis with respect to the aging study and clinical-preclinical ALS studies is the reduction of NAA. However, the interpretation of the significance of measuring reduced NAA is crucial for understanding the underlying condition. In 2015, Norsemen and co-workers reported the accumulation of NAA not only in neuronal tissue (grey matter) but also in myelin (white matter) and oligodendrocytes (Nordengen et al., 2015). Hence, their data suggest that NAA may not be a specific marker for neurons. These findings also implicate that NAA peaks visible in the MR spectrum reflect not only the neuronal density but also the state of oligodendrocyte and myelin. Therefore, it is reasonable to assume that a reduction of NAA detected in this thesis may not necessarily be exclusive to neuronal loss. Since NAA is produced in neuronal and oligodendrocytic mitochondria, (Patel et al., 1979; Madhavarao et al., 2003; Arun et al., 2009; Nordengen et al., 2015) the detected decrease in NAA may also indicate mitochondrial dysfunction (Clark et al., 1998), which is thought to play an important role in ALS pathogenesis. Considering our and previous findings, we suspect that the NAA decrease in ALS patients and mouse models of ALS measured by ^{1}H-MRS may in fact indicate a multi-factorial pathology.

In fact, utilization of whole-brain magnetic resonance spectroscopic imaging (MRSI) with image segmentation methods have the potential to estimate the grey and white matter NAA contribution from a particular VOI (Gasparovic et al., 2006). By using such methods coupled with other advanced MRS techniques such as diffusion MRS (DW-MRS) (Najac et al., 2016) we may be able to better understand the compartmentalization of NAA in the brain. The DW-MRS technique is currently being implemented at our site.

Apart from the technical limitations, the ALS clinical study was also subjected to patient recruitment limitations, meaning that the patient cohorts available for the study are lower due to subject-related barriers such as disease severity, age, family objections, and social circumstances. However, these recruitment barriers are not exclusive to patients but also affect the recruitment of control subjects. Furthermore, the crossectional nature of the study reflect different stages of the disease, making the interpretation of the data more complex.

Regarding the preclinical studies, our group-based acquisition protocol is one of the main limitations in this thesis. To improve the detection of disease-related changes, one might opt for a dynamic acquisition protocol based on monitoring individual animals. However, this strategy may be challenging concerning logistics and statistical analysis. Another limitation of the preclinical studies is the relatively small sample size (due to availability, breeding issues, mortality) and, variability of onset of disease between animals and mortality issues/diet.

It is reasonable to assume that the variations in neurometabolites reported in clinical and preclinical MRS studies could be due to sensitivity (coils used, echo-times, number of averages) and spatial

resolution (voxel size, placement) differences as well as the variability of the SOD1^{G93A} mouse model (gene promoters, gene copy number, overexpression rate, gender etc.) (Ludolph *et al.*, 2010).

Despite the limitations, the work presented in this thesis has demonstrated that *in vivo* MR spectroscopy can provide valuable information on normal aging and ALS. The significance of the information could be further maximized by combining PET with multi-parametric MR techniques as well as advanced data acquisition and data processing protocols.

MRS coupled with other modalities has the potential for monitoring disease state and therapeutic interventions in preclinical ALS models and in patients. There is considerable evidence from the work presented in this thesis and from previous studies that support the value of MRS in ALS.

Although MRS is a promising technique, it is not yet widely implemented in clinical routine. This may be due to several reasons. The technical complexity of the method requires expert knowledge in for the acquisition, processing and interpretation of the data, which is regarded as the most limiting factor for the clinical use of MRS. Therefore, new methods are needed that simplify and/ or automate the use and interpretation of MRS and allow clinical centers with less experience to use the technique whenever its information may be of relevance for patient management.

This need is currently addressed by several academic and industrial initiatives. For example, BrainSpec is a recently established health technology company that aims to diagnose brain disorders using an efficient approach that involves MRS and clinically applicable software. The Company was formed through the iHub at Brigham & Women's Hospital with Dr. Alexander Lin, the director of the hospital's Center for Clinical Spectroscopy and Alex Zimmerman at Harvard Business School. BrainSpec and other initiatives aim to address the current limitations of the use of MRS in a clinical setting by developing a fully automated post-processing pipeline for MRS and assisting clinicians in the analysis and interpretation of MRS data. Those approaches combine linear combination model based post-processing with a highly intuitive and user-friendly front-end web-based user interface. This combination allows for high analytical performance while maintaining ease of use. This results in reduced processing time, leading to higher throughput and lower costs.

8.3   Conclusion

Neuroimaging and neurospectroscopy offer excellent ways to investigate structural and metabolic aspects of ALS-associated pathology in transgenic animal models and clinical populations alike. An important feature of non-invasive procedures concerns the possibility of performing longitudinal investigations and using different techniques on one and the same subject, allowing for a simultaneous or step-wise analysis of structure and function.

MR is still an evolving technology, and more revelations are undoubtedly around the corner. At present, MRI has become the most versatile and widely used imaging modality available today. The combination of MRI and MR spectroscopy enables us to obtain information from the molecular level through cells, tissues, animal models, and humans. The necessity of animal models in research dictates the development of dedicated animal research systems. With proper use and quality control, MR offers the

potential for greatly reducing the number of animals that would otherwise be required to move forward in our understanding of intact biological systems.

8.4   References

Atassi N, Xu M, Triantafyllou C, Keil B, Lawson R, Cernasov P, Ratti E, Long CJ, Paganoni S, Murphy A, Salibi N, Seethamraju R, Rosen B, Ratai EM. Ultra high-field (7tesla) magnetic resonance spectroscopy in Amyotrophic Lateral Sclerosis. *PLoS One*. 2017; 12(5).

Arai T, Hasegawa M, Akiyama H, Ikeda K, Nonaka T, Mori H, Mann D, Tsuchiya K, Yoshida M, Hashizume Y, Oda T. TDP-43 is a component of ubiquitin-positive tau-negative inclusions in frontotemporal lobar degeneration and amyotrophic lateral sclerosis. Biochem Biophys Res Commun. 2006 Dec 22; 351(3):602-11.

Bendotti C, Calvaresi N, Chiveri L, Prelle A, Moggio M, Braga M, *et al*. Early vacuolization and mitochondrial damage in motor neurons of FALS mice are not associated with apoptosis or with changes in cytochrome oxidase histochemical reactivity. Journal of the neurological sciences. 2001; 191(1–2):25–33.

Bendotti C, Carri MT. Lessons from models of SOD1-linked familial ALS. Trends Mol Med. 2004; 10(8):393–400.

Brand, A., Richter-Landsberg, C., and Leibfritz, D. (1993). Multinuclear NMR studies on the energy metabolism of glial and neuronal cells. *Dev. Neurosci.* 15, 289–298.

Brooks BR, Miller RG, Swash M, Munsat TL. El Escorial revisited: revised criteria for the diagnosis of amyotrophic lateral sclerosis. Amyotroph Lateral Scler Other Motor Neuron Disord. 2000; 1(5):293–9.

Caron I, Micotti E, Paladini A, *et al*. Comparative Magnetic Resonance Imaging and Histopathological Correlates in Two SOD1 Transgenic Mouse Models of Amyotrophic Lateral Sclerosis. *PLoS One*. 2015; 10(7):e0132159. Published 2015 Jul 1. doi:10.1371/journal.pone.0132159.

Cervo A., Cocozza S., Saccà F., Giorgio S. M. D. A., Morra V. B., Tedeschi E., *et al*. (2015). The combined use of conventional MRI and MR spectroscopic imaging increases the diagnostic accuracy in amyotrophic lateral sclerosis. *Eur. J. Radiol.* 84 151–157.

Choi JK, Kustermann E, Dedeoglu A, *et al*. Magnetic resonance spectroscopy of regional brain metabolite markers in FALS mice and the effects of dietary creatine supplementation. Eur J Neurosci 2009; 30: 2143–2150.

Choi, J. K., Dedeoglu, A., and Jenkins, B. G. (2007). Application of MRS to mouse models of neurodegenerative illness. *NMR Biomed.* 20, 216–237.

Cheong I, Marjańska M, Deelchand DK, Eberly LE, Walk D, Öz G. Ultra-High Field Proton MR Spectroscopy in Early-Stage Amyotrophic Lateral Sclerosis. Neurochem Res. 2017; 42(6):1833-1844.

Costa J, Swash M, de Carvalho M. Awaji criteria for the diagnosis of amyotrophic lateral sclerosis: a systematic review. Arch Neurol. 2012; 69(11):1410–6.

Ding, X.Q., Maudsley, A.A., Sabati, M., Sheriff, S., Schmitz, B., Schütze, M., Bronzlik, P., Kahl, K.G., Lanfermann, H., 2016. Physiological neuronal decline in healthy aging human brain - An *in vivo* study with MRI and short echo-time whole-brain1H MR spectroscopic imaging. NeuroImage 137, 45–51.

Double KL, Halliday GM, Kril JJ, *et al*. Topography of brain atrophy during normal aging and Alzheimer's disease. *Neurobiol Aging* 1996; 17:513-521.

Ellis CM, Simmons A, Dawson JM, Williams SC, Leigh PN. Distinct hyperintense MRI signal changes in the corticospinal tracts of a patient with motor neuron disease. Amyotroph Lateral Scler Other Motor Neuron Disord. 1999; 1: 41 – 4. 42.

Evans MC, Gaillard PJ, de Boer M, Appeldoorn C, Dorland R, Sibson NR, Turner MR, Anthony DC, Stolp HB. CNS-targeted glucocorticoid reduces pathology in mouse model of amyotrophic lateral sclerosis. Acta Neuropathol Commun. 2014 Jun 13; 2:66.

Filippi, M. *et al*. EFNS guidelines on the use of neuroimaging in the management of motor neuron diseases. *Eur. J. Neurol.* **17**, 526-e20 (2010).

Foerster BR, Carlos RC, Dwamena BA, *et al*. Multimodal MRI as a diagnostic biomarker for amyotrophic lateral sclerosis. *Annals of Clinical and Translational Neurology*. 2014; 1(2):107-114.

Grachev, I.D., Apkarian, A.V., 2001. Chemical network of the living human brain: Evidence of reorganization with aging. Cogn. Brain Res. 11, 185–197.

Griffin, J. L., Bollard, M., Nicholson, J. K., and Bhakoo, K. (2002). Spectral profiles of cultured neuronal and glial cells derived from HRMAS (1)H NMR spectroscopy.

Han J, Ma L. Study of the features of proton MR spectroscopy ((1)H-MRS) on amyotrophic lateral sclerosis. *J Magn Reson Imaging*. 2010; **31**(2):305-8.

Kalra S, Hanstock CC, Martin WR, Allen PS, Johnston WS. Detection of cerebral degeneration in amyotrophic lateral sclerosis using high-field magnetic resonance spectroscopy. Arch Neurol. 2006 Aug; 63(8):1144-8.

Kalra S, Seres P, Choi C. *In vivo* quantification of excitatory and inhibitory neurotransmitters in amyotrophic lateral sclerosis. Proceedings of the 21st Annual Meeting of the International Society for Magnetic Resonance in Medicine; Salt Lake City, UT, USA. 2013. p. 1017.

Kantarci K, Smith GE, Ivnik RJ, *et al*. 1H magnetic resonance spectroscopy, cognitive function, and apolipoprotein E genotype in normal aging, mild cognitive impairment and Alzheimer's disease. *J Int Neuropsychol Soc*. 2002; 8(7):934-42.

Kong J, Xu Z. Massive mitochondrial degeneration in motor neurons triggers the onset of amyotrophic lateral sclerosis in mice expressing a mutant SOD1. J Neurosci. 1998; 18(9):3241–50.

Lei H, Dirren E, Poitry-Yamate C, Schneider BL, Gruetter R, Aebischer P. Evolution of the neurochemical profiles in the G93A-SOD1 mouse model of amyotrophic lateral sclerosis. J Cereb Blood Flow Metab. 2018 Feb 5:271678X18756499.

Lim KO, Spielman DM. Estimating NAA in cortical gray matter with applications for measuring changes due to aging. *Magn Reson Med* 1997; 37:372-377.

Lombardo F., Frijia F., Bongioanni P., Canapicchi R., Minichilli F., Bianchi F., *et al*. . (2009). Diffusion tensor MRI and MR spectroscopy in long lasting upper motor neuron involvement in amyotrophic lateral sclerosis. Arch. Ital. Biol. 147, 69–82.

Ludolph AC, Bendotti C, Blaugrund E, Chio A, Greensmith L, Loeffler JP, Mead R, Niessen HG, Petri S, Pradat PF, Robberecht W, Ruegg M, Schwalenstöcker B, Stiller D, van den Berg L, Vieira F, von Horsten S. Guidelines for preclinical animal research in ALS/MND: A consensus meeting. *Amyotroph Lateral Scler*. 2010;11(1-2):38-45.

Matsumae M, Kikinis R, Morocz I, *et al*. Age-related changes in intracranial compartment volumes in normal adults assessed by magnetic resonance. *J Neurosurg* 1996; 84:982-991.

Modrego PJ, Fayed N, Sarasa M. Magnetic resonance spectroscopy in the prediction of early conversion from amnestic mild cognitive impairment to dementia: a prospective cohort study. BMJ Open. 2011 Feb 23; 1(1).

Mullins PG, McGonigle DJ, O'Gorman RL, Puts NA, Vidyasagar R, Evans CJ, and Cardiff Symposium on MRS of GABA. Edden RA Neuroimage. 2014 Feb 1; 86():43-52.

Neumann M, Sampathu DM, Kwong LK, Truax AC, Micsenyi MC, Chou TT, Bruce J,Nicolay K *et al*, Diffusion NMR spectroscopy. NMR Biomed, 14:94-111 (2001).

Niessen HG, Debska-Vielhaber G, Sander K, *et al*. Metabolic progression markers of neurodegeneration in the transgenic G93A-SOD1 mouse model of amyotrophic lateral sclerosis. Eur J Neurosci 2007; 25: 1669–1677.

Palombo M, Shemesh N, Ronen I, Valette J, Insights into brain microstructure from *in vivo* DW-MRS, NeuroImage (2017), doi: 10.1016/j.neuroimage.2017.11.028.

Pohl C, Block W, Karitzky J, Träber F, Schmidt S, Grothe C, Lamerichs R, Schild H, Klockgether T. Proton magnetic resonance spectroscopy of the motor cortex in 70 patients with amyotrophic lateral sclerosis. Arch Neurol. 2001 May; 58(5):729-35.

Porges EC, Woods AJ, Lamb DG, Williamson JB, Cohen RA, Edden RAE, Harris AD.Impact of tissue correction strategy on GABA-edited MRS findings. Neuroimage.2017 Nov 15; 162:249-256.

Puts NAJ, Edden RAE. *In vivo* magnetic resonance spectroscopy of GABA: a methodological review. Prog Nucl Magn Reson Spectrosc. 2012 Jan; 60:29–41.

Ronen I and Valette J, Diffusion-weighted magnetic resonance spectroscopy. eMagRes. Volume 4. John Wiley & Sons, Ltd, Chichester, United Kingdom, p 733-750 (2015).

Ross AJ, Sachdev PS, Wen W, Brodaty H. Longitudinal changes during aging using proton magnetic resonance spectroscopy. J Gerontol A Biol Sci Med Sci. 2006 Mar; 61(3):291-8. PubMed PMID: 16567380.

Russell WMS, Burch RL: The Principles of Humane Experimental Technique. London, Methuen, 1959.

Schuck T, Grossman M, Clark CM, McCluskey LF, Miller BL, Masliah E, Mackenzie IR, Feldman H, Feiden W, Kretzschmar HA, Trojanowski JQ, Lee VM. Ubiquitinated TDP-43 in frontotemporal lobar degeneration and amyotrophic lateral sclerosis. Science. 2006 Oct 6; 314(5796):130-3. PubMed PMID: 17023659.

Simic G, Kostovic I, Winblad B, Bogdanovic N. Volume and number of neurons of the human hippocampal formation in normal aging and Alzheimer's disease. *J Comp Neurol* 1997; 379:482-494.

Simmons, M. L., Frondoza, C. G., and Coyle, J. T. (1991). Immunocytochemical localization of N-acetyl-aspartate with monoclonal antibodies. *Neuroscience* 45, 37–45.

Tumati S, Opmeer EM, Marsman JC, *et al*. Lower Choline and Myo-Inositol in Temporo-Parietal Cortex Is Associated With Apathy in Amnestic MCI. *Front Aging Neurosci*. 2018; 10:106.

Turner MR, Kiernan MC, Leigh PN, *et al*. Biomarkers in amyotrophic lateral sclerosis. Lancet Neurol 2009; 8: 94–109.

Turner, M. R. & Modo, M. Advances in the application of MRI to amyotrophic lateral sclerosis. *Expert Opin. Med. Diagn.* **4**, 483–496 (2010).

Unrath A, Ludolph AC, Kassubek J. Brain metabolites in definite amyotrophic lateral sclerosis. A longitudinal proton magnetic resonance spectroscopy study. J Neurol. 2007 Aug; 254(8):1099-106.

Verma G, Woo JH, Chawla S, *et al*. Whole-brain analysis of amyotrophic lateral sclerosis by using echo-planar spectroscopic imaging. *Radiology*. 2013; 267(3):851-7.

Waragai M. MRI and clinical features in amyotrophic lateral sclerosis. Neuroradiology. 1997; 39:847 – 51. Evans MC, Serres S, Khrapitchev AA, *et al*. T_2-weighted MRI detects presymptomatic pathology in the SOD1 mouse model of ALS. *J Cereb Blood Flow Metab*. 2014; 34(5):785-93.

Zhao, Z., Lange, D. J., Voustianiouk, A., MacGrogan, D., Ho, L., Suh, J., *et al*. (2006). A ketogenic diet as a potential novel therapeutic intervention in amyotrophic lateral sclerosis. *BMC Neurosci.* 7:29. doi: 10.1186/1471-2202-7-29

Personal Contribution

All experiments reported in chapter 4, 5 and 6 were designed, conducted, analyzed and reported by Akila Weerasekera with the supervision of Professor Uwe Himmelreich. The study reported in chapter 2 was conducted in collaboration with Dr. Oron Levin and Professor Stephan Swinnen. Dr. Levin and Akila Weerasekera contributed equally to the data processing, analysis and writing of the manuscript. The study reported in chapter 7 was designed by Akila Weerasekera and Melissa Crabbé with the supervision of Professor Himmelreich and Professor Philip Van Damme. MRI data acquisition and processing was done by Akila Weerasekera, PET data acquisition, processing and statistical analysis was performed Melissa Crabbé. Histological analysis was performed by Sandra Tomé. Akila Weerasekera and Melissa Crabbé contributed equally to overall analysis of data and the writing of the manuscript.

Scientific Acknowledgement

Chapter 3

Chapter 4

Chapter 5

Chapter 6

Chapter 7

Conflict of Interest

The candidate declares that there are no other conflicts of interest.

Curriculum Vitae

Personal details

Name:	Akila Sasantha Weerasekera
Address:	Mgr Van Wayenberghlaan 40/102, Leuven 3000, Belgium
(Mobile) Phone number :	+32-488879091
E-mail:	akila.weerasekera@kuleuven.be
	akila.weerasekera4@gmail.com
Date and place of birth:	April 10th, 1979, Colombo, Sri Lanka
Nationality:	Sri Lankan

Education

2014-2019	Doctor of Biomedical Sciences, University of Leuven, Leuven, Belgium
2007-2009	Master of Science in Chemistry California State University Eastbay, Hayward, CA, USA
2001-2006	Bachelor in Chemistry Minnesota State University, Moorhead, MN, USA

Scholarships

Marie Curie Fellow

TRANSACT, a European Union funded FP7-PEOPLE Marie Curie Initial Training Network (PITN-GA-2012-316679) with the aim of Transforming Magnetic Resonance Spectroscopy into a Clinical Tool.

Scientific Publications

Published in peer-reviewed journals

Weerasekera A, Sima DM, Dresselaers T, Van Huffel S, Van Damme P, Himmelreich U. Non-invasive assessment of disease progression and neuroprotective effects of dietary coconut oil supplementation

in the ALS SOD1(G93A) mouse model: A (1)H-magnetic resonance spectroscopic study. *Neuroimage Clin*. 2018; 20:1092-1105.

de Laat B, **Weerasekera A**, Leurquin-Sterk G, Bormans G, Himmelreich U, Casteels C, Van Laere K. Glutamatergic Biomarkers for Cocaine Addiction: A Longitudinal Study Using MR Spectroscopy and mGluR5 PET in Self-Administering Rats. *J Nucl Med*. 2018; 59(6):952-959.

Salas IH, **Weerasekera A**, Ahmed T, Callaerts-Vegh Z, Himmelreich U, D'Hooge R, Balschun D, Saido TC, De Strooper B, Dotti CG. High fat diet treatment impairs hippocampal long-term potentiation without alterations of the core neuropathological features of Alzheimer disease. *Neurobiol Dis*. 2018; 113:82-96.

de Laat B, **Weerasekera A**, Leurquin-Sterk G, Gsell W, Bormans G, Himmelreich U,Casteels C, Van Laere K. Effects of alcohol exposure on the glutamatergic system: a combined longitudinal (18) F-FPEB and (1) H-MRS study in rats. Addict Biol. 2018 May 23. doi: 10.1111/adb.12635.

Leurquin-Sterk G, Ceccarini J, Crunelle CL, **Weerasekera A**, de Laat B, Himmelreich U, Bormans G, Van Laere K. Cerebral dopaminergic and glutamatergic transmission relate to different subjective responses of acute alcohol intake: an *in vivo* multimodal imaging study. *Addict Biol*. 2018; 23(3):931-944.

Crabbé M, Van der Perren A, **Weerasekera A**, Himmelreich U, Baekelandt V, Van Laere K, Casteels C. Altered mGluR5 binding potential and glutamine concentration in the 6-OHDA rat model of acute Parkinson's disease and levodopa-induced dyskinesia. *Neurobiol Aging*. 2018; 61:82-92.

Chu W, **Weerasekera A**, Kim CH. On the conformational stability of the smallest RNA kissing complexes maintained through two G·C base pairs. *Biochem Biophys Res Commun*. 2017; 483(1):39-44.

Leurquin-Sterk G, Van den Stock J, Crunelle CL, de Laat B, **Weerasekera A**, Himmelreich U, Bormans G, Van Laere K. Positive Association Between Limbic Metabotropic Glutamate Receptor 5 Availability and Novelty-Seeking Temperament in Humans: An 18F-FPEB PET Study. *J Nucl Med*. 2016; 57(11):1746-1752.

Kruger R, Funk S, Jeppson P, Sawarynski M, Thronson H, **Weerasekera A**, Shastri A. The suitability of the signal difference to noise ratio (SDNR) and signal to noise ratio (SNR) as MRI quality control parameters: An evaluation based on the assessed image quality of 300 clinical MRI scanners. Medical Physics 2002 June; 29(6):1218-1218.

Manuscript in preparation or submitted

Weerasekera A, Peeters R, Sima D, Dresselaers T, Sunaert S, De Vocht J, Claeys K, Van Huffel S, Van Damme P, Himmelreich U. (2018). Motor Cortex metabolite alterations in Amyotrophic Lateral Sclerosis assessed *in vivo* using edited and non-edited magnetic resonance spectroscopy. **Under review for publication in Brain Research.**

A.Weerasekera†, M. Crabbé†, Sandra Tomé ,Willy Gsell, Diana Sima, Tom Dresselaers, Christophe Deroose, Sabine Van Huffel, Dietmar Thal, Philip Van Damme, Koen Van Laere, Uwe Himmelreich. (2018). Functional changes observed by positron emission tomography and magnetic resonance imaging precede nuclear clearance and aggregation of transactive-response DNA-binding protein TDP-43 in hTDP-43A315T transgenic mice. **In preparation**.

Oron Levin*, **Akila Weerasekera***, Brad R. King2, Kirstin F. Heise, Diana Sima, Peter van Ruitenbeek P, Lize Heremans2, Ronald Peeters, Ian Greenhouse, Koen Cuypers, Sabine Van Huffel, Uwe Himmelreich† , Stephan P. Swinnen† .(2018). The neurometabolic correlates of motor performance across the adult lifespan: a study on the effects of age and gender. **In preparation**.

Matteo Riva, Roxanne Wouters, **Akila Weerasekera**, Sarah Belderbos, David Nittner, Thaïs Baert, Roberto Giovannoni, Willy Gsell, Uwe Himmelreich, An Coosemans and Marc Van Ranst. (2018). CT-2A neurospheres culture enriches tumor stem cells and increase immune suppression in a high-grade glioma mouse model. **Under review for publication in Journal for ImmunoTherapy of Cancer**.

Abstracts in proceedings of conferences

Akila Weerasekera, Diana Sima, Ronald Peeters, Tom Dresselaers, Oron Levin, Stephan Swinnen, Sabine Van Huffel, Uwe Himmelreich. Comparison of GABA and Glx Quantification from Edited and Unedited MR Spectra – assessment of age effects: ISMRM, Paris, France 2018.

Bart de Laat**, Akila Weerasekera***, Gwen Schroyen, Cesar Molinos, Uwe Himmelreich, Cindy Casteels, Koen Van Laere, Willy Gsell. Acute changes in rat brain metabolism after intravenous administration of alcohol, cocaine, and nicotine: A simultaneous PET/MR study with dynamic ^{1}H-MRS and continuous infusion ^{18}FDG: ISMRM, Paris, France 2018.

Akila Weerasekera, Melissa Crabbé*, Willy Gsell, Diana Sima, Tom Dresselaers, Christophe Deroose, Sabine Van Huffel, Philip Van Damme, Koen Van Laere, Uwe Himmelreich. Non-invasive assessment of the onset and progression of amytrophic lateral sclerosis in a novel hTDP-43^{A315T} mouse model: findings from a PET-MR study: EMIM, San Sebastian, Spain 2018.

Akila Weerasekera, Diana Sima, Philip Van Damme, Tom Dresselaers, Sabine Van Huffel, Uwe Himmelreich. Non-Invasive Longitudinal Anatomical and Metabolic MR characterization of Transgenic Amyotrophic Lateral SclerosisTDP-43^{A315T} and SOD1^{G93A} Mouse Models. EMIM, Cologne, Germany 2017.

Akila Weerasekera, Diana Sima, Philip Van Damme, Tom Dresselaers, Sabine Van Huffel, Uwe Himmelreich. Non-invasive assessment of progression and therapy in in amyotrophic lateral sclerosis (ALS) mice using Magnetic Resonance Imaging and Spectroscopy: ESMRMB, Vienna, Austria, 2016.

Akila Weerasekera, Diana Sima, Philip Van Damme, Tom Dresselaers, Sabine Van Huffel, Uwe Himmelreich. Non-invasive assessment of metabolic therapy of amyotrophic lateral sclerosis (ALS) mice using Magnetic Resonance Spectroscopy (MRS): coconut oil as a potential novel therapeutic

intervention and MRS as a diagnostic and therapy monitoring tool in ALS: Knowledge for Growth, Ghent, Belgium 2016.

Akila Weerasekera, Diana Sima, Philip Van Damme, Tom Dresselaers, Sabine Van Huffel, Uwe Himmelreich. Potential metabolic markers for progression of neurodegeneration in the transgenic TDP-43^{A315T}, SOD1^{G93A} mouse models and patients of amyotrophic lateral sclerosis using magnetic resonance spectroscopy: YBMRS, Blankenberge, Belgium 2015.

Akila Weerasekera, Diana Sima, Philip Van Damme, Tom Dresselaers, Sabine Van Huffel, Uwe Himmelreich. Non-invasive assessment of the onset and progression of amyotrophic lateral sclerosis in transgenic animal models using magnetic resonance spectroscopy. Belgian Molecular Imaging Community (BMIC) conference. Brussels, Belgium 2015.

Akila Weerasekera, Diana Sima, Philip Van Damme, Tom Dresselaers, Sabine Van Huffel, Uwe Himmelreich. Non-invasive assessment of the onset and progression of amyotrophic lateral sclerosis in transgenic animal models using magnetic resonance spectroscopy: YBMRS, Spa, Belgium 2014.

Thesis guidance

Cop-promoter
Joint-master thesis of Jeroen Buvé and Joren Bosman (2017)

Neurometabolic profile of the healthy aging brain as a predictor of age-related changes in motor performance.